HIGH FREQUENCY ACOUSTIC BACKSCATTERING ENHANCEMENTS FOR FINITE CYLINDRICAL SHELLS IN WATER AT OBLIQUE INCIDENCE

By

SCOT FRANKLIN MORSE

A dissertation submitted in partial fulfillment of
the requirements for the degree of

DOCTOR OF PHILOSOPHY

WASHINGTON STATE UNIVERSITY
Department of Physics

AUGUST 1998

To the Faculty of Washington State University:

The members of the Committee appointed to examine the dissertation of SCOT FRANKLIN MORSE find it satisfactory and recommend that it be accepted.

_____
Chair

_____

_____

_____

ACKNOWLEDGMENTS

This dissertation is the result of research performed at Washington State University, in Pullman, Washington which I began in 1992. In coming to this point in my life, truly I can give thanks to only one—thank you God for my life and all the blessings you've given me. Thank you for allowing and equipping me to do something I enjoy. It seems I have learned more about the Truth these last 6 years than anything having to do with science. And I believe that is as it should be,

For the wisdom of this world is foolishness with God —1 Cor. 3:19.

Thank you Mom and Dad for always supporting me. I took you up on your offer to support me for as long as I wanted to go to school. Thank you Beth, my wife, for your love.

This dissertation is not, of course, something I could have done alone. Thank you Professor Marston for all the work you've put into me. You truly care about your students. Thank you David Ermer for putting up with me over the years and for all the philosophical discussions over coffee. I would never have studied as much as I did for prelims if it weren't for you. Thank you Greg Kaduchak for your friendship and all the help you've given me with many aspects of this work. Greg contributed significantly to the work involving the approximate partial wave series calculations (Chapters 2 and 5) and the synthetic aperture images (Chapter 3). I would also like to thank all the members of the group who have been a part of my life these years: John Stroud, Tom Asaki, David Thiessen, Karen Gipson, Chris Kwiatkowski, Mark Marr-Lyon, Todd Hefner, Florian Blonigen and Julie Foster. Without all your help I probably wouldn't have been able to get anything to run. Thank you Bill Alspach. You taught me how to use a machine shop and helped me in building many pieces of my experiments; but having known you is what I value. Thank you Mickey Daniels, Marilyn Burns and Shirley Kanzler for all the administrative and business work that you have done for me, so often without notice.

This research was supported by the Office of Naval Research.

HIGH FREQUENCY ACOUSTIC BACKSCATTERING ENHANCEMENTS FOR FINITE CYLINDRICAL SHELLS IN WATER AT OBLIQUE INCIDENCE

Abstract

by Scot Franklin Morse, Ph.D.
Washington State University
August 1998

Chair: Philip L. Marston

The scattering of sound by finite cylindrical shells in water is investigated. Both experimental and theoretical examinations are performed which include comparisons of measured backscattering enhancements with a quantitative ray theory and an approximate partial wave series solution. Broadband backscattering experiments are carried out for the full range of tilt angles (measured with respect to the cylinder's axis) to identify regions of enhanced backscattering from moderately thick-walled steel cylindrical shells (having thickness-to-radius ratios of 7.6% and 16.3%). It is found that the backscattering is significantly enhanced when conditions arise such that a generalization of a leaky Lamb wave is launched on the shell. This surface guided wave reflects off the shell truncation, which is flat and perpendicular to the cylinder axis, and reradiates into the backscattering direction. In addition to various helical ray contributions, particularly large enhancements are observed for a ray propagating along the cylinder's meridian. The meridional ray enhancement for the generalization of the lowest order antisymmetric leaky Lamb wave is observed over a large range of tilt angles, nearing end-on incidence in the coincidence frequency region. Coupling conditions are determined which locate the various enhancements in frequency-angle space. High-frequency narrowband backscattering experiments are used to make quantitative measurements of enhancement amplitudes, which agree well with theoretical predictions. For highly oblique tilt angles the meridional ray amplitudes are several times greater than the specular reflection amplitude for scattering from a rigid sphere of like radius. Both air-filled and water-filled cylindrical shells are examined. An abrupt drop in the backscattered meridional ray amplitude is

observed at very high frequencies. This drop is the result of the next antisymmetric leaky Lamb mode and mode conversion upon reflection at the cylinder's end. Simplified calculations display aspects of this threshold behavior. In addition experimental procedures are described for obtaining transient and wide bandwidth backscattering data using a PVDF sheet source in water for frequencies extending up to 1 MHz.

TABLE OF CONTENTS

Page

LIST OF TABLES

LIST OF FIGURES

CHAPTER 1

CHAPTER 2

CHAPTER 3

CHAPTER 6

CHAPTER 7

1

Introduction

1.1 Overview and Motivation

The subject of this investigation concerns the scattering of sound by truncated cylindrical objects in water. Investigations of this sort are clearly not new as the field of acoustic scattering from submerged elastic objects has been of great importance for national defense and safety related purposes since the early part of the century. A large amount of research has been carried out in an attempt to better understand the way sound interacts with structures (both natural and man-made), through scattering and radiation. Applications of this basic research can be found in numerous fields which include: anti-submarine warfare, mine countermeasures, remote sensing, fish identification and counting, and non-destructive evaluation. In these types of fields, with the exception of the last two, the processes of acoustic interaction that have been studied most are found at low frequencies, say below 10 kHz. This is due to a number of factors, one of which is the fact that submarines and ships are large structures with fairly low frequency resonance or modal behavior. Another influencing factor is that the range to the structure of interest is

often somewhat large, on the order of kilometers. But over these distances high frequency sound is attenuated significantly more than low frequency sound. Most of the investigations that relate to the scattering of sound by finite cylindrical objects have been low frequency studies (see Section 2.1 for references to relevant papers); or at least they assume the mechanics of the shell can be adequately modeled by thin shell theories. This typically requires low frequencies, where the wavelength of the incident sound is large in comparison to the thickness of the shell.

With relatively recent advances in microelectronics, data acquisition, array systems and processing, and transducer design, acoustical imaging systems have become popular and are now fairly inexpensive. High frequency -- high resolution systems are now frequently employed in research as well as in industrial applications. Examples of applications include high-resolution side-scan sonar, synthetic aperture sonar and even short range diver hand-held imaging sonar. This increased interest in high-frequency systems brings with it a need to more fully understand acoustic interaction problems at high frequencies. In these high-frequency interaction problems, where the acoustic wavelength can be on the order of the wall thickness in shell-like structures, it is generally not possible to simplify the variations in stress and displacement components across the wall thickness as done in some thin shell theories. As a result full solutions must be used, which take into account the three-dimensional nature of the elasto-dynamical problem. This increases the difficulty of the problem and often hampers the interpretation of results in terms of simple concepts.

One example of a high-frequency application is described in a paper by Kaduchak[1] and in a dissertation by Dodd[2]. In these investigations a high-frequency high-resolution scanning sonar system was used to study the backscattering from freely-flooded submerged finite cylindrical shells over a range of incidence angles. At certain angles a large enhancement was observed which greatly enhanced the visibility of the ends of the cylinder. These enhancements were attributed to the launching of leaky Lamb waves on the shell which reflected off the cylinder truncation and reradiated into the backscattering direction. These results quite clearly demonstrated that at high frequencies, where geometric acoustics effects are commonly thought to dominate the scattering from

structures, elastic wave effects are present and can be significantly stronger than rigid-body-like diffraction effects.

The purpose of this dissertation research is to characterize scattering enhancements for thick finite cylindrical shells and to advance the understanding of the physical processes which are responsible for the observed enhancements. The first step taken toward this goal is to explore the broader conditions under which these enhancements are observable. Much use is made throughout this dissertation of a quantity called a form function, so a brief review is warranted. Scattering from objects is typically very frequency dependent; therefore, most investigations usually quantify the scattering process in terms of the complex pressure response as a function of frequency. In the far field, where the dependence on the distance to the target can be represented in a simple analytic form, this complex pressure is directly related to a dimensionless quantity called a form function, which contains the dependence on the orientation angles of the scatterer and observer with respect to the incident sound. In spherical coordinates the relationship between the scattered pressure and the form function is,

$$p(r, \theta, \phi; \omega, t) = p_{inc}\left(\frac{a}{2}\right) f(\theta, \phi; \omega) \frac{e^{ikr}}{r} e^{-i\omega t} \tag{1.1}$$

where f is the form function. Also p_{inc} is a reference pressure corresponding to the incident pressure amplitude, a is a length scale appropriate for the scatterer (e.g. the radius if the scatterer is a sphere), the set (r, θ, ϕ) defines the spherical coordinate system with respect to a chosen location at the scatterer, $k = \omega/c$ is the wavenumber in the surrounding medium, ω is angular frequency and t is time. This form is appropriate for a monochromatic steady state scattering problem. Using the above convention, the form function magnitude for backscattering from a perfectly rigid sphere is unity in the high frequency limit. This is a convenient choice since the mathematical rigid sphere is commonly used as a reference in scattering theories. Also, hard spheres are frequently used as a standard calibration in actual sonar systems. In cylindrical coordinates, where the spreading of wavefronts is often dominated by an inverse square root dependence on distance, the form function is defined in the following relation:

$$p(\rho, \psi, z;\omega, t) = p_{inc}\sqrt{\frac{a}{2}} f(\psi;\omega)\frac{e^{ik\rho}}{\sqrt{\rho}} e^{i(k_z z-\omega t)} \tag{1.2}$$

where the set (ρ, ψ, z) defines a cylindrical coordinate system. For a cylindrical scatterer a is usually the outer radius of the cylinder. This expression assumes translational invariance along the z direction; as such, only a traveling wave z dependence is found on the right hand side. This is the expected form for an infinitely long cylinder.

In Chapter 2 the scattering response of thick finite cylindrical shells is examined as a function of frequency, through both experiment and theory. Using the method of impulse excitation (a short duration pressure pulse, either unipolar or bipolar, having broad spectral content), the response of the target can be measured over a broad range of frequencies during a single experiment. When properly normalized this response is equivalent to a band-limited or filtered version of the form function. This experimentally measured spectrum, subsequently labelled $|S|$ in the figures, is then compared with the appropriate portion of an approximate theoretical form function, labelled $|f|$. The development of this theoretical model is the subject of Chapter 5. Since the scattering response of the finite cylindrical shell is highly dependent on the orientation of the incident sound and the observer, the backscattering response is measured over a range of orientation angles. For simplicity in the experiment and subsequent analysis only backscattering is considered and only one orientation angle is varied. This angle is called the tilt or aspect angle and measures the angle between a specific radial vector, which is perpendicular to the axis of the shell, and the incident acoustic wavevector. The reference radial vector lies in the plane containing the axis of the cylinder and the incident wavevector (see Figs. 2.1 and 2.3). Because of the axial symmetry of the cylinder only one Euler angle, corresponding to the tilt angle, needs to be specified.

The results of these experiments and calculations are displayed in a color density plot format that clearly shows the locations of enhancements and their progression through frequency-angle space. The enhancements observed in Refs. [1] & [2] are confirmed for shells having a larger wall thickness and found to be present over a range of angles and frequencies. These enhancements are accurately identified through comparison with

coupling loci (displayed in frequency - angle space as well) calculated with approximate dispersion curves for the appropriate waves on the cylindrical shell. After locating and identifying the enhancements in Chapter 2, the remaining chapters attempt to more fully understand the processes at work. Chapter 3 examines the backscattered response in the time - angle domain. Besides a direct look at the raw backscattered time records, both experimental and synthesized, the short time fourier transform (STFT) is used to examine the time records at selected tilt angles and a simple implementation of a synthetic aperture algorithm is applied to the experimental data to "image" a cylinder. This last analysis technique aids in picturing where on the shell the enhancements originate from. The time domain analysis reveals distinct contributions from both meridional (see Section 2.1), and helical waves excited on the shell.

Since a knowledge of the dispersion curves for various waves on the shell is useful in identifying measured enhancements, and for gaining an understanding of such things as radiation characteristics, Chapter 4 is devoted to calculating dispersion curves for the infinite cylindrical shell using full 3-D elasticity theory. Dispersion curves for several types of waves for several mode numbers are calculated. Chapter 5, as mentioned previously, discusses the approximate partial wave series (PWS) calculation used to calculate the form function for backscattering from finite cylindrical shells. Besides the two shells examined throughout this thesis, the form function for several other shell thicknesses are calculated.

Another step taken in understanding the physics of these high-frequency enhancements is to attempt to simplify the scattering process in terms of a ray theory. This way the factors which contribute most significantly to the observed enhancements can be identified. If the ray theory correctly models the behavior of the response over regions in which its assumptions hold it is considered to represent most of the physics involved in the process. In this way the ray theory becomes a useful tool in identifying and estimating the response of more complicated systems. Chapter 6 presents the results of a ray theory developed by Marston[3-6] for the scattered meridional ray amplitude in the meridional plane of an infinite cylindrical shell when the tilt angle is close to a leaky wave coupling angle. These results are compared with the exact PWS solution for scattering from an

infinite cylindrical shell at oblique incidence (introduced earlier in Chapter 4). The comparisons are very good and confirm that the ray approach is applicable to cylindrical shells, where the response is due to leaky Lamb waves, and not just to Rayleigh waves on solid cylinders as shown in Refs. [5] and [7]. Chapter 7 presents the results of quantitative experimental measurements of the backscattered meridional ray amplitudes for finite cylindrical shells. Comparisons of these results are made with an extension of the ray theory discussed in Chapter 6 and with the approximate PWS solution of Chapter 5. The comparisons are quite good and serve to confirm that the ray approach works well for finite cylinders also. The comparisons are limited in the sense that the backscattered meridional ray amplitude is dependent on the reflection coefficient for reflection of the meridional leaky wave off the cylinder truncation. Calculating this reflection coefficient is extremely difficult and can only be approached in an approximate fashion. Chapter 8 addresses this problem as well as that of the possibility of mode conversion when the leaky wave reflects from the truncation. It is noteworthy that while the calculated infinite cylinder form function may be expressed using Eq. (1.2), the finite cylinder case uses Eq. (1.1) with a taken to be the radius of the cylinder.

The measurements confirm one astonishing prediction about the meridional ray backscattering enhancement from finite cylindrical shells: the amplitude of the enhancement can be several times larger (nearly 7 times larger in one case examined) than the specular reflection from a rigid sphere having the same radius as the cylinder. This for *highly tilted* cylinders too — up to 60 degrees from broadside incidence — where transmission loss upon reflection from the end is present. This is a significant result recalling that a standard measure of sonar target strength is the rigid sphere and that the high-frequency scattering from a highly tilted rigid cylinder with flat ends has been usually taken to be extremely small.

While not developed here, the aforementioned result has implications for the backscattering by certain hemispherically capped cylinders. Over a range of frequencies and tilt angles of a hemispherically (or similarly) capped cylindrical shell, the meridional ray backscattering response from the far end of the shell (or perhaps at an impedance

discontinuity, i.e. ring stiffener, weld, joint, or slope discontinuity) may be significantly larger than the specular reflection off the front end cap. The effect of an impedance discontinuity other than a simple truncation on the meridional ray enhancement has not been examined here.

A word about the organization of this dissertation is appropriate. The author has intended that each chapter be somewhat complete and independent in its own scope. Therefore the Introduction section found in each chapter may overlap with and be somewhat redundant to that in other chapters. Most of Chapter 2, with slight omissions, was published in 1997 in the Journal of the Acoustical Society of America (JASA) (Ref. [8]). (Reprinted with permission from Ref. [8]. Copyright 1998 Acoustical Society of America.) Appendix A of that paper has been expanded and is now Chapter 5 on page 135; additionally Appendix B has been incorporated into Appendix A on page 277. Chapter 3 is an expanded version of a paper written by myself for the Structural Acoustics and Vibration Student Paper competition at the 134^{th} meeting of the Acoustical Society of America in San Diego. Chapters 6 and 7 are written with an expectation of submitting them for publication in JASA with minor changes and omissions only.

[This page is intentionally left blank.]

2

High-Frequency Backscattering Enhancements by Thick Finite Cylindrical Shells in Water at Oblique Incidence: Experiments, Interpretation and Calculations

2.1 Introduction

Recent high frequency sonar images of truncated cylindrical shells indicate that the visibility of the ends of the shell can be improved by an elastic response of the shell.[1] The enhancements are associated with a category of leaky ray shown in Fig. 2.1. The enhancement occurs when the tilt angle γ of the cylinder is close to the leaky wave coupling angle $\theta_l = \sin^{-1}(c/c_l)$, where c_l is the phase velocity of the leaky wave and c is the speed

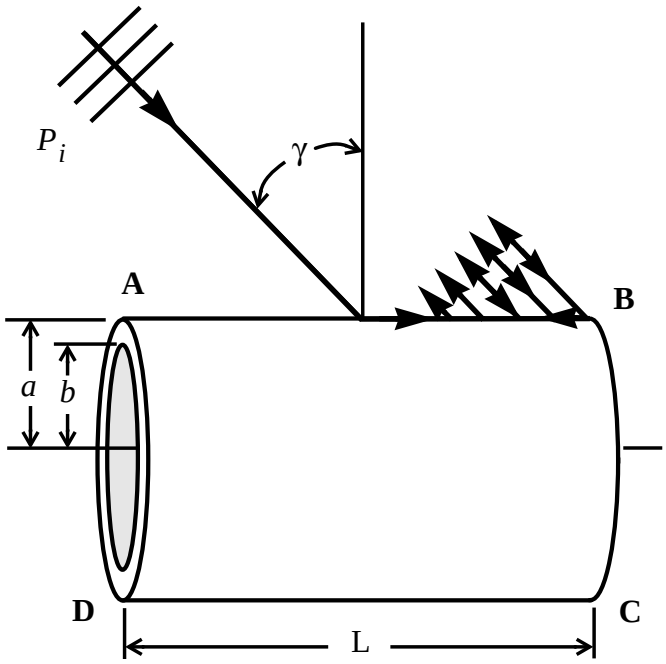

FIG. 2.1 Scattering geometry and ray diagram of a meridional leaky ray on a finite cylindrical shell.

of sound in the surrounding water. This ray is referred to as a meridional ray[5] since it is propagated along the meridian defined by the direction of the incident wave vector and the cylinder's axis. An analysis shows that the backscattering enhancement is associated with the vanishing of Gaussian curvature of the wavefront backscattered in the direction of the receiver. The enhancements reported[1] were for tilts in the vicinity of 18° and 35° corresponding to the excitation of symmetric and antisymmetric (s_0 and a_0) generalizations of leaky Lamb waves on the fluid-filled stainless steel cylinder used in those experiments. The purpose of this chapter is to document the existence of high frequency backscattering enhancements for tilted cylindrical shells relevant to larger values of the tilt γ and in some cases, extending to γ = 90° (i.e. end-on incidence).

The method of our investigation concerns the global response in the *frequency - angle domain* rather than the spatial responses emphasized in Ref. 1. There are several reasons for identifying such high-frequency enhancement mechanisms. For example, such enhancements may be relevant to the use of backscattering by cylinders lying at random angles on the sea bottom to facilitate detection at the greatest practical range. Other

potential applications include remote ultrasonic detection of cracks or junctions in pipes. Scattering mechanisms of interest are not limited to meridional rays since in certain situations strong backscattering contributions from end-reflected helical leaky and subsonic rays are also evident. The frequency range investigated extends far above the coincidence frequencies of the thick and moderately thick shells studied. The combination of frequency range and shell thickness investigated are such that the elastic responses of the shell may not be adequately modeled with the assumptions of thin-shell mechanics.[9-11] It is noteworthy, however, that frequency-angle domain displays of backscattering data used previously for thin fluid-loaded shells[10,12,13] and various methods of approximation previously used for such systems (see Chapter 5) are relevant to the present investigation.

The investigations mentioned above, as well as several by other authors[14-17], have demonstrated that significant backscattering enhancements from tilted cylindrical shells result from the reradiation of surface guided waves for a range of tilt angles somewhat near broadside incidence. Large backscattering levels arise from the launching of helical leaky waves which reflect off the shell truncation and reradiate into the backscattering direction. Leaky waves are launched at an angle θ_l with respect to the local shell normal according to the trace velocity matching condition $\theta_l = \sin^{-1}(c/c_l)$. Figure 2.2 shows a ray diagram for launching either a meridional or helical leaky wave. These helical waves are launched symmetrically about the shell at the polar angles $\pm\phi_l$ and travel along the helix angles $\pm\Psi_l$, defined with respect to a line parallel to the cylinder axis (i.e. a meridian). These angles may be found by the relations[1,6,16]: $\cos\phi_l = \cos\theta_l/\sin\gamma$ and $\cos\Psi_l = \sin\gamma/\sin\theta_l$. Two types of waves contribute strongly to the scattering: longitudinal and shear. For the general problem of propagation on tilted cylinders these waves are also known as quasicompressional and quasishear, since it is generally not possible to completely uncouple shear and compressional displacements. The compressional wave, whose behavior at low frequency is similar to a compressional wave in a plate, can be launched within the region from broadside incidence to a cutoff angle $\gamma_s = \sin^{-1}(c/c_p)$, defined by the plate speed c_p[18]. Shear waves can also be launched within a range of angles around broadside, limited by cutoff at an angle given by

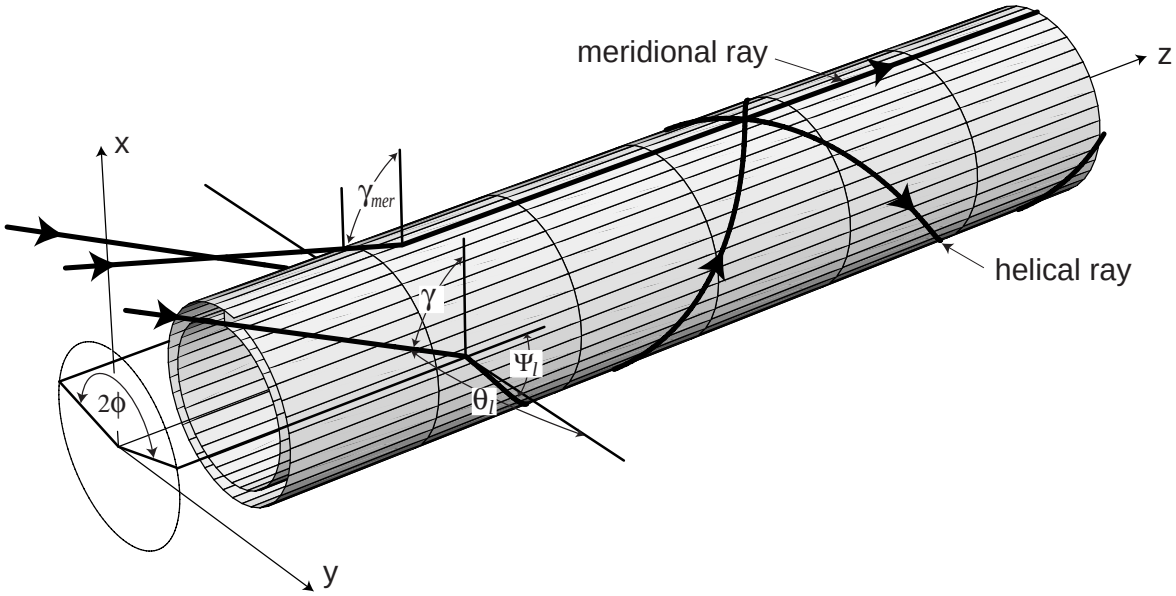

FIG. 2.2 Ray diagram for launching a meridional or helical leaky ray by trace velocity matching. When $\gamma = \theta_l = \sin^{-1}(c/c_l)$, here shown as γ_{mer}, a meridional ray is launched which travels along the cylinder meridian (in the *x*-*z* plane at $y = 0$). For smaller angles of incidence rays are launched at symmetric points off the cylinder meridian (at the polar angles $\pm\phi$), which travel helical paths defined by the helix angle Ψ_l. At greater angles of incidence the leaky waves of this class launched on the cylinder no longer have a propagating character and are said to be "cutoff". For subsonic helical rays the launching points are tangent to the cylinder at $\phi = \pm\pi/2$ and coupling occurs through evanescent tunnelling.

$\gamma_T = \sin^{-1}(c/c_s)$, where c_s is the shear speed in the shell material. Using the values given in Table 2.2 for SS304 these cutoff angles are $\gamma_s = 16.5°$ and $\gamma_T = 28.2°$. At each of these cutoff angles the helix angle Ψ_l is zero and propagation is strictly along the axial direction. For purely circumferential propagation on an infinite cylindrical shell these waves are identified in the lowest order case as the s_0 leaky Lamb wave and horizontally polarized shear wave T_0, respectively. Acoustic coupling to these waves is cutoff for γ in excess of γ_s and γ_T, respectively. Coupling to the flexural wave, denoted by a_0 for broadside incidence, should be possible, however, for tilt angles greater than γ_T[19]. Section 2.3 of this paper describes the results of backscattering experiments carried out on two different shells

where the tilt of the cylinder was allowed to vary from broadside to end-on incidence. These results are compared with theoretical predictions of the backscattering spectral magnitude, which is the subject of Chapter 5. Section 2.4 describes an approximate calculation for the frequency-angle loci which correspond to launching and circumferential resonance conditions for helical surface waves of interest. These curves are used to identify the elastic responses observed at mid to high tilt angles.

2.2 Scattering Experiment

Broadband backscattering experiments were carried out for slender cylindrical shells in a large redwood water tank. A schematic of the experimental setup is given in Fig. 2.3. An air filled finite cylindrical shell is placed in the *near field* of a PVDF sheet source, which radiates an approximately plane pressure impulse over the dimensions of the target. A hydrophone records the pressure response backscattered through the sheet. This nonconventional placement of the acoustically transparent PVDF source between the scatterer and receiver has been discussed previously[20]. The cylindrical shell was suspended at each endcap by thin monofilament fishing line. Flat Plexiglas endcaps were used, and a watertight seal was maintained by rubber O-rings and a light elastic strand stretched between the endcaps inside the shell. (Pictures of one of the cylinders along with an endcap can be found in Figs. A.1 - A.3 in Appendix A.) The center of the target was placed approximately 25 cm from the source. The receiver, a piston-like piezoelectric transducer (Panametrics, model V302), was placed oppositely a distance of approximately 100 cm from the source. The sheet source is constructed of 110 μm thick PVDF film[21] with silver surface metallization and a 1 mil layer of Mylar on each side. It measures 71 x 71 cm. An approximately unipolar pressure pulse is generated when a voltage step is applied to the sheet. A discussion of the source spectral properties and normalization can be found in Appendix A. A high current pulse generator (Avtech Electrosystems LTD., model AVO-8C-C) was used to supply a long duration square wave input during the experiment. The trailing voltage step-down was delayed until after the backscattered signal was received.

Due to the finite dimensions of the sheet source, edge contributions delayed relative to the initial pressure impulse will contribute to the measured backscatter. These edge contributions are delayed in proportion to the difference in path length between the scatterer and the center and edges of the sheet. Because the scatterer is placed near the sheet source the effects due to these contributions are expected primarily at low frequencies; no attempt has been made to incorporate these effects in the present analysis. Two stainless steel (SS304) scatterers with thickness to radius ratios of 7.6% and 16.3% were examined separately and are labelled A and B, respectively. Tables 2.1 and 2.2 list the dimensions of each shell as well as relevant material properties.

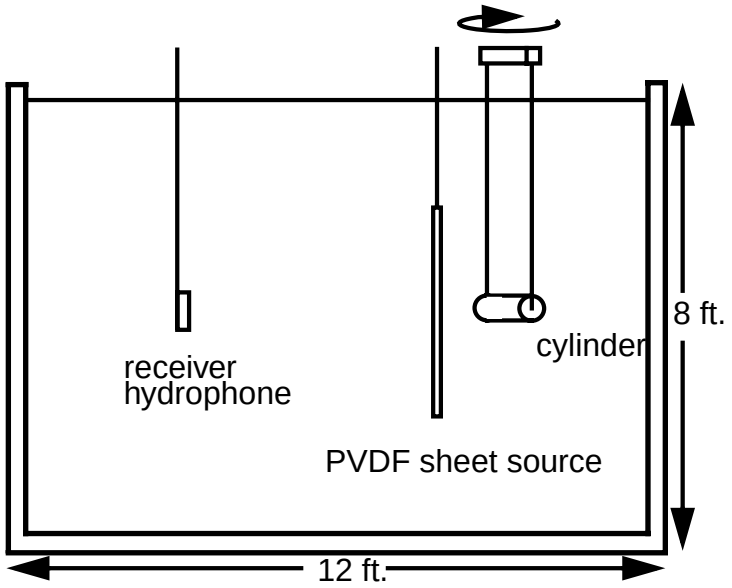

FIG. 2.3 Experimental setup. A cylindrical shell is suspended from a rotation stage in a cylindrical redwood tank. The sheet source generates an approximately unipolar pressure impulse from both its front and back sides. Backscattered signals from the shell propagate through the acoustically transparent sheet source to the hydrophone.

Time records were recorded for the full range of incidence angles, spanning end-on and broadside incidence. Multiple time signals were recorded and averaged at each angle; a background record, taken with the target removed, was then subtracted to remove signals arriving directly from the source. The time window chosen for the experiment excluded reflections from the tank walls. The background subtracted time series data was Fourier

transformed (FFT) and the modulus normalized according to the source-receiver system impulse response to obtain the backscattering spectrum. In the region near end-on incidence, reflections from the flat endcaps are clearly observable and quite localized in time. Because the scatterers in this experiment were slender, the specular reflection from the endcap closest to the source was well separated in time from the elastic responses of interest excited on the shell. To isolate the elastic backscattering response of the shell, a rectangular window which excluded the leading endcap reflection was applied to all time records before computing an FFT.

2.3 Measured and Calculated Backscattering Spectrum

Figures 2.4 and 2.5 compare measured and calculated spectral magnitudes for the two shells studied. Figure 2.4(b) shows the measured backscattering spectral magnitude from the thinner of the two shells, A, over a range of aspect angles from end-on ($\gamma = 90°$) to broadside ($\gamma = 0°$) incidence, in 0.3° increments (1 kHz resolution). Figure 2.4(a) is the theoretical form function magnitude resulting from an *approximate* calculation for a simply supported finite cylindrical shell, which is the subject of Chapter 5. The relative scattering levels are set such that 0 dB corresponds to the maximum scattering response found at broadside incidence in each figure for the frequency range shown. The reader may wish to refer to the discussion of dispersion relations for thick shells given in Section 2.A. The highest amplitude feature in each figure is found at $\gamma = 0°$. This feature corresponds to broadside incidence and includes the specular reflection from the cylinder. It is composed of broad peaks and oscillations which are not easily resolved in the figures due to the amplitude scale chosen. Figure 2.6 shows a comparison between the corresponding broadside records in Figs. 2.4(a) and (b) and Figs. 2.5(a) and (b), with the exact partial wave series (PWS) solution for backscattering at normal incidence from an infinite, air-filled thick cylindrical shell. Section 2.B discusses the alteration of the approximate PWS results which

enables the above comparison. This comparison reveals good agreement in the location and spacing of the broad peaks and dips for each shell (however the cause of the apparent mismatch in "phase" in Fig. 2.6(a) between the data and the calculated form functions above 200 kHz is not clear). This is the expected behavior for scattering from a slender finite shell at normal incidence when the length of the shell significantly exceeds the width of the first Fresnel zone[22,3], as is the case for most frequencies of interest here. These broad features are associated with the a_0 antisymmetric leaky Lamb wave in the region where that wave is supersonic[23,24]. (For broadside incidence the narrow resonances are expected to be more strongly affected by the finite length of the cylinder.) Also clearly observable in Figs. 2.4 and 2.5 are regions of high backscatter between broadside incidence and the cutoff angle for shear wave propagation, corresponding to enhancements from helical leaky waves (s_0 and T_0) as discussed in Section 2.1. This is evident by comparison with the loci shown in Fig. 2.7(b) discussed subsequently.

Table 2.1: Shell parameters

	Outer radius	Thickness	Length		
Shell	a (mm)	h (mm)	L (mm)	h/a	L/a
A	19.05	1.45	228.60	0.076	12.0
B	21.02	3.42	245.05	0.1625	11.658

Table 2.2: Material parameters

	Density	Longitudinal velocity	Shear velocity	Plate speed
Material	(g/cm^3)	(mm/μs)	(mm/μs)	(mm/μs)
Stainless Steel 304	7.57	5.675	3.141	5.232
Water	1.00	1.483		

FIG. 2.4 Scattering from Shell A: (a) Calculated and (b) measured backscattered spectral magnitude of the impulse response as a function of frequency and aspect angle for an empty SS304 cylindrical shell with thickness to radius ratio $h/a = 0.076$ and slenderness $L/a = 12.0$. The maximum frequency displayed ($f = 400$kHz) corresponds to $ka = 32.3$. Calculated values beyond $\gamma = 80°$ in (a) have been floored (shown as black) due to increased error in the numerical calculation at high aspect angles. These color raster images represent the sampling intervals: (a) $\Delta ka = 0.05$ ($\Delta f = 619$ Hz), $\Delta\gamma = 0.3125°$; (b) $\Delta ka = 0.081$ ($\Delta f = 1000$ Hz), $\Delta\gamma = 0.3°$.

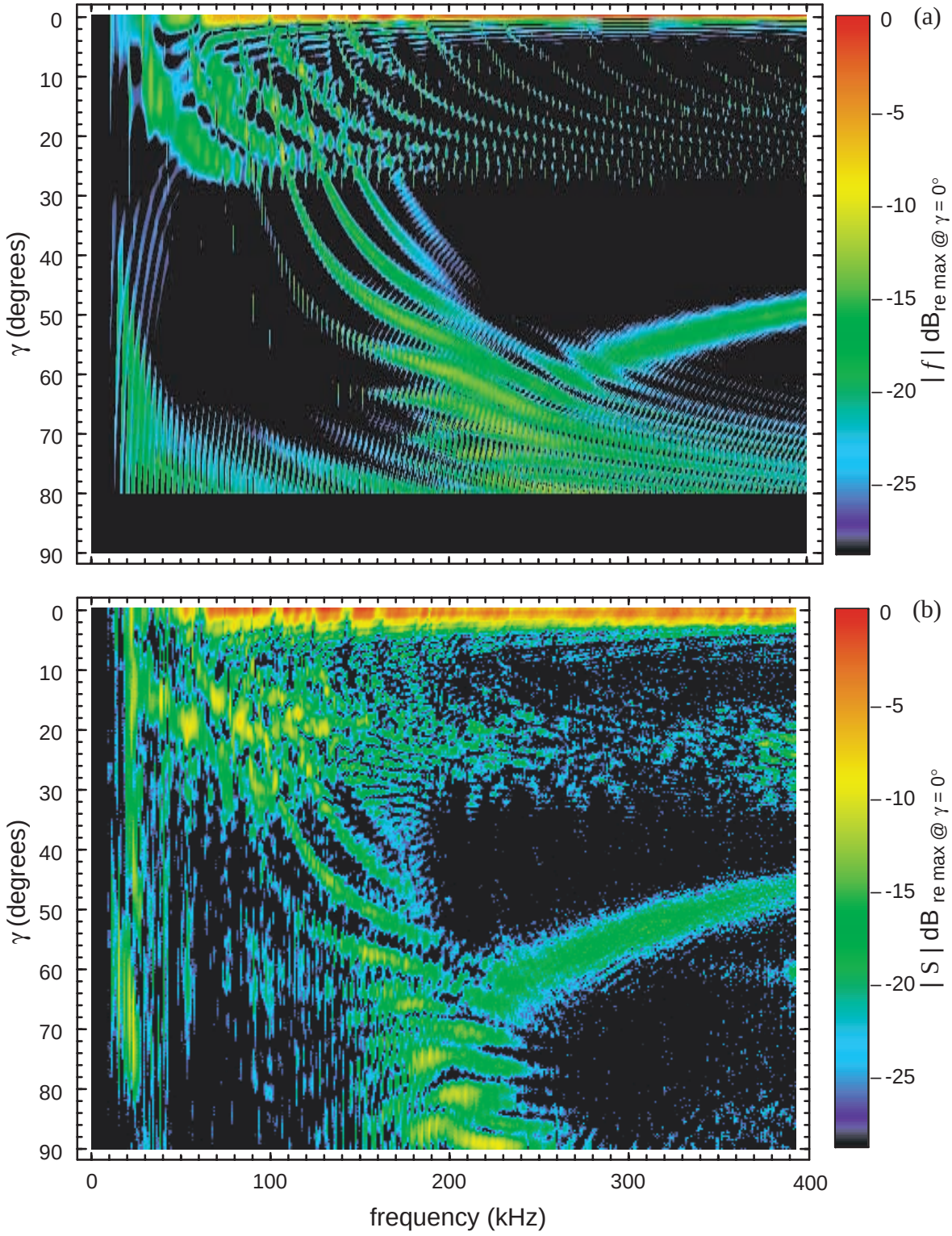
(a)
(b)
γ (degrees)
frequency (kHz)
0
10
20
30
40
50
60
70
80
90
100
200
300
400
-5
-10
-15
-20
-25
| f | dB re max @ γ = 0°
| S | dB re max @ γ = 0°

FIG. 2.5 Scattering from Shell B: Same as Fig. 2.4 except $h/a = 0.1625$ and $L/a = 11.658$. The maximum frequency displayed (f = 300 kHz) corresponds to $ka = 26.7$. These color raster images represent the sampling intervals: (a) $\Delta ka = 0.05$ (Δf = 561 Hz), $\Delta\gamma = 0.3125°$; (b) $\Delta ka = 0.089$ (Δf = 1000 Hz), $\Delta\gamma = 0.3°$.

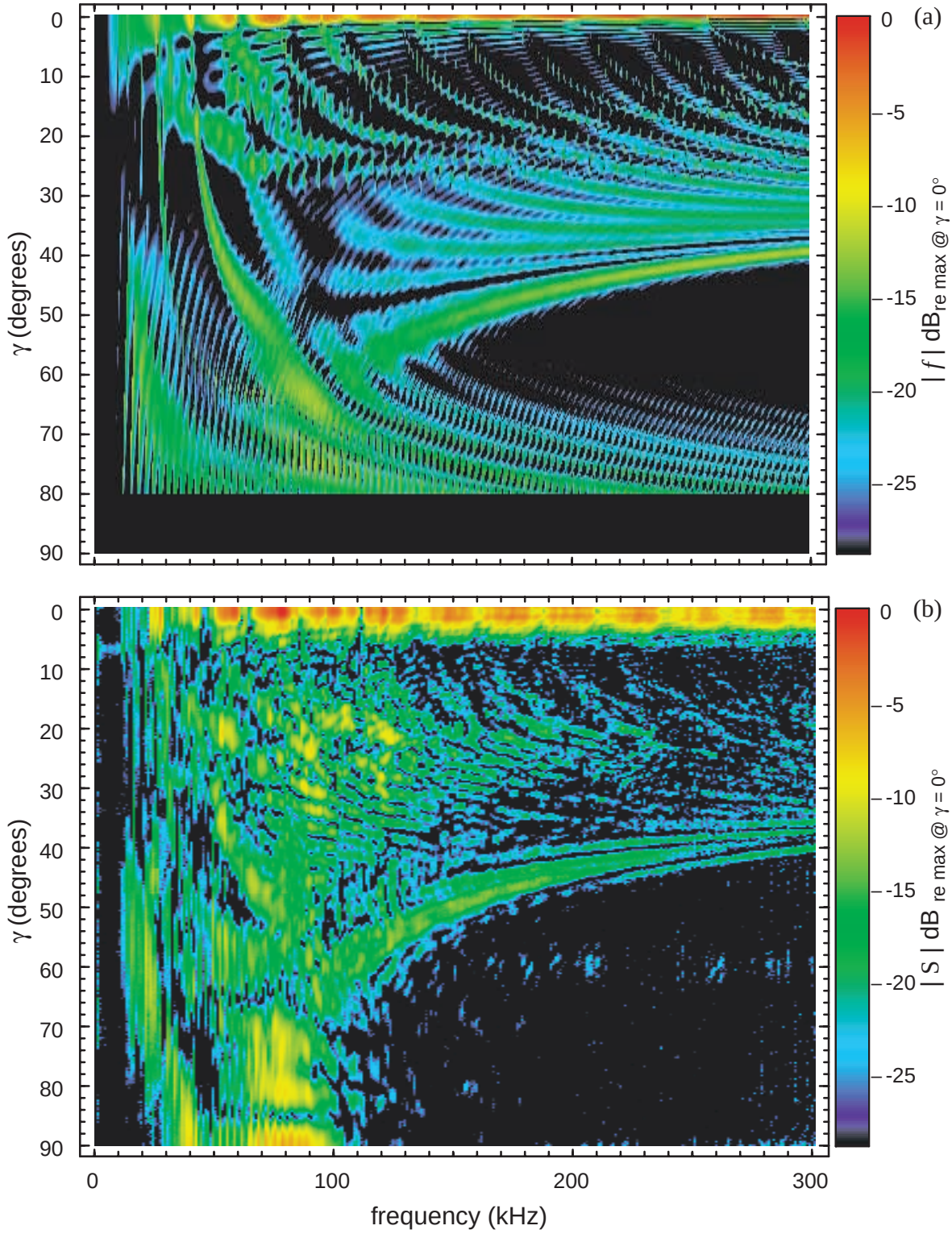
(a)
(b)
γ (degrees)
frequency (kHz)
0
10
20
30
40
50
60
70
80
90
100
200
300
-5
-10
-15
-20
-25
| f | dB re max @ γ = 0°
| S | dB re max @ γ = 0°

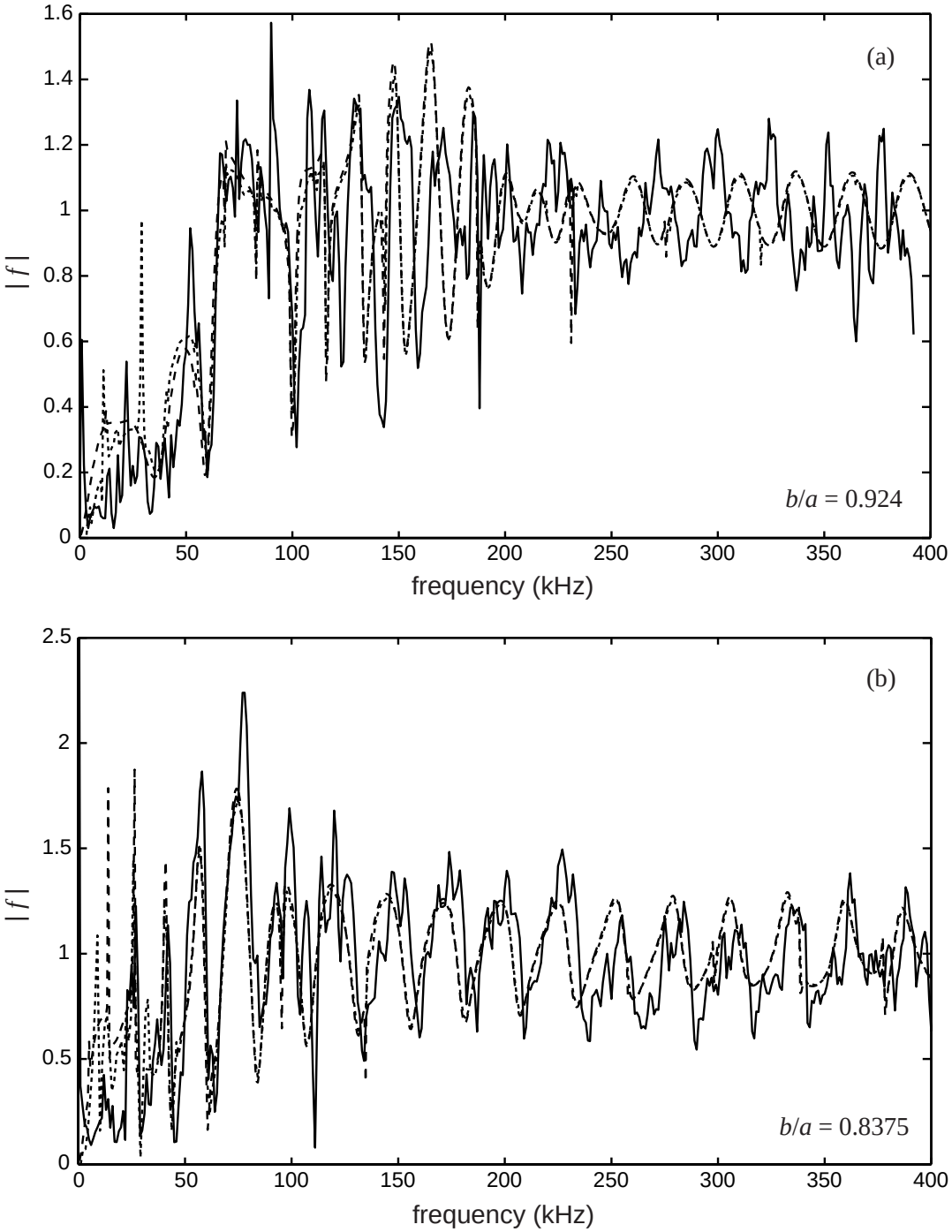

FIG. 2.6 Comparison of broadside ($\gamma = 0°$) measured spectra of Figs. 2.4 (b) and 2.5 (b), (solid lines) with the calculated spectrum (short dashed lines, modified as described in Section 2.B) from Figs. 2.4 (a) and 2.5 (a) respectively. (a) Shell A, (b) Shell B. The long dashed lines are calculated for an infinite cylindrical shell at broadside incidence. In each case the experimental data was multiplied by an overall amplitude factor to qualitatively match the calculated curves. See Fig. A.14 for an extension of (b) up to $f = 1$ MHz.

The most striking features evident in Fig. 2.4(a) and (b), and the principal focus of this paper, are the regions of high backscatter which extend beyond the cutoff angle for shear wave propagation ($\gamma = \gamma_T = 28.2°$) to end-on incidence. Two features are distinguishable. The first is the broad peak curving from $\gamma = 46°$ at the right edge of each figure to $\gamma = 90°$ at $f \approx 200$ kHz. The peak value along this curve in the experimental result reaches approximately -17 dB. The second feature is composed of multiple frequency-angle curves which extend from broadside incidence to $\gamma = 65°$. The two features merge near the coincidence frequency [f = 193 kHz; ka = 15.6, see Fig. 2.9(a)] and exhibit strong backscattering (up to -11 dB) out to end-on incidence. The first of these two features can be associated with the meridional (axial) propagation of the a_0 antisymmetric leaky Lamb wave along the front side of the cylinder, as shown in the ray diagram in Fig. 2.1. Recall that coupling to the meridional ray, and subsequent backscattering enhancement, occurs at tilt angles $\gamma = \theta_l = \sin^{-1}(c/c_l)$. To a good approximation in this frequency range the phase velocity of the a_0 wave can be modeled by the phase velocity calculated for a plate of the same material and thickness. The solid curve in Fig. 2.7(a) shows where the above launching condition is satisfied for the a_0 wave, using phase velocity values calculated with the exact solution for a plate fluid loaded on one side with water. Good agreement is found between this curve and the broad feature evident in both the experimental and theoretical figures. The dashed curves show the results of a similar approximation applied to the helical propagation of the subsonic Lamb wave a_{0^-} which will be discussed in the following section.

Figure 2.5 shows theoretical and experimental results for a considerably thicker shell, labelled B in Table 2.1. The coincidence frequency is now found at a lower frequency f = 82 kHz (ka = 7.3). Figure 2.8(a) displays phase matching conditions for the meridional propagation of the a_0 wave in the same way as for the thinner shell in Fig. 2.7(a). The broad curve extending from $\gamma = 40°$ at the right edge of the figure to $\gamma = 90°$ at $f \approx 80$ kHz is similarly identified as resulting, at least in part, from the launching of the a_0 wave in a meridional fashion. Also observable are what appear to be the higher order circumferential resonances of the helical a_0 supersonic waves, whose resonance loci are discussed below

[in conjunction with the discussion of Fig. 2.8(b)]. Near the coincidence frequency, within 25° of end-on incidence, backscattering levels are considerable, reaching -10 dB at $\gamma = 80°$ and -7 dB at $\gamma = 90°$. Below the coincidence frequency the backscattering response is generally high over a large range of aspect angles although some frequency-angle ridges and valleys are distinguishable.

2.4 Circumferential Resonances

An approximation will now be discussed which describes the frequency-angle loci corresponding to circumferential resonances of helical waves. It is known that backscattering is enhanced when resonances of the shell are excited. For the tilted finite cylinder these are usually associated with circumferential and axial propagation. Only resonances associated with *circumferential* propagation will be examined here. Resonances associated with *axial* propagation are not considered in our analysis because for the high frequency guided waves of interest (the a_0 and a_{0^-} waves), the radiation damping is usually sufficiently large to inhibit scattering contributions from repeated axial reflections. Counter-examples of this are the s_0 and T_0 meridional and helical waves which do exhibit axial resonance features (e.g. see Fig. 5.4). Consequently the frequency response is expected to depend only weakly on the length L when L is large. Circumferential resonance occurs for helical waves when the azimuthal wave path on the cylinder equals an integer number of wavelengths. If it is assumed that reflection of the surface wave off the truncation only introduces a change in sign of the axial wavevector, the previous condition combined with the launching condition serves to define specific frequency-angle combinations wherein high levels of backscattering *are possible*. In terms of the dimensionless frequency ka and the aspect angle γ, where k is the wavenumber in the fluid medium and a is the outer radius of the cylinder, the following relationship describes circumferential resonance conditions[25,26]:

$$(ka)^2\left[\left(\frac{c}{c_l}\right)^2 - \sin^2\gamma\right] = n^2 \qquad n = 0, 1, 2, \ldots , \tag{2.1}$$

where the integer n is the circumferential mode number. It should be emphasized that this relation only specifies where there exists an axial wavenumber matching between the incident wavevector and a certain "resonant" mode of the shell. The term resonant is here used loosely as it is not a global resonance of the structure under consideration, which would involve *both* axial and circumferential resonances. Whether or not an enhancement exists at these locations depends on many other factors, such as the nature of the coupling between the fluid and the shell, radiation losses, and the shape of the outgoing wavefront in the direction of the observer. The solution for $n = 0$ does not correspond to a resonance, but rather describes purely axial propagation of a supersonic guided wave. For this case Eq. (2.1) reduces to the trace velocity matching condition of a meridional ray, $\gamma = \sin^{-1}(c/c_l)$. For sufficiently high frequencies the phase velocity for propagation of a guided wave on a tilted cylinder is approximately independent of helix angle [see Figs. 4.10(a) and 4.12(a)]. In this frequency region the phase velocity for all angles of incidence in Eq. (2.1) can be approximated by the values calculated for broadside incidence or for a plate. Figure 2.7(b) shows the frequency-angle loci which satisfy Eq. (2.1) for the s_0, T_0 and a_0 waves for Shell A. For each set of loci, except the a_0 wave, the $n = 0$ curve enters at the lowest frequency while higher order curves emerge with increasing frequency. For the a_0 wave the $n = 0$ curve corresponds to the limiting solid curve on the lower right side of the figure. For comparison the solid curve from Fig. 2.7(c), corresponding to propagation on a plate, has been included and is now described by the long dashed curve. Figure 2.8(b) displays analogous results for Shell B. Phase velocity and radiation damping curves for the relevant waves, as well as a description of the method used to calculate them and a discussion of their applicability, are given in Section 2.A. Due to the aforementioned approximation, the frequency-angle loci displayed in Figs. 2.4, 2.5, 2.7 and 2.8 are to be used in identifying the responses excited on the shell and are not meant to be a precise description of resonance locations (Chapter 4 discusses exact dispersion curves for infinite shells). The agreement with calculated and measured results is quite good, which can be

shown by overlaying the calculated resonance loci on the backscattering response figures, and the qualitative agreement serves to identify the wave types.

The regions of scattering below the coincidence frequency deserve attention. The resonance loci for the a_0 wave in Figs. 2.7 (b) and 2.8 (b) have been carried through to the region where the a_0 wave becomes subsonic. Any coupling to this wave in this latter region must occur through evanescent tunneling at the azimuthal angles $\psi = \pm\pi/2$. For Shell A the scattering contribution is not expected to be significant due to the high radiation damping β_l for $l = a_0$ suggested by Fig. 2.9(b). The features evident in Fig. 2.4, primarily at and below the coincidence frequency at mid to high angles might better be associated with the slightly subsonic a_{0-} wave, which has been shown to lead to large backscattering enhancements from spherical shells and right-circular cylindrical shells[27-31]. The dashed curves in Fig. 2.7(a) show the resonance loci for helical propagation of the a_{0-} wave, calculated using Eq. (2.1) with $n > 0$ and the cylindrical shell phase velocity. Coupling to the a_{0-} wave would occur at $\psi = \pm\pi/2$ through evanescent tunneling. Referring to Fig. 2.9(b) the radiation damping of the a_{0-} wave is small for $f < 100$ kHz and increases quickly through the coincidence frequency region[27-29]. It is through this region where the a_{0-} wave moves from exhibiting "trapped wave" to "creeping wave" behavior as the thickness of the evanescent coupling layer decreases[32]. Significant coupling to this wave is expected in this region. The interpretation for Shell B near and below the coincidence region does not follow directly from the thinner shell results and is not as clear from the present analysis. The radiation damping of the a_{0-} wave, seen in Fig. 2.10(b) is large near the coincidence frequency region while the damping of the a_0 wave is relatively low. For completeness the frequency-angle loci for helical propagation of the a_{0-} and a_0 waves are extended below the coincidence frequency in Fig. 2.8 (a) and (b).

Comparison of the solid curves in Fig. 2.8(b) in the region above 100 kHz with the observations in Fig. 2.5(b) shows that several of the a_0 helical wave coupling loci are visible even when n is not small. Inspection of Fig. 2.10(b) suggests that this may be a consequence of the relatively weak damping of the a_0 wave in comparison to the thinner shell case shown in Fig. 2.9(b). It is also noteworthy that towards end-on incidence in Figs.

2.4(b) and 2.5(b) there are significant backscattering enhancements near 20 and 40 kHz, respectively, which are not present in Figs. 2.4(a) and 2.5(a). The cause of these enhancements is not presently identified but is discussed in greater detail in Chapter 3.

FIG. 2.7 Approximate coupling loci for Shell A calculated with Eq. (2.1). (a) The solid curve shows the frequency-angle locus for launching the meridional ray depicted in Fig. 2.1. It is calculated using the phase velocity for the a_0 wave on a fluid loaded plate having the same thickness as the shell. The dashed curves show the approximate resonance loci (n = 6 - 14) for a_0- helical waves, while in (b) the solid lines are $l = a_0$, n = 0 - 10; alternating long and short dashes, $l = T_0$, n = 0 - 14, and short dashes, $l = s_0$, n = 0 - 8. These are all calculated using phase velocity values calculated for an infinite, empty, thick cylindrical shell at broadside incidence as discussed in Appendix C. The curve with the long dashes is the solid curve from (a) for the meridional ray.

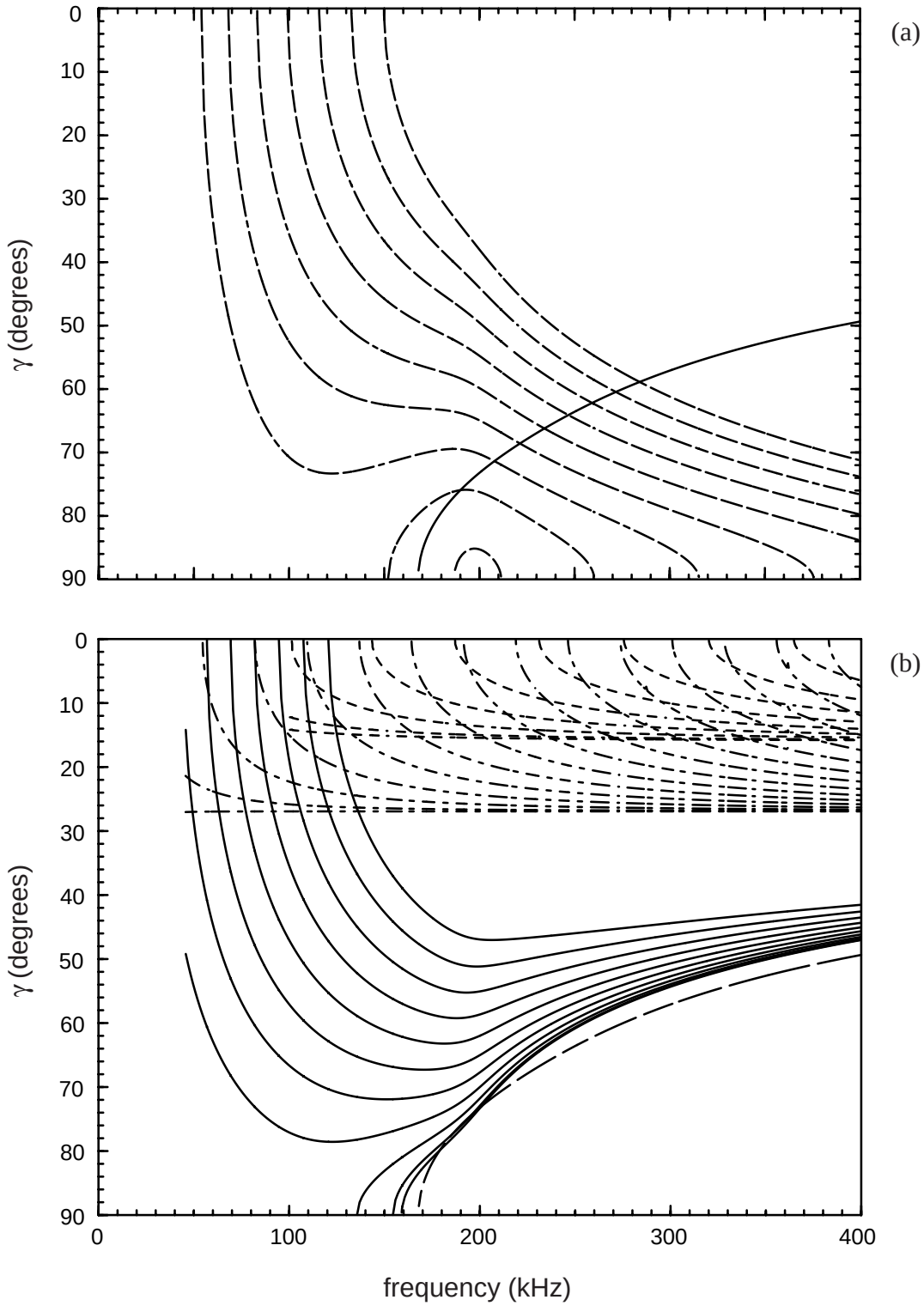
(a)
(b)
γ (degrees)
frequency (kHz)
0
10
20
30
40
50
60
70
80
90
100
200
300
400

FIG. 2.8 Approximate coupling loci for Shell B (same as Fig. 2.7) calculated with Eq. (2.1). The family of dashed curves in (a) correspond to resonance conditions $n = 2$ - 11 for the a_{0}-. In (b) the solid lines are for $l = a_0$, $n = 0$ - 10; alternating long and short dashes, $l = T_0$, $n = 0$ - 11, and short dashes, $l = s_0$, $n = 0$ - 7. The curve with the long dashes is the solid curve from (a) for the meridional ray.

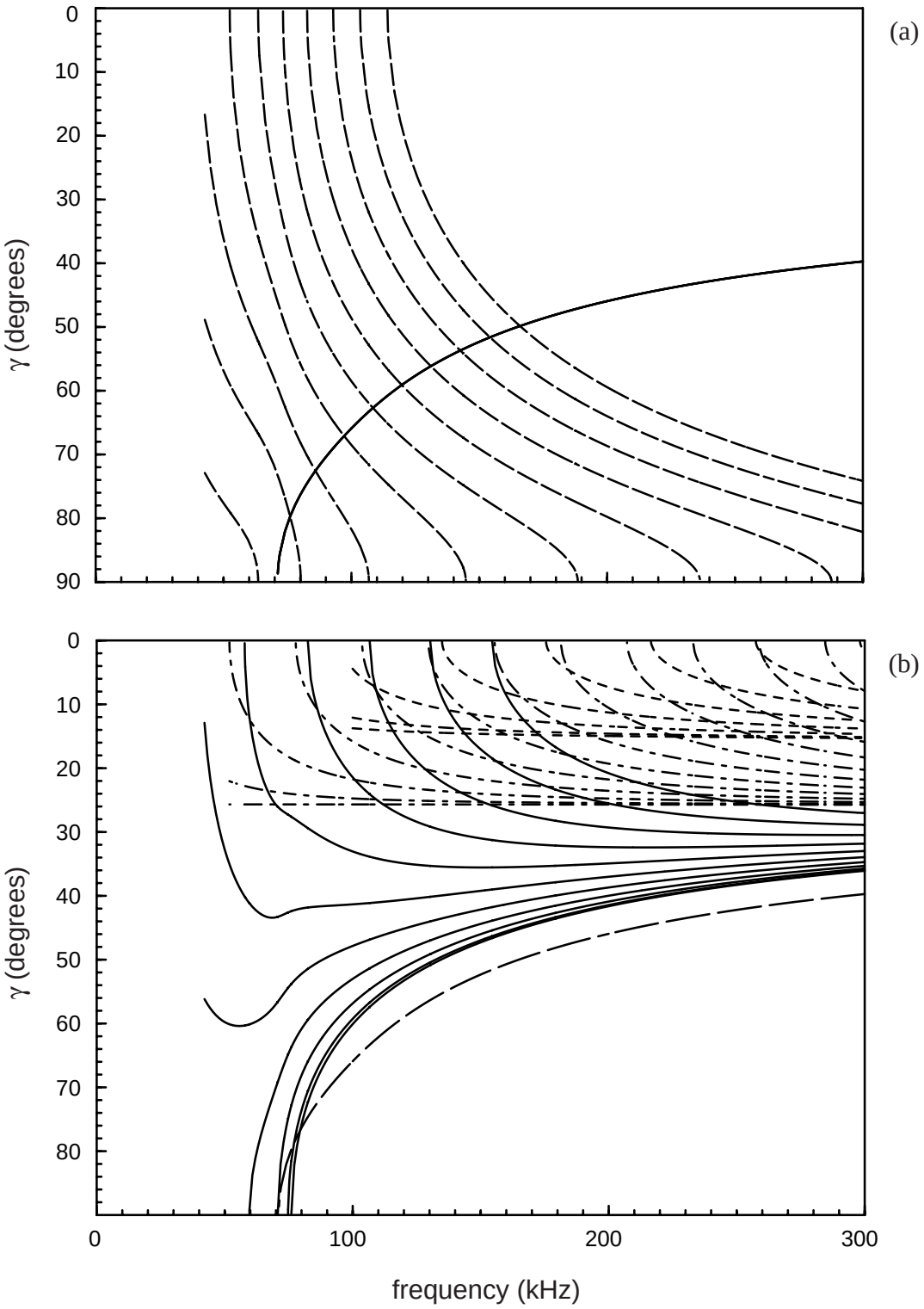
(a)
(b)
γ (degrees)
γ (degrees)
0
10
20
30
40
50
60
70
80
90
0
100
200
300
frequency (kHz)

2.5 Discussion and Conclusions

The experimental data presented for backscattering from thick cylindrical shells clearly shows regions of high backscatter at aspect angles considerably beyond the cutoff for shear wave excitation on the shells. An approximate theoretical treatment of the scattering problem of a plane wave incident on a finite cylindrical shell using full elasticity theory has been presented. The agreement in the frequency-angle domain between the experimental data and the theoretical locations of the ridges of enhanced backscattering is very good, except in the region of aspect angles nearing end-on incidence where the numerical evaluation of Eq. (5.42) becomes difficult. One feature evident for both shells in the region above the coincidence frequency is identified as the backscattering contribution of an end-reflected meridional ray. The location in frequency-angle space of this backscattering mechanism is easily approximated with knowledge of the phase velocity for the a_0 leaky Lamb wave on an infinite cylindrical shell or plate (the results for a plate in vacuum are very similar) in this frequency range. It should be emphasized that this mechanism does not depend on the back side of the shell and is a local synchronization, rather than a resonance phenomena in a global sense. The associated backscattering amplitude is expected to depend only weakly on the length L of the shell when, as in the present case, $\beta_l L/a >> 1$ where β_l/a approximates the spatial attenuation rate of the a_0 wave (see Appendix C). The one-way attenuation factor for propagation down the length of the shell becomes $exp(-\beta_l L/a) << 1$. A second feature, identified primarily for the thinner shell, is associated with helical wave coupling loci for the subsonic a_{0-} wave at and below the coincidence frequency. Distinct helical wave coupling loci can be resolved on the thick shell for the supersonic a_0 wave at high frequencies.

The frequency-angle domain response plots shown in Figs. 2.4 and 2.5 are only one of several multidimensional plots which may be used for identifying the large number of high frequency elastic scattering contributions. Another example includes time-frequency domain response plots for a fixed scattering angle or target orientation[33-35]. The plots shown in Figs. 2.4 and 2.5 are especially relevant to the operation of high frequency sonar

systems because the dependence on aspect angle is displayed.

Acknowledgments

This work was supported by the Office of Naval Research and the Applied Research Laboratory (ARL: UT). The experiments were carried out at research facilities at Washington State University.

2.A Wave properties for thick cylindrical shells

This appendix discusses the guided wave properties for the thick cylindrical shell and their applicability to the circumferential resonance condition given in Section 2.4. Figure 2.9 displays the wave properties for an infinite empty cylindrical shell having the same radii and material parameters as Shell A. It displays the normalized phase velocity and radiation damping (in Np/rad) parameters as a function of frequency where the angular damping rate is for purely circumferential propagation. Figure 2.10 displays analogous results for a cylinder corresponding to Shell B. The wave parameters given in these figures are calculated using the Watson methodology applied to the exact partial wave series (PWS) solution for an infinite cylindrical shell insonified at normal incidence[1,23,24]. These curves are exact only for circumferential propagation (non-oblique incidence) on an infinite cylinder. In Figs. 2.9(a) and 2.10(a) the curve defined by the points corresponds to the normalized phase velocity for the a_0 Lamb wave on a plate of the same material and thickness in vacuum. Notice that unlike Fig. 2.9(a), in Fig. 2.10(a) the a_0 and a_{0-} curves for c_l/c cross in the coincidence region. This crossing behavior is representative of the coincidence behavior for thick shells in contrast to the repulsion for thin shells evident in Fig. 2.9(a).

The phase velocities calculated above for the case of broadside incidence are a good estimate for the phase velocities encountered at oblique incidence provided the frequency is sufficiently high. For the case of thin shells this criteria is usually that the frequency is

sufficiently above the cylindrical "ring" frequency of the shell. In Figs. 2.7 and 2.8 the low end of the resonance loci are terminated at a somewhat arbitrary frequency, at or above an estimate of the "ring" frequency for each shell.

One consequence of using the phase velocities given above in Eq. (2.1) for the estimated resonance loci is apparent by noting the difference between the a_0 phase velocity curves for the cylinder compared with the plate. Evident in both Figs. 2.9(a) and 2.10(a) is a shift toward higher phase velocities for the cylinder above the coincidence frequency. This shift can be attributed to the effects of curvature present in the cylinder analysis[36]. For the meridional ray ($n = 0$) the behavior of the a_0 wave would be expected to follow that for the plate, while for increasing n the behavior would tend toward that for the cylinder. In Figs. 2.7(b) and 2.8(b) the lower order resonance loci for the supersonic a_0 wave (solid curves) tend to congregate very close together; furthermore, they are displaced relative to the plate curve. Removing the effect of curvature for low orders of n would have the effect of broadening the spacing of these curves toward the plate curve.

For situations where the phase velocity c_l is somewhat larger than c, it is anticipated that the spatial leaky wave damping rate depends only weakly on curvature for those waves where β_l is shown in Figs. 2.9(b) and 2.10(b). The spatial leaky wave damping rate may be estimated as β_l/a where a is the radius of the cylinder. The relevant propagation distance is determined by the cumulative length of the meridional or helical leaky ray on the cylinder.

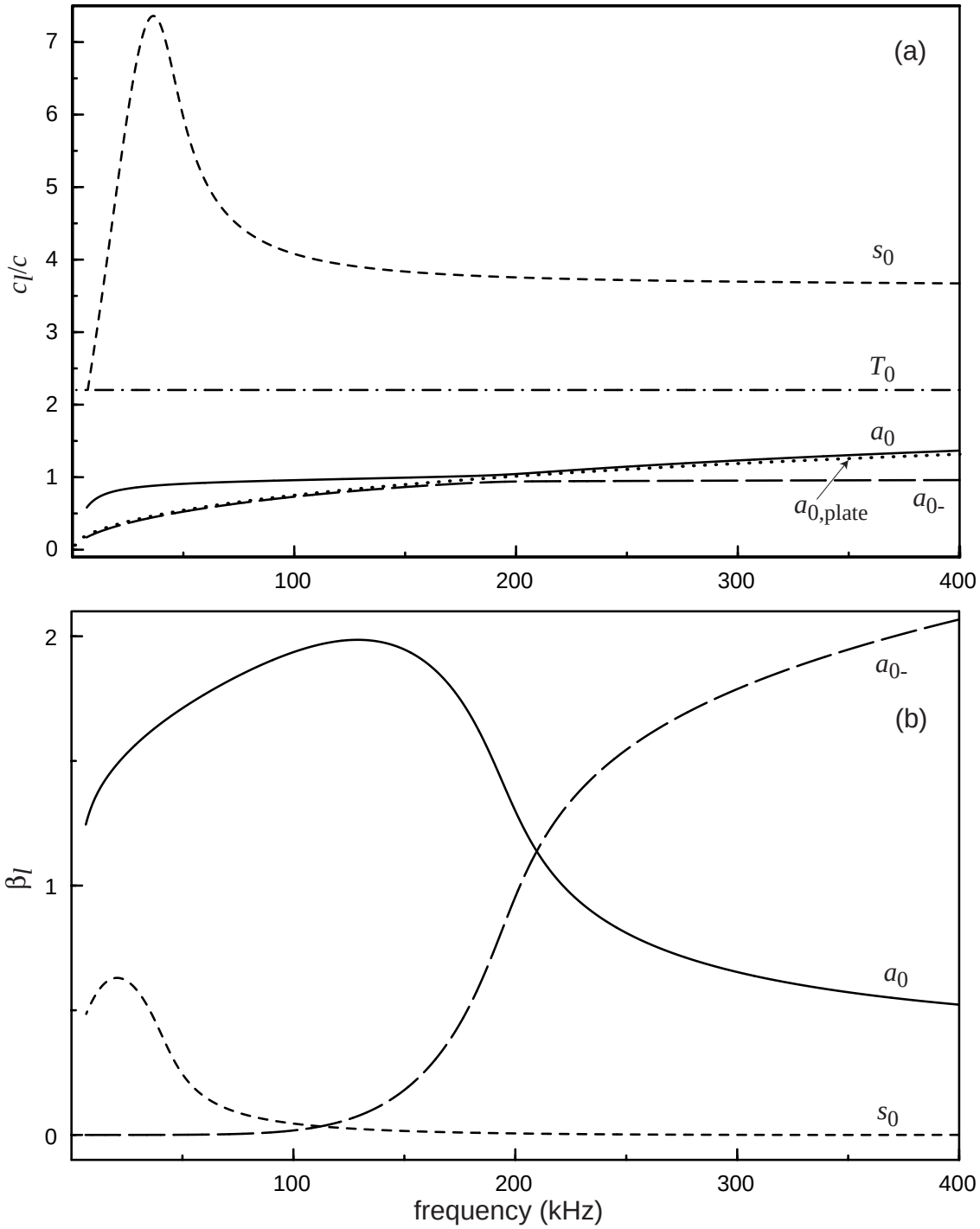

FIG. 2.9 (a) Normalized phase velocity and (b) radiation damping for guided waves on an infinite, empty, thick cylindrical shell corresponding to Shell A for broadside incidence. The curve defined by the points shows the normalized phase velocity for the a_0 wave on a plate of the same thickness in vacuum. The coincidence frequency is defined as the frequency where this normalized phase velocity is equal to unity, which in this case is 193 kHz.

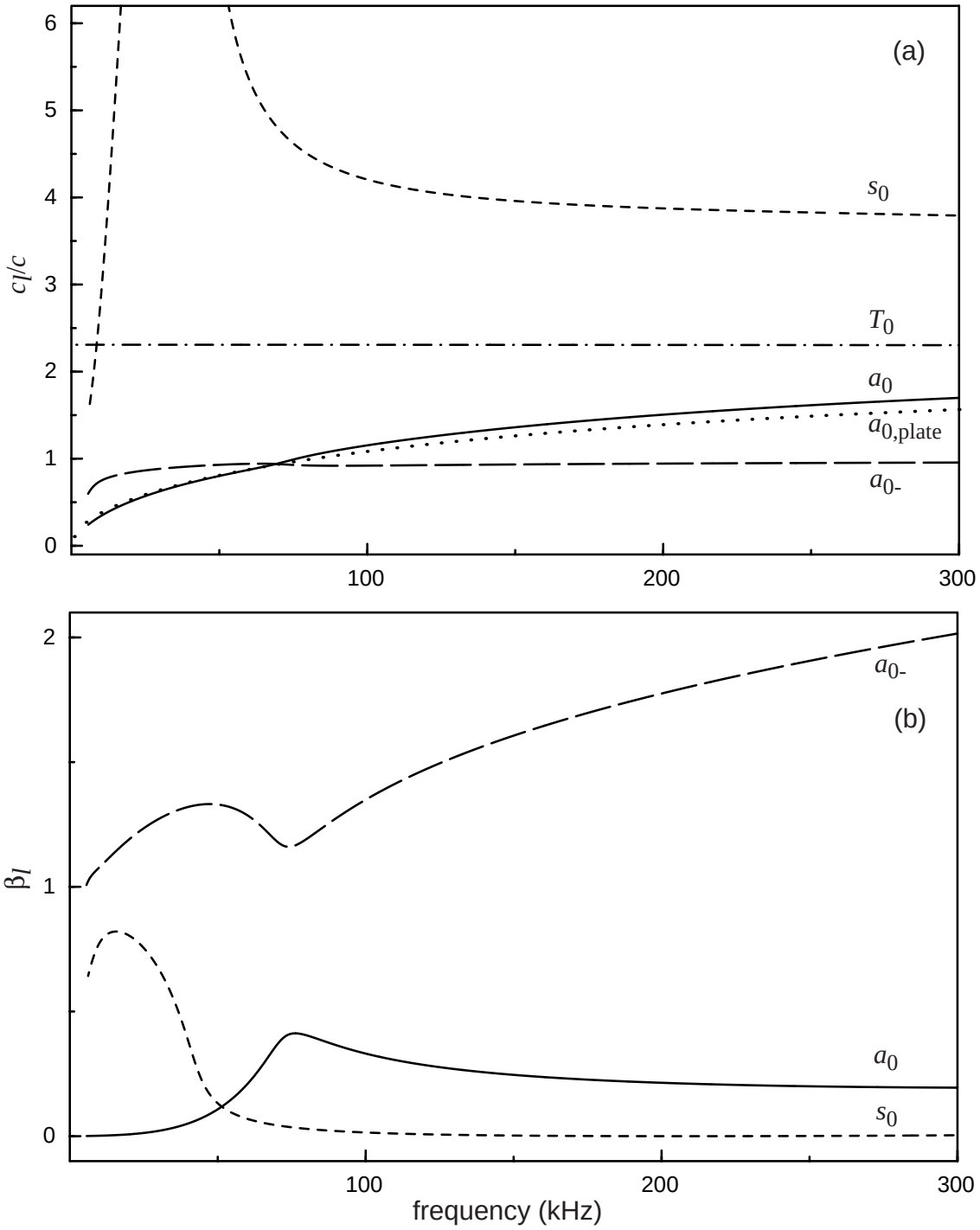

FIG. 2.10 (a) Normalized phase velocity and (b) radiation damping values for Shell B. The coincidence frequency for this shell is 82 kHz.

2.B Form Function Comparison: Finite and Infinite Cylinder PWS Results at Broadside Incidence

This appendix section describes the steps necessary to compare, at broadside incidence, the approximate finite cylinder PWS form function (Chapter 5) with the exact infinite cylinder PWS form function. The infinite cylinder form function is defined in Eq. (1.2). In this case the cylindrical spreading of the far-field wavefronts causes a $1/\sqrt{\rho}$ amplitude dependence. For objects of finite dimensions, i.e. spheres and in this case the finite cylinder, the form function defined in spherical coordinates is most often used. This form function is defined in Eq. (1.1) and the far-field spreading of wavefronts causes a $1/r$ amplitude dependence. At distances very large compared to the dimensions of the scatterer, $r \gg (1/2)k(L/2)^2$, it is expected that the scattering amplitude will display this behavior. In each of these cases the magnitude of the form function for backscattering by a rigid infinite cylinder or sphere approaches unity for $ka \to \infty$ (Ref. [82]).

There is, however, a caveat. For the case of the finite right circular cylinder, one of the principle radii of curvature is infinite. The Gaussian curvature of the reflected wavefront therefore vanishes and one expects a far-field caustic. This far-field caustic affects the spreading of the wavefront and is built into the normalization for the infinite cylinder form function. For the tilted finite cylinder this caustic is located in the specular direction. At broadside incidence it is in the backscattering direction. It can be shown (Sect. 2.12 of Ref. [82]) in this case that the far-field form function for backscattering by a rigid finite cylinder is approximately

$$f_{cyl}^{rigid}(\gamma = 0) \approx \frac{2}{a}\left(e^{-i(\pi/4)}L\sqrt{\frac{ka}{4\pi}}\right), \tag{2.2}$$

where the definition of the form function is as in Eq. (1.1) for spherical coordinates. The form function displays a $\sqrt{ka}$ dependence and therefore diverges as $ka \to \infty$. This behavior is also found in the approximate PWS solution for the finite cylindrical shell. The

form function increases with *ka* in a general square root behavior. Therefore to make a comparison with the PWS result for the infinite cylindrical shell it is necessary to normalize the approximate PWS result with Eq. (2.2). More specifically the approximate PWS form function plotted in Figs. 2.6(a) and (b) (short dashed lines) is calculated with

$$|f| = \frac{\left|f_{cyl}^{app}\right|}{\left|f_{cyl}^{rigid}\right|}, \tag{2.3}$$

where f_{cyl}^{app} is the approximate form function described in Chapter 5. The comparison between the infinite and finite cylinder results is then quite good, except at low frequencies. The experimental data seems to match these calculated curves very well. In general this indicates that the receiver is not in the true far-field of the finite cylinder of length L and the scattering is dominated by wavefronts which spread according to $1/\sqrt{r}$. The fact that the comparison with the measurements is so good indicates that the receiver is however in the "far-field" when considering the other dimension of the shell, the radius a, and the scattering is found to be weakly dependent on the finite length of the shell. These same arguments do not apply to the backscattering by a tilted finite cylindrical shell. A more in-depth discussion of the far-field criteria may be found in Section A.3 of Appendix A.

[This page is intentionally left blank.]

3

Time Domain Analysis of the Backscattering from Finite Cylindrical Shells

3.1 Introduction

Historically, the scattering of sound by finite cylindrical objects in water has been an important problem to understand. There has been recent interest in gaining a better understanding of scattering processes in the high frequency regime. In particular, high frequency sonar images of finite cylindrical shells have displayed enhancements which *increase the visibility of the ends*[1]. These enhancements are associated with elastic effects on the cylinder. Specifically, the work in Ref. [1] found enhancements for a 5.5% thick (b/a = 0.945, where b and a are the inner and outer radii, respectively) water-filled steel shell near 600 kHz (ka = 145.6, where $k = \omega/c$) at various cylinder aspect angles. The enhancements were found to occur when the aspect angle of the cylinder neared a leaky wave coupling

angle, given by $\theta_l = \sin^{-1}(c/c_l)$. Here c_l is the phase velocity of the l^{th} class of leaky wave and c is the speed of sound in the surrounding water. The idea of launching surface waves on tilted cylinders, which might then give enhanced backscattering after reflection from the cylinder truncation, is obviously not new and experimental[10] and theoretical[10,11,16,32] reports have been made concerning this. A consequence, however, of the greater fractional shell thickness and higher frequencies which are important for specific imaging applications is that thin shell mechanics is not suitable to describe the scattering processes in these cases. To address high frequency scattering Marston[5] developed a ray model for meridional rays which qualitatively describes the results of Ref. [1] (see Fig. 2.1; meridional rays are purely axial and travel along the meridian, or front face, of the cylinder). Furthermore he noted that the amplitude of the backscattered meridional ray should be "significantly stronger" than the end diffraction predicted, e.g., by GTD by a rigid cylinder. Aspects of high frequency helical wave excitation have also been analyzed[6].

To explore these high frequency scattering and coupling processes, Morse, *et al*[8] carried out backscattering experiments with thick and moderately thick finite cylindrical shells. This is the subject of Chapter 2. Impulse response measurements made with a broadband PVDF sheet source[20] revealed various enhancements over the full range of cylinder aspect angles which were identified with the generalizations of the a_0, $a_{0\text{-}}$, s_0, and T_0 (transverse shear) leaky waves. Figure 2.4 shows some results from that investigation. It displays frequency-angle domain representations of the experimental and calculated backscattered spectrum showing regions of high backscatter [Figs. 2.4 (a) and (b)] which were found to be associated with favorable coupling conditions [Figs. 2.7 (a) and (b)] for meridional and helical leaky waves calculated *for infinite cylinders*. In addition to these conditions, called coupling loci, it is important to gain an understanding of how the scattering processes are manifest in the time domain. Doing so will provide further insight into the scattering problem. The present investigation aims to further this understanding with the use of time series analysis applied to the experiments of Chapter 2.

FIG. 3.1 Measured time series of the backscattered pressure versus cylinder aspect angle for Shell A. The linear color scale represents a logarithmic scale where red is positive high voltage (1 --> 0 dB), blue is negative high voltage (-1 --> -0dB) and white corresponds to low levels (-45 $dB_{re\ max\ @\ \gamma = 0^\circ}$). The sheet source was used in the bipolar pulse mode for this data. The response shown is the measured direct backscattered signal where a background record has been subtracted from each trace. This background is recorded with the cylinder removed and includes signals propagating directly from the source to the receiver. Two backgrounds were used in this figure: one for the angles 0°-90° and one for 90.4°-180.4°. This was done to improve the subtraction for the late time response over the latter range of angles since an unknown experimental "drift" occurred over the duration of the experiment (≈ 7 hours). The improved subtraction can be seen near 700 μs at $\gamma = 90^\circ$.

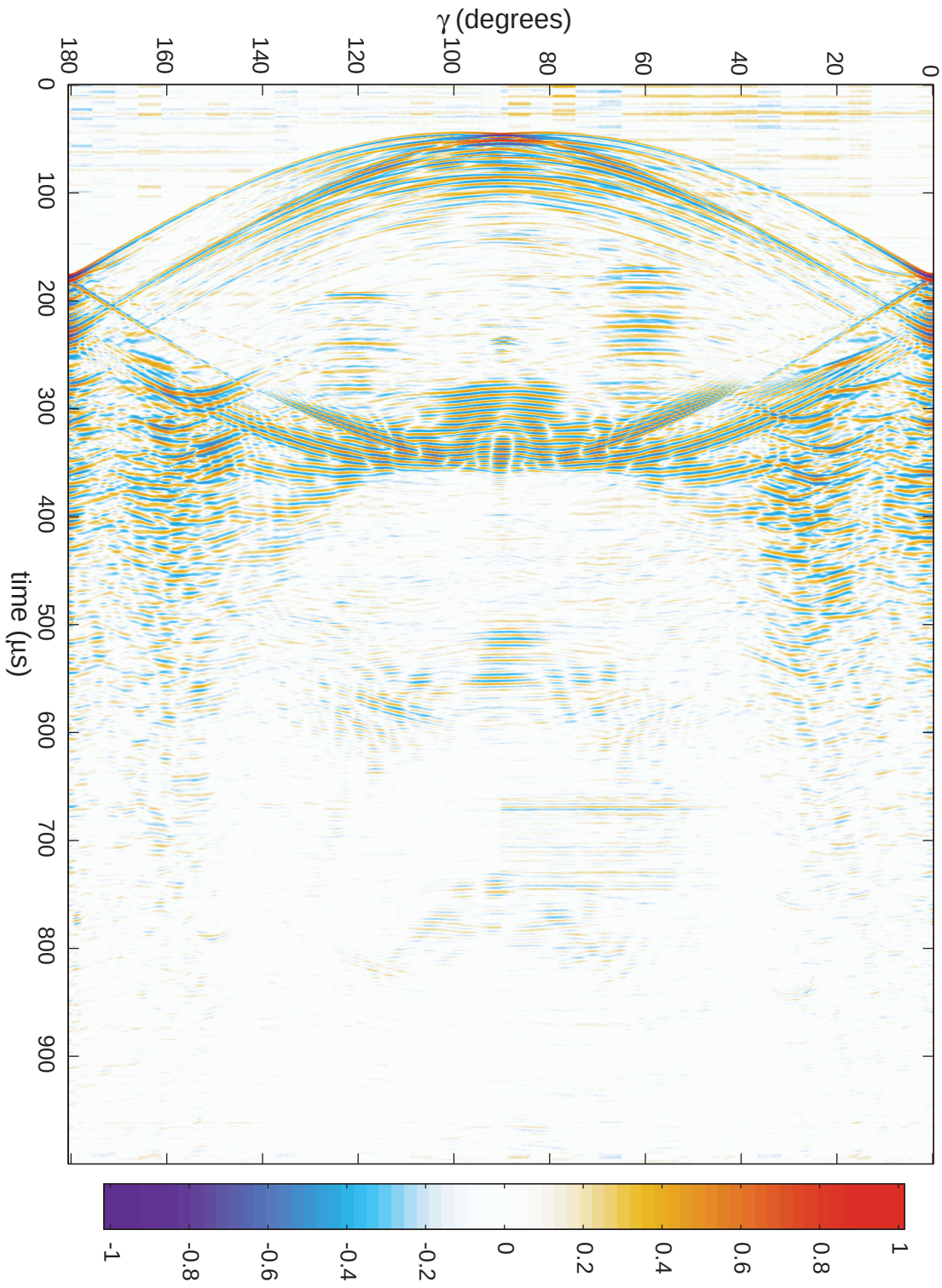
γ (degrees)
180
160
140
120
100
80
60
40
20
0
time (μs)
0
100
200
300
400
500
600
700
800
900
-1
-0.8
-0.6
-0.4
-0.2
0
0.2
0.4
0.6
0.8
1

3.2 Experimental Results

Figure 3.1 shows the raw time series data versus cylinder aspect angle for impulse response backscattering from an air-filled, slender, finite cylindrical shell. A background record has been subtracted from each time record to eliminate signals arriving directly from the source. This is the same shell and experimental setup as Shell A in Chapter 2 and Ref. [8]. A description of the endcaps used for this experiment may be found in Appendix A on page 278. Broadside incidence corresponds to $\gamma = 0°$ while end-on is $\gamma = 90°$ and the step size is 0.4°. Recall the properties of the shell found in Table 2: stainless steel 304, b/a = 0.924, a = 19.05 mm, L/a = 12.0, where L is the cylinder length. There are two minor differences in the experimental setup in this case. The first is that the source was driven in the bipolar pulse mode (see Appendix A for a discussion of the two modes of operation). This mode was chosen since the bipolar mode results in less low frequency clutter after the background subtraction is performed and increases high frequency performance. The second difference from the data presented earlier is that the separation distance between the center of the cylinder and the receiver is 1.55 m as opposed to 1.25 m.

Figure 3.2 is a close-up of the first 500 μs of Fig. 3.1. The overlaid solid black lines are the calculated return times for direct propagation from the source to the four "corners" of the cylinder and back to the receiver. Expressions for the corresponding return times are given in Section 3.B where account is made for the finite target-receiver distance. These points are labelled A through D in Fig. 2.1. They would have the same locations in space as the corners of a rectangle of dimensions $2a$ x L lying in the plane of rotation of the cylinder and centered about the bisection of the cylinder. These locations on the cylinder are henceforth referred to as corners. The two lines having the earliest arrival times (lower values of time) correspond to reflection from corners A and D while the lagging two correspond to B and C. This helps place the scattered response in perspective. The earliest arrivals are diffracted off the nearest corner edges. Later arrivals are evident from the closest rear corner [B, or C ($\gamma > 90°$)] but these tend to be overwhelmed by the elastic response.

At this point it is possible to make a few comments about the elastic response. Within 30 degrees of broadside incidence ($30° > \gamma > 0°$ and $180° > \gamma > 150°$ for the ranges shown) the response is very complicated. This is the region where, in Chapter 2, it was shown that coupling to the helical waves of the s_0, T_0, and a_0 waves are possible. Coupling to the s_0 meridional ray is possible as well, but is excluded for the T_0 meridional ray due to the nature of its propagation characteristics. Recall that the cutoffs for the s_0 and T_0 helical waves are roughly 16.5° and 28.2°, respectively. Within these ranges of angles many orders (circumferential, labelled n) of helical waves may be launched. For the frequency range shown in Fig. 2.7 the possibility exists of exciting 9 helical modes of the s_0 and 14 modes of the T_0. If excited, these are expected to exhibit low levels of radiation damping (see Fig. 2.9) and as a result the response would persist for some time. This is generally what is observed in Figs. 3.1 and 3.2. At this point it is important to note that the next higher modes, the s_1 and T_1, have mode thresholds well above the highest frequencies available in this experiment. As a result no contributions are expected from these higher modes. Somewhat beyond the cutoff angle for shear wave propagation (about 28 degrees) the elastic response is relatively short-lived, indicative of an elastic response with significant damping. In this region the only types of surface waves that may contribute are those with phase velocities less than the T_0 wave. Referring to Fig. 2.9 this leaves only the antisymmetric waves a_0 and a_{0^-}. These both exhibit larger levels of damping than the s_0 and T_0, and so their backscattered response would not persist as long. One very interesting characteristic of the response between $\gamma = 40°$ and $\gamma = 140°$ is that some of it *precedes* the geometrical timing to the closest rear corner (t_B or t_C). This is especially true at end-on incidence ($\gamma = 90°$). The only way this is possible is if the surface-wave wavepacket responsible is launched prior to the closest rear corner and possesses a group velocity greater than the sound speed in the water. Without further analysis, it is not possible to positively identify which of these contributions is the result of the a_0 meridional ray and which are due to the a_{0^-} helical rays. This will be the subject of the next section.

For the purpose of reminding the reader of the spectrum associated with Fig. 3.2, its normalized spectrum is displayed in Fig. 3.3 for the same range of angles. This can be

FIG. 3.2 Close up of Fig. 3.1 with overlaid black lines indicating the calculated return times for direct propagation through the water to each of the four "corners" of the cylinder (see Fig. 2.1). These times correlate well with observed diffraction returns. Expressions for these arrival times may be found in Section 3.B.

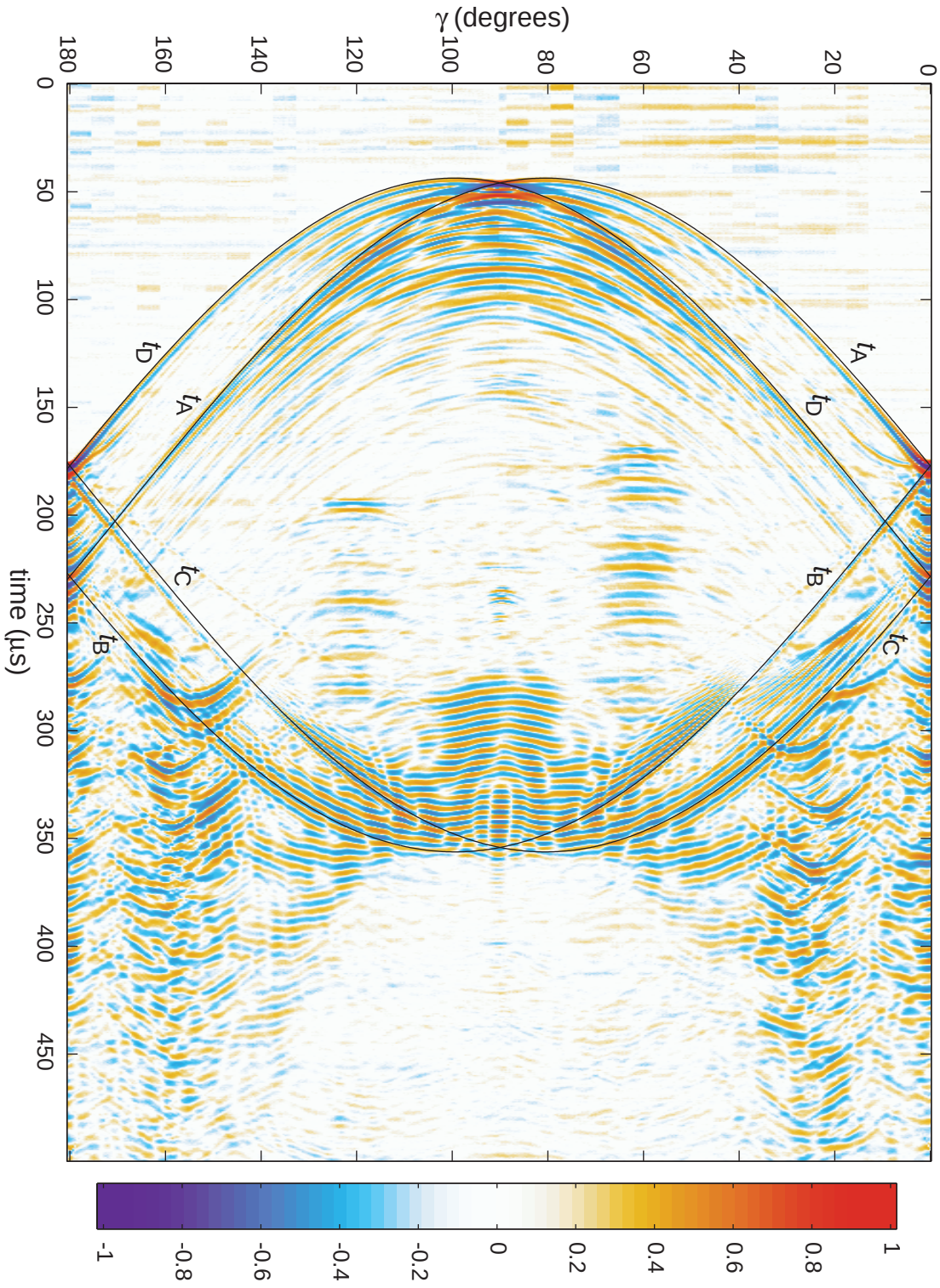
γ (degrees)
time (μs)
t_A
t_B
t_C
t_D
0
20
40
60
80
100
120
140
160
180
0
50
100
150
200
250
300
350
400
450
1
0.8
0.6
0.4
0.2
0
-0.2
-0.4
-0.6
-0.8
-1

FIG. 3.3 Magnitude of the spectrum of the backscattered response of Fig. 3.1 (or Fig. 3.2) normalized with the spectrum of the incident bipolar pulse (see Section A.4 of Appendix A). Most of the reflections from the earliest endcap are windowed out of the time signals of interest before performing the Fourier transform. Including the nearest endcap reflections results in a large broadband feature near $\gamma = 90°$ which is associated with the specular reflection from the flat endcap. Excluding this response simplifies the interpretation of the measured spectrum. The horizontal streaks in the data above 400 kHz are a result of the diminishing signal-to-noise ratio at high frequencies. The spectrum below 35 kHz has been "floored" (shown as black) because of poor source normalization for the bipolar pulse mode at low frequencies.

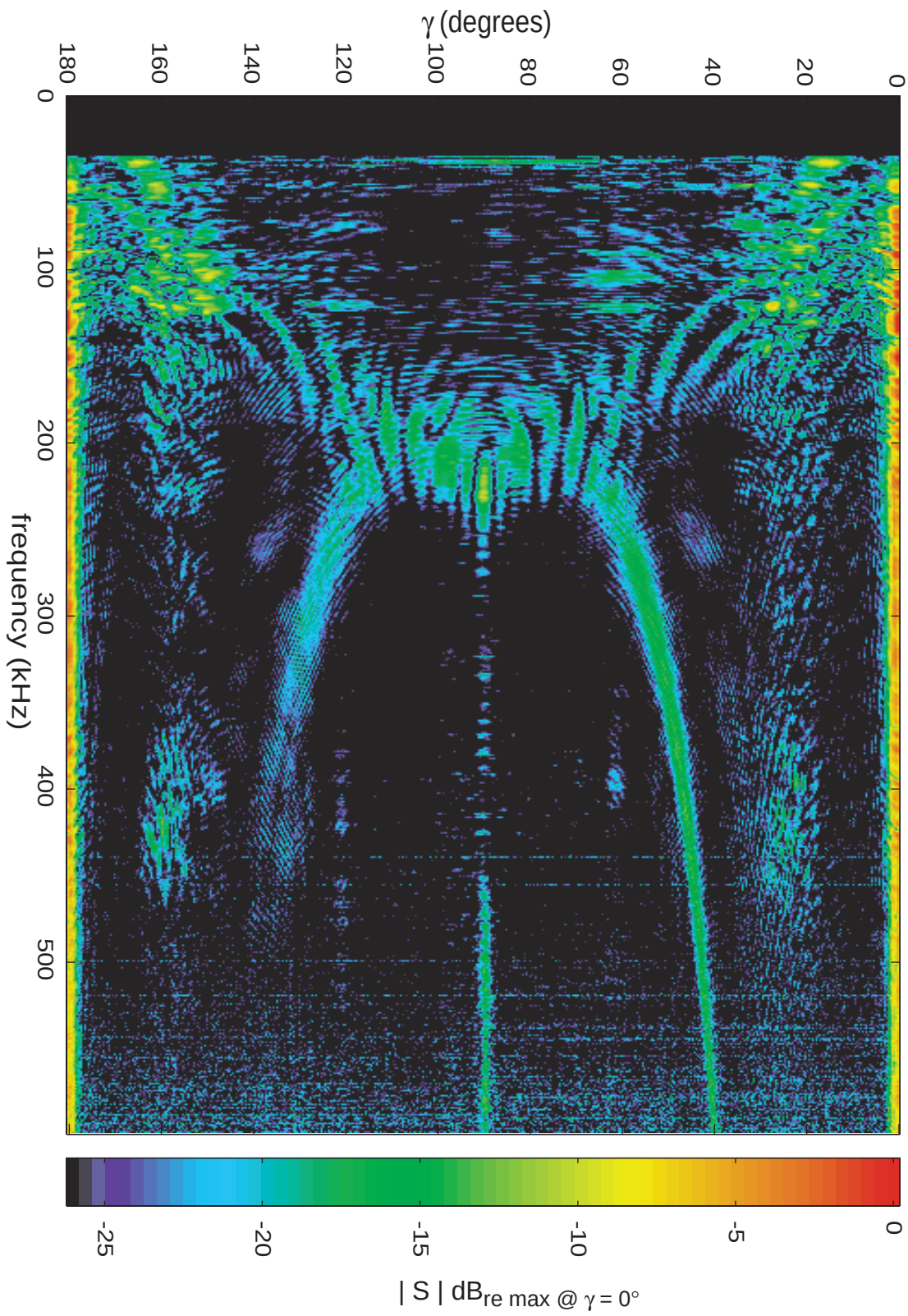
γ (degrees)
0
20
40
60
80
100
120
140
160
180
frequency (kHz)
0
100
200
300
400
500
| S | dB re max @ γ = 0°
0
-5
-10
-15
-20
-25

compared directly with the spectrum in Fig. 2.4(b). This figure is not quite symmetrical about $\gamma = 90°$. The cause of this is unknown.

3.3 Time-Frequency Analysis

Knowledge of the frequency response of a system is often very useful in identifying important features, as it was in Chapter 2. The corresponding time domain response can be quite complicated, as is the case here. One tool that is highly useful for making a connection between features in the frequency domain and those in the time domain is time-frequency analysis. There are many different approaches and flavors which include the Short Time Fourier Transform (STFT) and Wavelet Transform[33-35,37,38,39]. Slightly different approaches are global transforms such as the Wigner-Ville or Choi-Williams distributions. The simplest of these is the STFT which has been used extensively in the analysis of speech and is often referred to as a spectrogram. The goal is to find out what frequencies are present at a given time and at what amplitude in a time series signal. The process is straightforward: 1) out of the entire time signal select a small region of interest and apply a window function of length T_p which zeros out everything outside the window, and then 2) take the Fast Fourier Transform (FFT) of what's left. In this way one is essentially finding the frequencies present in a selected short span of time. Now take this window and FFT algorithm and move it along the time signal. This generates a 2-D representation of the signal with time on one axis (same as the original time axis) and frequency on the other. If the original time series is sampled at an interval of Δt up to a maximum time of $N\Delta t$ then the corresponding frequency interval will be $\Delta f = (N\Delta t)^{-1}$ for $N/2$ samples. One can see, however, in the STFT the actual frequency resolution is limited by the width of the window. The longer the window the greater the frequency resolution, but at a cost of time resolution in the time-frequency representation. Likewise, if the time window is made short to obtain better time resolution then the frequency resolution is decreased. For example, in the analysis to follow the sampling interval in the original signal is $\Delta t = 0.5\,\mu s$ for $N = 2000$ samples. This gives a frequency resolution for

the full transform of the original signal of $\Delta f = (N\Delta t)^{-1} = 1$ kHz. The length of window chosen is $T_p = 40\,\mu$s which would give a frequency resolution of 25 kHz for the window itself. Since we are not extracting out a 40 μs portion of the original signal and then doing a FFT the resulting frequency interval is not 1/40 μs = 25 kHz, but is still 1 kHz, in keeping with the overall 2000 sample window. The overall bandwidth of the windowed signal, however, is essentially determined by the length of the window (i.e. poor resolution ≈ 25 kHz) and the increased resolution (1 kHz) can be thought of as a smoothing of the spectrum. A good discussion of the considerations involved in performing time-frequency analysis can be found in the text by Cohen[39].

The actual expression used to calculate the STFT, *G(f,t')*, is identical to that used in Ref. [35] and is,

$$G(f,t') = FT[w(t-t')g(t)] \tag{3.1}$$

where *g(t)* is the original time signal, *w(t)* is the window function and *FT*[ ] represents the Fourier Transform of the quantity in brackets. The window used is the Blackman window given by,

$$w(t) = \left(\frac{1}{18608}\right)\left\{7938 + 9240\cos\left[2\pi\left(\frac{t}{T_p} - 0.5\right)\right] + 1430\cos\left[4\pi\left(\frac{t}{T_p} - 0.5\right)\right]\right\} \tag{3.2}$$

where T_p is the window length. For $t \notin [0, T_p]$ the window is zero. The routine is relatively easy to implement in a high-level programming language such as Matlab®. The code used is given in Appendix B.

Figures 3.4 - 3.9 display the results of applying this STFT algorithm to six individual time records from Fig. 3.1. Each has been normalized along the frequency axis with the spectrum of the incident pulse. Specifically they are $\gamma = 0°$, 39.6°, 44°, 52°, 71.2°, and 90°. Overlaid on each plot is a vertical white line which corresponds to the geometric reflection timing from the closest rear corner (at t_B, see Section 3.B). From the result for broadside incidence in Fig. 3.4, $\gamma = 0°$, one may identify strong contributions from the a_{0-} coincidence frequency enhancement[27,29,35] near 140 kHz as a series of individual wavepackets. (Recall

that the coincidence frequency is roughly 193 kHz.) Also present is a broadband a_0 wavepacket above the coincidence frequency just after the specular reflection. Consider now what happens as the tilt angle of the cylinder is allowed to increase. The response for angles less than the shear cutoff angle (≈ 28°) is complicated and no new individual contributions are evident, i.e. individual wavepackets due to s_0 or T_0 helical waves are not distinguishable. As the tilt angle increases further, only a few features are left. At $\gamma = 39.6°$ (Fig. 3.5) three features are clear. The first is the broadband wavepacket at about 165 μs corresponding to the corner reflection from the closest corner (labelled A). The second feature is evident below 200 kHz as a series of regularly spaced wavepackets. The third feature is barely distinguishable near 500 kHz right at the corner timing, t_B. These last two features may be identified by inspecting Figs. 2.4, 2.7 and 3.3. The contribution previously identified as the a_0 meridional ray should be present around 600 kHz for this angle. Furthermore it should appear fairly broadband due to the slope of the meridional ridge in Fig. 3.3. What is seen in Fig. 3.5 is the lower frequency portion of the a_0 meridional ray wavepacket. The other feature at lower frequencies, appearing as 6 individual wavepackets delayed from the corner timing, is identified through the same process as several helical returns of the $a_{0\text{-}}$. These contributions have traversed a helical path on the cylinder and as a result are delayed with respect to the meridional ray wavepacket, which only propagates along the cylinder front meridian. They have been reflected once at or near point C in Fig. 2.1. Now tilt the cylinder further away from broadside to $\gamma = 44°$ (Fig. 3.6). The a_0 meridional ray wavepacket is now fully distinguishable at about 460 kHz as the most prominent feature. The visible $a_{0\text{-}}$ helical wavepackets have decreased in number to three and are now closer together. At $\gamma = 52°$ (Fig. 3.7) the a_0 meridional ray wavepacket has moved down in frequency to 330 kHz. The $a_{0\text{-}}$ helical wavepackets are no longer distinguishable as separate wavepackets but they still lag the corner reflection time. At $\gamma = 71.2°$ (Fig. 3.8) these two features have merged in time and frequency and are indistinguishable. This merging in the frequency domain is also seen in Figs. 2.4 and 3.3. The timing of this feature is roughly coincident with the closest rear corner timing (at t_B). At end-on incidence, $\gamma = 90°$ (Fig. 3.9), these features are still indistinguishable but now

display three interesting characteristics, which together suggest an interpretation of the scattering mechanism. First of all the primary return precedes the corner timing significantly. This suggests that the wavepacket speed exceeds that of the speed of sound in water. Secondly, two additional returns are evident at equally spaced intervals behind the original. Thirdly, there appears to be one dominant frequency interval over which these features are found. To help in identifying the contributing mechanism consider the following: the time necessary for a wave to travel twice the length of the cylinder at the speed of sound in water is $2a(L/a)/c_w = 2 \cdot 19.05 \cdot 12/1.483 = 308\,\mu s$. The interval between the observed returns is roughly 225 μs. This corresponds to a wavepacket group speed of about 1.4 times c_w. This is consistent with what is known about the group velocity of the $a_{0\text{-}}$ wave in this frequency range. Figure 3.21 in Section 3.A of this chapter shows the phase and group velocities of the a_0 meridional ray and $n = 8$ $a_{0\text{-}}$ helical ray for this cylinder. Reference may also be made to Figs. 4.3, 4.4, 4.15 and 4.16. The group velocity of the $a_{0\text{-}}$ is supersonic in this frequency range and varies between 1.2 c_w and 1.4 c_w. Furthermore its damping is extremely small between 60 - 180 kHz, which would enable it to make the multiple traversals without additional losses due to radiation. Furthermore the multiple wavepackets are all found near 150 kHz. This is also suggestive of the propagation of the $a_{0\text{-}}$ for the following reason. For impulsive loading of a dispersive propagating system (such as in the present case) it is known that certain resulting disturbances may propagate over large distances with less attenuation than other disturbances having similar damping characteristics. This disturbance is associated with a group velocity extrema in the corresponding dispersion curve. This type of disturbance is well known and has been termed an Airy phase (see pp. 142-151 of Ref. [40] and Ref. [41]). In Fig. 3.21 it can be seen that the group velocity of the $a_{0\text{-}}$ wave indeed has a maxima near 150 kHz. The group velocity of the a_0 meridional ray is also supersonic and is comparable to the $a_{0\text{-}}$, however its damping is considerably larger and no extrema exists in this frequency range. The observations, therefore, suggest that the mechanism responsible for the early arrivals for $\gamma > 70°$ is primarily due to coupling to the $a_{0\text{-}}$ guided helical waves. For this to be the case near end-on incidence *the coupling process must primarily be associated*

with the cylinder truncations and endcaps as opposed to trace velocity matching on the outer surface of the shell. This is for the following reason. The a_{0-} wave on a fluid-loaded plate is subsonic (as it is on a cylinder) and therefore cannot be coupled to the external fluid through the typical trace velocity matching of wavevectors at the elastic-fluid interface. Coupling to the a_{0-} on a cylindrical shell at broadside incidence (or a spherical shell) is responsible for the coincidence frequency enhancement mentioned earlier. The coupling process in this case requires that the guiding structure have curvature. It is because of the curvature that the spacing between phase fronts a certain distance above the structure in the fluid can match an acoustic wave and radiate energy[27,32]. On a tilted cylinder the coupling to the a_{0-} becomes dependent on the tilt angle because the tilt angle determines the projected curvature along the direction of the incident wavevector. At broadside incidence the curvature is at a maximum and at end-on there is no curvature. At end-on incidence the a_{0-} could not, therefore, be excited except at the ends. A quantitative description of high-frequency coupling to elastic waves in a fluid-loaded structure at a discontinuity, such as a truncation on a cylinder or the edge of a semi-infinite plate is a relatively difficult problem.

One other feature of the scattering response is a large low frequency peak at high cylinder aspect angles seen to arrive *after* the closest rear corner timing, t_B. It is visible in Fig. 3.8 ($\gamma = 71.2°$) and in Fig. 3.9 ($\gamma = 90°$) near 25 kHz and is not an artifact of the relatively poor spectral magnitude source normalization below 25 kHz. This is slightly below the ring frequency (≈ 40 kHz) for an infinite cylinder and is much higher than modes associated with the volume of air enclosed by the cylinder. This feature can also be seen in Fig. 2.4(b) between $\gamma = 50°$ and $\gamma = 80°$. It is not presently identified. Another feature not identified is the high-frequency relatively broadband response found at about 230 μs in Fig. 3.9.

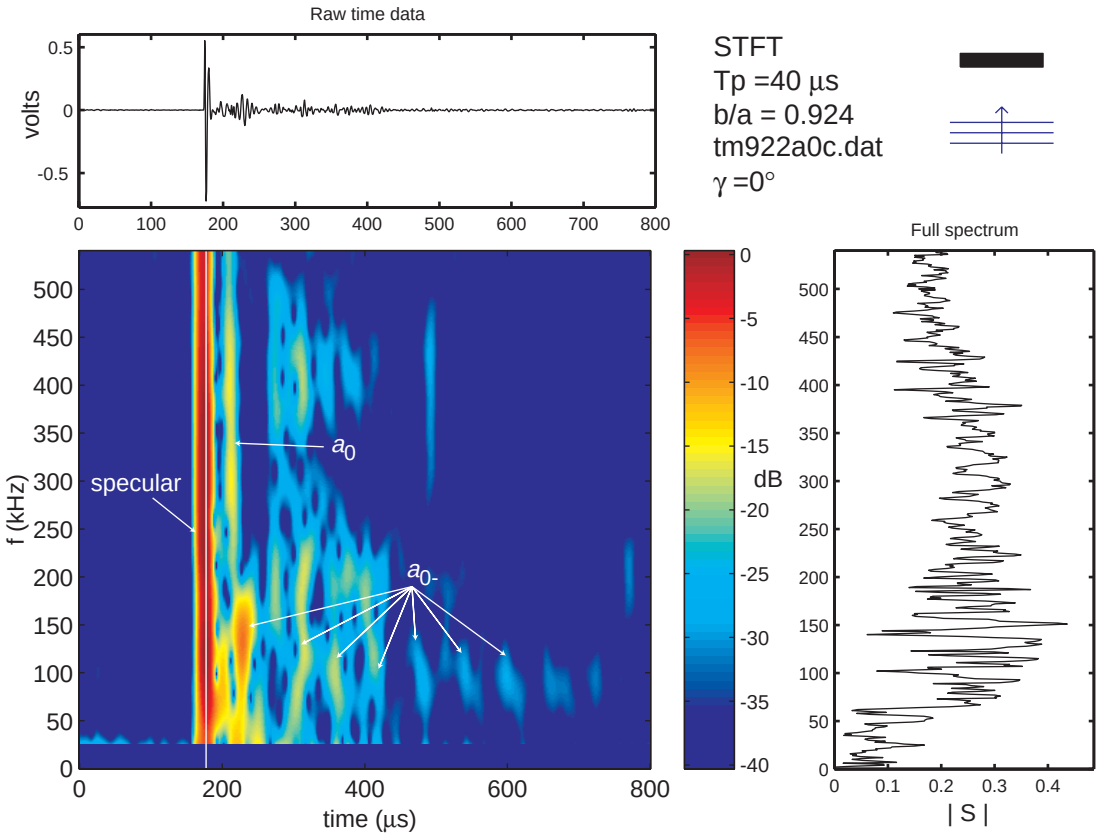

FIG. 3.4 Time-frequency analysis. Short Time Fourier Transform (STFT) of the bipolar impulse response of Shell A, ($b/a = 0.924$), at broadside incidence, $\gamma = 0°$. The full spectrum and the STFT are normalized with respect to the spectrum of the incident pulse. The vertical white line corresponds to t_B.

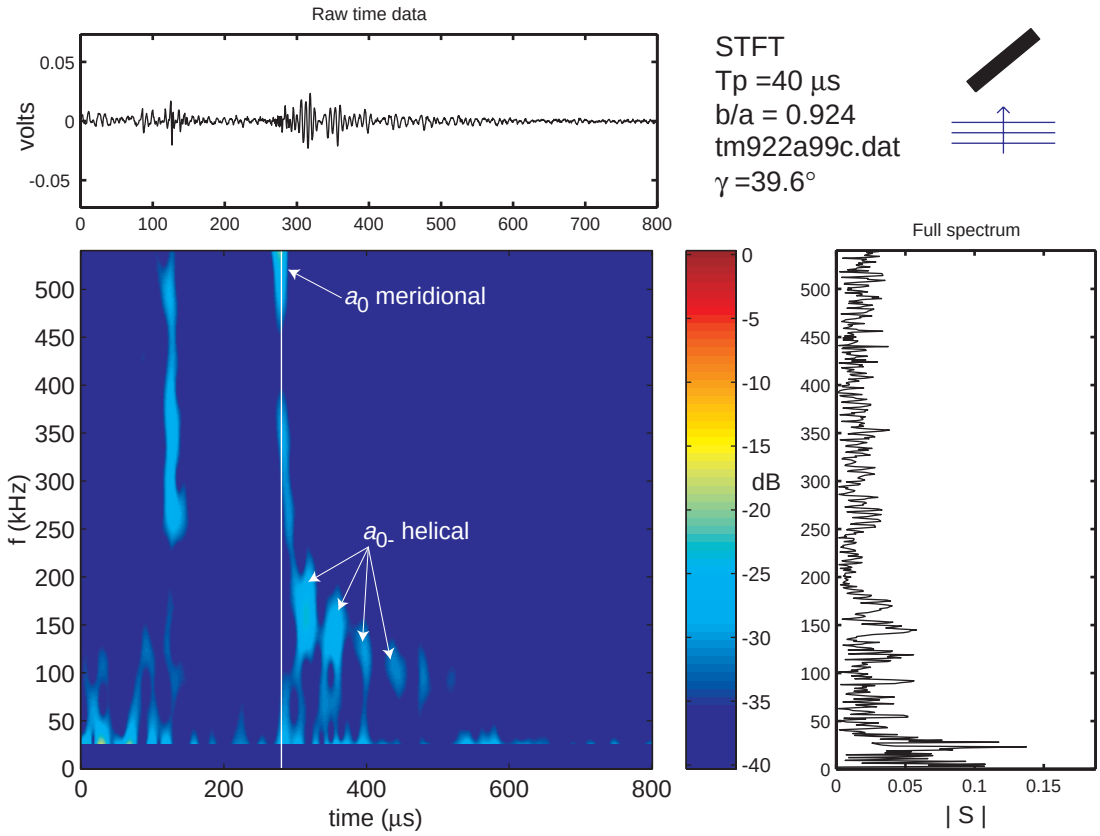

FIG. 3.5 Time-frequency analysis. Short Time Fourier Transform (STFT) of bipolar impulse response of Shell A, $(b/a = 0.924)$, at $\gamma = 39.6°$. The full spectrum and the STFT are normalized with respect to the spectrum of the incident pulse. The vertical white line corresponds to t_B.

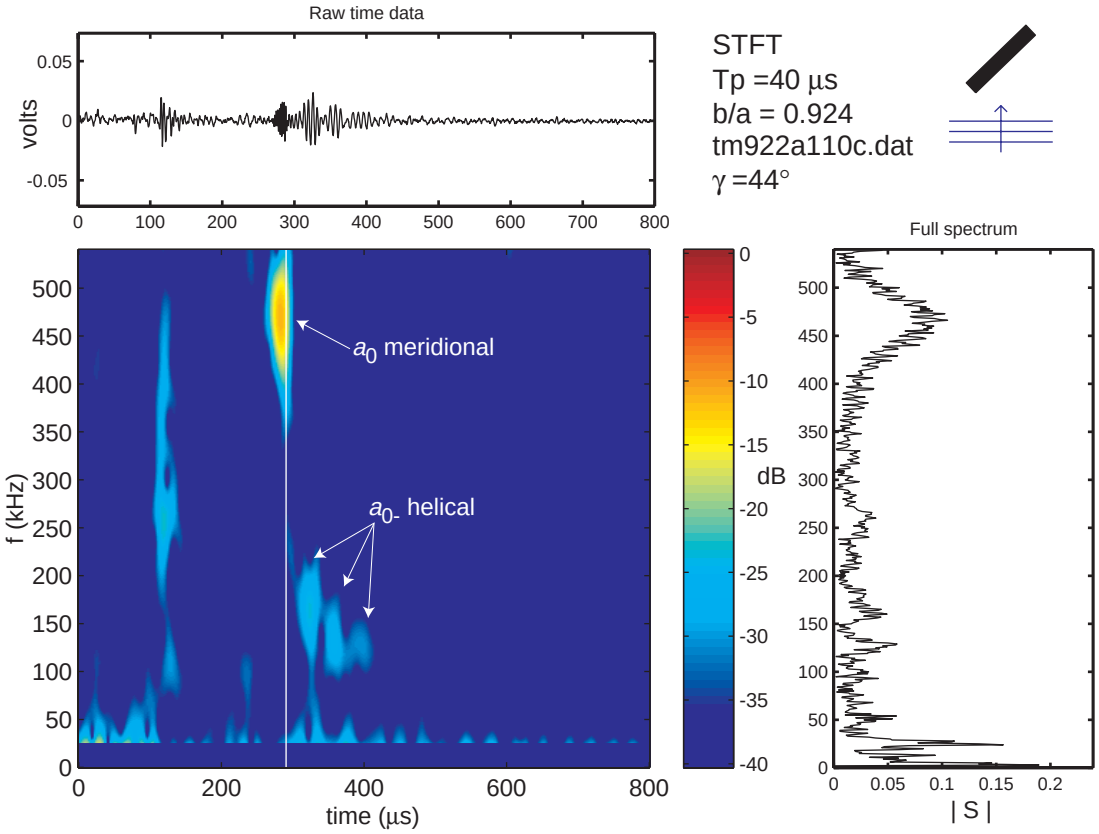

FIG. 3.6 Time-frequency analysis. Short Time Fourier Transform (STFT) of bipolar impulse response of Shell A, $(b/a = 0.924)$, at $\gamma = 44.0°$. The full spectrum and the STFT are normalized with respect to the spectrum of the incident pulse. The vertical white line corresponds to t_B.

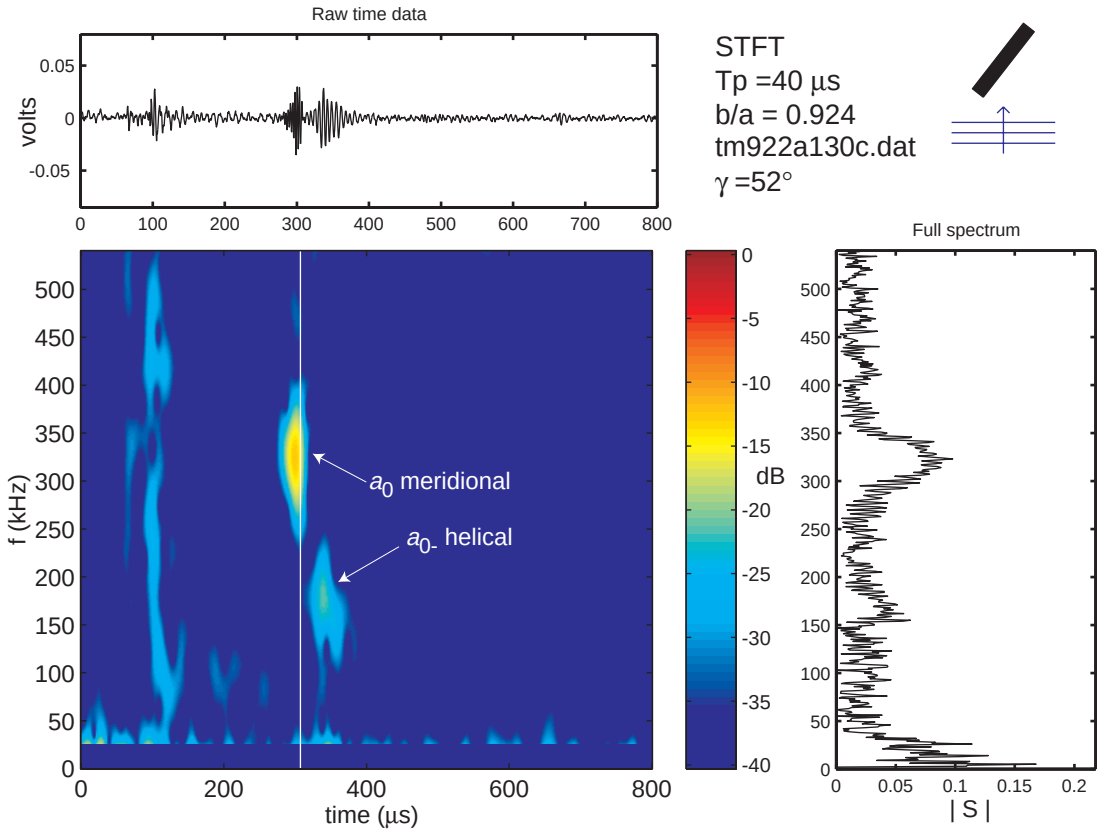

FIG. 3.7 Time-frequency analysis. Short Time Fourier Transform (STFT) of bipolar impulse response of Shell A, $(b/a = 0.924)$, at $\gamma = 52.0°$. The full spectrum and the STFT are normalized with respect to the spectrum of the incident pulse. The vertical white line corresponds to t_B.

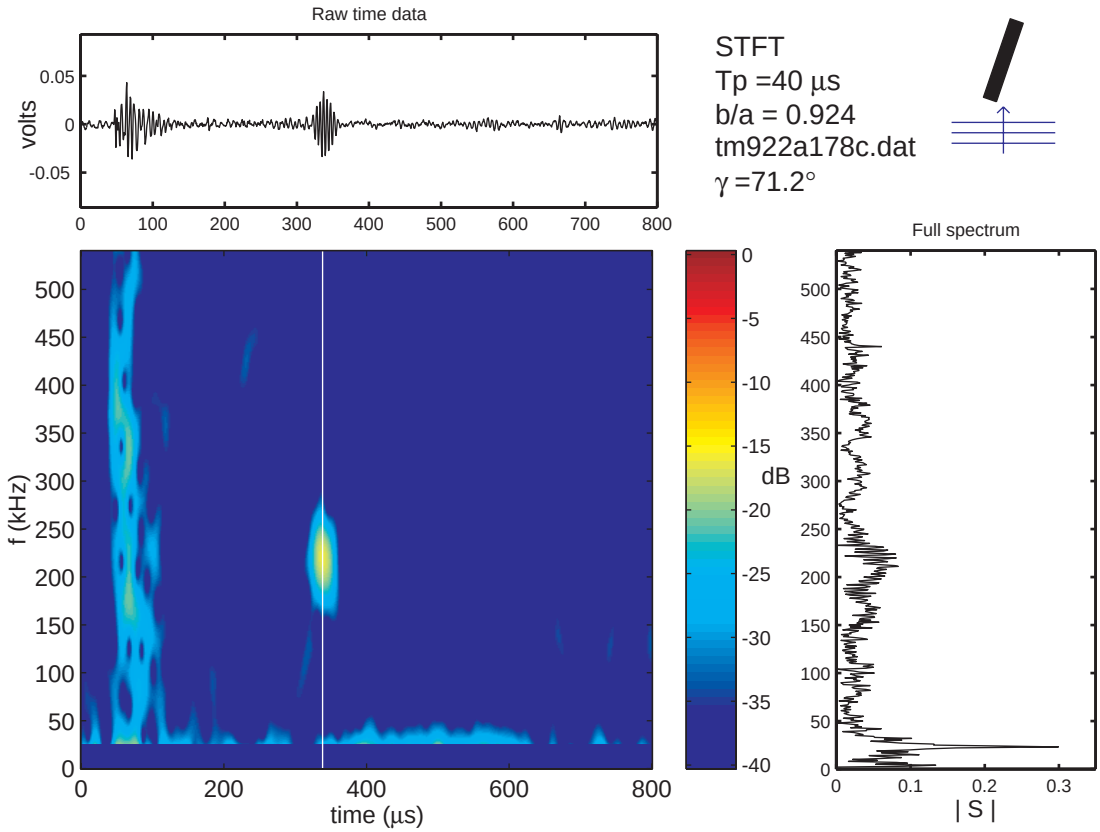

FIG. 3.8 Time-frequency analysis. Short Time Fourier Transform (STFT) of bipolar impulse response of Shell A, $(b/a = 0.924)$, at $\gamma = 71.2°$. The full spectrum and the STFT are normalized with respect to the spectrum of the incident pulse. The vertical white line corresponds to t_B.

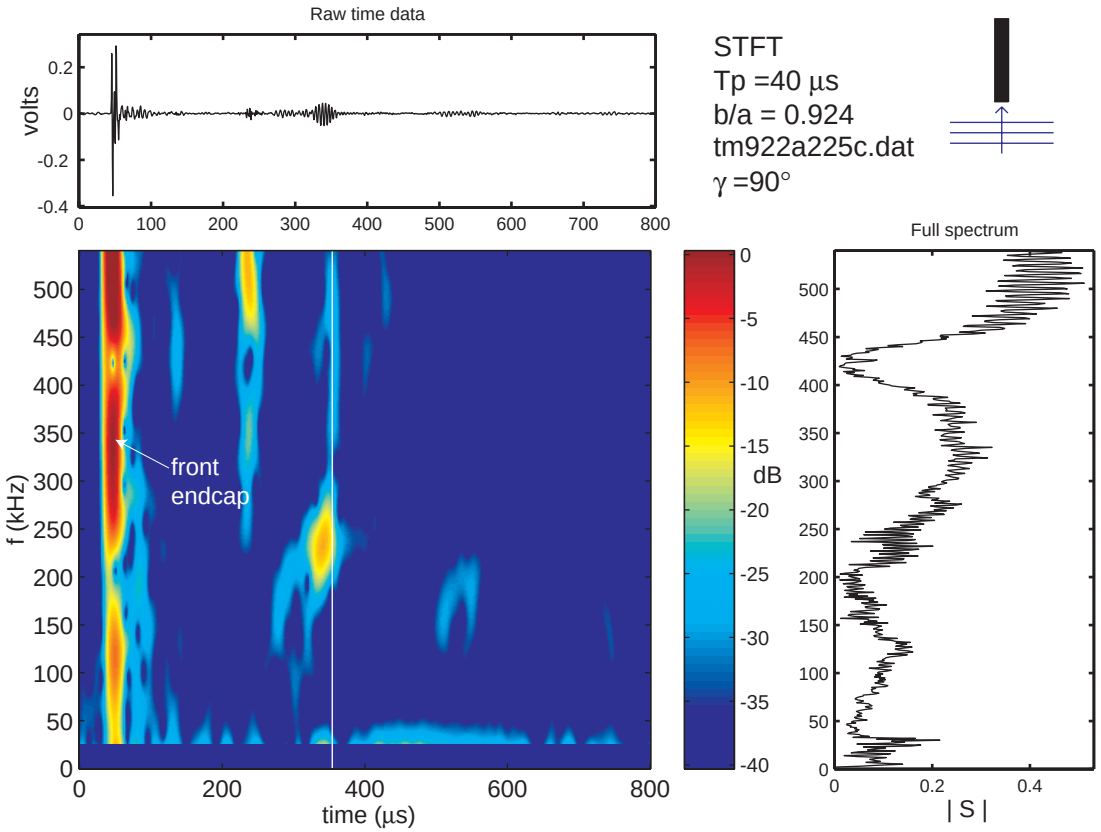

FIG. 3.9 Time-frequency analysis. Short Time Fourier Transform (STFT) of bipolar impulse response of Shell A, ($b/a = 0.924$), at end-on incidence, $\gamma = 90.0°$. The full spectrum and the STFT are normalized with respect to the spectrum of the incident pulse. The vertical white line corresponds to t_B.

3.4 Interpretation of the Angle-Time Domain Data and Comparison with Synthesized Time Series

With the interpretation given above one may then return to the raw time data of Figs. 3.1 and 3.2 to observe the evolution of these processes over cylinder aspect angle. The meridional ray contribution lies along the overlaid closest rear corner timing (t_B, t_C) and slightly precedes it. The helical $a_{0\text{-}}$ wavepackets follow behind this timing in arcs until γ nears 60° where they begin to merge with the meridional ray return.

One feature not presently identified is the relatively low-frequency early arrival near γ = 60° and 120°, between 170 and 300 μs in Fig. 3.2. This response appears in Fig. 3.3 at about 100 kHz. It does not correspond to reflections off the lines used to suspend the cylinder.

It is useful to know which of these features are present in the approximate calculated scattering response, which compared very well with the experimental data in the frequency domain (e.g. see Figs. 2.4 and 2.5). An impulse response can be synthesized from the form function by performing an inverse Fourier Transform[20,27]. Figure 3.10 shows the first 90° of Fig. 3.2, which is the experimental data corresponding to impulse response backscattering from Shell A. (The impulse in this case is a bipolar pulse which is shown in Fig. A.8 on page 290.) Figure 3.11 shows the results of synthesizing the time series for this shell using the computed far-field band-limited form function shown in Fig. 2.4(a). The relatively poor resolution and wrap-around effect due to the Fourier Transform are due to the fact that the approximate form function (see Chapter 5) is numerically costly to calculate on available computers. As a result the data set is undersampled and does not lead to a clean calculation of the time series. As it is, however, it easily displays relevant scattering features. Notably present are the a_0 meridional ray wavepacket which slightly precedes the closest rear corner timing (t_B), and the $a_{0\text{-}}$ helical wavepacket arcs. Notably lacking are any responses at high tilt angles which significantly precede the rear corner timing. In addition the anomalous structure near γ = 60° is not present. This is expected

FIG. 3.10 Same as Fig. 3.2 but only showing the region 0° - 90°. This experimental data was acquired with the sheet source driven in bipolar mode. Dynamic range displayed is 45 dB. Compare this with the synthesized far-field impulse response backscattering in Fig. 3.11.

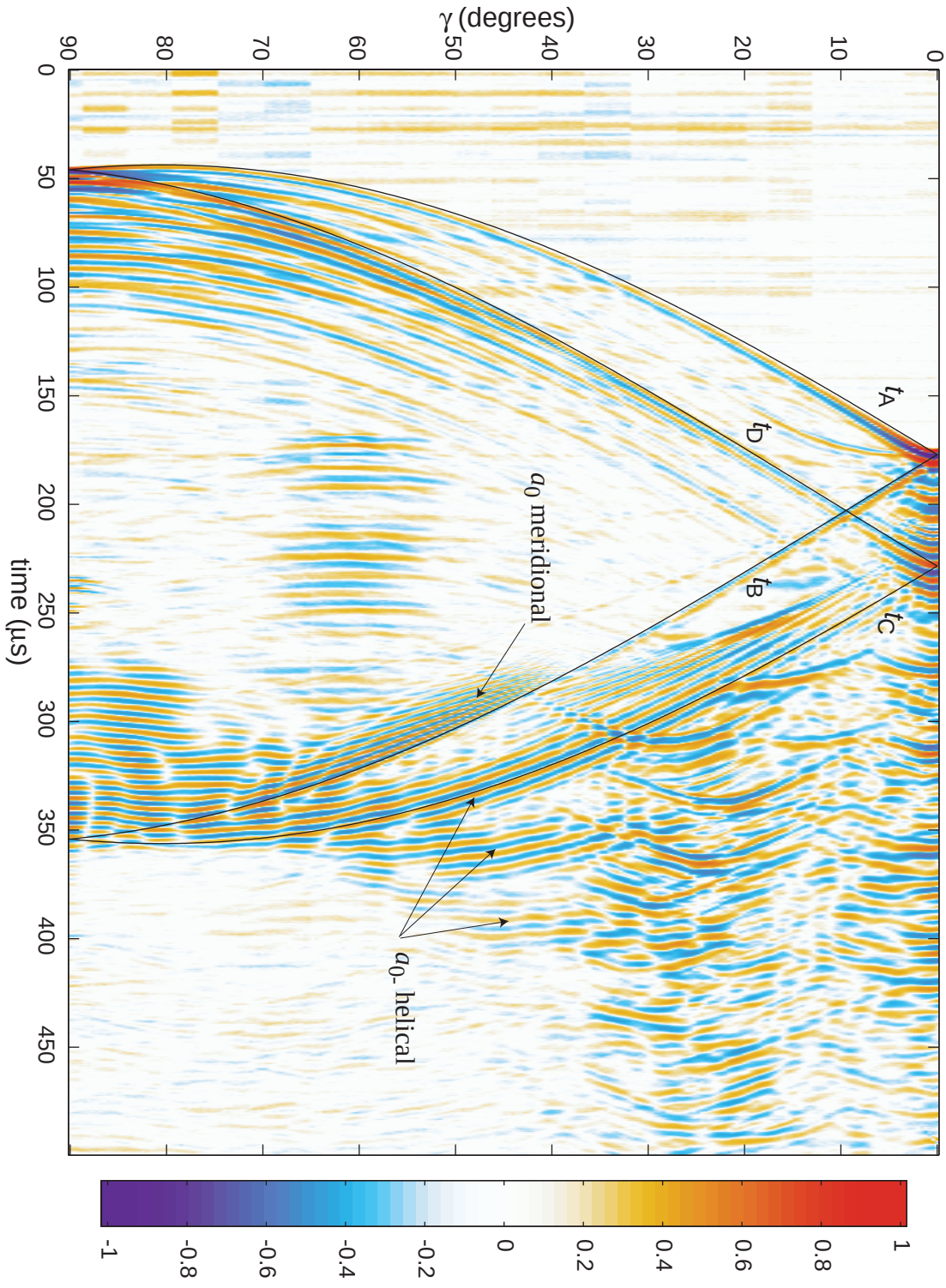
γ (degrees)
time (μs)
t_A
t_B
t_C
t_D
a_0 meridional
a_{0-} helical

FIG. 3.11 Band-limited *synthesized* impulse response time series for Shell A. Dynamic range shown is 65 dB. This time series was obtained by inverse Fourier transforming the calculated backscattering form function shown in Fig. 2.4(a). The form function used had a maximum normalized frequency of $ka = 45$ and was sampled at $\Delta ka = 0.05$.

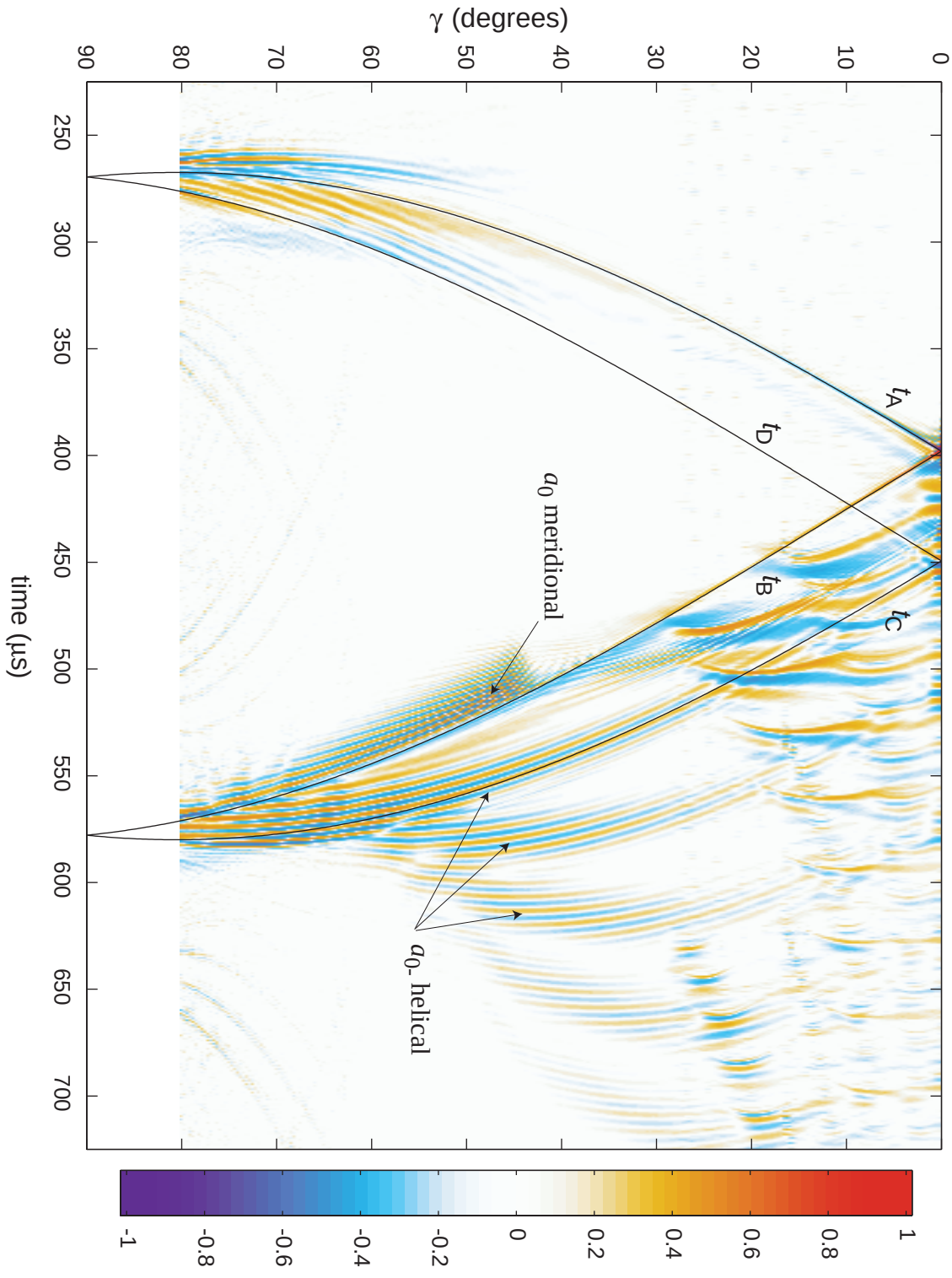
γ (degrees)
time (μs)
t_A
t_B
t_C
t_D
a_0 meridional
a_0- helical

FIG. 3.12 Measured backscattering for Shell B analogous to Fig. 3.10 for Shell A. This experimental data was acquired with the sheet source driven in unipolar (step) mode. Dynamic range displayed is ± 45 dB.

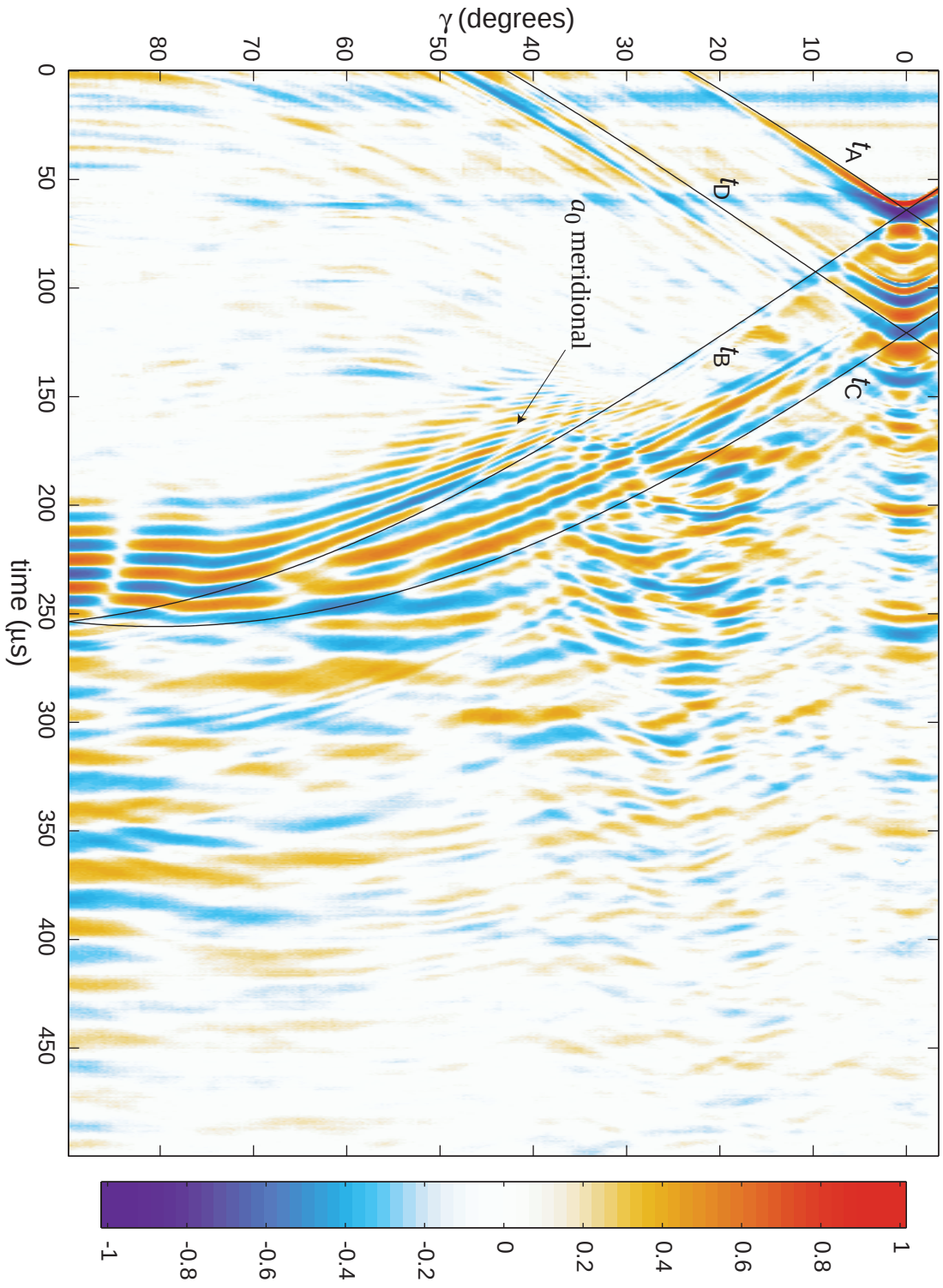
γ (degrees)
time (μs)
t_A
t_B
t_C
t_D
a_0 meridional

FIG. 3.13 Band-limited *synthesized* impulse response time series for Shell B. Dynamic range shown is 65 dB. This time series was obtained by inverse Fourier transforming the calculated backscattering form function shown in Fig. 2.5(a). The form function used had a maximum normalized frequency of $ka = 45$ and was sampled at $\Delta ka = 0.05$.

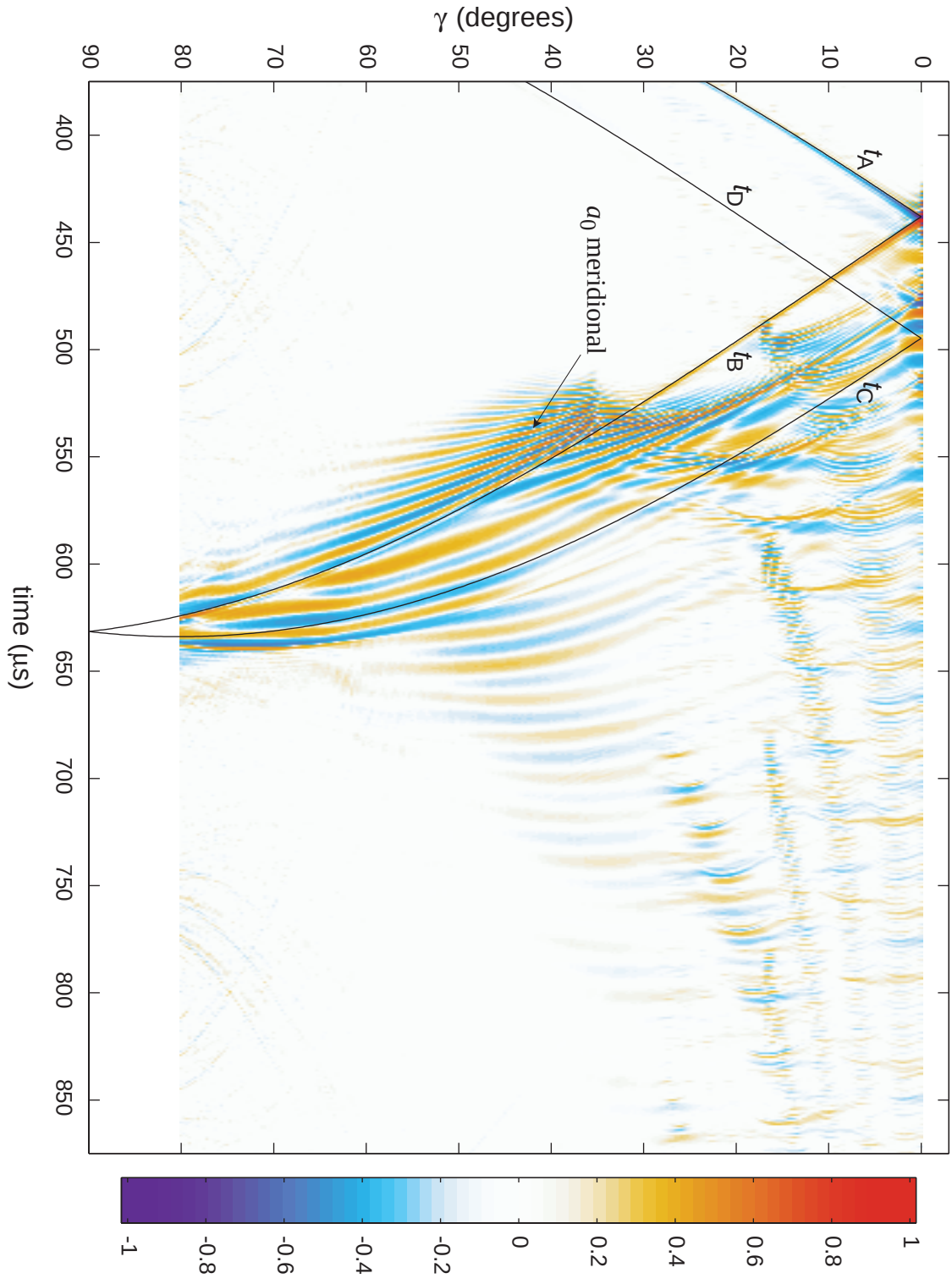
γ (degrees)
time (μs)
t_A
t_B
t_C
t_D
a_0 meridional

since the approximate calculation does not include any mechanics of the end in the coupling process. Figures 3.12 and 3.13 show similar results for the thicker of the two shells studied, Shell B. Similar responses are observed. In calculating Figs. 3.11 and 3.13, no filtering was performed to approximate the spectral response of the source. The only conditioning of the form function included was the application of a raised cosine window to the highest spectral components (ka_{max}-5 < ka < ka_{max}). This allowed for a smooth transition to $|f| = 0$ at high frequencies. This is important in regions where there is considerable response at the edge of the calculated region, such as the highest frequency region of the meridional ray feature.

3.5 Broadband Synthetic Aperture Images

Another tool with which to examine time series data is the synthetic aperture image[42-44]. Applied to a sequence of time records (typically pulse-echo type measurements) representing a spatial aperture the synthetic aperture algorithm coherently sums the scattered response to yield a "picture" of the target. This technique has been used extensively in radar systems including ground, airborne and space based systems to increase cross-range resolution. The idea behind it is quite simple: increase the effective aperture length or width and the cross-range resolution increases. This can be understood through a simple example. In an ideal diffraction limited imaging system (Fraunhofer regime) the theoretical resolution maximum is determined by wavelength and aperture. Using Rayleigh's criterion[45] for the resolution of a slit aperture of length l, which corresponds to a line array, one finds the minimum angular separation of two resolvable intensity peaks in the cross-range direction to be $\Delta\phi = 0.5(\lambda/l)$. A gain in resolution can therefore generally be made by decreasing the wavelength or increasing the length of the aperture. The synthetic aperture itself is typically made up of measurements taken at specific locations along a track, such as the path of a satellite or an ocean surface vessel. With detailed knowledge of each measurement position, the individual scattering records may be processed in software to yield an image of a specific location. It should be noted

that a popular technique used to increase range resolution is to use chirp waveforms. Using a matched filter decompression-compression process, in hardware or software, a chirped signal may be compressed to yield a narrower pulse than a simple pulse generated manually, and at significantly greater power transmission levels. The shorter the pulse the better the range discrimination of the radar or sonar. The higher peak power also greatly increases signal-to-noise. The author has implemented pulse compression in the present scattering system with success: a linear FM chirp burst transmitted by the sheet source can be compressed to yield a very short pulse (< 2μs FWHM) at much higher peak levels than can be generated by the sheet in impulse mode. However, one unavoidable consequence of the pulse compression technique is the presence of sidelobes in the compressed time signal. It was observed that the sidelobes of the specular reflection at broadside incidence from the finite cylindrical shells studied were of comparable amplitude to the elastic responses observed at later times. Also it is not clear what the effects of pulse compression are on the elastic responses themselves. Since the present use of the synthetic aperture technique is concerned with visualizing the elastic scattering processes and not simply identifying targets, no pulse compression methods were used. For a discussion on the effect of chirping the incident pulse in backscattering by a thin spherical shell in the coincidence frequency region see Ref. [46].

A very simple synthetic aperture consists of a fixed source/receiver and a rotating target. This is equivalent to a source/receiver that moves in a circular arc centered about the center of rotation of the target. The synthetic aperture algorithm is fairly simple to implement in this case. Qualitatively, here is how the algorithm works in this case: 1) Multiply the time element entry of each time series record at each orientation angle by 2 times the speed of propagation in the surrounding medium (i.e. the sound speed in water) to account for the round trip travel times inherent in the pulse-echo setup, 2) compute the analytic signal (see Section B.2 of Appendix B) to obtain a complex representation of the real time signal, 3) shift this signal so that the zero distance corresponds to the center of rotation of the target, 4) define a 2-D square *x-y* position matrix with the origin at the center of rotation, setting the discretization equal to 2 times the spatial length of one time interval

sample in the original signal (i.e. 2*$c\Delta t$), 5) for orientation angle number 1, fill all the rows of this matrix with the complex signal for that angle, then 6) rotate the matrix so its orientation is correct for that angle and add it to the original position matrix (unrotated), which is initially full of zeros or the values for the first angle, as closely as possible point for point, 7) finally, repeat steps 5 and 6 for each remaining orientation angle in the aperture. After each angle is included, the absolute magnitude of the position matrix is taken, forming an image in spatial coordinates. One can see that this method is sensitive to the angular sampling interval as well as the temporal sampling rate. This is because rotating the filled-in position matrix requires sampling of the original waveform at points in-between the data points.

This synthetic aperture algorithm was applied in a straightforward manner to the time series data of Fig. 3.1. The results are shown in Figs. 3.14 - 3.19. The white rectangle in each plot is the calculated position of the outline of the cylinder, based on the timing of the specular at broadside incidence. Using the full range of available angles in the algorithm results in Fig. 3.14. The locations of the specular reflections off the cylinder accurately reflect the target's position. The effects of the finite target-receiver distance were not fully taken into account, which has resulted in straight surfaces appearing slightly curved. The primary image in Fig. 3.14 is what one would expect for an image of the reflection from a rigid cylinder. But other significant contributions are also present which are the result of the elastic effects discussed above. For the full aperture the effects are difficult to interpret; however, for selected smaller apertures particular elastic effects are more noticeable. Figures 3.15 and 3.16 cover a range of angles from $\gamma = 0°$ to 40° for apertures of 20° in angular width and should include helical contributions of the s_0 and T_0 waves. Large amplitude echoes are seen to appear away from the cylinder's position. As the center angle is increased to 50° and 70° these contributions are cutoff and the a_0 meridional ray and $a_{0\text{-}}$ helical ray contributions are clearly observable. The a_0 meridional contribution appears as a bright spot right over the closest rear corner, considerably brighter than even the nearest corner diffracted signals. The $a_{0\text{-}}$ helical contributions are seen in Fig. 3.17 to the right of the meridional ray peak as a series of regularly spaced peaks starting at the rear corner.

With the aperture centered about end-on incidence (Fig. 3.19) the elastic responses clearly precede the end of the cylinder, as discussed in the previous section.

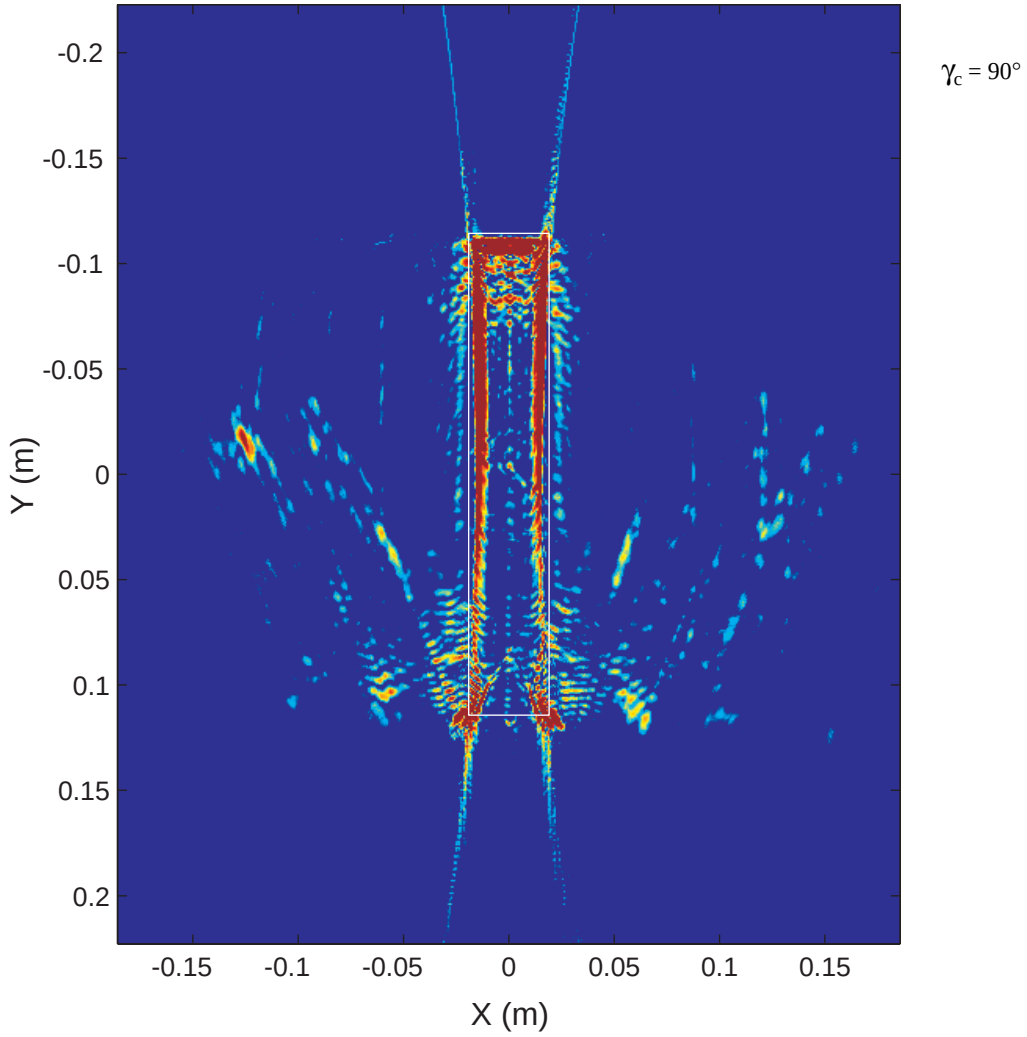

FIG. 3.14 Synthetic aperture image of Shell A. Angular aperture is 180° centered about γ_c = 90°. The white rectangular outline is the calculated position of the cylinder. The dynamic range displayed in this figure, as well as the next 5 figures, is 20 dB with respect to a fixed arbitrary initial voltage [i.e. the amplitude (color) scale is the same for all 6 figures]: red is high, blue is low. The features extending off the end of the cylinder along each broadside face are sidelobe features inherent in the processing of the image. The sidelobe structure could be reduced by increasing the angular sampling interval.

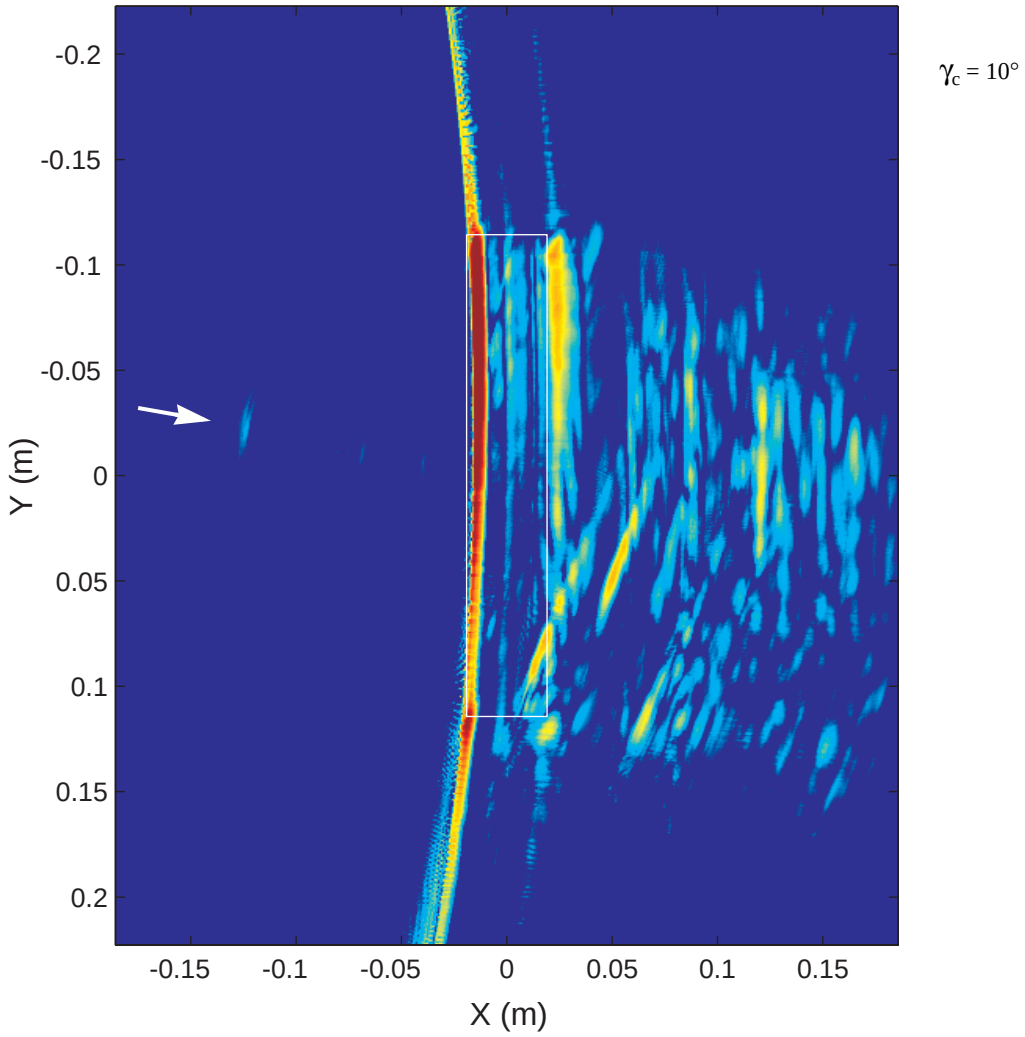

FIG. 3.15 Synthetic aperture image of Shell A. Angular aperture is 20° centered about γ_c = 10°. The white arrow indicates the direction of the incident sound at the center angle, while the white rectangular outline is the calculated position of the cylinder.

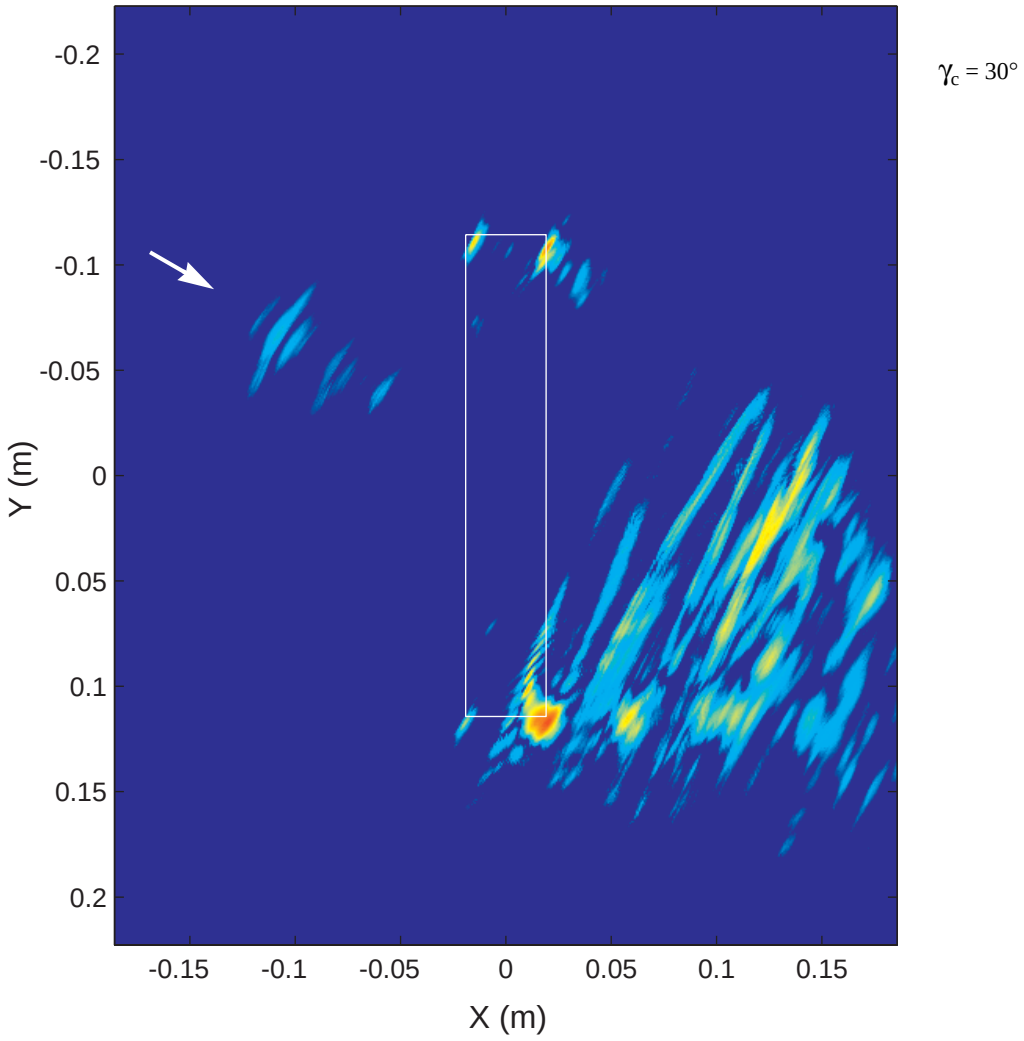

FIG. 3.16 Synthetic aperture image of Shell A. Angular aperture is 20° centered about γ_c = 30°. The white arrow indicates the direction of the incident sound at the center angle, while the white rectangular outline is the calculated position of the cylinder.

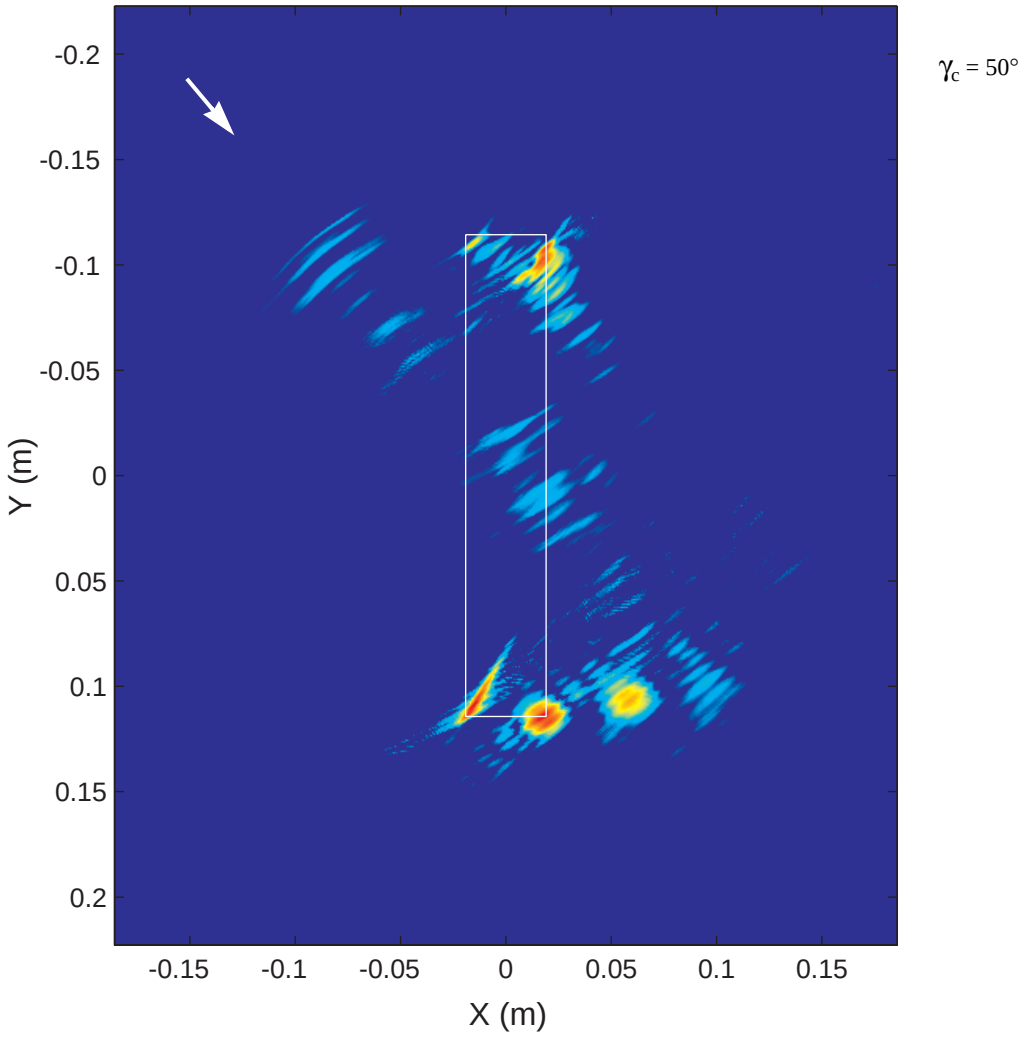

FIG. 3.17 Synthetic aperture image of Shell A. Angular aperture is 20° centered about γ_c = 50°. The white arrow indicates the direction of the incident sound at the center angle, while the white rectangular outline is the calculated position of the cylinder.

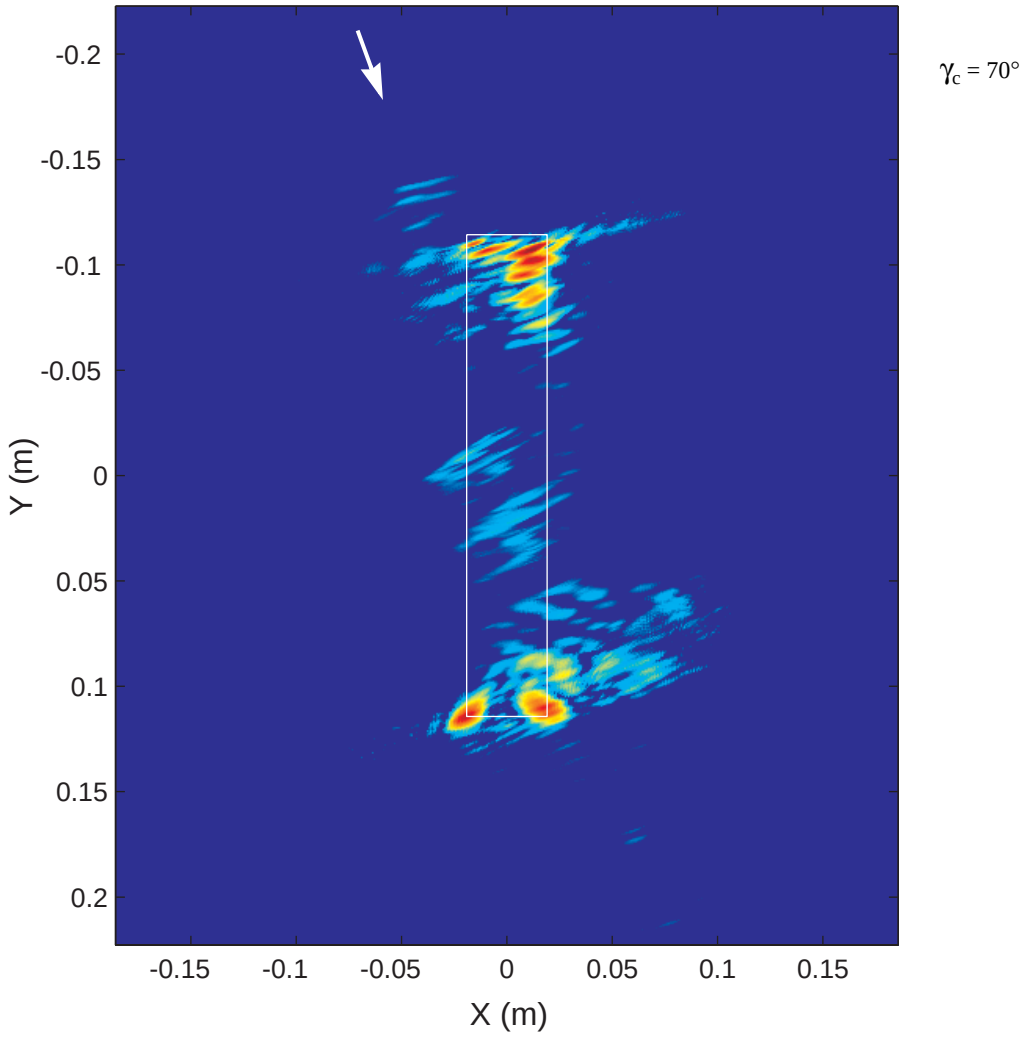

FIG. 3.18 Synthetic aperture image of Shell A. Angular aperture is 20° centered about $\gamma_c = 70°$. The white arrow indicates the direction of the incident sound at the center angle, while the white rectangular outline is the calculated position of the cylinder.

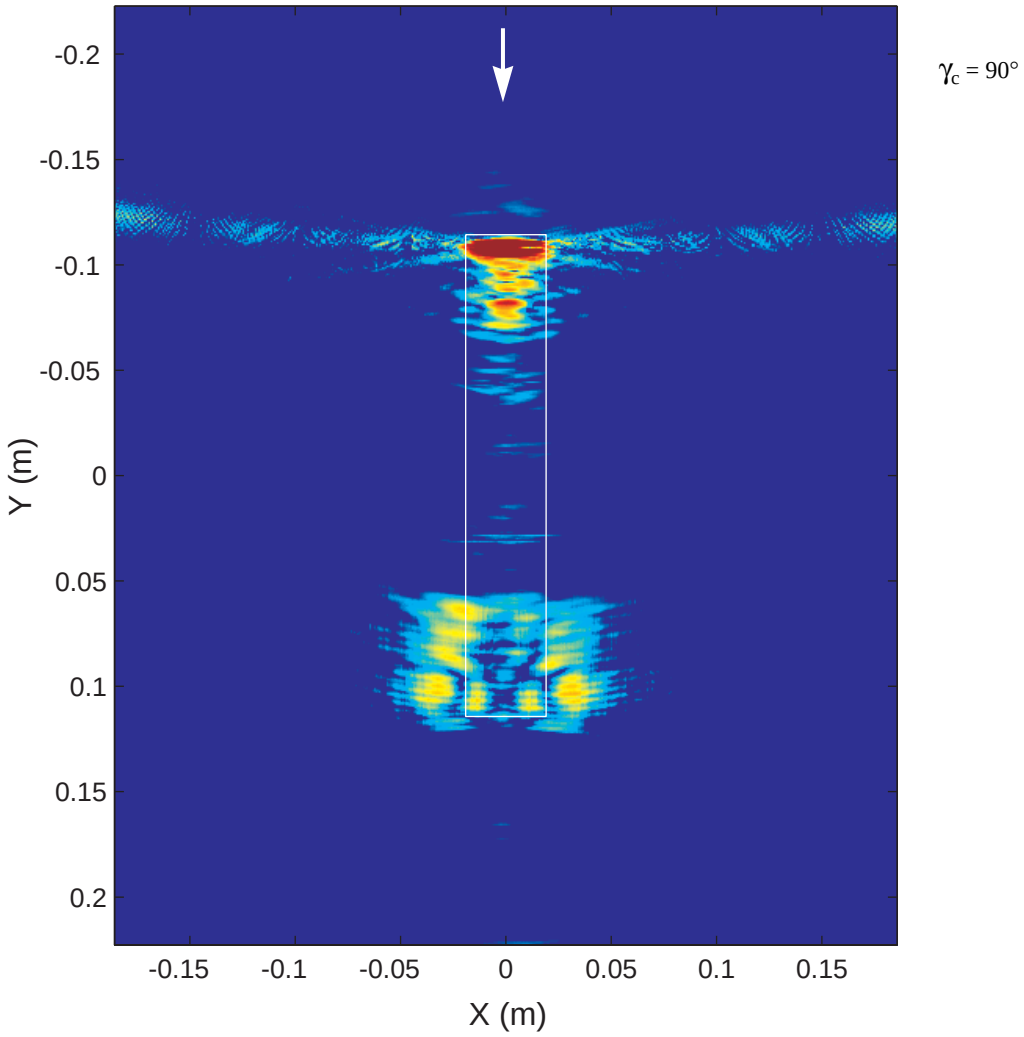

FIG. 3.19 Synthetic aperture image of Shell A. Angular aperture is 20° centered about γ_c = 90°. The white arrow indicates the direction of the incident sound at the center angle, while the white rectangular outline is the calculated position of the cylinder.

3.6 Relevance of the Results and Conclusion

Analysis of the time domain data for high frequency backscattering by thick finite cylindrical shells has provided insight into the coupling and radiation mechanisms responsible for enhanced backscattering over the full range of incidence angles. Time-frequency representations allow for the identification of individual elastic wave contributions in time and synthetic aperture images help to show where on the cylinder responses appear to originate. The analysis has shown that the meridional leaky ray contribution is large and arrives at or slightly prior to the geometric corner arrival time from the closest rear corner, in the case of the a_0. This shows that, for far-field backscattering, the most important spatial region on the cylinder for the meridional ray "reflection" process is a fairly small region at the closest rear corner. If this were not the case the arrival time would be expected to significantly precede the rear corner timing. This can be understood by looking at Fig. 3.21 which shows that the group velocity of the a_0 is supersonic in this frequency range. If the principle meridional ray enhancement process was described by the path ABE shown in Fig. 3.20 then the arrival time would precede the rear corner geometrical timing (EBE) by

$$\Delta t_{mer} = \frac{L}{c}\left(\frac{1}{c_{gl}/c} - \sin\gamma\right) = L\left(\frac{1}{c_{gl}} - \frac{1}{c_l}\right) \tag{3.3}$$

where c_{gl} and c_l are the group and phase velocities of the wavepacket. Since the a_0 meridional wave is dispersive this equation must be understood as approximating the arrival time of the spectral component of the wavepacket used in the evaluation of c_{gl} and c_l; this frequency is taken to be the primary spectral component of interest. The second expression uses the definition of the meridional ray coupling angle γ in Eq. (2.1). Note that if the phase and group velocities are approximately equal, as is the case for high-frequency meridional Rayleigh waves on a tilted solid cylinder or half space, then the arrival time is always coincident with the corner geometrical timing. For chosen values from Fig. 3.21 this advancement would be on the order of -45 μs, for c_{gl}/c = 1.85 and c_l/c =1.2 (≈ 300 kHz).

This amount of advance is not observed for any of the cylinders examined. Instead the small advances are consistent with launching near the closest rear corner over a length scale on the order of an attenuation length. The attenuation length for a leaky wave is defined to be the propagation length over which the leaky wave amplitude decreases by a factor of e^{-1} due to radiation losses. In terms of the imaginary part of the axial wavenumber-radius product this corresponds to a length

$$L_e = \frac{a}{Im[k_z a]}. \tag{3.4}$$

For the cylinder examined here this length is on the order of 25 mm (compare with the cylinder length of 228.6 mm). The leaky wave launched a greater distance away from the corner is largely attenuated before reaching the corner and will not contribute significantly to the backscattering. This also explains why the observed meridional ray enhancement does not appear to exhibit characteristics of axial resonances, which would give a modulation of the amplitude periodic in frequency. The primary path for the meridional ray should be understood as that of FA'BA'F in Fig. 3.20 (or simply EBE) as opposed to ABE. Incidentally this is not always expected to be the case for all wave types. For example Bao[16] determined delay times for helical waves on a very thick finite cylindrical shell for launching positions over the entire cylinder length and found good agreement with experimental results. In addition, Gipson[47] recently compared delay times in a similar fashion for meridional and helical leaky Rayleigh wave propagation on a finite solid cylinder and found good agreement with experiment.

The analysis of this chapter has also shown that the large coincidence frequency response observed near end-on incidence arrives considerably ahead of the geometric rear corner arrival time and also displays multiple axial reflections in the long time signature. Due to their propagation characteristics these contributions are most likely due to subsonic a_{0^-} waves corresponding to small azimuthal mode indices, for tilt angles approaching end-on incidence, and the subsonic a_{0^-} $n = 0$ mode at end-on incidence. A notable characteristic is that the backscattered contributions of these waves is not diminished at end-on incidence, suggesting the coupling mechanism includes end effects.

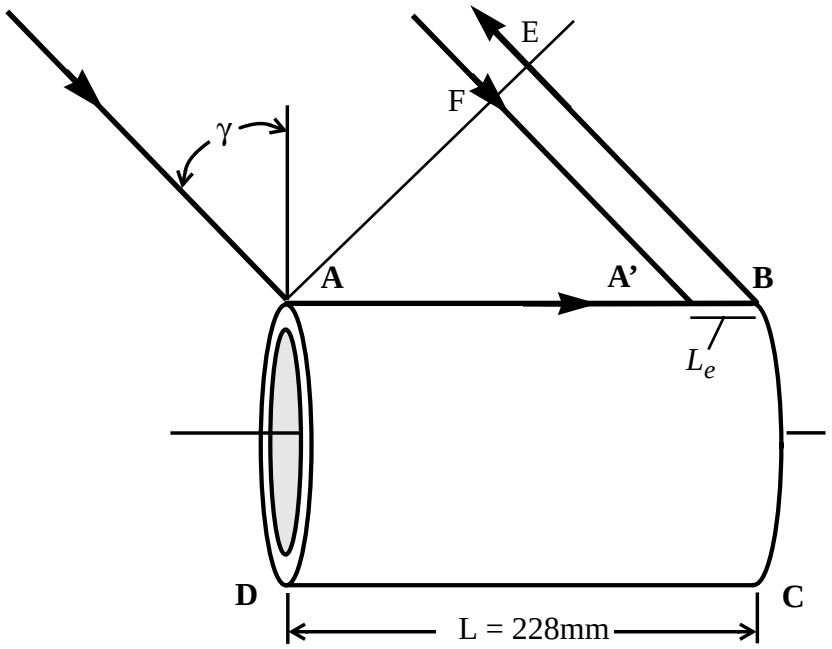

FIG. 3.20 Because the meridional ray enhancement wavepacket arrives at or just prior to the geometric reflection from point B it is not principally due to a wave launched at A which travels the length of the cylinder L, reflects at B and radiates into the backscattering direction (path ABE). The radiation damping is too high to allow significant scattering amplitudes from this process. Rather the significant contributing spatial region is just prior to the corner B; having a length comparable to the attenuation length of $L_e = a/Im[k_z a] \approx 25$ mm. The enhancements, then, are the result of the process FA'BA'F.

The author would like to point out that in addition to the examples presented for the time-frequency plots and the synthetic aperture images, movies were constructed for each of these which very nicely display changes with tilt angle. These movies are in MPEG format (relatively low quality) and on VHS tape (high quality). Visualizing the changes in this way helps in the identification process.

Acknowledgments

The author would like to thank Greg Kaduchak for his help in preparing the synthetic

aperture images. The core of the synthetic aperture code was written by him and he has graciously allowed its use here.

3.A Phase and Group Velocities

Figure 3.21 shows the calculated total phase and group velocities, and damping, for the a_0 meridional wave ($n = 0$) and a selected a_{0-} helical wave ($n = 8$). They are calculated by numerically solving $D_n(ka, k_z a) = 0$ where D_n is the denominator of the n^{th} partial wave series for the problem of scattering of an obliquely incident plane wave by an infinite, empty, thick cylindrical shell[14]. The index n corresponds to the azimuthal mode index and $k_z a$ is the axial wavenumber. Solving this equation for a particular azimuthal mode index and normalized frequency, ka, yields the complex axial wavenumber, from which the phase and group velocity may be calculated. See Chapter 4 for a complete discussion on the calculated wave parameters for an infinite cylindrical shell and the method used to compute them. Plotted in Fig. 3.21 are the phase and group velocity in the direction of propagation on the shell, computed using Eqs. (4.13) and (4.14) of Chapter 4. For the helical wave these are the total phase and group velocities along the helical arc which describes the propagation of the helical wave on the shell. For the meridional wave, $n = 0$, these total phase and group velocities coincide with the axial phase and group velocities as the wave propagates purely in the axial direction.

For the present analysis, calculating the $n = 0$ root for the a_{0-} wave would have been more relevant to the discussion in this chapter. It has not been calculated because of difficulties in isolating and evaluating the root in question with the present root finding routine. The computations in Chapter 4, however, show that at high frequencies above the coincidence frequency the phase and group velocities for different azimuthal mode orders depend only weakly on n provided n is not very large.

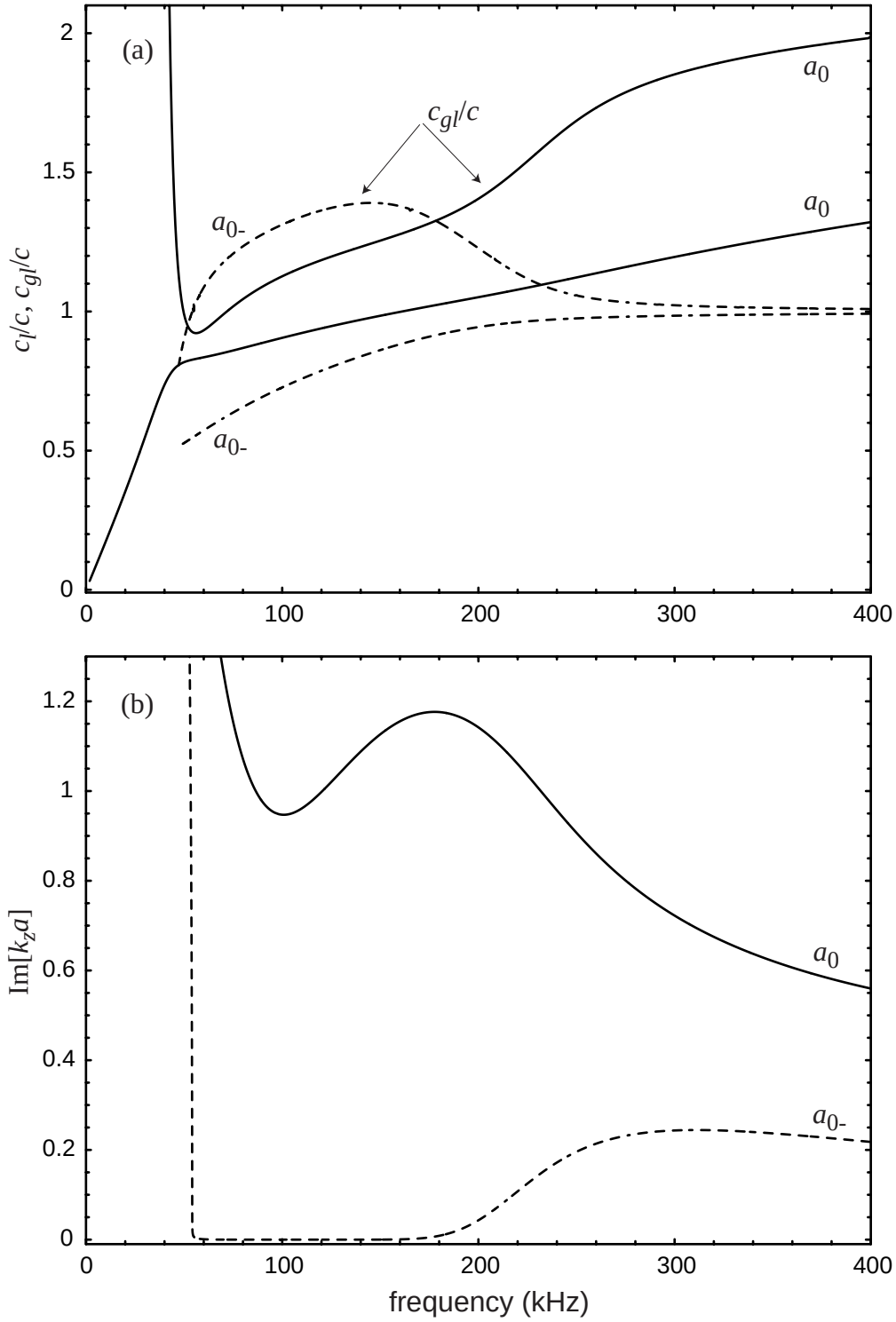

FIG. 3.21 (a) Phase and group velocities and (b) damping for the a_0, $n = 0$ (solid) and a_{0-} $n = 8$ (dashed) leaky Lamb waves on an empty infinite cylindrical shell (Shell A) submerged in water. The group velocity of the a_{0-} in this case is supersonic over a range of frequencies. Similar behavior is found for the a_{0-} on a plate or cylindrical shell at broadside incidence.

3.B Corner Reflection Timing

This appendix section gives the expressions for the return times for geometrical propagation through the water from the source to each of the four "corners" of the cylinder and back to the receiver. Since the sheet source was used exclusively in the experiments described in this chapter, only timings for this setup will be given. Consider the scattering setup shown in Fig. 3.22. The distances from each of the four corners to the receiver can easily be shown to be:

$$\begin{aligned} R_A &= [(r_c \sin\delta_-)^2 + (R_{rec} - r_c\cos\delta_-)^2]^{1/2} \\ R_B &= [(r_c \sin\delta_+)^2 + (R_{rec} + r_c\cos\delta_+)^2]^{1/2} \\ R_C &= [(r_c \sin\delta_-)^2 + (R_{rec} + r_c\cos\delta_-)^2]^{1/2} \\ R_D &= [(r_c \sin\delta_+)^2 + (R_{rec} - r_c\cos\delta_+)^2]^{1/2} \end{aligned} \tag{3.5}$$

where

$$\begin{aligned} r_c &= \sqrt{\left(\frac{L}{2}\right)^2 + a^2} \\ \delta_- &= (90° - \gamma) - \tan^{-1}\left(\frac{a}{L/2}\right) \\ \delta_+ &= (90° - \gamma) + \tan^{-1}\left(\frac{a}{L/2}\right). \end{aligned} \tag{3.6}$$

For propagation through water, having a sound speed of c_w, the travel times *referenced to the timing of the specular reflection at broadside incidence* are given by:

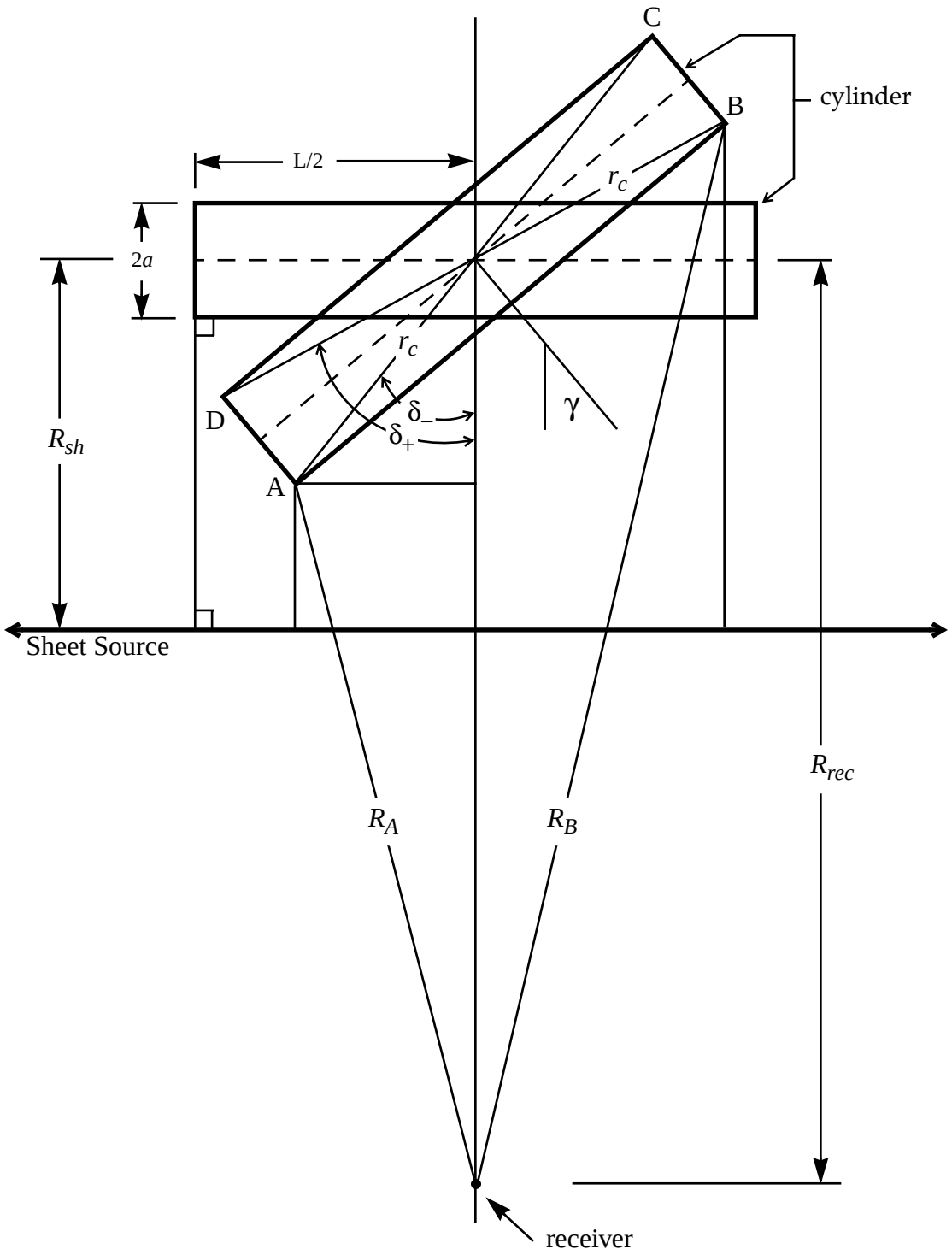

FIG. 3.22 Geometry used to determine the return timings (t_A, t_B, t_C, t_D) for geometrical reflection from each of the four "corners" of the cylinder. Distances to corners A and B are shown; those to C and D are analogous. Diagram is not shown to scale.

$$
\begin{aligned}
t_A &= \left(\frac{1}{c_w}\right)[R_A - r_c\cos\delta_- - R_{rec} + 2a] \\
t_B &= \left(\frac{1}{c_w}\right)[R_B + r_c\cos\delta_+ - R_{rec} + 2a] \\
t_C &= \left(\frac{1}{c_w}\right)[R_C + r_c\cos\delta_- - R_{rec} + 2a] \\
t_D &= \left(\frac{1}{c_w}\right)[R_D - r_c\cos\delta_+ - R_{rec} + 2a].
\end{aligned}
\tag{3.7}
$$

For the figures in this chapter containing overlays of these timings with experimental data it is required to know the timing of the broadside specular feature in addition to the separation distance R_{rec}. These may be obtained by examining the broadside time trace directly and an overall long time scattering signature also at broadside incidence. The latter of these includes three important features: 1) an initial voltage spike followed by a relatively slow decay corresponding to the direct *electrical* signal propagating through the water from the sheet source to the receiver and the subsequent RC decay of the receiver/preamp system; 2) an impulse voltage signal corresponding to the direct *acoustic* signal from the sheet source; and 3) the specular reflection from the cylinder at broadside. From these features it is possible to deduce R_{rec} and R_{sh}. The electrical coupling mentioned in 1) has been reduced significantly by coating the sheet source with an electrically insulating waterproof layer of epoxy and/or varnish (for the frame pieces) and mylar and/or Kapton® tape (for the PVDF film). It is, however, difficult to eliminate the electrical coupling completely. Appendix A discusses the sheet source in greater detail.

For the synthesized impulse response figures (Figs. 3.11 and 3.13) the scattering is strictly in the far-field. This may be approximated in the above equations by allowing R_{rec} to be a very large number with respect to the length of the cylinder, or by explicitly reducing the equations for an infinite cylinder-to-receiver distance.

4

Meridional and Helical Wave Properties on an Infinite Cylindrical Shell from Complex Root Analysis

4.1 Introduction

In Chapter 2 it was demonstrated that the backscattering from finite thick cylindrical shells is enhanced along certain curves in frequency-angle space. These curves extend beyond the shear wave cutoff angle in several cases and represent considerable scattering amplitudes which dominate the response. An approximate partial wave series (PWS) solution, the details of which will be discussed in Chapter 5, displays these same enhancement curves over a broad range of angles for the shells studied. This form of theoretical investigation is very useful for predicting the response of other shells of interest and for estimating the extent to which the ends influence the scattering mechanics (by comparing the results with experiments). It is very poor, however, for providing insight

into the specific coupling, propagation and radiation mechanisms which are responsible for the enhancement features. To fill this gap in understanding, a very simple ray approximation was introduced in Chapter 2 which allowed certain leaky wave processes to be identified as the primary enhancement mechanisms. This simple approach was based on two assumptions. The first being that at sufficiently high frequencies, or equivalently for large radius of curvature, the propagation characteristics of leaky waves on a cylindrical shell, e.g. phase velocity, group velocity and radiation damping, should be nearly isotropic, i.e. independent of the direction of propagation on the shell. In other words the curvature of the shell does not significantly affect the elasto-dynamics of propagation. This assumption is often quite adequate and can be checked for simple structures by comparing the exact dispersion curves for the guided waves of interest on the curved structure with those for a planar structure. These types of comparisons have been made for leaky waves on spheres[48], spherical shells[24,28] and infinite solid cylinders[49] and for circumferential waves on cylindrical shells[50,8]. When examining these types of results it may be noticed that the dispersion curves for a planar structure are slightly offset although they follow the exact behavior in a parallel sense. This difference can sometimes be accounted for through simple geometric kinematic curvature corrections[36]. The second assumption concerns the process of reflection of the leaky wave from the cylinder truncation (assumed to be sharp, flat and perpendicular to the cylinder axis). To first order the reflection process was taken to be as simple as possible, namely that the axial component of the wavevector of the impinging leaky wave simply experiences a change in sign upon interaction with the end. This corresponds to ideal reflection. In the case of helical leaky waves this produces no change in sign of the circumferential component of the wavevector. These two assumptions, combined with the trace velocity matching condition for supersonic leaky waves and axial wavevector matching for subsonic leaky waves, were sufficient to qualitatively model the observed enhancement features near and above the coincidence frequency for each shell. These calculated "coupling loci" as they were called, were used to identify the leaky waves responsible for the enhancements. For this purpose these approximations are sufficient. It is anticipated, however, that a better

understanding of the propagation characteristics of leaky waves on an infinite cylindrical shell is needed. For example, knowledge of the leaky wave phase velocity and damping are crucial parameters in some quantitative ray theories[5,6,51]. In Chapters 6 and 7 a ray theory is tested for these enhancement mechanisms which requires knowledge of the phase velocity and damping of the leaky wave under consideration. For certain cases, approximating these wave parameters with those for a flat plate or a cylindrical shell at broadside incidence may not be sufficient. The purpose of this chapter is to present the results of exact calculations for meridional and helical leaky wave dispersion curves for an infinite thick cylindrical shell. The *primary hypothesis* is that, at sufficiently high frequencies, the propagating characteristics of meridional and helical leaky waves which are launched on a tilted cylindrical shell by an incident plane wave may be described by the dispersion curves for the normal modes of vibration of a fluid-loaded infinite cylindrical shell. It is expected that the axisymmetric modal solutions ($n = 0$) are the ones which most closely correspond to meridional rays, though the actual excitation will ordinarily consist of a superposition of modes.

4.2 Review of the Boundary Value Problem

In order to compute the exact dispersion curves, i.e. normal modes, for the propagation of Lamb-type waves on an infinite tilted cylindrical shell, the general boundary value problem must first be solved. For the case of plane wave scattering by an infinite cylindrical shell fluid loaded both on the inside and outside, the exact solution was first published in detail by Léon, *et al* (Ref. [14]) although results appeared in the Soviet literature earlier by Veksler, *et al* (Ref. [25]). This solution is just a more complicated extension of the infinite solid cylinder solution first published by Flax, *et al* (Ref. [52]) which drew from the solution for an infinite cylindrical inclusion in an infinite elastic solid given by White (Ref. [53]). It should also be noted that an approximate solution for a thin cylindrical shell at oblique incidence was derived by Lyamshev (Ref. [54]). For the case of hollow infinite cylindrical shells with no external fluid loading the exact solution for

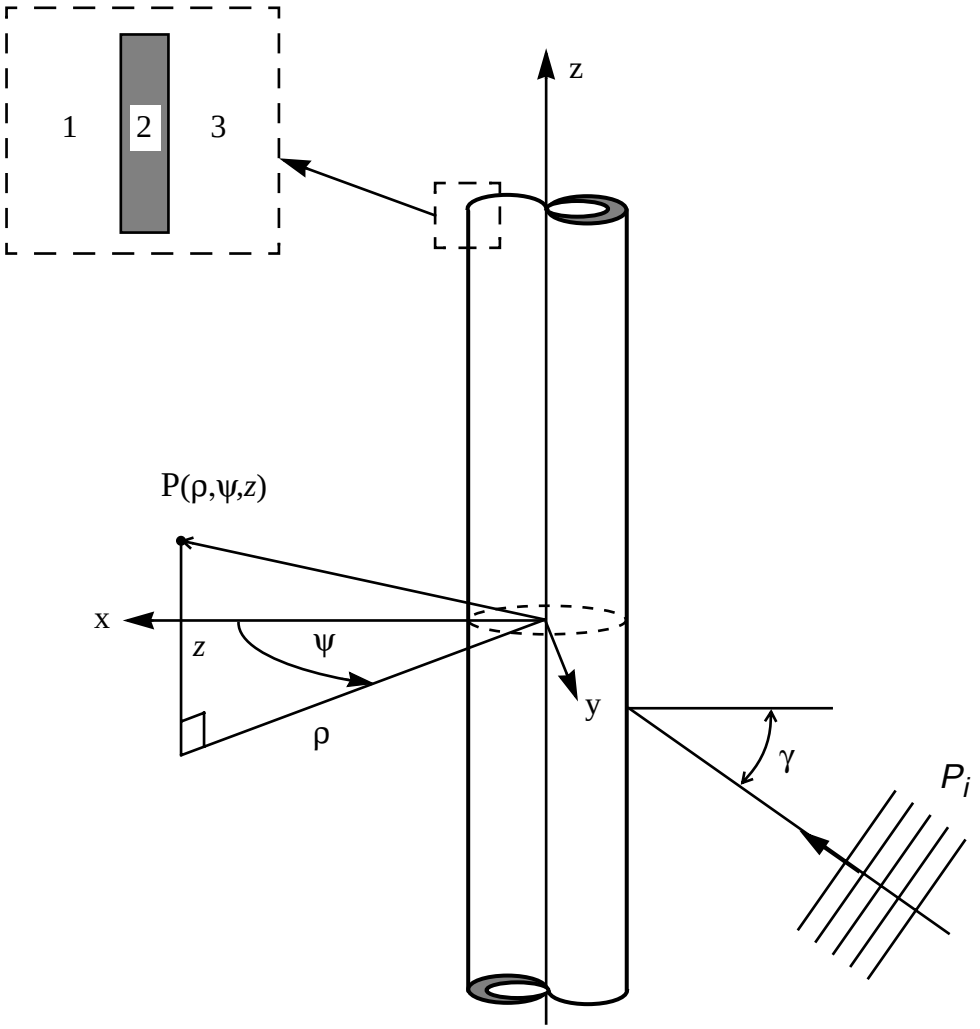

FIG. 4.1 Scattering geometry for an infinite cylindrical shell. A plane wave is incident at an angle γ and the scattered pressure is desired at the location (ρ,ψ,z) described in terms of cylindrical coordinates.

normal mode vibrations is attributable to Greenspon (Refs. [55] and [56]). Work published at nearly the same time by Gazis (Ref. [57]) and later by Armenakas and Gazis (Ref. [58]) covers similar material and provides a large set of numerical calculations.

The approach taken here is exactly that given in the paper by Léon, *et al* (Ref. [14]). It is not necessary, therefore, to present a thorough derivation of the solution here. For the purposes of clarity and convenience a short outline of the solution, in nearly the same

notation, is given below.

Figure 4.1 shows the scattering geometry under consideration. A time harmonic plane wave of infinite extent is incident on an infinite cylindrical shell at an angle defined by γ with respect to the cylinder normal. The incident pressure may be expanded in cylindrical coordinates as

$$\begin{aligned} P_i &= P_o e^{i[(k_{xi}x + k_{zi}z) - \omega t]} \\ P_i &= P_o e^{i(k_{zi}z - \omega t)} \sum_{n=0}^{\infty} i^n \varepsilon_n J_n(k_{\perp i}\rho)\cos(n\psi) \end{aligned} \tag{4.1}$$

where $k_{zi} = k\sin\gamma$, $k_{xi} = k_{\perp i} = k\cos\gamma$, $k = \omega/c_1$ (ω is the angular frequency) and J_n is the n^{th} order ordinary Bessel function. The term ε_n is called Neumann's factor[80] and is defined to be

$$\varepsilon_n \equiv \begin{cases} 1 & n = 0 \\ 2 & n \neq 0. \end{cases} \tag{4.2}$$

The outer fluid is characterized by its sound speed, c_1, density, ρ_1 and Lamé constant λ_1; similarly, the inner fluid has parameters c_3, ρ_3 and λ_3. The elastic shell material is characterized by its longitudinal (dilatational) sound speed, c_L, shear sound speed, c_S, density, ρ_2, Lamé constants λ_2 and μ_2, and inner and outer radii b and a, respectively. The scattered pressure may be written in the form

$$P_s = e^{i(k_{zi}z - \omega t)} \sum_{n=0}^{\infty} i^n \varepsilon_n g_n H_n^{(1)}(k_{\perp i}\rho)\cos(n\psi), \tag{4.3}$$

where the g_n are the expansion coefficients to be determined by the boundary conditions and $H_n^{(1)}$ is the Hankel function of the first kind. The boundary conditions in this case are that the tangential stress vanish (4 conditions) and the normal stress (2 conditions) and displacement (2 conditions) be continuous on the inner and outer surfaces of the shell.

These eight conditions lead to eight equations in eight scattering unknowns. The resulting set of linear equations can be written in matrix form as

$$\boldsymbol{M} \cdot \boldsymbol{A} = \boldsymbol{C} \tag{4.4}$$

where $\boldsymbol{M}$ is an 8 x 8 square matrix and $\boldsymbol{C}$ is an 8 element column vector. The column vector $\boldsymbol{A}$ contains the 8 unknown scattering coefficients. The solution for the i^{th} coefficient may be written using Cramer's rule as $a_i = \boldsymbol{N}_i / \boldsymbol{D}$ where $\boldsymbol{D} = det[\boldsymbol{M}]$, $\boldsymbol{N}_i = det[\boldsymbol{M}_i]$ and $\boldsymbol{M}_i$ is the matrix defined by replacing the i^{th} column of $\boldsymbol{M}$ with the column vector $\boldsymbol{C}$. This system has a unique solution if and only if $D \neq 0$. The elements of $\boldsymbol{M}$, $\boldsymbol{A}$ and $\boldsymbol{C}$ may be found in Section 4.B. In this way the scattered pressure may be written as

$$P_s = e^{i(k_{zi}z - \omega t)} \sum_{n=0}^{\infty} i^n \varepsilon_n \left(\frac{\boldsymbol{N}_1}{\boldsymbol{D}} \right)_n H_n^{(1)}(k_{\perp i}\rho) \cos(n\psi) . \tag{4.5}$$

The subscript n for the ratio of determinants above is to remind the reader that the elements of these matrices are functions of the partial wave index n, in addition to the non-dimensional frequency, $ka = 2\pi a f / c_1$ and angle of incidence, γ. Using the asymptotic representation of the Hankel function

$$H_n^{(1)}(\xi) \approx \sqrt{\frac{2}{\pi\xi}} e^{i\left(\xi - \frac{\pi}{2}n - \frac{\pi}{4}\right)} \qquad |\xi| \to \infty \tag{4.6}$$

the far field form function [see definition in Eq. (1.2)] is found from Eq. (4.5) to be

$$f(\gamma, ka, \psi) = \frac{2e^{-i(\pi/4)}}{\sqrt{\pi(ka)\cos\gamma}} \sum_{n=0}^{\infty} \varepsilon_n \left(\frac{\boldsymbol{N}_1}{\boldsymbol{D}} \right)_n \cos(n\psi) . \tag{4.7}$$

Note that $e^{-i(\pi/2)n} = (-i)^n$ and $e^{i(\pi/4)} = \sqrt{i}$. In the meridional plane, $\psi = \pi$ and Eq. (4.7) simplifies to

$$f(\gamma, ka, \pi) = \frac{2e^{-i(\pi/4)}}{\sqrt{\pi(ka)\cos\gamma}} \sum_{n=0}^{\infty} (-1)^n \varepsilon_n \left(\frac{\boldsymbol{N}_1}{\boldsymbol{D}} \right)_n \tag{4.8}$$

since $\cos(n\pi) = (-1)^n$. If the cylinder were perfectly rigid, requiring the normal component of the velocity to vanish in the outer fluid at the surface of the cylinder, then the determinants $\boldsymbol{N}_1$ and $\boldsymbol{D}$ reduce to simple forms and Eq. (4.8) becomes

$$f_{rigid}(\gamma, ka, \pi) = \frac{2e^{-i(\pi/4)}}{\sqrt{\pi(ka)\cos\gamma}} \sum_{n=0}^{\infty} (-1)^n \varepsilon_n \left[\frac{-H_n^{(1)\prime}((ka)\cos\gamma)}{J_n{}'((ka)\cos\gamma)} \right], \tag{4.9}$$

where the primes denote differentiation with respect to the argument. Equations (4.8) and (4.9) will prove useful later in Chapter 6 where the form function is evaluated near a meridional wave contribution and compared with an approximate ray theory. For the purposes of comparison, the rigid cylinder form function is subtracted out of the full elastic form function. This is an example of an attempt to subtract out a "background" contribution to the scattering to yield only the elastic response.

For the purposes of this chapter only a portion of the full scattering solution, Eq. (4.8), is required. We wish to find the natural modes of vibration of the infinite cylindrical shell. The previous scattering solution is a "forced" solution, i. e. the infinite cylindrical shell is "driven" by the incident plane wave. A forced problem can usually be manifest as an inhomogeneous equation, whether it be the original differential equation or a set of linear equations to be solved. This is the case here, where the set of linear equations to be solved is inhomogeneous, i.e. the column vector $\boldsymbol{C}$ above has non-zero elements. There exists a unique solution to this set of linear equations only when $\boldsymbol{D} = det[\boldsymbol{M}] \neq 0$. But it is precisely the condition $\boldsymbol{D} = det[\boldsymbol{M}] = 0$ that defines the natural modes of vibration of the shell. To find the natural modes of vibration of the shell one solves the homogeneous problem. This is the problem where there exists no incident sound. By examining the solution reviewed above more closely, e.g. see the matrix elements in Section 4.B, one finds that removing the incident plane wave simply results in the vanishing of the elements of the column vector $\boldsymbol{C}$. This reduces the problem to solving the homogeneous set of linear equations,

$$\boldsymbol{M} \cdot \boldsymbol{A} = \boldsymbol{0}, \tag{4.10}$$

which has a non-trivial solution only when

$$\boldsymbol{D} = det[\boldsymbol{M}] = 0. \tag{4.11}$$

This transcendental equation is often referred to as the characteristic equation. These non-trivial solutions correspond to the natural modes of vibration of the shell. One finds, then, that the natural modes of vibration of the infinite cylindrical shell correspond to the zeros of the determinant of $\boldsymbol{M}$, which is precisely the denominator in the scattering solution Eq. (4.8).

For the inhomogeneous problem the incident pressure wave determines the axial wavevector of the shell, k_z, through the incidence angle γ. In the homogeneous problem k_z is the quantity to be determined that, together with the azimuthal integer n and non-dimensional frequency ka, defines the normal mode of vibration. In the present analysis ka and n are taken to be purely real quantities while the "root" of Eq. (4.11) to be found is located in terms of k_z, which is complex. This form of analysis is found to be more convenient for interpreting the scattering in terms of a ray theory than analyzing Eq. (4.11) in terms of its complex eigenfrequencies (i.e. complex ka for real k_z). This latter form of analysis has proven useful in the Singularity Expansion Method (SEM) and in Resonance Scattering Theory (RST) (see e.g. Ref. [60]).

It is found to be convenient to write most quantities in non-dimensional form and so the normal modes are located in terms of the complex quantity $k_z a$. The modes of a cylindrical shell are often characterized by two integers (l,n)[14,25,26]. The first of these usually corresponds to the family to which the wave belongs, e.g. Rayleigh and Whispering Gallery waves for a solid cylinder and the generalizations of the waves a_0, $a_{0\text{-}}$ s_0, T_0, a_1, s_1, T_1, s_{2b}, . . . for a cylindrical shell. Presently the notation characterizing Lamb waves on plates will be used, as it is in other chapters, and should be understood as representing the families $l = a_0$, $l = a_{0\text{-}}$, $l = s_0$, $l = T_0$, . . . Subsequently the l notation will be dropped. The other integer, n, refers to the mode shape in the circumferential direction. An infinite number of integers n exist for each l. The lowest order, $n = 0$, corresponds to the axisymmetric case. The displacements in this case have components only in the radial and

axial directions. A theoretical and experimental examination of the axisymmetric solutions for infinite cylindrical shells with and without fluid loading was carried out by Sinha, *et al* (Ref. [61]). The $n = 0$ mode is expected to approximate the meridional ray, as it travels only in the axial direction. The $n = 1$ mode has one wavelength around its circumference and is characterized by a planar flexural motion of the entire shell at low frequencies (i.e. a bar bending motion). The $n = 2$ mode has two circumferential wavelengths.

For *high-frequency propagation* the mode order n may be regarded as the helical wavenumber of a surface guided helical wave[62,63]. This is because the eigenfunctions in Eqs. (4.3) and (4.5), representative of the eigenfunctions for the displacement equations in the shell, are standing wave solutions in the circumferential direction and may equivalently be written in exponential form representing traveling wave solutions[62,63]. The eigenfunction solutions then represent the sum of two counter-propagating traveling waves. The dispersion relation describing the propagation of these helical waves on the cylindrical shell is[62,63,64]

$$\begin{aligned} k_h^2 &= k_\psi^2 + k_z^2 \\ \frac{(ka)^2}{(c_l/c)^2} &= n^2 + (k_z a)^2 \end{aligned} \tag{4.12}$$

where k_h is the total wavenumber for helical propagation on the shell and $k = \omega/c$. Once $k_z a$ is found for a particular mode, the normalized helical or total phase velocity is determined by

$$\left(\frac{c_l}{c}\right) = \frac{ka}{\sqrt{n^2 + (Re[k_z a])^2}} \tag{4.13}$$

and the group velocity is

$$\left(\frac{c_{gl}}{c}\right) = \frac{\partial(ka)}{\partial(Re[k_h a])}, \tag{4.14}$$

which must be determined numerically. For the phase velocity corresponding to the axial wavevector one finds

$$\left(\frac{c_l}{c}\right)_z = \left(\frac{1}{c}\right)\cdot\frac{\omega}{Re[k_z]} = \frac{ka}{Re[k_z a]} \tag{4.15}$$

and the group velocity is similarly

$$\left(\frac{c_{gl}}{c}\right)_z = \frac{\partial(ka)}{\partial(Re[k_z a])}. \tag{4.16}$$

To calculate the phase and group velocities for various waves on the cylindrical shell one must first find the $k_z a$'s. To do this one chooses a value of n and ka, and then proceeds to solve Eq. (4.11).

The method used to find these roots is exactly as found in Ref. [59]. This method involves the computation of one contour integral in the complex $k_z a$ plane to isolate a single root and the evaluation of another to find the complex value of the root. An initial guess for $k_z a$ is required, which may be taken from the corresponding root for a flat plate. Once a root is found the value of ka is incremented or decremented by a small amount and the previous root is used as the guess for the new value of ka. In this way the root may be "tracked" in ka.

This method is chosen simply because it works very well. Other methods of finding roots of a complex function, such as the Newton-Raphson or Secant methods, either fail frequently or are extremely inefficient to implement in this case. The reason for this can be seen in Fig. 4.2 which displays a region of the complex $k_z a$ plane of Eq. (4.11) for chosen values of n and ka in a way that is easy to visualize the root. Near the root the function varies between very large positive and negative values over a very short length. It may change from 1 x 10^{+12} to -1 x 10^{+12} over a length shorter than $\Delta k_z a = 0.1$ while the regions away from the root are relatively slowly varying. On the scale of Fig. 4.2 a 1-D slice across the root often looks something like a step function. It is easy to see, therefore, how typical root finding routines, which often depend on evaluating derivatives, would have a very slow convergence rate. This behavior is lessened as the frequencies decrease and would pose less problems to traditional root finding routines below $ka = 1$.

The numerical scheme used to calculate the group velocities found in many of the

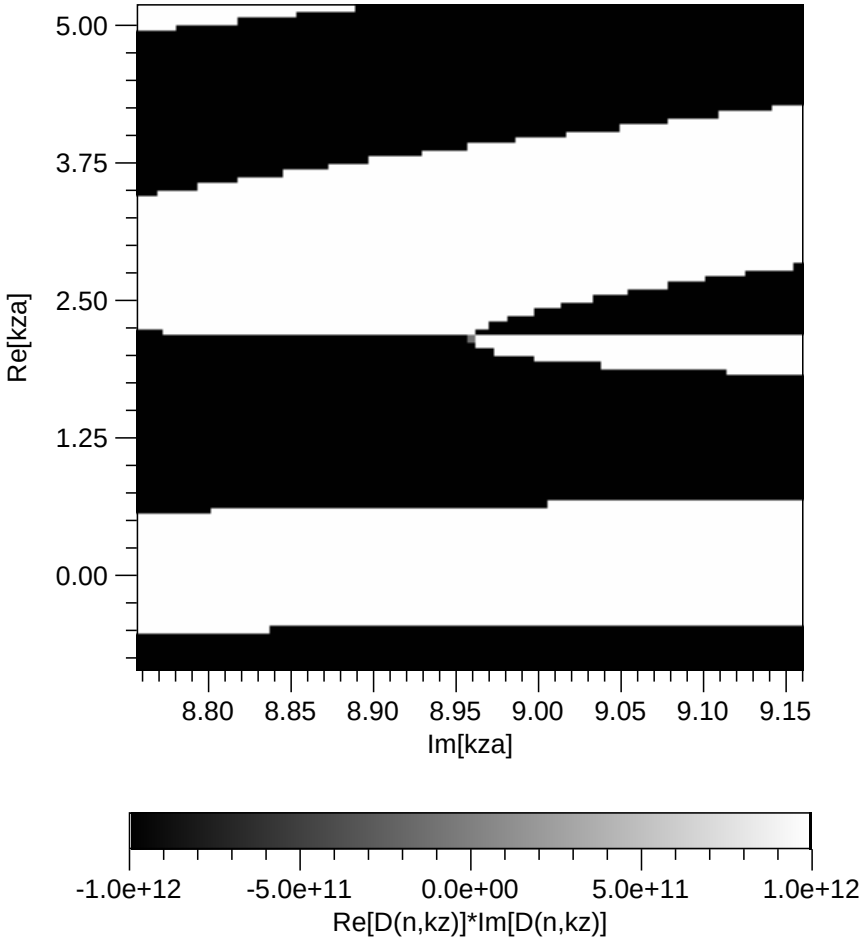

FIG. 4.2 An example of the complex $D_n(k_z a)$ space for an infinite cylindrical shell where a root is found. The quantity plotted is $Re[D_n(k_z a)] \cdot Im[D_n(k_z a)]$. Zeros (roots) are manifest in this figure as a crossing of two zero lines, which are lines separating regions of opposite polarity. This case is for Shell A at $ka = 5.0208$ and $n = 11$, which corresponds to an a_0 helical wave. The root is at the center of the figure at $k_z a = 2.1560 + 8.9589i$. Very abrupt changes, such as 10 orders of magnitude over $\Delta k_z a = 0.1$, make root finding extremely difficult with traditional methods such as Newton-Raphson or Secant.

following graphs is relatively simple. After having computed the axial wavenumber, $k_z a$, over a range of values of ka, at finely sampled intervals (such as $0.1 > \Delta ka > 0.001$), one proceeds to evaluate Eq. (4.14) or (4.16) numerically. The exact method used is a symmetrized derivative (or central difference) such as is found in Eq. (5.7.7) of Ref. [66]. It has the form of $f'(x) \approx [f(x+h) - f(x-h)]/(2h)$ where for our purposes $2h = \Delta ka$.

4.3 Numerical Results: Axisymmetric and Purely Circumferential Solutions

The first results presented are for the $n = 0$ (axisymmetric) solutions of Eq. (4.11). Before beginning a search for the roots of Eq. (4.11) the relevant roots were computed for a plate having the same thickness as the cylinder and fluid loaded on both sides with water[65]. (The case with fluid loading on only one side of the plate would be a better comparison with an empty cylindrical shell but is more complicated; nonetheless, the comparison is still good.) Roots for the a_0, $a_{0\text{-}}$, s_0, and a_1 were calculated for a plate having a thickness equal to the wall thickness of the thinner of the two shells (Shell A) studied in the earlier chapters. For a plate analogous to Shell B roots for the a_0, $a_{0\text{-}}$, s_0, a_1, s_{2b}, s_1, s_2, and a_2 were calculated. These roots were the starting points for finding the corresponding roots for the cylindrical shell. For Shell A the phase velocity [Eq. (4.13)] and damping are shown in Fig. 4.3. The $n = 0$ root of the $a_{0\text{-}}$ proved difficult to evaluate and is not shown. In addition the torsional waves, T_0 and T_1, were not computed as they are not coupled to the external fluid in the axisymmetric case (or in the purely circumferential case for that matter). The group velocity for each of these waves is shown in Fig. 4.4. Also displayed in these figures are the corresponding curves for purely circumferential propagation. Figures 4.5 and 4.6 show similar results for Shell B. Purely circumferential propagation is characterized by displacements in the $\rho - \psi$ plane only. These waves propagate strictly around the cylinder and are important for example in scattering at normal incidence from an infinite cylinder. They are calculated as in Ref. [23]. It is apparent in these figures that the phase velocity for purely circumferential waves is almost always greater than the axisymmetric ($n = 0$) phase velocities. This difference can often be accounted for with curvature and thickness related corrections[36]. The comparison of the damping for the circumferential and axisymmetric waves is to be understood in the following sense. For axisymmetric waves the damping on the surface of the cylinder goes as $e^{-Im[k_z]z}$ while for purely circumferential waves it is $e^{-\beta_l \psi}$, where β_l is the angular damping rate determined through the use of the Sommerfeld-Watson transformation applied to that problem[23]. Considering propagation

of these waves over a surface length on the shell comparable to $\Delta z = a(\Delta\psi)$, where a is the outer radius of the shell, one finds that $\beta_l \approx Im[k_z a]$ for equivalent spatial damping rates. As the relative thickness of the shell increases the Lamb-type surface wave propagation is not strictly along the outer surface at radius a, but may be regarded as propagating along the arc at the median radius $(a + b)/2$ (see Ref. [36]). This shift is not applied in the comparisons shown here.

As mentioned previously, related axisymmetric solutions for a thick cylindrical shell with and without fluid loading were investigated by Sinha, *et al*[61]. The results presented here are consistent with the dispersion curves given in their work although some discrepancies are present (see below for comments). The steel shell they studied had a thickness to radius ratio of 16.7% which makes it close for comparison with Shell B (16.25%). Furthermore their figures cover frequencies up to $ka = 50$ which is within the region examined here. With external fluid loading they identified a new branch, which they labelled the (S-T) slow tube branch, in addition to the "steel" branches labelled S_1, S_2, and S_3. These correspond to the a_{0-}, a_0, s_0, and a_1 waves, respectively, discussed here.

A comment is appropriate concerning the discrepancies mentioned above. First of all it is important to stress that Sinha, *et al* locate complex ka roots of Eq. (4.11) while the present work isolates complex $k_z a$ roots. A connection between the two, for appreciable imaginary values of ka or $k_z a$, is not well understood. With this in mind a direct comparison of much of the results of that paper with the present work is not possible. However, Sinha, *et al* computed the phase slowness (reciprocal of the phase velocity) in terms of frequency for the various modes and performed experiments in order to compare with their theoretical results. Knowledge of the phase velocities for various modes (here including helical modes) is also one of the goals at present. Therefore it is reasonable to make a qualitative comparison of the respective phase velocities. At mid to high frequencies the slowness results of that paper correspond well with the calculations presented in Figs. 4.5. In the next section it will be shown that the effect of fluid loading is prominent at low frequencies and has a marked effect on the axisymmetric mode characteristics (see Fig. 4.11). Principally the phase velocity results calculated in the next section for a *free cylindrical shell*

(no fluid loading) agree very well over all frequencies with the results of the paper by Sinha, *et al*. However, at low frequencies the present results for exterior fluid loading show a significant change from the free shell results, while Sinha's results show *no discernible change* (aside from the generation of a new subsonic root which is analogous to the splitting of the antisymmetric Lamb wave on a fluid loaded plate). One would expect the fluid to have a large effect on the propagation characteristics at low frequencies, in particular near the "ring" frequency, where for the lowest compressional root (here s_0) the particle motion in the shell is primarily radial in nature. This effect should be manifest in the radiation damping and phase velocity curves. The author has not definitively identified the cause of the discrepancies just mentioned. It is interesting to note that Sinha did not explain the reasoning behind the choice of analyzing the complex eigenfrequencies of the problem or give a discussion as to its validity for the fluid loaded problem where radiation damping is important. It has been stated by Scott[67] concerning the use of zeros of the real part of the dispersion relation (i.e. real k_z) that, "this is, of course, perfectly correct over those parts of the real [k_z] (or ω) axis for which the dispersion relation *is* real (subsonic modes of propagation), but when the fluid-loading is important it is not at all obvious that roots in other parts represent genuine complex roots." His examination of the infinite thin cylindrical shell problem showed that the presence of fluid loading has a pronounced effect on the roots below the ring frequency. Furthermore the fluid loading effect did not diminish with an increase in the fractional shell thickness, but in fact caused the imaginary part of the roots to increase. This suggests the fluid loading is very significant, especially at low frequencies.

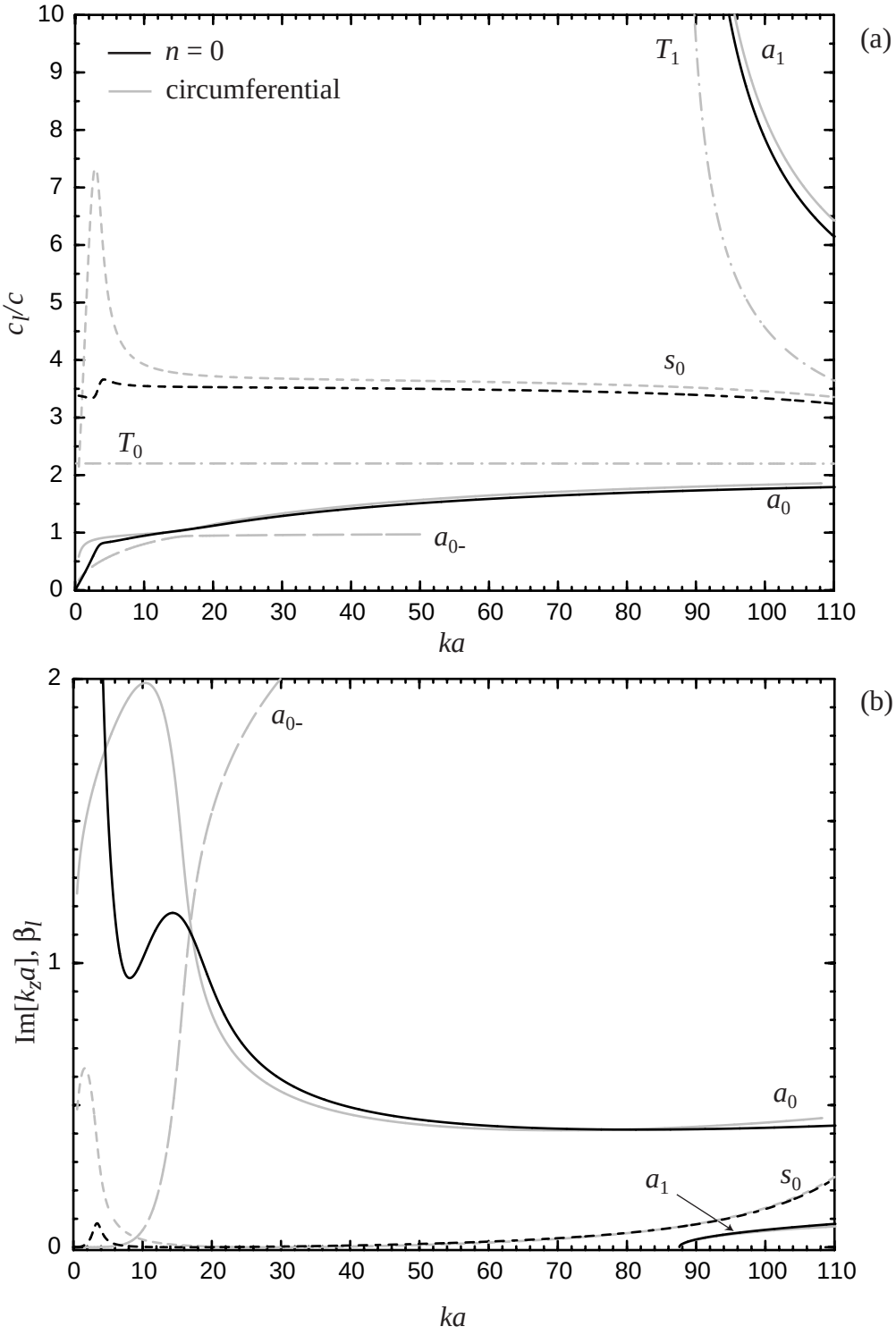

FIG. 4.3 Axisymmetric (n = 0 solutions) and purely circumferential (corresponding to broadside incidence) wave properties for a submerged empty infinite cylindrical shell corresponding to Shell A (h/a = 0.076). (a) Phase velocity, and (b) damping.

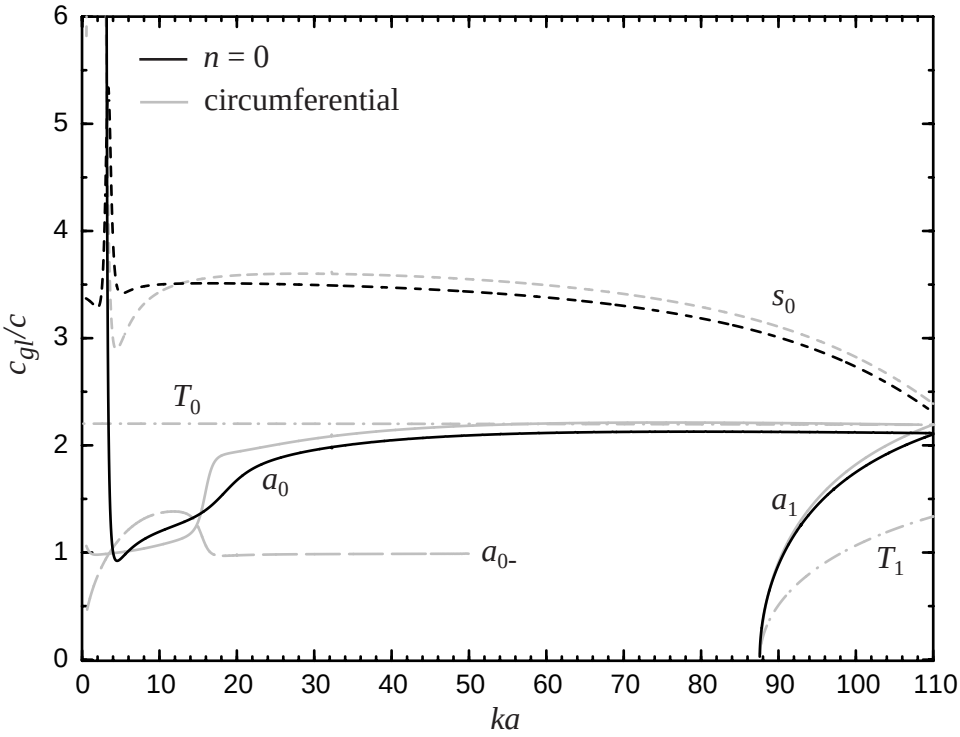

FIG. 4.4 Axisymmetric ($n = 0$ solutions) and purely circumferential (corresponding to broadside incidence) wave group velocities for a submerged empty infinite cylindrical shell corresponding to Shell A ($h/a = 0.076$).

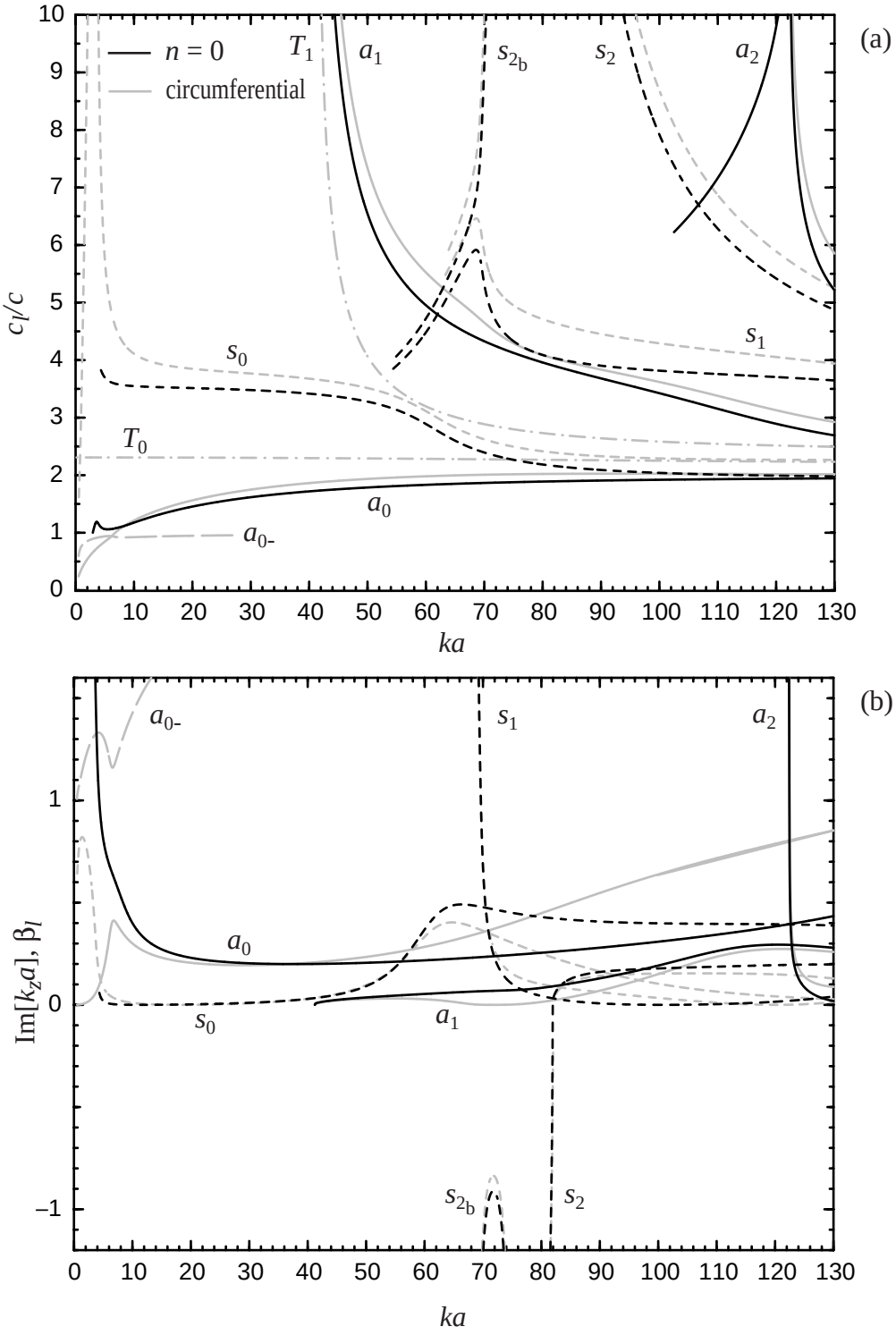

FIG. 4.5 Axisymmetric (n = 0 solutions) and purely circumferential (corresponding to broadside incidence) wave properties for a submerged empty infinite cylindrical corresponding to Shell B (h/a = 0.1625). (a) Phase velocity, and (b) damping.

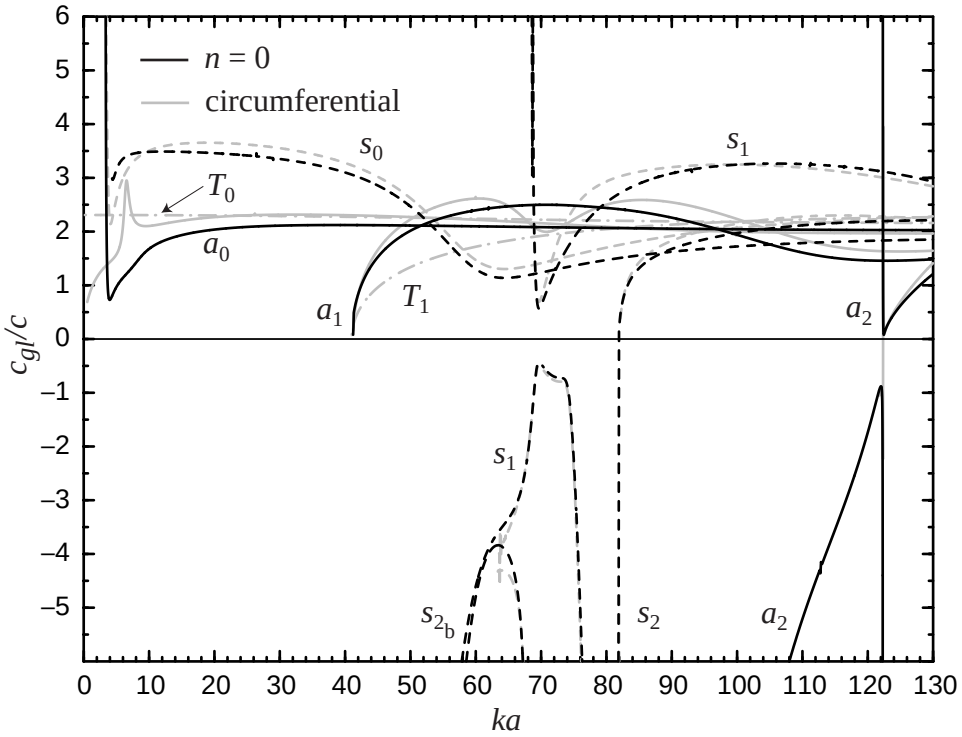

FIG. 4.6 Axisymmetric ($n = 0$ solutions) and purely circumferential (corresponding to broadside incidence) wave group velocities for a submerged empty infinite cylindrical corresponding to Shell B ($h/a = 0.1625$).

4.4 Numerical Results: Helical Solutions with and without Fluid Loading

Consider now solutions of the characteristic equation, Eq. (4.11), for $n \geq 0$, that include non-axisymmetric mode shapes. At high frequencies these solutions may be regarded as helical waves. Besides locating these solutions for use in ray theory approaches to scattering, it is important to understand the propagation characteristics of the helical wave solutions themselves. In particular it is useful to know the effects of exterior fluid loading on the dispersion curves as well as the effect of the helical mode number. Take as the starting point the solutions for the cylindrical shell without fluid loading and consider the case of the solution identifiable as the a_0 wave at high frequencies. Figures 4.7(a) and 4.8(a)

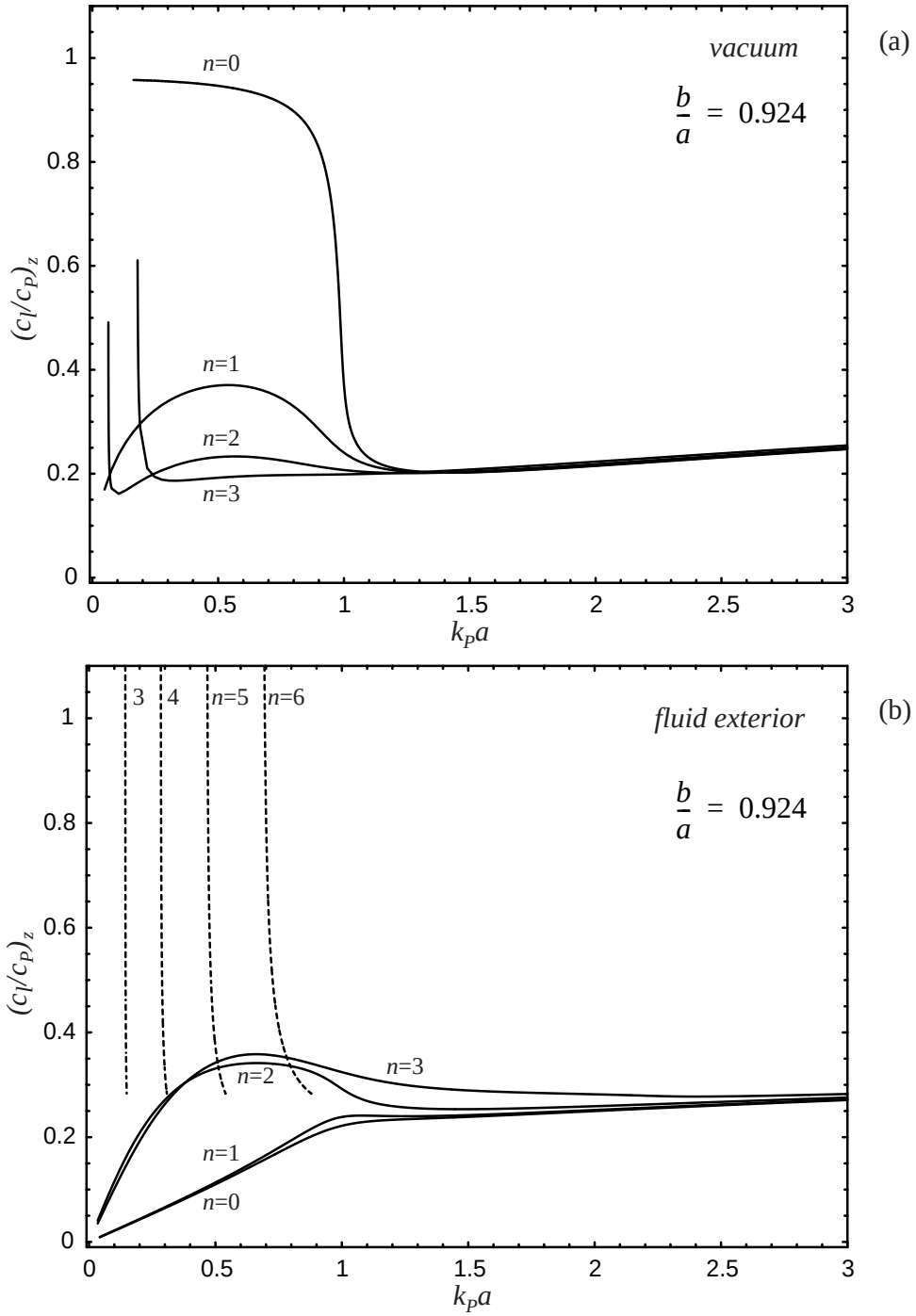

FIG. 4.7 Axial phase velocity for the first 4 modes of a (a) free and (b) exteriorly fluid loaded cylindrical shell (Shell A). In each case the solid curves belong to the family which corresponds to the a_0 Lamb wave. For the fluid loaded case there are also curves corresponding to the a_{0^-}, of which the supersonic portions of the curves are plotted for several values of n. The normalization is with respect to the plate speed (c_P = 5.232 mm/μs). The fluid loading has considerable effect at low frequencies near the ring frequency ($k_Pa \approx 1$).

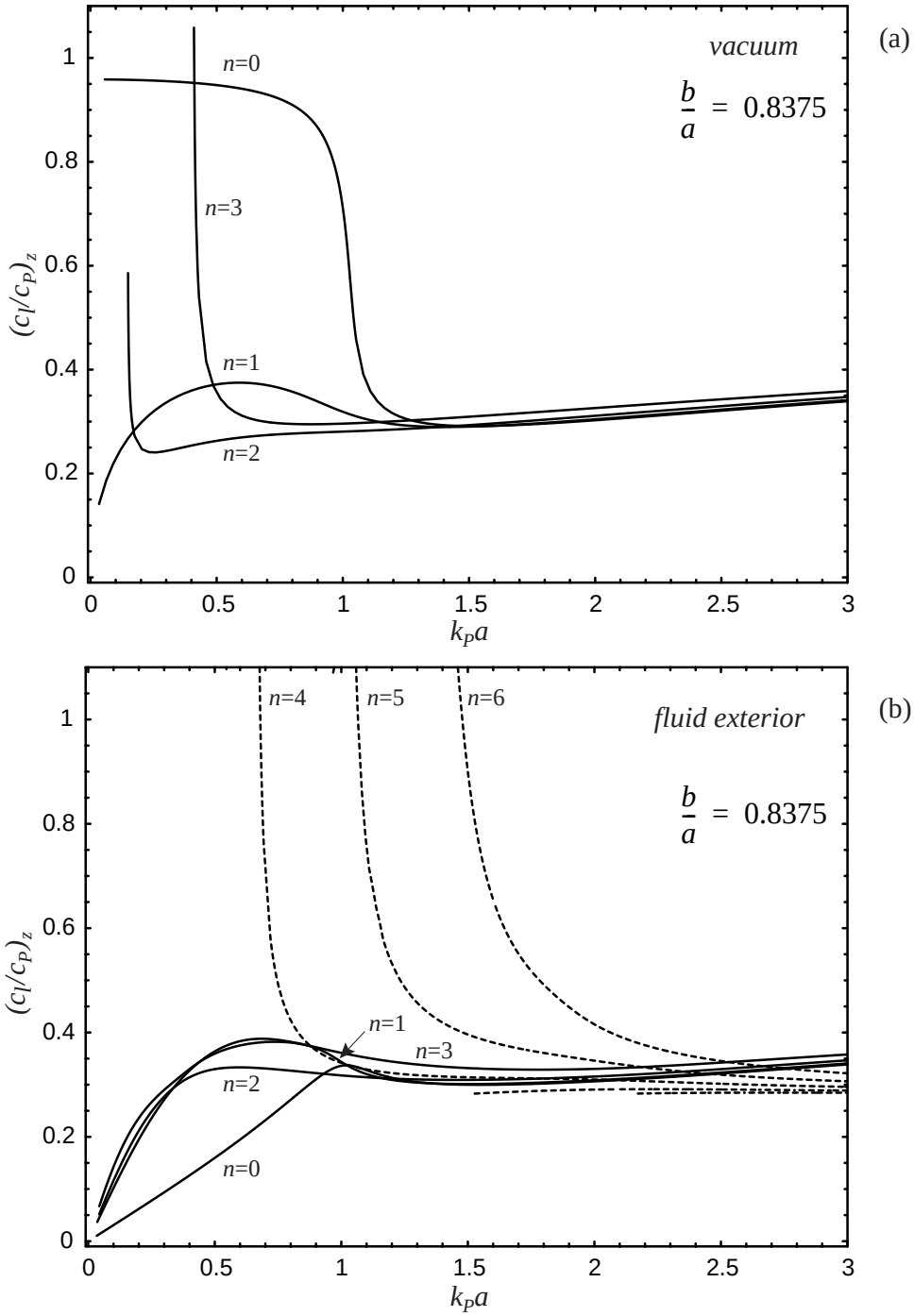

FIG. 4.8 Axial phase velocity for the first 4 modes of a (a) free and (b) exteriorly fluid-loaded cylindrical shell (Shell B). In each case the solid curves belong to the family which corresponds to the a_0 Lamb wave. For the fluid loaded case there are also curves corresponding to the $a_{0\text{-}}$, of which the supersonic portions of the curves are plotted for several values of n. The normalization is with respect to the plate speed (c_P = 5.232 mm/μs). The fluid loading has considerable effect at low frequencies near the ring frequency ($k_Pa \approx 1$).

show the axial phase velocities [Eq. (4.15)] of the lowest four modes of a *free* cylindrical shell for Shell A and Shell B, respectively. (The term free is used to denote a shell with vacuum on both the inside and outside of the shell.) Note that in this case the phase velocity and non-dimensional frequency are normalized to the *plate wave speed*[18] ($k_P = \omega / c_P$). The phase velocity for each mode is nearly identical above $k_P a \approx 1$. Below that the modes split. The $n = 0$ solution has an abrupt increase in phase velocity at about the ring frequency $k_P a \approx 1$. (The ring frequency is the frequency at which the wavelength of the lowest compressional wave in a thin cylindrical shell equals the circumference of the shell, i.e. $\lambda_P = 2\pi / k_P = 2\pi a$ or $k_P a = 1$.) It then approaches the plate speed at low frequencies. The $n = 1$ solution corresponds to flexural bending in a plane. All the higher solutions in this family are cutoff at particular frequencies. Similar plots to these may be found in Refs. [64] and [68] using the same convention. Figures 4.7(b) and 4.8(b) show the corresponding phase velocities with fluid loading (water) present. With the addition of a fluid the a_0 dispersion curves are split, just as for a fluid loaded plate for example, and one finds roots corresponding to the a_{0^-} waves as well. The supersonic portions of several of these solutions are shown as dashed lines. The curves for the a_0 change very little above $k_P a \approx 1$ but can be seen to behave drastically different below this value compared with the free cylinder solutions. It will be seen subsequently that the imaginary part of the axial wavevector for each of these modes becomes very large in this region, possibly indicating that these modes are cutoff. The cutoff conditions of the flexural modes (here the a_0) of a thin-walled free cylindrical shell are known[62,64]. The cutoff frequencies in Fig. 4.7 (a) agree well with at least the cutoff conditions in Ref. [62] (not listed here). The agreement in Fig. 4.8 (a), however, is not as good as this shell (Shell B) is fairly thick-walled. The cutoff condition (in the axial phase velocity) occurs when the axial wavevector goes to zero. This corresponds to letting $k_z a = 0$ in Eq. (4.13) which gives the condition for a cutoff of $(ka)_{cutoff} / n = (c_l / c)$. It may then be possible to approximate the cutoff condition simply with knowledge of an appropriate phase velocity curve. For the present cases it will be shown that the phase velocity curves are very similar to those for a flat plate provided n is not large. What is interesting about Figs. 4.7 (b) and 4.8 (b) compared to panel (a) of each

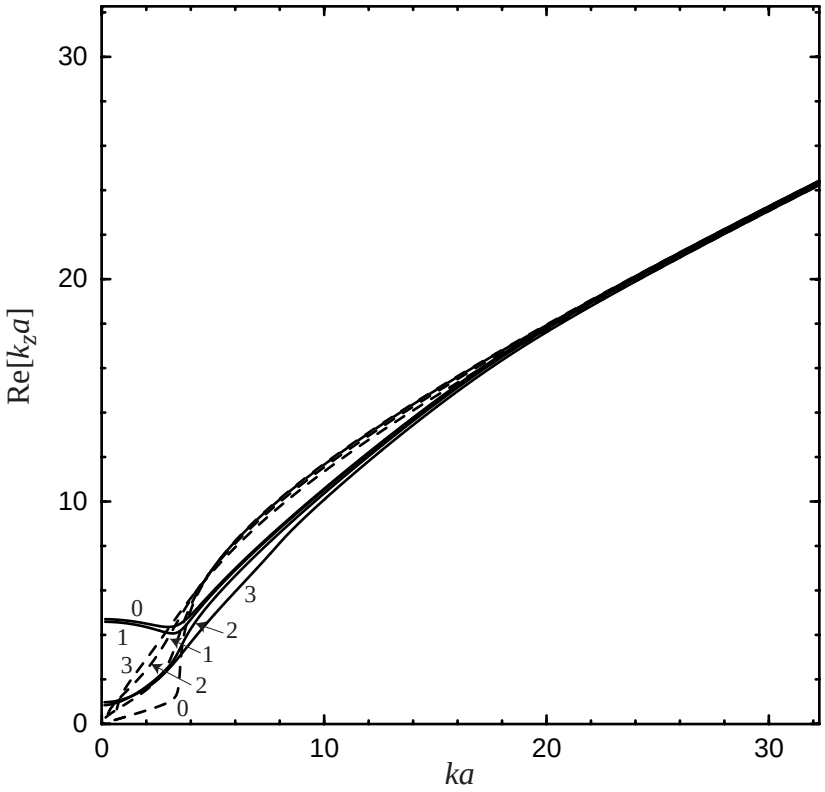

FIG. 4.9 Dispersion curves for the $n = 0$ - 3 solutions for a free cylindrical shell (dashed lines) and with an external fluid (solid lines), corresponding to Shell A. Above about $ka = 4$ these solutions are easily identifiable as the a_0 meridional ($n = 0$) and helical ($n > 0$) leaky waves.

figure is that it is the "subsonic" root, i.e. the a_{0-}, which displays the typical cutoff behavior and not the a_0. This raises the possibility that the axial phase velocity of the $n = 0$ mode of the a_{0-}, which was not easily evaluated in the present study, may actually turn upwards, as the $n = 0$ mode does for the free cylinder, and become supersonic near the ring frequency. This would enable acoustic coupling to this mode in this region through trace velocity matching of wavefronts and allow for an a_{0-} meridional wave. It is possible that this is the mechanism which gives rise to the observed scattering response at low frequencies (just below the ring frequency) and relatively large tilt angles discussed in Chapters 2 and 3. This response was not previously identified.

Now consider these same solutions in a more familiar form over a broader range of frequencies. Figure 4.9 shows the same $n = 0$ - 3 wavenumber dispersion curves for Shell A for both the free and exteriorly fluid loaded cases. Figure 4.10 shows the corresponding

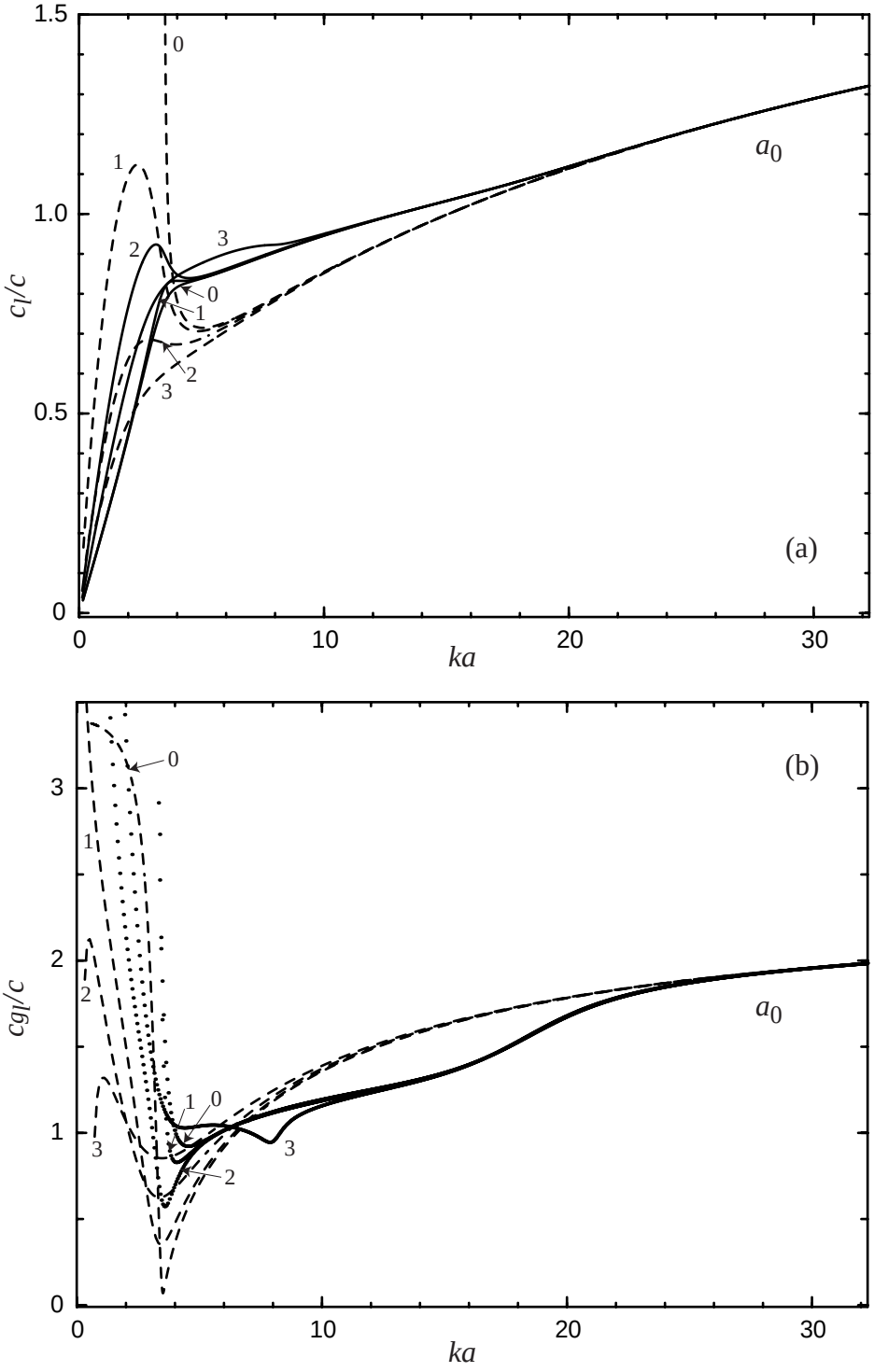

FIG. 4.10 (a) Phase and (b) group velocities for the n = 0 - 3 solutions for a free cylindrical shell (dashed lines) and with an external fluid [lines (top), points (bottom)], corresponding to Shell A. Above about ka = 10 (the coincidence frequency is about ka = 15.6) propagation of the helical waves (here a_0) on the shell is nearly isotropic, i.e. independent of propagation angle on the shell, for the lowest orders.

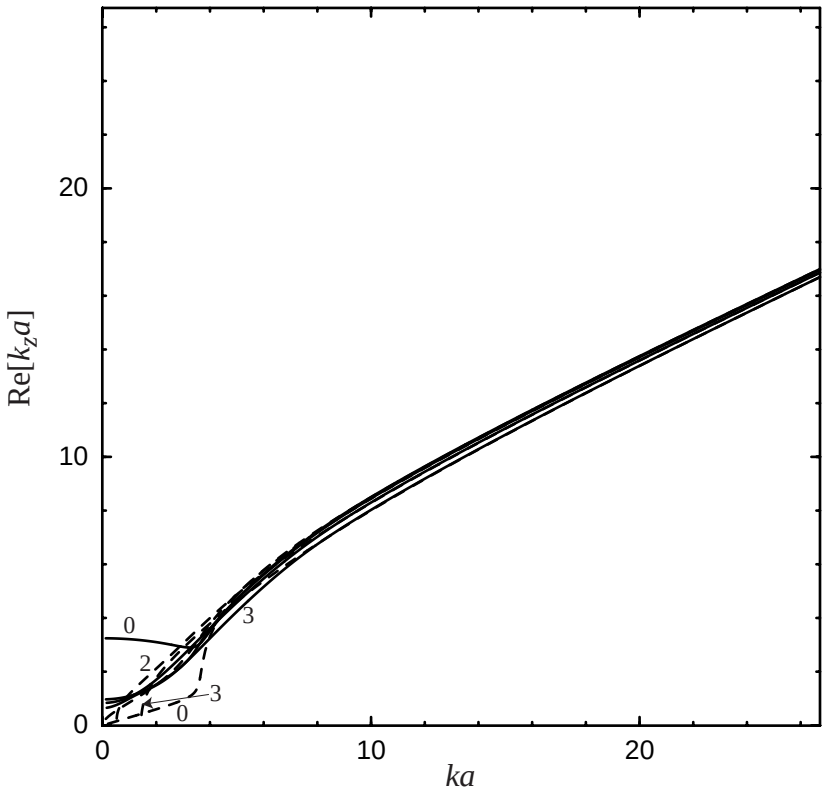

FIG. 4.11 Dispersion curves for the $n = 0$ - 3 solutions for a free cylindrical shell (dashed lines) and with an external fluid (solid lines), corresponding to Shell B. Above about $ka = 4$ these solutions are easily identifiable as the a_0 meridional ($n = 0$) and helical ($n > 0$) leaky waves.

phase and group velocities which are calculated from Eqs. (4.13) and (4.14), respectively. These are the *total* phase and group velocities on the shell, not just the axial component. As such they should only be regarded as applicable when the wave may be considered as a helical wave and not as a global mode of the shell. Figures 4.11 and 4.12 show similar results for Shell B. For each shell the effects of fluid loading are again seen to be small at high frequencies. It is in this region that the phase velocity is greater than the speed of sound in the outer fluid. Once the phase velocity in the fluid loaded case is comparable to the outer fluid sound speed the effect is generally to increase the phase velocities with respect to the free cylinder phase velocities. This similar shift due to fluid loading is present for fluid loaded plates[69,70], and cylindrical[8] and spherical shells[28].

The dependence on helical mode number is readily apparent in these figures as well.

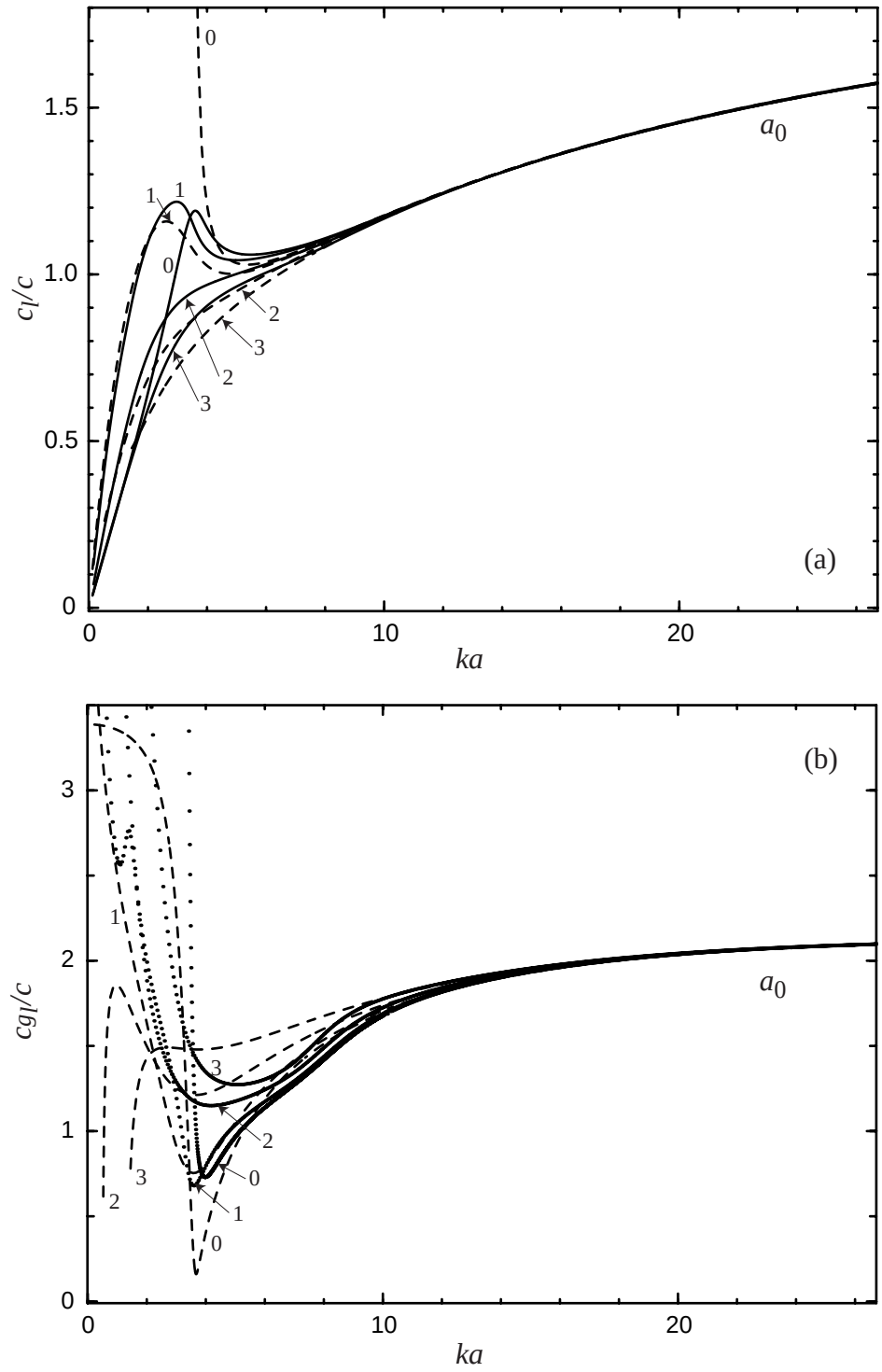

FIG. 4.12 (a) Phase and (b) group velocities for the n = 0 - 3 solutions for a free cylindrical shell (dashed lines) and with an external fluid [lines (top), points (bottom)], corresponding to Shell B. Above about ka = 12 (the coincidence frequency is about ka = 7.3) propagation of the helical waves (here a_0) on the shell is nearly isotropic, i.e. independent of propagation angle on the shell, for the lowest orders.

Unless the helical mode number is large (see the next section) the dispersion characteristics are nearly independent of helical mode number above $ka \approx 10$ ($ka \approx 12$) for Shell A (Shell B).

4.5 Numerical Results: Meridional and Helical Dispersion and Coupling Curves for the Fluid Loaded Case

A closer look at the fluid-loaded solutions is now made. The primary Lamb-type waves of interest in earlier chapters were the a_0 and a_{0^-}. For the frequency range studied these two types of waves were the major contributors in the backscattering enhancements. In calculating the approximate coupling conditions (Figs. 2.7 and 2.8) for these two types of waves on each of the shells studied it was assumed that the propagation of helical waves on the shell was isotropic (independent of propagation direction). Figures 4.10 and 4.12 showed that this is a good approximation above $ka \approx 10$ ($ka \approx 12$) for Shell A (Shell B), at least for $n = 0$ - 3. Figures 4.13(b) and 4.17(b) extend these calculations up to $n = 11$ and $n = 10$ for the a_0 on each shell. Figures 4.15(b) and 4.19(b) show dispersion curves for the a_{0^-} helical waves for $n = 3$ - 12 and $n = 2$ - 10 respectively. These show the regions over which the approximation of isotropic propagation is valid. In addition the curves for propagation of the corresponding Lamb wave on a doubly fluid-loaded plate are shown. Comparison with these curves show that the propagation behavior of helical waves on a cylindrical shell at high frequencies is very comparable to propagation on a plate. The similarities, however, are not as good for the thicker shell, where curvature plays a more important role. Also shown for reference are the real and imaginary parts of the wavenumber dispersion curves in Figs. 4.14, 4.18, and 4.16 and 4.20.

Just as in Figs. 2.7 and 2.8, coupling conditions may be computed for these "exact" helical wave dispersion curves for the infinite cylindrical shell. Figures 4.13(a) and 4.17(a) show these curves for the a_0 while Figs. 4.15(a) and 4.19(a) are for the a_{0^-}. These are

computed by simply matching the real part of the calculated axial wavenumber, $k_z a$, with the axial component of an incident plane wave $(k_z a)_{inc} = (ka)\sin\gamma$ which yields,

$$\gamma = \sin^{-1}\left(\frac{Re[k_z a]}{ka}\right), \qquad Re[k_z a] < ka\,. \tag{4.17}$$

The coupling conditions are terminated at an arbitrary point chosen to be when the damping, $Im[k_z a]$, exceeds 2.5. These coupling curves agree very well with the calculated and measured backscattering enhancements in Figs. 2.4 and 2.5. This may be seen by examining Figs. 4.21 and 4.22 in Section 4.A of this chapter which shows an overlay of Figs. 4.13 (a) and 4.15 (a) with Figs. 2.4 (a) and (b), and an overlay of Figs. 4.17 (a) and 4.19 (a) with Figs. 2.5 (a) and (b).

In examining the following figures it should be useful to recall the conversion from ka to f in kHz is:

$$\begin{aligned} f &= 12.39(ka) \qquad \text{Shell A} \\ f &= 11.23(ka) \qquad \text{Shell B.} \end{aligned} \tag{4.18}$$

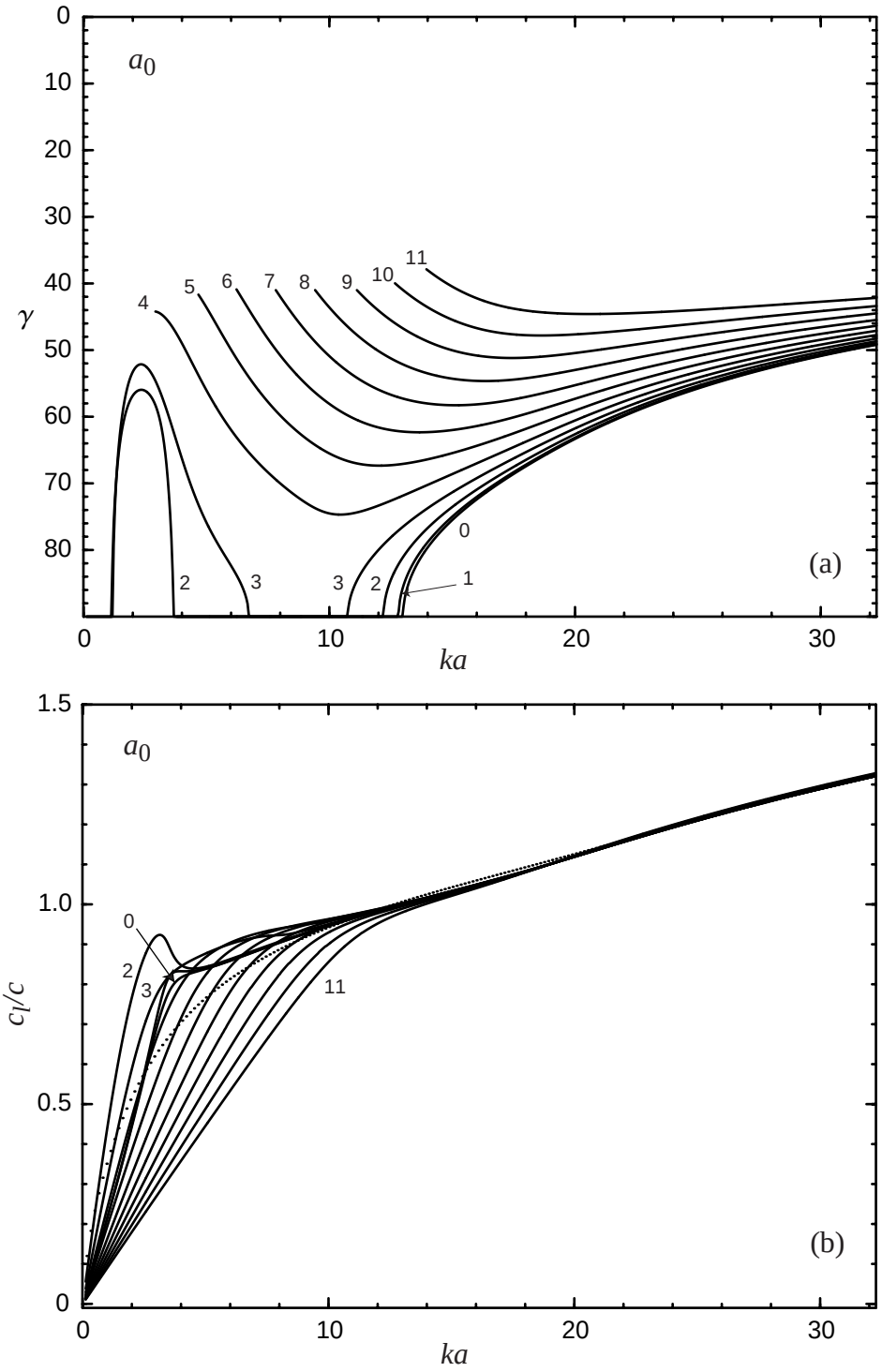

FIG. 4.13 (a) Coupling conditions and (b) phase velocities (see text for description) for the n = 0 - 11 solutions which correspond to the a_0 Lamb wave at high frequencies. (Shell A). The points correspond to the phase velocity for the a_0 Lamb wave on a plate having the same thickness as the cylinder wall and fluid loaded on both sides.

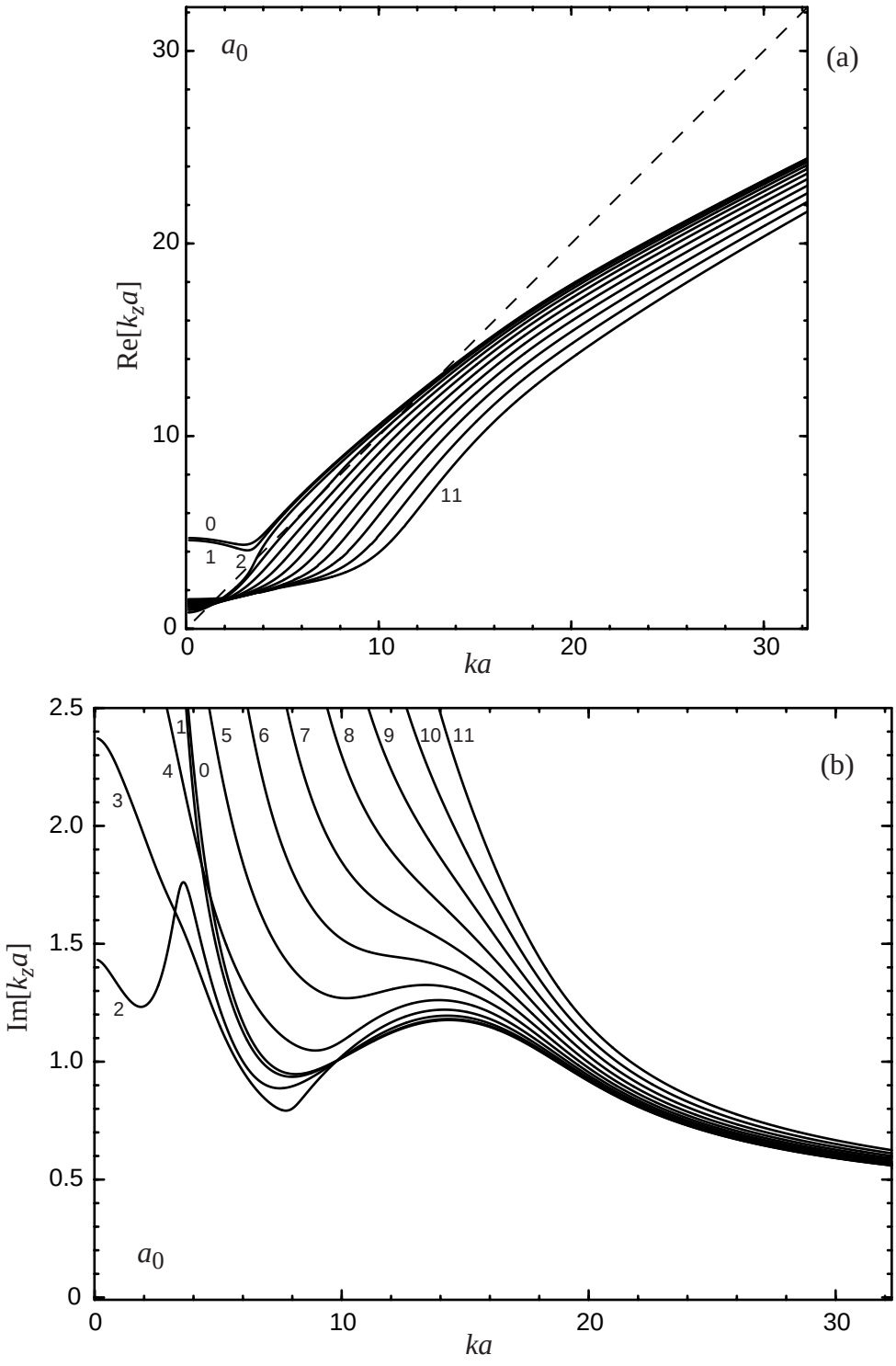

FIG. 4.14 The computed real, (a) and imaginary part, (b) of the axial wavevectors for the $n = 0$ - 11 solutions which correspond to the a_0 Lamb wave at high frequencies. (Shell A).

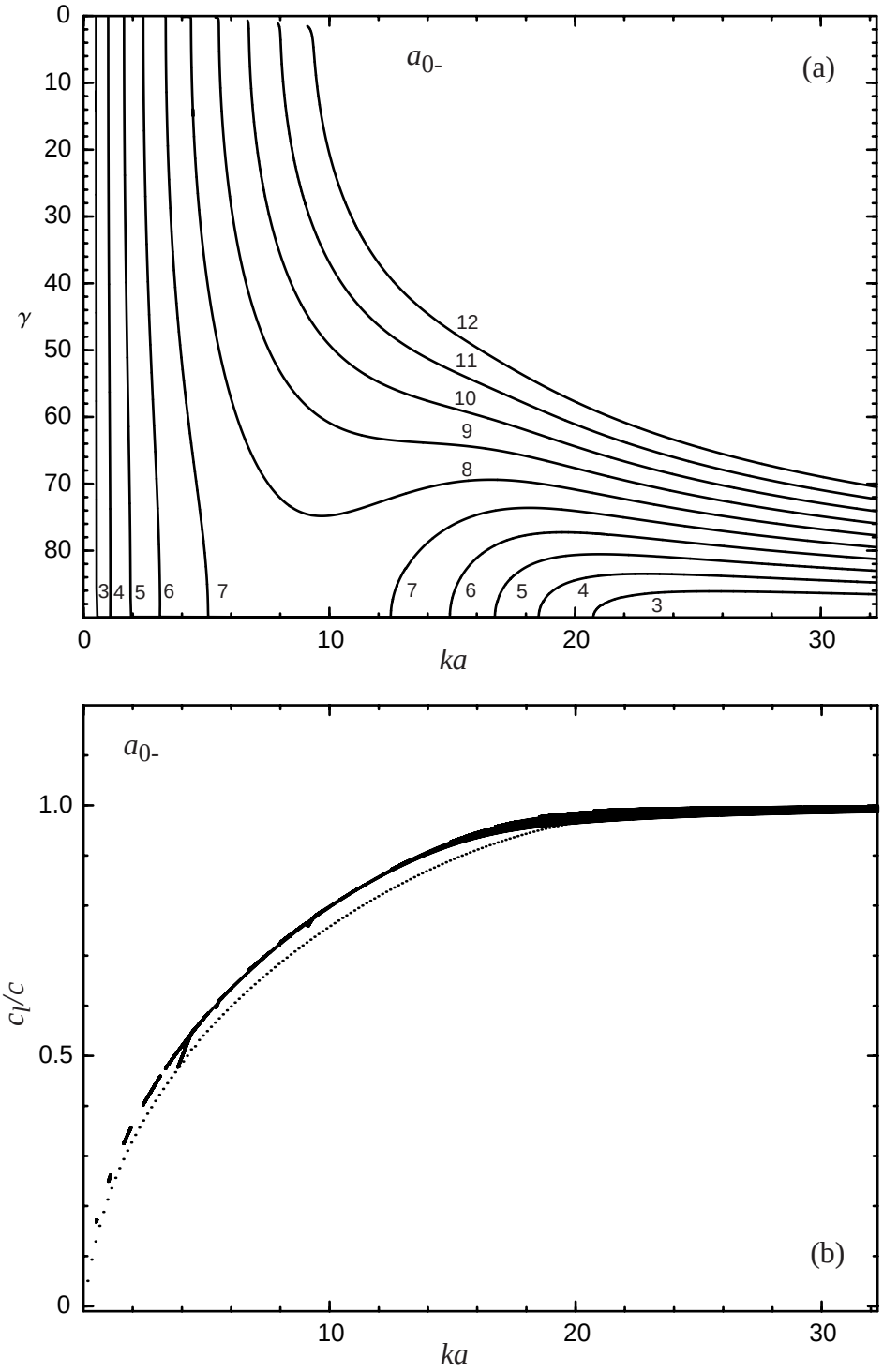

FIG. 4.15 (a) Coupling conditions and (b) phase velocities (see text for description) for the n = 3 - 12 solutions which correspond to the a_{0-} Lamb wave at high frequencies. (Shell A). The points correspond to the phase velocity for the a_{0-} Lamb wave on a plate having the same thickness as the cylinder wall and fluid loaded on both sides.

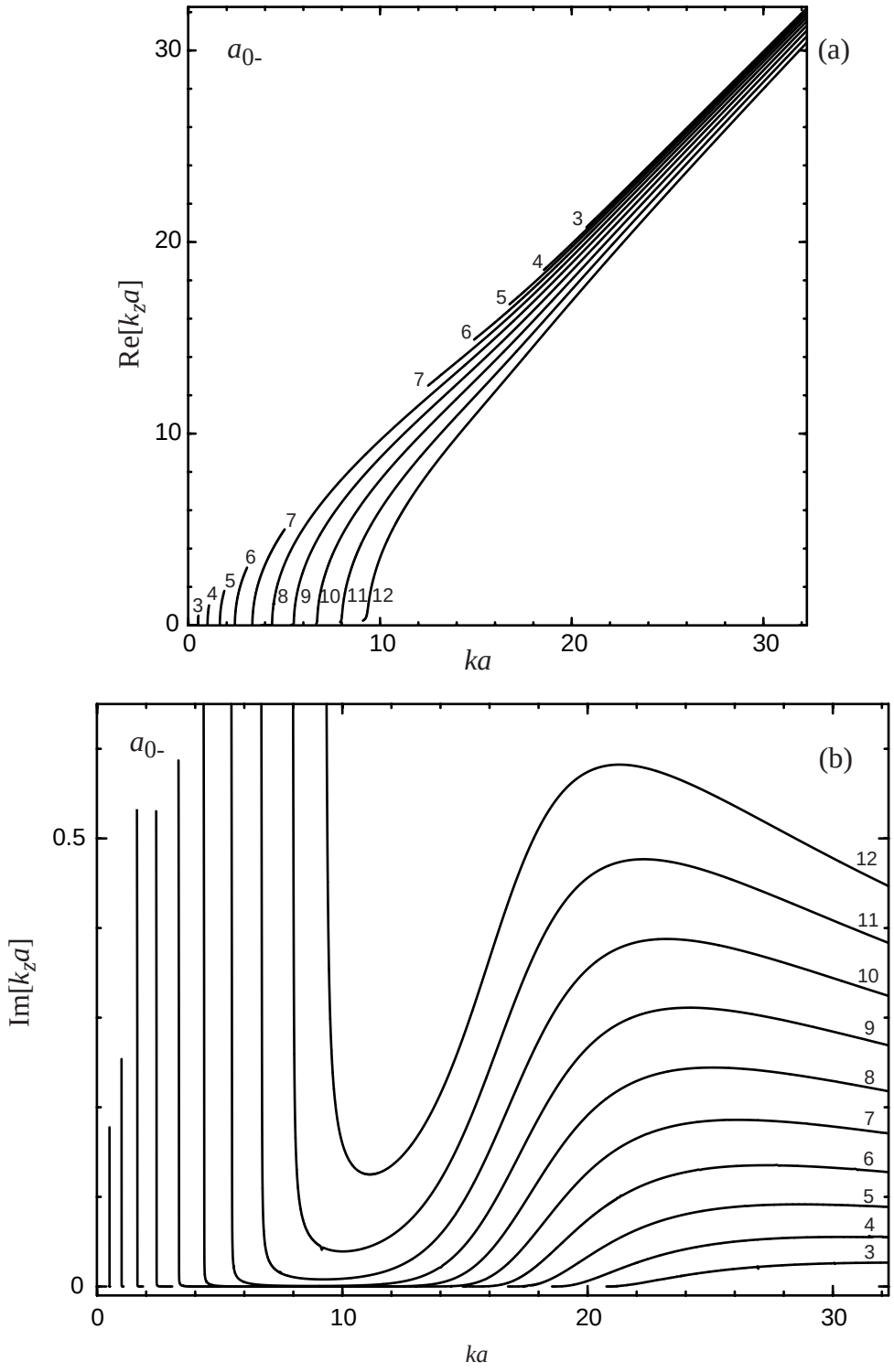

FIG. 4.16 The computed real, (a) and imaginary part, (b) of the axial wavevectors for the $n = 3$ - 12 solutions which correspond to the a_{0-} Lamb wave at high frequencies. (Shell A).

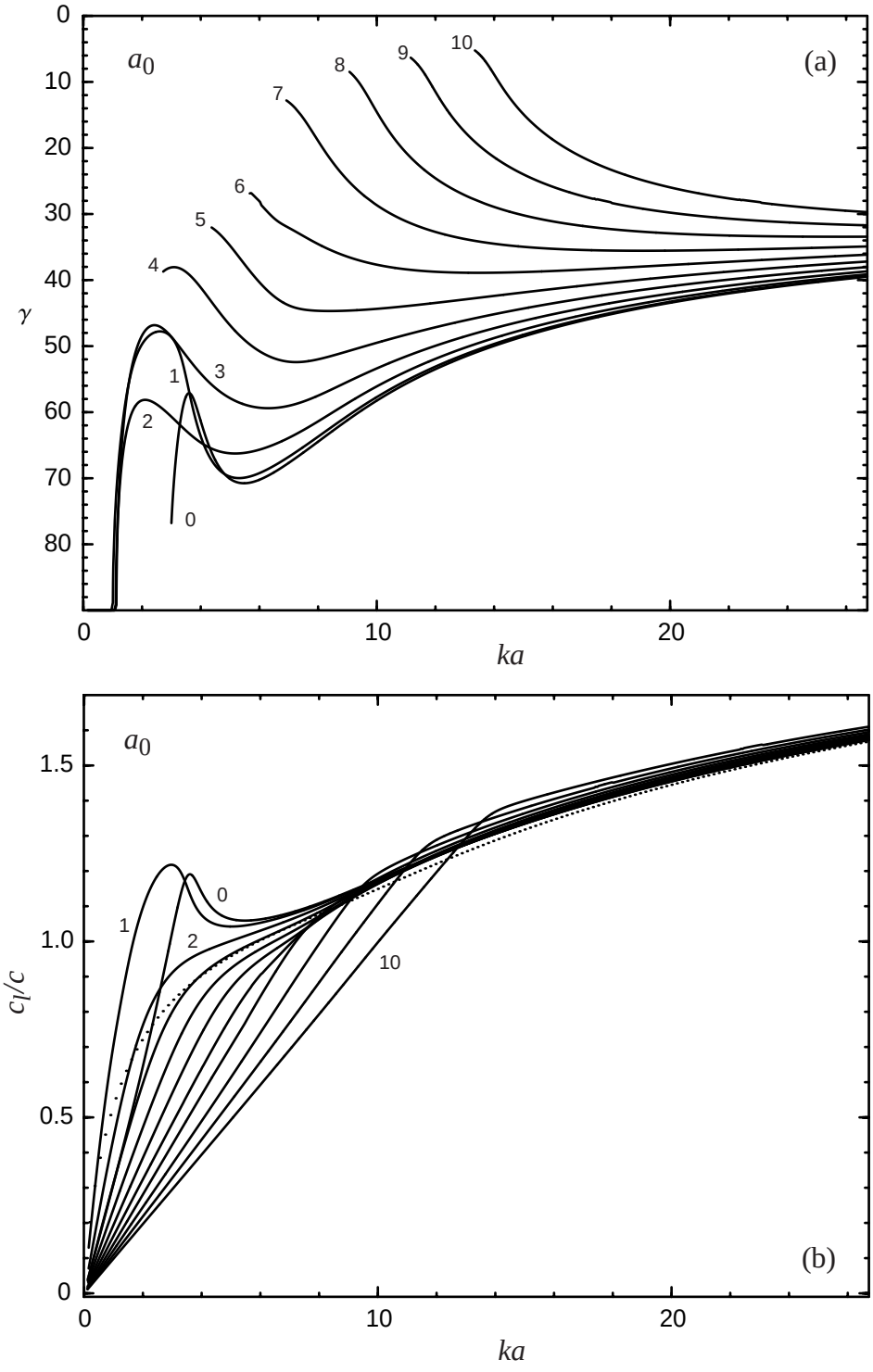

FIG. 4.17 (a) Coupling conditions and (b) phase velocities (see text for description) for the n = 0 - 10 solutions which correspond to the a_0 Lamb wave at high frequencies. (Shell B). The points correspond to the phase velocity for the a_0 Lamb wave on a plate having the same thickness as the cylinder wall and fluid loaded on both sides.

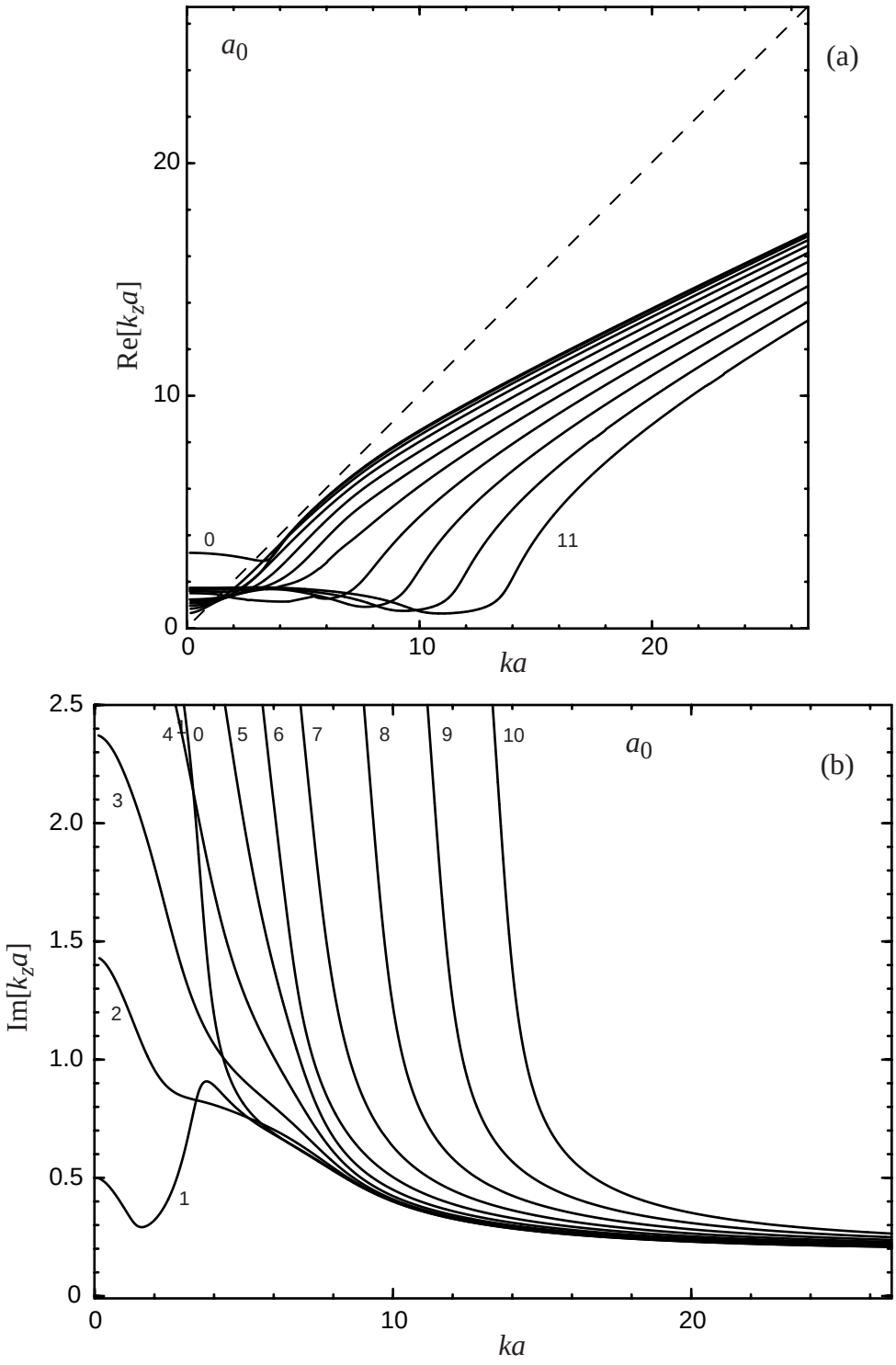

FIG. 4.18 The computed real, (a) and imaginary part, (b) of the axial wavevectors for the $n = 0$ - 10 solutions which correspond to the a_0 Lamb wave at high frequencies. (Shell B).

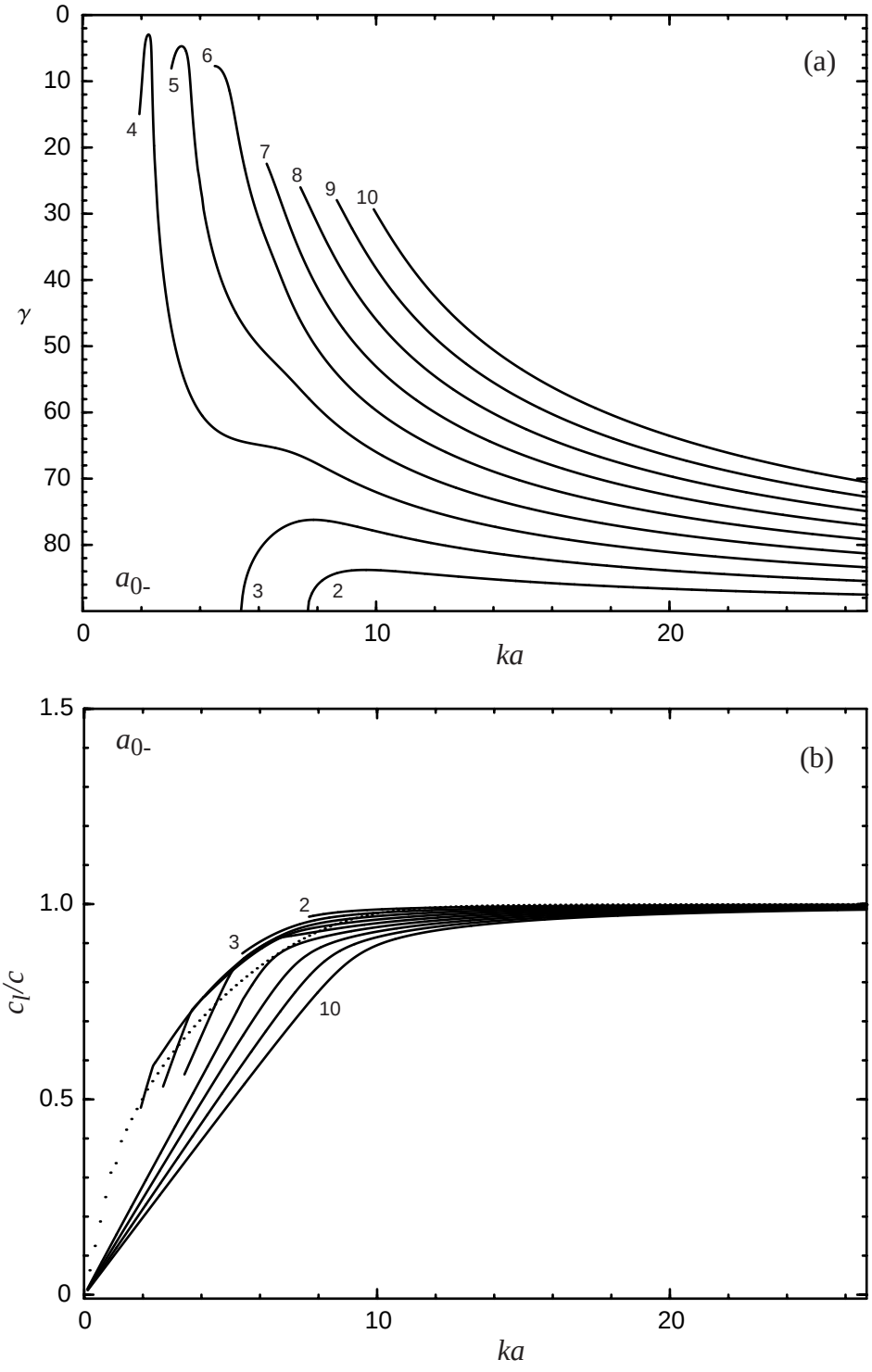

FIG. 4.19 (a) Coupling conditions and (b) phase velocities (see text for description) for the n = 2 - 10 solutions which correspond to the a_{0-} Lamb wave at high frequencies. (Shell B). The points correspond to the phase velocity for the a_0 Lamb wave on a plate having the same thickness as the cylinder wall and fluid loaded on both sides.

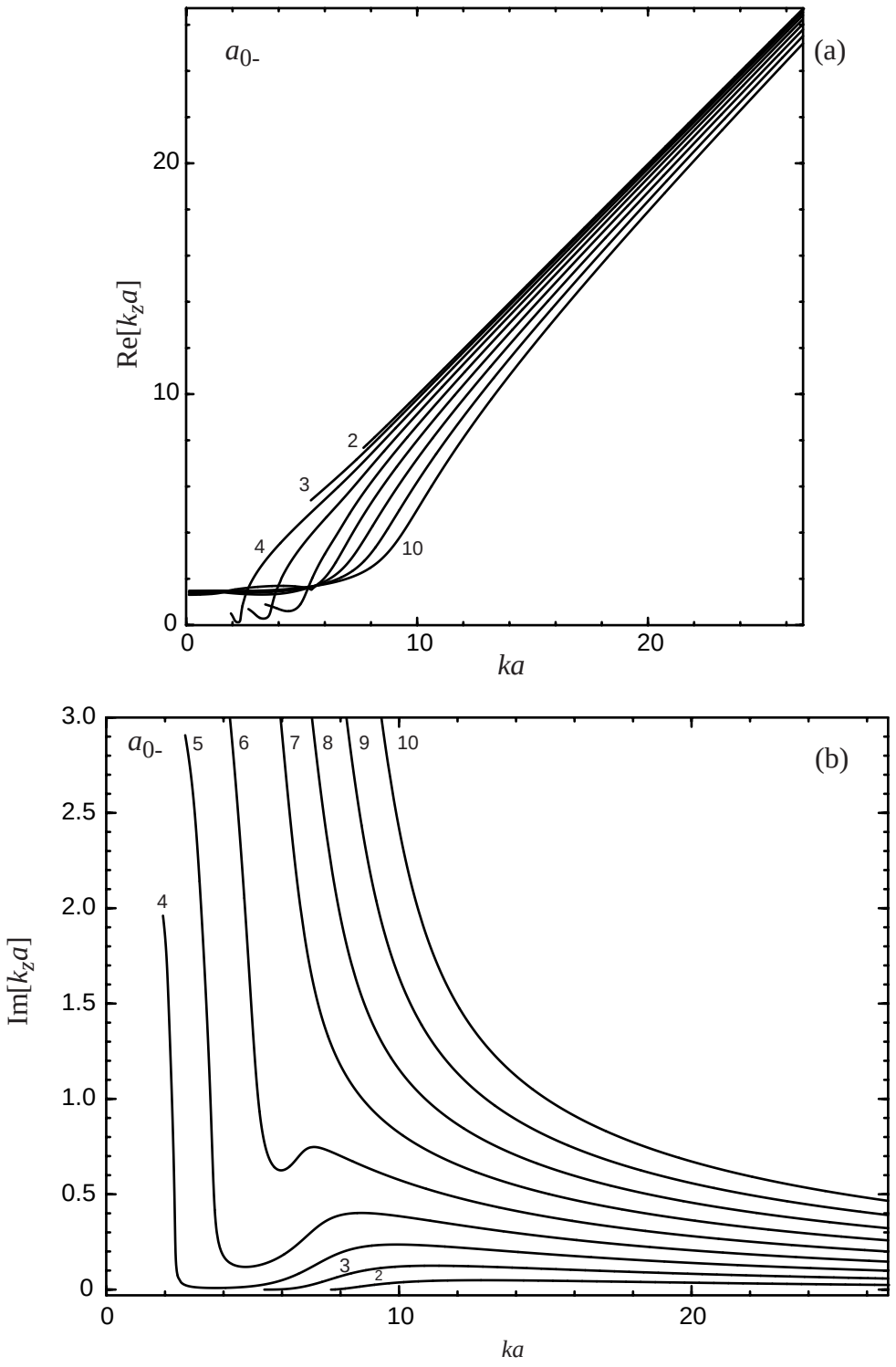

FIG. 4.20 The computed real, (a) and imaginary part, (b) of the axial wavevectors for the $n = 2$ - 10 solutions which correspond to the a_{0-} Lamb wave at high frequencies. (Shell B).

4.6 Discussion

The dispersion curves calculated in this chapter provide useful information about the propagation of meridional and helical leaky waves on an infinite cylindrical shell. At high frequencies the solutions of the characteristic equation for the normal modes of vibration of an exteriorly fluid-loaded cylindrical shell can be identified in terms of Lamb-type leaky waves, for both meridional and helical waves. Several Lamb waves were identified. The leaky waves responsible for the enhancements reported in Chapter 2 were confirmed to be the a_0 meridional and helical waves, and the a_{0^-} helical waves. The high-frequency coupling to these waves on a finite cylinder may be modeled using the dispersion curves for propagation on an infinite cylinder. Furthermore the damping of the a_0 meridional ray was determined and found to be in agreement with the suppositions stated in Chapters 2 and 3. This was that the damping of the a_0 meridional ray is large enough that the attenuation length is small compared to the length of the finite cylinder. This has the consequence that multiple axial resonances are not likely for the a_0. It was also confirmed that the propagation of low azimuthal order a_0 and a_{0^-} helical waves is nearly isotropic on the cylinder above certain frequencies. For the a_0 this corresponds to the region where the phase velocity is greater than the sound speed in the outer fluid. The effect of fluid loading on these helical waves was investigated and it was shown that the effects are mostly limited to low frequencies.

4.A Comparison of the Calculated Coupling Curves with the Measured and Calculated Backscattering

FIG. 4.21 Overlays of the calculated coupling curves with the calculated form function and measured backscattering spectrum (Shell A). The backscattering plots are from Figs. 2.4 (a) and (b) of Chapter 2 and the coupling curves are from Figs. 4.13 (a) and 4.15 (a). Compare these coupling curves with those of Figs. 2.7. The comparison here supports the identification of scattering features made in Chapter 2 for the a_{0-} helical waves and a_0 meridional wave.

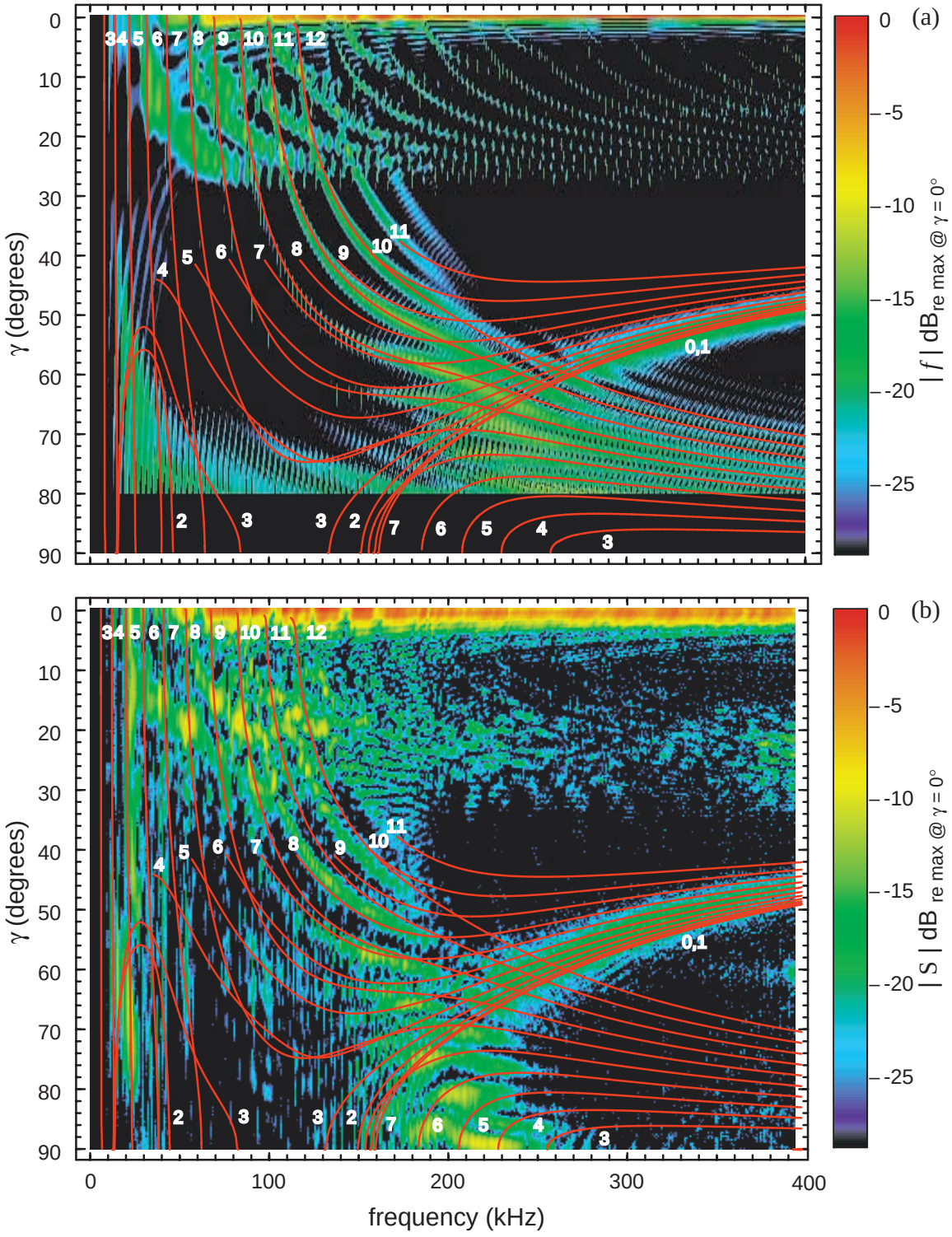
(a)
(b)
γ (degrees)
frequency (kHz)
0
100
200
300
400
10
20
30
40
50
60
70
80
90
-5
-10
-15
-20
-25
| f | dB re max @ γ = 0°
| S | dB re max @ γ = 0°
0,1

FIG. 4.22 Overlays of the calculated coupling curves with the calculated form function and measured backscattering spectrum (Shell B). The backscattering plots are from Figs. 2.5 (a) and (b) of Chapter 2 and the coupling curves are from Figs. 4.17 (a) and 4.19 (a). Compare these coupling curves with those of Figs. 2.8. The comparison here supports the identification of the a_0 meridional ray and a_0 helical wave features made in Chapter 2. In addition three of the ridges of high backscatter at low frequencies in the top figure are identified as resulting from the n = 4, 5, and 6, a_{0-} helical waves. The progression of change between the backscattering features displayed by Shell A and those by Shell B may be seen in Figs. 5.6. For thin shells (e.g. Shell A or the 2% thick shell in Fig. 5.5) the backscattering is dominated by the a_0 meridional and a_{0-} helical features. In contrast, the thicker shells display greater enhancements by a_0 helical waves.

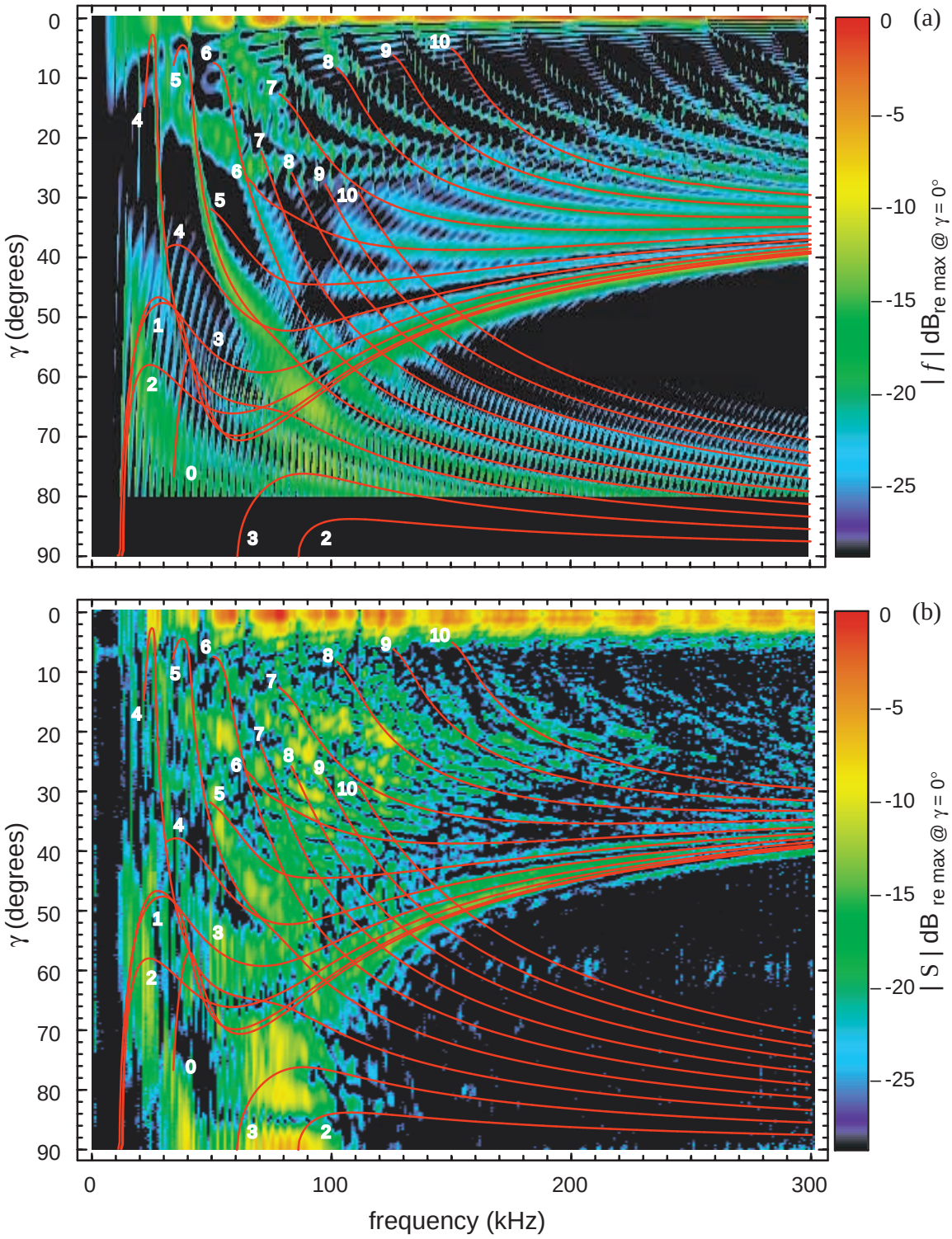
(a)
(b)
γ (degrees)
frequency (kHz)
0
10
20
30
40
50
60
70
80
90
100
200
300
-5
-10
-15
-20
-25
| f | dB re max @ γ = 0°
| S | dB re max @ γ = 0°

4.B Matrix Elements

This appendix section gives the matrix and vector elements in the characteristic equation $\boldsymbol{M} \cdot \boldsymbol{A} = \boldsymbol{C}$. These matrix elements were first published in detail in Ref. [14]. The elements listed here are identical (some notation is different) although the unsimplified versions are given for each element. When such lengthy mathematical expressions are given it is sometimes a good idea to explicitly give the expressions in raw form. These are often the easiest to confirm. These are explicitly given here for clarity and convenience only; nothing new is presented. First a few quantities must be defined. The wavevector components for the system are defined in the following way.

$$\begin{aligned} k_{\perp i} &= \sqrt{\left(\frac{\omega^2}{c_1^2} - k_z^2\right)} = k\sqrt{(1-\sin^2\gamma)} \\ h &= \sqrt{\pm\left(\frac{\omega^2}{c_L^2} - k_z^2\right)} \\ K &= \sqrt{\pm\left(\frac{\omega^2}{c_S^2} - k_z^2\right)} \\ h_3 &= \sqrt{\pm\left(\frac{\omega^2}{c_3^2} - k_z^2\right)} \end{aligned} \tag{4.19}$$

The following convention is used in the matrix elements:

	$k_z^2 < \frac{\omega^2}{c_L^2}$	$\frac{\omega^2}{c_L^2} < k_z^2 < \frac{\omega^2}{c_S^2}$	$\frac{\omega^2}{c_S^2} < k_z^2$
$h=$	$\sqrt{\omega^2/c_L^2 - k_z^2}$	$\sqrt{k_z^2 - \omega^2/c_L^2}$	$\sqrt{k_z^2 - \omega^2/c_L^2}$
$K=$	$\sqrt{\omega^2/c_S^2 - k_z^2}$	$\sqrt{\omega^2/c_S^2 - k_z^2}$	$\sqrt{k_z^2 - \omega^2/c_S^2}$
$U_n(ha, hb)=$	$J_n(ha, hb)$	$I_n(ha, hb)$	$I_n(ha, hb)$
$V_n(ha, hb)=$	$N_n(ha, hb)$	$K_n(ha, hb)$	$K_n(ha, hb)$
$U_n(Ka, Kb)=$	$J_n(Ka, Kb)$	$J_n(Ka, Kb)$	$I_n(Ka, Kb)$
$V_n(Ka, Kb)=$	$N_n(Ka, Kb)$	$N_n(Ka, Kb)$	$K_n(Ka, Kb)$
$\delta=$	1	-1	-1
$\kappa=$	1	1	-1

(4.20)

The terms N_n, I_n and K_n are the Bessel function of the second kind, and modified Bessel functions, respectively. The terms δ and κ are used for bookkeeping purposes because the matrix elements contain derivatives, and different Bessel functions have different recursion relations. Depending on whether the appropriate Bessel function is to be evaluated on the inner (*b*) or outer (*a*) surface determines which argument is used, either *Kb* or *Ka*, for example. The matrices are

$$\boldsymbol{M} = \begin{bmatrix} M_{11} & 0 & M_{13} & M_{14} & M_{15} & M_{16} & M_{17} & M_{18} \\ 0 & M_{22} & M_{23} & M_{24} & M_{25} & M_{26} & M_{27} & M_{28} \\ M_{31} & 0 & M_{33} & M_{34} & M_{35} & M_{36} & M_{37} & M_{38} \\ 0 & M_{42} & M_{43} & M_{44} & M_{45} & M_{46} & M_{47} & M_{48} \\ 0 & 0 & M_{53} & M_{54} & M_{55} & M_{56} & M_{57} & M_{58} \\ 0 & 0 & M_{63} & M_{64} & M_{65} & M_{66} & M_{67} & M_{68} \\ 0 & 0 & M_{73} & M_{74} & M_{75} & M_{76} & M_{77} & M_{78} \\ 0 & 0 & M_{83} & M_{84} & M_{85} & M_{86} & M_{87} & M_{88} \end{bmatrix} \qquad \boldsymbol{A} = \begin{bmatrix} g_n \\ q_n \\ a_n \\ b_n \\ c_n \\ d_n \\ e_n \\ f_n \end{bmatrix} \tag{4.21}$$

$$\boldsymbol{C} = \frac{\rho_2}{\rho_1} \begin{bmatrix} -(k_{\perp i}a)J_n'(k_{\perp i}a) = -[nJ_n(k_{\perp i}a) - (k_{\perp i}a)J_{n+1}(k_{\perp i}a)] \\ 0 \\ -\lambda_1\left(\frac{\omega a}{c_1}\right)^2 J_n(k_{\perp i}a) \\ 0 \\ 0 \\ 0 \\ 0 \\ 0 \end{bmatrix} \tag{4.22}$$

The coefficients to be determined in $\boldsymbol{A}$ belong to the solutions in the three regions of space.

$$
\begin{aligned}
\Phi^{(1)} &= \frac{-1}{\rho_1\omega^2}\sum_{n=0}^{\infty}\varepsilon_n i^n\left[J_n(k_{\perp i}\rho)+g_n\begin{Bmatrix}H_n^{(1)}(h_1\rho)\\K_n(h_1\rho)\end{Bmatrix}\right]\cos(n\psi)e^{ik_z z}\\
\Phi^{(2)} &= \frac{1}{\rho_2\omega^2}\sum_{n=0}^{\infty}\varepsilon_n i^n\left[a_n\begin{Bmatrix}J_n(h\rho)\\I_n(h\rho)\end{Bmatrix}+b_n\begin{Bmatrix}N_n(h\rho)\\K_n(h\rho)\end{Bmatrix}\right]\cos(n\psi)e^{ik_z z}\\
A_\rho &= \frac{1}{\rho_2\omega^2}\sum_{n=0}^{\infty}\varepsilon_n i^n\left[c_n\begin{Bmatrix}J_{n+1}(K\rho)\\I_{n+1}(K\rho)\end{Bmatrix}+d_n\begin{Bmatrix}N_{n+1}(K\rho)\\K_{n+1}(K\rho)\end{Bmatrix}\right]\sin(n\psi)e^{ik_z z}\\
A_\psi &= \frac{1}{\rho_2\omega^2}\sum_{n=0}^{\infty}\varepsilon_n i^n\left[-c_n\begin{Bmatrix}J_{n+1}(K_p\rho)\\I_{n+1}(K_p\rho)\end{Bmatrix}-d_n\begin{Bmatrix}N_{n+1}(K\rho)\\K_{n+1}(K\rho)\end{Bmatrix}\right]\cos(n\psi)e^{ik_z z}\\
A_z &= \frac{1}{\rho_2\omega^2}\sum_{n=0}^{\infty}\varepsilon_n i^n\left[e_n\begin{Bmatrix}J_n(K\rho)\\I_n(K\rho)\end{Bmatrix}+f_n\begin{Bmatrix}N_n(K\rho)\\K_n(K\rho)\end{Bmatrix}\right]\sin(n\psi)e^{ik_z z}\\
\Phi^{(3)} &= \frac{-1}{\rho_3\omega^2}\sum_{n=0}^{\infty}\varepsilon_n i^n q_n\begin{Bmatrix}J_n(h_3\rho)\\I_n(h_3\rho)\end{Bmatrix}\cos(n\psi)e^{ik_z z}
\end{aligned}
\tag{4.23}
$$

The following convention is used,

$$
\begin{aligned}
\boldsymbol{U} &= \boldsymbol{U}_L + \boldsymbol{U}_S\\
\boldsymbol{U}_L &= \nabla\Phi \qquad \boldsymbol{U}_S = \nabla\times\boldsymbol{A}\\
\nabla\times\boldsymbol{U}_L &= 0 \qquad \nabla\bullet\boldsymbol{U}_S = 0
\end{aligned}
\tag{4.24}
$$

and the equations of motion in the shell are

$$
\begin{aligned}
\nabla^2\Phi - \frac{1}{c_L^2}\frac{\partial^2\Phi}{\partial t^2} &= 0\\
\nabla^2\boldsymbol{A} - \frac{1}{c_S^2}\frac{\partial^2\boldsymbol{A}}{\partial t^2} &= 0
\end{aligned}
\tag{4.25}
$$

for the scalar and vector displacement potentials. Each of the eight boundary conditions provide and equation which is then combined into the matrix equation given above. Going from top to bottom the rows of the matrix equation are filled with the following boundary condition equations and elements.

$$[u_\rho^{(1)} - u_\rho^{(2)}]\Big|_{\rho = a} = 0 : \tag{4.26}$$

$$\begin{aligned}
M_{11} &= \frac{\rho_2}{\rho_1}(k_{\perp i}a)\begin{Bmatrix} H_n^{(1)\prime}(k_{\perp i}a) \\ K_n'(k_{\perp i}a) \end{Bmatrix} = \frac{\rho_2}{\rho_1}\left[n\begin{Bmatrix} H_n^{(1)}(k_{\perp i}a) \\ K_n(k_{\perp i}a) \end{Bmatrix} - (k_{\perp i}a)\begin{Bmatrix} H_{n+1}^{(1)}(k_{\perp i}a) \\ K_{n+1}(k_{\perp i}a) \end{Bmatrix}\right] \\
M_{12} &= 0 \\
M_{13} &= (ha)U_n'(ha) = [nU_n(ha) - \delta(ha)U_{n+1}(ha)] \\
M_{14} &= (ha)V_n'(ha) = [nV_n(ha) - (ha)V_{n+1}(ha)] \\
M_{15} &= i(k_z a)U_{n+1}(Ka) \\
M_{16} &= i(k_z a)V_{n+1}(Ka) \\
M_{17} &= nU_n(Ka) \\
M_{18} &= nV_n(Ka)
\end{aligned} \tag{4.27}$$

$$[u_\rho^{(2)} - u_\rho^{(3)}]\Big|_{\rho = b} = 0 : \tag{4.28}$$

$$\begin{aligned}
M_{21} &= 0 \\
M_{22} &= \frac{\rho_2}{\rho_3}(h_3 b)\begin{Bmatrix} J_n'(h_3 b) \\ I_n'(h_3 b) \end{Bmatrix} = \frac{\rho_2}{\rho_3}\left[n\begin{Bmatrix} J_n(h_3 b) \\ I_n(h_3 b) \end{Bmatrix} - (h_3 b)\begin{Bmatrix} J_{n+1}(h_3 b) \\ -I_{n+1}(h_3 b) \end{Bmatrix}\right] \\
M_{23} &= (hb)U_n'(hb) = [nU_n(hb) - \delta(hb)U_{n+1}(hb)] \\
M_{24} &= (hb)V_n'(hb) = [nV_n(hb) - (hb)V_{n+1}(hb)] \\
M_{25} &= i(k_z b)U_{n+1}(Kb) \\
M_{26} &= i(k_z b)V_{n+1}(Kb) \\
M_{27} &= nU_n(Kb) \\
M_{28} &= nV_n(Kb)
\end{aligned} \tag{4.29}$$

$$[T_{\rho\rho}^{(1)} - T_{\rho\rho}^{(2)}]\Big|_{\rho = a} = 0 : \tag{4.30}$$

$$\begin{aligned}
M_{31} &= \lambda_1 \frac{\rho_2}{\rho_1}\left(\frac{\omega a}{c_1}\right)^2 \begin{Bmatrix} H_n^{(1)}(k_{\perp i}a) \\ K_n(k_{\perp i}a) \end{Bmatrix} \\
M_{32} &= 0 \\
M_{33} &= -2\mu(ha)^2 U_n''(ha) + \lambda\left(\frac{\omega a}{c_L}\right)^2 U_n(ha) \\
&= \lambda\left(\frac{\omega a}{c_L}\right)^2 U_n(ha) - 2\mu[(n^2 - \delta(ha)^2 - n)U_n(ha) + \delta(ha)U_{n+1}(ha)] \\
M_{34} &= -2\mu(ha)^2 V_n''(ha) + \lambda\left(\frac{\omega a}{c_L}\right)^2 V_n(ha) \\
&= \lambda\left(\frac{\omega a}{c_L}\right)^2 V_n(ha) - 2\mu[(n^2 - \delta(ha)^2 - n)V_n(ha) + (ha)V_{n+1}(ha)] \\
M_{35} &= -i2\mu(k_z a)(Ka)U_{n+1}'(Ka) = -i2\mu(k_z a)[-(n+1)U_{n+1}(Ka) + (Ka)U_n(Ka)] \\
M_{36} &= -i2\mu(k_z a)(Ka)V_{n+1}'(Ka) = -i2\mu(k_z a)[-(n+1)V_{n+1}(Ka) + \kappa(Ka)V_n(Ka)] \\
M_{37} &= -2\mu n[(Ka)U_n'(Ka) - U_n(Ka)] = -2\mu n[(n-1)U_n(Ka) - \kappa(Ka)U_{n+1}(Ka)] \\
M_{38} &= -2\mu n[(Ka)V_n'(Ka) - V_n(Ka)] = -2\mu n[(n-1)V_n(Ka) - (Ka)V_{n+1}(Ka)]
\end{aligned} \tag{4.31}$$

$$[T_{\rho\rho}^{(2)} - T_{\rho\rho}^{(3)}]\Big|_{\rho = b} = 0 : \tag{4.32}$$

$$\begin{aligned}
M_{41} &= 0 \\
M_{42} &= \lambda_3 \frac{\rho_2}{\rho_3}\left(\frac{\omega b}{c_3}\right)^2 \begin{Bmatrix} J_n(h_3 b) \\ I_n(h_3 b) \end{Bmatrix} \\
M_{43} &= -2\mu(hb)^2 U_n''(hb) + \lambda\left(\frac{\omega b}{c_L}\right)^2 U_n(hb) \\
&= \lambda\left(\frac{\omega b}{c_L}\right)^2 U_n(hb) - 2\mu[(n^2 - \delta(hb)^2 - n)U_n(hb) + \delta(hb)U_{n+1}(hb)] \\
M_{44} &= -2\mu(hb)^2 V_n''(hb) + \lambda\left(\frac{\omega b}{c_L}\right)^2 V_n(hb) \\
&= \lambda\left(\frac{\omega b}{c_L}\right)^2 V_n(hb) - 2\mu[(n^2 - \delta(hb)^2 - n)V_n(hb) + (hb)V_{n+1}(hb)] \\
M_{45} &= -i2\mu(k_z b)(Kb)U_{n+1}'(Kb) = -i2\mu(k_z b)[-(n+1)U_{n+1}(Kb) + (Kb)U_n(Kb)] \\
M_{46} &= -i2\mu(k_z b)(Kb)V_{n+1}'(Kb) = -i2\mu(k_z b)[-(n+1)V_{n+1}(Kb) + \kappa(Kb)V_n(Kb)] \\
M_{47} &= -2\mu n[(Kb)U_n'(Kb) - U_n(Kb)] = -2\mu n[(n-1)U_n(Kb) - \kappa(Kb)U_{n+1}(Kb)] \\
M_{48} &= -2\mu n[(Kb)V_n'(Kb) - V_n(Kb)] = -2\mu n[(n-1)V_n(Ka) - (Ka)V_{n+1}(Ka)]
\end{aligned} \tag{4.33}$$

$$T^{(2)}_{\rho\psi}\Big|_{\rho = a} = 0 : \tag{4.34}$$

$$\begin{aligned}
M_{51} &= 0 \\
M_{52} &= 0 \\
M_{53} &= -2n[(ha)U_n'(ha) - U_n(ha)] = 2n[(1-n)U_n(ha) + \delta(ha)U_{n+1}(ha)] \\
M_{54} &= -2n[(ha)V_n'(ha) - V_n(ha)] = 2n[(1-n)V_n(ha) + (ha)V_{n+1}(ha)] \\
M_{55} &= i(k_z a)[(Ka)U_{n+1}'(Ka) - (n+1)U_{n+1}(Ka)] \\
&= i(k_z a)[-2(n+1)U_{n+1}(Ka) + (Ka)U_n(Ka)] \\
M_{56} &= i(k_z a)[(Ka)V_{n+1}'(Ka) - (n+1)V_{n+1}(Ka)] \\
&= i(k_z a)[-2(n+1)V_{n+1}(Ka) + \kappa(Ka)V_n(Ka)] \\
M_{57} &= 2(Ka)U_n'(Ka) + [(Ka)^2 - 2n^2]U_n(Ka) \\
&= [-2n^2 + \kappa(Ka)^2 + 2n]U_n(Ka) - 2\kappa(Ka)U_{n+1}(Ka) \\
M_{58} &= 2(Ka)V_n'(Ka) + [(Ka)^2 - 2n^2]V_n(Ka) \\
&= [-2n^2 + \kappa(Ka)^2 + 2n]V_n(Ka) - 2(Ka)V_{n+1}(Ka)
\end{aligned} \tag{4.35}$$

$$T^{(2)}_{\rho\psi}\Big|_{\rho = b} = 0 : \tag{4.36}$$

$$\begin{aligned}
M_{61} &= 0 \\
M_{62} &= 0 \\
M_{63} &= -2n[(hb)U_n'(hb) - U_n(hb)] = 2n[(1-n)U_n(hb) + \delta(hb)U_{n+1}(hb)] \\
M_{64} &= -2n[(hb)V_n'(hb) - V_n(hb)] = 2n[(1-n)V_n(hb) + (hb)V_{n+1}(hb)] \\
M_{65} &= i(k_z b)[(Kb)U_{n+1}'(Kb) - (n+1)U_{n+1}(Kb)] \\
&= i(k_z b)[-2(n+1)U_{n+1}(Kb) + (Kb)U_n(Kb)] \\
M_{66} &= i(k_z b)[(Kb)V_{n+1}'(Kb) - (n+1)V_{n+1}(Kb)] \\
&= i(k_z b)[-2(n+1)V_{n+1}(Kb) + \kappa(Kb)V_n(Kb)] \\
M_{67} &= 2(Kb)U_n'(Kb) + [(Kb)^2 - 2n^2]U_n(Kb) \\
&= [-2n^2 + \kappa(Kb)^2 + 2n]U_n(Kb) - 2\kappa(Kb)U_{n+1}(Kb) \\
M_{68} &= 2(Kb)V_n'(Kb) + [(Kb)^2 - 2n^2]V_n(Kb) \\
&= [-2n^2 + \kappa(Kb)^2 + 2n]V_n(Kb) - 2(Kb)V_{n+1}(Kb)
\end{aligned} \tag{4.37}$$

$$T_{\rho z}^{(2)}\Big|_{\rho = a} = 0 : \tag{4.38}$$

$$\begin{aligned}
M_{71} &= 0 \\
M_{72} &= 0 \\
M_{73} &= i2(k_z a)(ha)U_n'(ha) = i2(k_z a)[nU_n(ha) - \delta(ha)U_{n+1}(ha)] \\
M_{74} &= i2(k_z a)(ha)V_n'(ha) = i2(k_z a)[nV_n(ha) - (ha)V_{n+1}(ha)] \\
M_{75} &= -n(Ka)U_{n+1}'(Ka) + [(Ka)^2 - n(n+1) - (k_z a)^2]U_{n+1}(Ka) \\
&= [\kappa(Ka)^2 - (k_z a)^2]U_{n+1}(Ka) - n(Ka)U_n(Ka) \\
M_{76} &= -n(Ka)V_{n+1}'(Ka) + [(Ka)^2 - n(n+1) - (k_z a)^2]V_{n+1}(Ka) \\
&= [\kappa(Ka)^2 - (k_z a)^2]V_{n+1}(Ka) - \kappa n(Ka)V_n(Ka) \\
M_{77} &= in(k_z a)U_n(Ka) \\
M_{78} &= in(k_z a)V_n(Ka)
\end{aligned} \tag{4.39}$$

$$T_{\rho z}^{(2)}\Big|_{\rho = b} = 0 : \tag{4.40}$$

$$\begin{aligned}
M_{81} &= 0 \\
M_{82} &= 0 \\
M_{83} &= i2(k_z b)(hb)U_n'(hb) = i2(k_z b)[nU_n(hb) - \delta(hb)U_{n+1}(hb)] \\
M_{84} &= i2(k_z b)(hb)V_n'(hb) = i2(k_z b)[nV_n(hb) - (hb)V_{n+1}(hb)] \\
M_{85} &= -n(Kb)U_{n+1}'(Kb) + [(Kb)^2 - n(n+1) - (k_z b)^2]U_{n+1}(Kb) \\
&= [\kappa(Kb)^2 - (k_z b)^2]U_{n+1}(Kb) - n(Kb)U_n(Kb) \\
M_{86} &= -n(Kb)V_{n+1}'(Kb) + [(Kb)^2 - n(n+1) - (k_z b)^2]V_{n+1}(Kb) \\
&= [\kappa(Kb)^2 - (k_z b)^2]V_{n+1}(Kb) - \kappa n(Kb)V_n(Kb) \\
M_{87} &= in(k_z b)U_n(Kb) \\
M_{88} &= in(k_z b)V_n(Kb)
\end{aligned} \tag{4.41}$$

5

Approximate Partial Wave Series Solution to the Scattering of a Plane Wave by a Finite Elastic Cylindrical Shell at Oblique Incidence

5.1 Introduction

In studying the scattering of sound from complex elastic objects it is of the foremost importance to thoroughly understand scattering from simpler objects. Great focus has been placed, therefore, on studying the "canonical" shapes of the elastic sphere and infinite cylinder, for which analytical solutions may be found within the framework of linearized elasticity (i.e. wave equations). These solutions are typically in the form of infinite series

solutions [commonly called partial wave series solutions (PWS)] and can be quite complicated depending on the exact geometry and material under consideration. For example the infinite series solution for a transversely isotropic cylinder[71] is considerably more weighty than for a solid cylinder, even though the method of solution is similar. To the best of the author's knowledge the following persons were responsible for the first publication of comprehensive "exact" solutions to the following problems: solid sphere, Faran, Ref. [72]; spherical shell, Goodman and Stern, Ref. [73]; infinite solid cylinder at normal incidence, Faran, Ref. [72]; infinite cylindrical shell at normal incidence, Doolittle and Überall, Ref. [74]; infinite solid cylinder at oblique incidence, Flax, *et al*, Ref. [52]; and, infinite cylindrical shell at oblique incidence, Léon, *et al*, Ref. [14] (earlier results were published by Veksler, *et al*, Ref. [25] but did not include the comprehensive solution). Exact solutions exist for these shapes primarily because: 1) all the boundaries of each object can be described by holding one or more coordinates fixed (and the wave equation is separable in the defined coordinate system), and 2) the boundary conditions required at the object boundaries uniquely specify a solution and do not over-determine the problem. When it is not possible to write a series solution one must often resort to approximate methods.

The case considered here, of a finite elastic cylinder or shell, presents a considerably more difficult problem than the infinite cylinder. In this case the wave equation is of course separable in cylindrical coordinates. The difficulty arises in specifying boundary conditions at the cylinder ends simultaneously with those on the surface of the cylinder. The infinite cylinder problem is well defined, but the additional boundary conditions for the ends of the finite cylinder seem to over-determine the problem. According to Lur'e[75], "not a single solution is known which satisfies completely and rigorously all the boundary conditions on the side surface and on the ends of a cylinder." One must then resort to numerical methods, such as finite difference time domain, finite element or transition matrix (T-matrix) calculations, or to approximate analytical methods. The approach presented here is associated with the latter. The frequency range investigated in the previous chapters is high enough that global resonances of the finite cylinder are not important for the enhancements studied. These frequencies are, however, high enough to

present significant difficulties to numerical approaches where the spatial discretization of field quantities must be on the order of many points per wavelength. The analytical approach presented here is based on a partial wave series (PWS) solution, like the canonical solutions mentioned above. These solutions are known to be efficient to implement numerically over the frequencies of interest here. At much higher frequencies, however, this approach becomes numerically inefficient.

The solution presented here was originally worked out by Greg Kaduchak, but was first published in a combined paper with the present author (Ref. [8], Chapter 2) and Philip L. Marston. It can be thought of as an extension of the work presented by Muzychenko (Ref. [17]) and somewhat by Tran-Van-Nhieu (Ref. [15]). (Also relevant to this discussion is a paper by Ye (Ref. [76]) for a finite fluid cylinder.) In those papers the behavior of a finite cylindrical shell is modeled by a section of a corresponding infinite shell with appropriate periodic axial constraints. The resulting modal behavior is composed of the normal infinite shell solution with a Fourier sum axial dependence. The scattering effect of this section of the shell is then evaluated in the far-field. Both of these published solutions assume that the mechanics of the shell can be modeled with thin shell theories. Because of the range of frequencies and thicknesses investigated presently, thin shell mechanics is not sufficient and full 3-D elasticity must be incorporated. This chapter presents the derivation of the finite cylindrical shell solution using the approach of Ref. [17] but incorporating full 3-D elasticity.

5.2 Kirchhoff Diffraction Integral Solution

A finite scatterer bounded by the surface S is placed within the closed volume V having the surface S_V. The displacement potential anywhere in the region exterior to the surface S and inside the volume V can be written in the following form, known as the scalar Kirchhoff integral[45,77]:

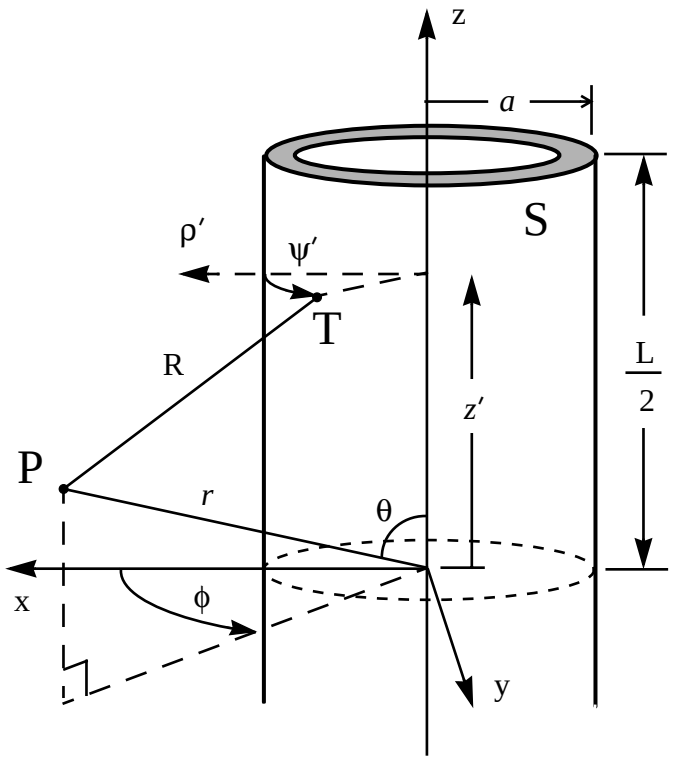

FIG. 5.1 Scattering geometry used in the approximate analysis. Defined with respect to the origin at the center of the cylinder, a point T on the surface is defined by the cylindrical coordinates ($\rho' = a$, ψ', z'); the observation point P is defined by the spherical coordinates (r, θ, ϕ). The surface S is the outer surface of the cylinder at $r = a$ and includes the end surfaces at $z' = +/- L/2$. (In the derivation that follows the contribution to Eq. (5.1) from the end surfaces is left out.)

$$\Phi(\boldsymbol{x}) = \frac{-1}{4\pi}\int_{S_V+S}\frac{e^{ikR}}{R}\hat{\boldsymbol{n}}'\cdot\left[\nabla'\Phi(x') + ik\left(1+\frac{i}{kR}\right)\frac{\boldsymbol{R}}{R}\Phi(x')\right]dS' \tag{5.1}$$

where $\boldsymbol{R} = (\boldsymbol{x} - \boldsymbol{x}')$, $R = |\boldsymbol{R}|$ and $\boldsymbol{x}$ and $\boldsymbol{x}'$ are locations in the volume V (field point) and on the surface S (source point) respectively. For the finite cylinder geometry Fig. 5.1 defines the coordinates and the surface S used in the evaluation of Eq. (5.1).

The surface S_V is taken to be at infinity. Assuming the radiation condition at infinity is satisfied the contribution to Eq. (5.1) from S_V vanishes. The scattered field is then

determined solely with the knowledge of the displacement potential and its normal derivative on the surface S.

The source-to-field point distance (T - P) can be written

$$\begin{aligned} R &= [(r\sin\theta\cos\phi - a\cos\psi')^2 + (r\sin\theta\sin\phi - a\sin\psi')^2 + (r\cos\theta - z')^2]^{1/2} \\ &= r\left[1 + \frac{a^2}{r^2} + \frac{z'^2}{r^2} - \frac{2}{r}(a\sin\theta\cos(\psi' - \phi) + z'\cos\theta)\right]^{1/2} \end{aligned} \tag{5.2}$$

and the vector relationship $\hat{\boldsymbol{n}}' \cdot \boldsymbol{R}$ is

$$\hat{\boldsymbol{n}}' \cdot \boldsymbol{R} = r\left(\sin\theta\cos(\psi' - \phi) - \frac{a}{r}\right). \tag{5.3}$$

In the far field, where $a/r \ll 1$ and $z'/r \ll 1$, the Fraunhofer approximation may be used. Taking $R \cong r - (\boldsymbol{x} \cdot \boldsymbol{x}')$ in the exponential and $R \cong r$ in the denominator, while keeping only lowest order terms in $(1/r)$, Eq. (5.1) becomes,

$$\Phi_{scatt}(\boldsymbol{x}) \cong \frac{-1}{4\pi}\frac{e^{ikr}}{r}\int_S e^{-ik(\hat{\boldsymbol{x}} \cdot \boldsymbol{x}')}[\hat{\boldsymbol{n}}' \cdot \nabla'\Phi(x') + ik(\hat{\boldsymbol{n}}' \cdot \boldsymbol{x})\Phi(x')]dS'. \tag{5.4}$$

Substituting

$$\hat{\boldsymbol{n}}' \cdot \boldsymbol{x} = r\sin\theta\cos(\psi' - \phi) \tag{5.5}$$

and

$$\hat{\boldsymbol{x}} \cdot \boldsymbol{x}' = a\sin\theta\cos(\psi' - \phi) + z'\cos\theta \tag{5.6}$$

into Eq. (5.4) gives the integral relation for the scattered pressure in the far field:

$$\begin{aligned} P_s(r, \theta, \phi) &\cong \frac{-1}{4\pi}\frac{e^{ikr}}{r}[\mathrm{I_I} + \mathrm{I_{II}}] \\ \mathrm{I_I} &= \int_S e^{-ik(a\sin\theta\cos(\psi' - \phi) + z'\cos\theta)}\left[\frac{\partial}{\partial\rho'}(-\rho_1\omega^2\Phi(x'))\right]ad\psi'dz' \\ \mathrm{I_{II}} &= \int_S e^{-ik(a\sin\theta\cos(\psi' - \phi) + z'\cos\theta)}[ik\sin\theta\cos(\psi' - \phi)(-\rho_1\omega^2\Phi(x'))]ad\psi'dz'. \end{aligned} \tag{5.7}$$

The familiar relation for time harmonic fields,

$$P = -\rho\omega^2\Phi \tag{5.8}$$

has been used.

It remains, then, to find a suitable expression for the displacement potential on the surface of the finite cylinder. In the next section the solution to the infinite cylindrical shell problem is derived when the axial eigenfunctions are those corresponding to a periodic quasi "simply supported" cylinder. The displacement potential found from this analysis will then be inserted into Eq. (5.7) above to find the approximate far field scattered pressure.

5.3 Solution of the Infinite Shell Problem in Terms of Periodic "Simply Supported" Axial Eigenfunctions

Consider a plane wave travelling in the $+x$ and $+z$ direction at an angle γ and incident on an infinite cylindrical shell having an outer radius a and inner radius b. The shell is an isotropic, linear elastic material (medium 2) and is surrounded by an ideal fluid (medium 1). The shell is also filled with another ideal fluid (medium 3). Figure 5.2 shows the scattering geometry and coordinate axes. The shell is quasi "simply supported" at regular intervals of length L. The incident pressure is given by

$$\begin{aligned} P_i &= P_o e^{i[(k_{xi}x + k_{zi}z) - \omega t]} \\ P_i &= P_o e^{i(k_{zi}z - \omega t)} \sum_{n=0}^{\infty} i^n \varepsilon_n J_n(k_{\perp i}\rho)\cos(n\psi) \end{aligned} \tag{5.9}$$

where $k_{zi} = k\sin\gamma$, $k_{xi} = k_{\perp i} = k\cos\gamma$ and $k = \omega/c_1$ (ω is the angular frequency and c_1 is the speed of sound in the outer fluid). In anticipation of the form of the axial eigenfunctions describing motion on the shell we expand the z-dependence of the incident

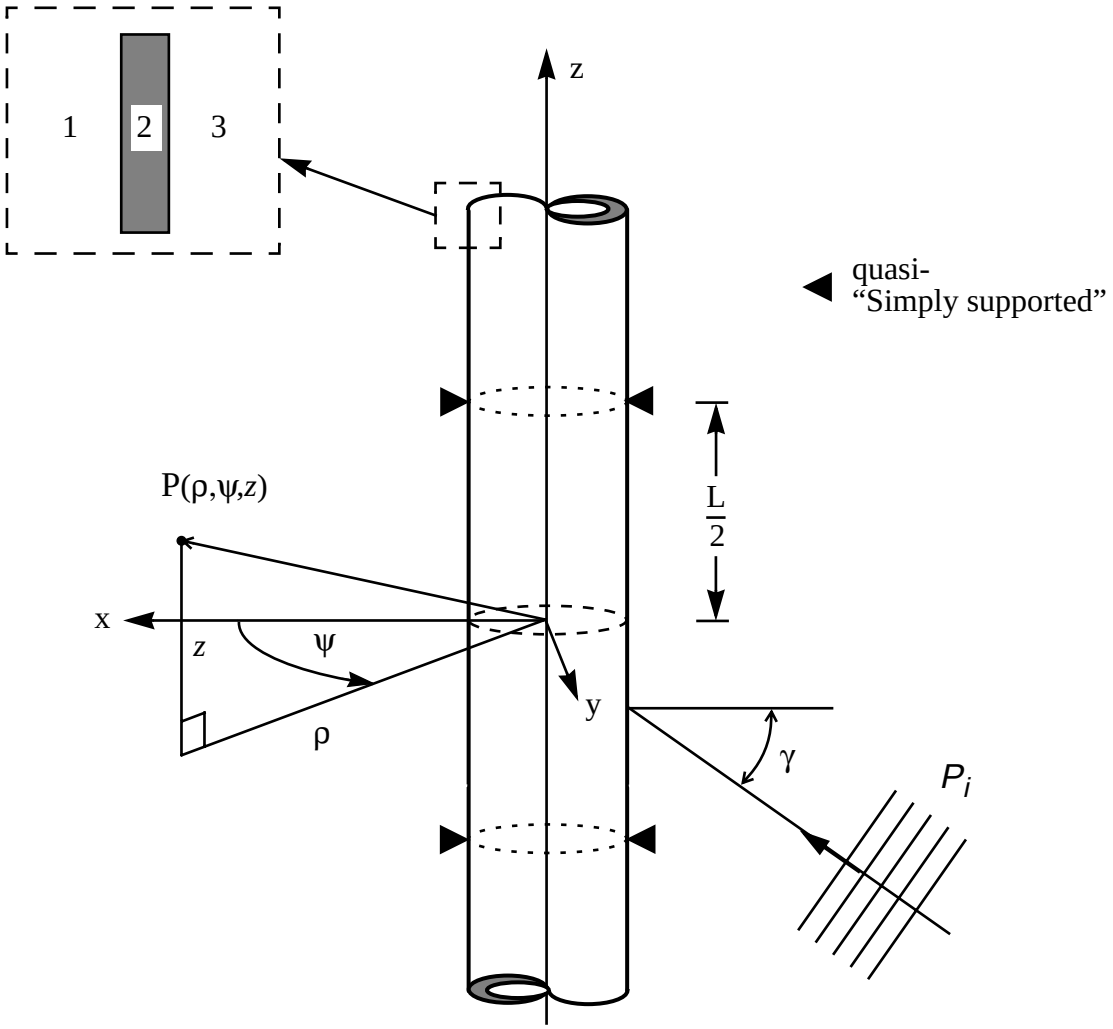

FIG. 5.2 Scattering geometry for the infinite cylindrical shell. The shell is quasi "simply supported" at periodic intervals of L. A plane wave is incident at an angle γ and the scattered pressure is desired at the location (ρ,ψ,z) described in terms of cylindrical coordinates.

plane wave in eigenfunctions corresponding to periodic quasi "simply supported" conditions by

$$e^{ik_{zi}z} = \sum_{p=1}^{\infty} \beta_p \sin\left[k_{zp}\left(z+\frac{L}{2}\right)\right], \qquad k_{zp} = \frac{p\pi}{L}$$
$$\beta_p = i^{(p-1)}\left\{\frac{\sin\left[(k_{zi}+k_{zp})\frac{L}{2}\right]}{(k_{zi}+k_{zp})\frac{L}{2}} - (-1)^p \frac{\sin\left[(k_{zi}-k_{zp})\frac{L}{2}\right]}{(k_{zi}-k_{zp})\frac{L}{2}}\right\}. \tag{5.10}$$

This can easily be shown by noting the following orthogonality condition,

$$\int_0^{\pi} \sin(pu)\sin(su)du = \frac{\pi}{2}\delta_{ps}. \tag{5.11}$$

This form of the axial dependence leads to simply supported end conditions in the thin shell case[10,15,78]. The rigorousness of the "simply supported" definition for the thick shell case has not been presently investigated and therefore the end boundary conditions used presently are referred to as quasi "simply supported" to denote the similarity to the thin shell case. The incident pressure now takes the following form:

$$P_i = P_o e^{i\omega t} \sum_{n=0}^{\infty}\sum_{p=1}^{\infty} \varepsilon_n i^n \beta_p J_n(k_{\perp i}\rho)\cos(n\psi)\sin\left[k_{zp}\left(z+\frac{L}{2}\right)\right] \quad . \tag{5.12}$$

The displacement amplitudes in each region are derived from scalar (Φ) and vector ($\boldsymbol{A}$) displacement potentials, corresponding to irrotational and equivoluminal motion, respectively, with the following convention

$$\begin{aligned} \boldsymbol{U} &= \boldsymbol{U}_L + \boldsymbol{U}_S \\ \boldsymbol{U}_L = \nabla\Phi \qquad & \boldsymbol{U}_S = \nabla\times\boldsymbol{A} \\ \nabla\times\boldsymbol{U}_L = 0 \qquad & \nabla\bullet\boldsymbol{U}_S = 0 \end{aligned} \tag{5.13}$$

Explicitly the displacements are

$$
\begin{aligned}
u_\rho &= \frac{\partial \Phi}{\partial \rho} + \left(\frac{1}{\rho} \frac{\partial A_z}{\partial \psi} - \frac{\partial A_\psi}{\partial z} \right) \\
u_\psi &= \frac{1}{\rho} \frac{\partial \Phi}{\partial \psi} + \left(\frac{\partial A_\rho}{\partial z} - \frac{\partial A_z}{\partial \rho} \right) \\
u_z &= \frac{\partial \Phi}{\partial z} + \left(\frac{1}{\rho} \frac{\partial}{\partial \rho} (\rho A_\psi) - \frac{1}{\rho} \frac{\partial A_\rho}{\partial \psi} \right).
\end{aligned}
\tag{5.14}
$$

The equations of motion for the potentials are the uncoupled wave equations

$$
\begin{aligned}
\nabla^2 \Phi - \frac{1}{c_L^2} \frac{\partial^2 \Phi}{\partial t^2} &= 0 \\
\nabla^2 \boldsymbol{A} - \frac{1}{c_S^2} \frac{\partial^2 \boldsymbol{A}}{\partial t^2} &= 0
\end{aligned}
\tag{5.15}
$$

where in cylindrical coordinates,

$$
\nabla^2 = \frac{\partial^2}{\partial \rho^2} + \frac{1}{\rho} \frac{\partial}{\partial \rho} + \frac{1}{\rho^2} \frac{\partial^2}{\partial \psi^2} + \frac{\partial^2}{\partial z^2}
\tag{5.16}
$$

and

$$
\nabla^2 \boldsymbol{A} = \hat{\boldsymbol{e}}_\rho \left(\nabla^2 A_\rho - \frac{A_\rho}{\rho^2} - \frac{2}{\rho^2} \frac{\partial A_\psi}{\partial \psi} \right) + \hat{\boldsymbol{e}}_\psi \left(\nabla^2 A_\psi - \frac{A_\psi}{\rho^2} + \frac{2}{\rho^2} \frac{\partial A_\rho}{\partial \psi} \right) + \hat{\boldsymbol{e}}_z (\nabla^2 A_z) \, .
\tag{5.17}
$$

The subscript notation referring to the shell (medium 2) in the sound speeds is disregarded where the elastic terms L and S are now used to refer to longitudinal (dilatational) and shear (transverse) wave speeds, respectively. Equations (5.15) constitute 6 equations for the 6 unknown potentials, $(\Phi^{(1)}, \Phi^{(2)}, \Phi^{(3)})$ and (A_ρ, A_ψ, A_z), in the three regions. (Since an ideal fluid cannot sustain shear motion its displacement is completely described by a scalar potential; thus, there are only the three components of the vector potential in the shell that are unknown and the superscript (2) is dropped for convenience.) In the coordinate system chosen the wave equation, Eqs. (5.15), are separable. The general solution can be written as a product of the solutions for each coordinate variable. The solutions take the following

general form

$$\begin{aligned}
\rho\text{:} \quad & \begin{Bmatrix} J_{n,n+1} & N_{n,n+1} \\ I_{n,n+1} & K_{n,n+1} \\ & H_n^{(1)} \end{Bmatrix} \\
\psi\text{:} \quad & \begin{Bmatrix} \sin n\psi \\ \cos n\psi \end{Bmatrix} \\
z\text{:} \quad & \sin[k_{zp}(z + L/2)]
\end{aligned} \tag{5.18}$$

where J_n, N_n, I_n, K_n, $H_n^{(1)}$ are Bessel functions of integer order n and real argument. With the scattering geometry in mind the general solutions of these equations of motion in the three regions can be reduced to

$$\begin{aligned}
\Phi^{(1)} &= \frac{-1}{\rho_1\omega^2}\sum_{n=0}^{\infty}\sum_{p=1}^{\infty}\varepsilon_n i^n\left[\beta_p J_n(k_{\perp i}\rho) + g_{n,p}\begin{Bmatrix} H_n^{(1)}(h_{1p}\rho) \\ K_n(h_{1p}\rho) \end{Bmatrix}\right]\cos(n\psi) \\
&\quad \times \sin[k_{zp}(z + L/2)] \\
\Phi^{(2)} &= \frac{1}{\rho_2\omega^2}\sum_{n=0}^{\infty}\sum_{p=1}^{\infty}\varepsilon_n i^n\left[a_{n,p}\begin{Bmatrix} J_n(h_p\rho) \\ I_n(h_p\rho) \end{Bmatrix} + b_{n,p}\begin{Bmatrix} N_n(h_p\rho) \\ K_n(h_p\rho) \end{Bmatrix}\right]\cos(n\psi) \\
&\quad \times \sin[k_{zp}(z + L/2)] \\
A_\rho &= \frac{1}{\rho_2\omega^2}\sum_{n=0}^{\infty}\sum_{p=1}^{\infty}\varepsilon_n i^n\left[c_{n,p}\begin{Bmatrix} J_{n+1}(K_p\rho) \\ I_{n+1}(K_p\rho) \end{Bmatrix} + d_{n,p}\begin{Bmatrix} N_{n+1}(K_p\rho) \\ K_{n+1}(K_p\rho) \end{Bmatrix}\right]\sin(n\psi) \\
&\quad \times \cos[k_{zp}(z + L/2)] \\
A_\psi &= \frac{1}{\rho_2\omega^2}\sum_{n=0}^{\infty}\sum_{p=1}^{\infty}\varepsilon_n i^n\left[-c_{n,p}\begin{Bmatrix} J_{n+1}(K_p\rho) \\ I_{n+1}(K_p\rho) \end{Bmatrix} - d_{n,p}\begin{Bmatrix} N_{n+1}(K_p\rho) \\ K_{n+1}(K_p\rho) \end{Bmatrix}\right]\cos(n\psi) \\
&\quad \times \cos[k_{zp}(z + L/2)] \\
A_z &= \frac{1}{\rho_2\omega^2}\sum_{n=0}^{\infty}\sum_{p=1}^{\infty}\varepsilon_n i^n\left[e_{n,p}\begin{Bmatrix} J_n(K_p\rho) \\ I_n(K_p\rho) \end{Bmatrix} + f_{n,p}\begin{Bmatrix} N_n(K_p\rho) \\ K_n(K_p\rho) \end{Bmatrix}\right]\sin(n\psi) \\
&\quad \times \sin[k_{zp}(z + L/2)] \\
\Phi^{(3)} &= \frac{-1}{\rho_3\omega^2}\sum_{n=0}^{\infty}\sum_{p=1}^{\infty}\varepsilon_n i^n q_{n,p}\begin{Bmatrix} J_n(h_{3p}\rho) \\ I_n(h_{3p}\rho) \end{Bmatrix}\cos(n\psi)\sin[k_{zp}(z + L/2)]
\end{aligned} \tag{5.19}$$

where

$$
\begin{aligned}
h_{1p} &= \sqrt{\pm\left(\frac{\omega^2}{c_1^2} - k_{zp}^2\right)} \\
k_{\perp i} &= \sqrt{\left(\frac{\omega^2}{c_1^2} - k_{zi}^2\right)} = k\sqrt{(1 - \sin^2\gamma)} \\
h_p &= \sqrt{\pm\left(\frac{\omega^2}{c_L^2} - k_{zp}^2\right)} \\
K_p &= \sqrt{\pm\left(\frac{\omega^2}{c_S^2} - k_{zp}^2\right)} \\
h_{3p} &= \sqrt{\pm\left(\frac{\omega^2}{c_3^2} - k_{zp}^2\right)}.
\end{aligned}
\tag{5.20}
$$

The upper functions in Eqs. (5.19) correspond to the plus signs in Eqs. (5.20) while the lower functions correspond to the minus signs. These correspond to solutions of Eqs. (5.15) when the respective wavevectors are real or imaginary, respectively. Two things are important to mention at this point about the form of the solutions in Eqs. (5.19). The first is the order of the Bessel functions in A_ρ and A_ψ. These possess order n+1 while the remaining potentials have order n. This is a result of the specific form of the differential equation for these two components of the vector potential. It stems from the added terms present in the vector relationship Eq. (5.17) for $\hat{\boldsymbol{e}}_\rho$ and $\hat{\boldsymbol{e}}_\psi$ in comparison with $\hat{\boldsymbol{e}}_z$. The second thing to clarify concerning Eqs. (5.19) is the choice of expansion coefficients in the expression for A_ψ. One may notice that the coefficients of A_ρ and A_ψ are the same, i.e. $c_{n,p}$ and $d_{n,p}$. This is a result of the fact that Eq. (5.13) is invariant under a transformation of gauge (i.e. the displacement field displays gauge invariance); i.e. the vector displacement $\boldsymbol{U}$ remains unchanged under the transformation

$$\boldsymbol{A} \rightarrow \boldsymbol{A} + \nabla a \tag{5.21}$$

where a is a completely arbitrary scalar function. Choosing the gauge $\nabla \bullet \boldsymbol{A} = 0$ enables the 3 components of the vector potential to be reduced to 2 independent components. A clear example of this process can be seen in Ref. [57]. Gazis states in this paper that

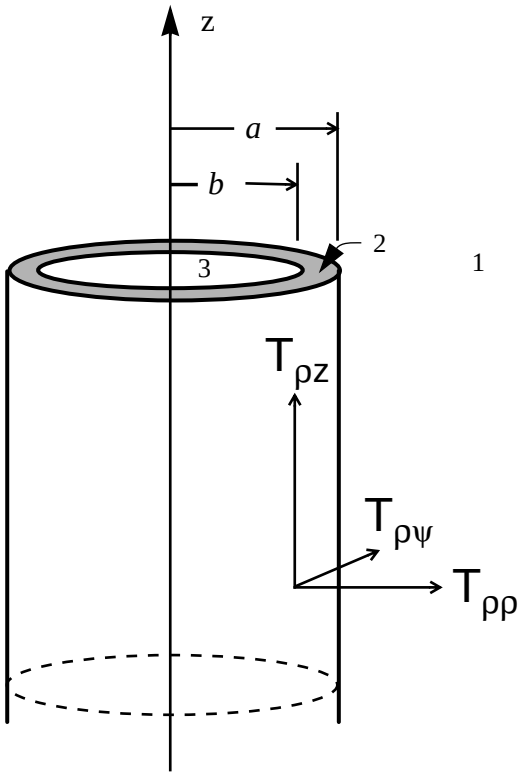

FIG. 5.3 Stress components used in the boundary conditions. $T_{\rho z}$ and $T_{\rho\psi}$ are tangential stresses which must vanish at the interfaces with the fluids. $T_{\rho\rho}$ is the radial stress which, along with the radial displacements, must be continuous at these interfaces.

"physically, this implies that the displacement field corresponding to an equivoluminal potential [A_ρ, A_ψ or A_z] . . . can also be derived by a combination of the other two equivoluminal potentials."

The reduced general solutions, Eqs. (5.19), must satisfy the boundary conditions on the shell. Figure 5.3 shows pictorially the nature of the stresses on the shell. The tangential stress must vanish on each surface,

$$\begin{aligned} T^{(2)}_{\rho z}\big|_{\rho = a} &= 0 \qquad T^{(2)}_{\rho\psi}\big|_{\rho = a} = 0 \\ T^{(2)}_{\rho z}\big|_{\rho = b} &= 0 \qquad T^{(2)}_{\rho\psi}\big|_{\rho = b} = 0 \end{aligned} \tag{5.22}$$

and there must be continuity of normal stress,

$$\begin{aligned} [\mathrm{T}_{\rho\rho}^{(1)} - \mathrm{T}_{\rho\rho}^{(2)}]\Big|_{\rho = a} &= 0 \\ [\mathrm{T}_{\rho\rho}^{(2)} - \mathrm{T}_{\rho\rho}^{(3)}]\Big|_{\rho = b} &= 0 \end{aligned} \tag{5.23}$$

as well as radial displacement

$$\begin{aligned} [u_{\rho}^{(1)} - u_{\rho}^{(2)}]\Big|_{\rho = a} &= 0 \\ [u_{\rho}^{(2)} - u_{\rho}^{(3)}]\Big|_{\rho = b} &= 0. \end{aligned} \tag{5.24}$$

Equations (5.22) - (5.24) represent 8 equations which allow the unique determination of the 8 unknown constants in Eqs. (5.19): $g_{n,p}$, $q_{n,p}$, $a_{n,p}$, $b_{n,p}$, $c_{n,p}$, $d_{n,p}$, $e_{n,p}$ and $f_{n,p}$. To evaluate these we need expressions for the stresses in terms of the displacement potentials. This is afforded by the tensor form of Hooke's Law (summation convention is used),

$$\mathrm{T}_{ij} = \lambda \mathrm{E}_{kk}\delta_{ij} + 2\mu \mathrm{E}_{ij} \tag{5.25}$$

and the strain tensor,

$$\underline{\mathbf{E}} = \frac{1}{2}(\boldsymbol{U}\nabla + \nabla\boldsymbol{U}). \tag{5.26}$$

Explicitly, in cylindrical coordinates, Eq. (5.26) is

$$\begin{aligned} \mathrm{E}_{\rho\rho} &= \frac{\partial u_{\rho}}{\partial \rho} \qquad \mathrm{E}_{\rho\psi} = \frac{1}{2}\left(\frac{1}{\rho}\frac{\partial u_{\rho}}{\partial \psi} + \frac{\partial u_{\psi}}{\partial \rho} - \frac{u_{\psi}}{\rho}\right) \qquad \mathrm{E}_{\rho z} = \frac{1}{2}\left(\frac{\partial u_z}{\partial \rho} + \frac{\partial u_{\rho}}{\partial z}\right) \\ \mathrm{E}_{\psi\psi} &= \frac{1}{\rho}\frac{\partial u_{\psi}}{\partial \psi} + \frac{u_{\rho}}{\rho} \qquad \mathrm{E}_{\psi z} = \frac{1}{2}\left(\frac{\partial u_{\psi}}{\partial z} + \frac{1}{\rho}\frac{\partial u_z}{\partial \psi}\right) \qquad \mathrm{E}_{zz} = \frac{\partial u_z}{\partial z} \end{aligned} \tag{5.27}$$

and Eq. (5.25) is

$$
\begin{aligned}
T_{\rho\rho} &= \lambda(E_{\rho\rho} + E_{\psi\psi} + E_{zz}) + 2\mu E_{\rho\rho} = (\lambda + 2\mu)\frac{\partial u_\rho}{\partial \rho} + \lambda\left(\frac{1}{\rho}\frac{\partial u_\psi}{\partial \psi} + \frac{u_\rho}{\rho} + \frac{\partial u_z}{\partial z}\right) \\
T_{\rho\psi} &= 2\mu E_{\rho\psi} = \mu\left(\frac{1}{\rho}\frac{\partial u_\rho}{\partial \psi} + \frac{\partial u_\psi}{\partial \rho} - \frac{u_\psi}{\rho}\right) \\
T_{\rho z} &= 2\mu E_{\rho z} = \mu\left(\frac{\partial u_z}{\partial \rho} + \frac{\partial u_\rho}{\partial z}\right) \\
T_{\psi\psi} &= \lambda(E_{\rho\rho} + E_{\psi\psi} + E_{zz}) + 2\mu E_{\psi\psi} = (\lambda + 2\mu)\left(\frac{1}{\rho}\frac{\partial u_\psi}{\partial \psi} + \frac{u_\rho}{\rho}\right) + \lambda\left(\frac{\partial u_\rho}{\partial \rho} + \frac{\partial u_z}{\partial z}\right) \\
T_{\psi z} &= 2\mu E_{\psi z} = \mu\left(\frac{\partial u_\psi}{\partial z} + \frac{1}{\rho}\frac{\partial u_z}{\partial \psi}\right) \\
T_{zz} &= \lambda(E_{\rho\rho} + E_{\psi\psi} + E_{zz}) + 2\mu E_{zz} = (\lambda + 2\mu)\left(\frac{\partial u_z}{\partial z}\right) + \lambda\left(\frac{\partial u_\rho}{\partial \rho} + \frac{1}{\rho}\frac{\partial u_\psi}{\partial \psi} + \frac{u_\rho}{\rho}\right).
\end{aligned}
\tag{5.28}
$$

At this point it is instructive to note the z-dependence of the above stresses as they relate to the boundary conditions at the "ends" of the cylinder at $z = \pm L/2$ for the assumed general solutions in Eqs. (5.19). Substituting Eqs. (5.19) into Eqs. (5.14) and then into Eqs. (5.28) above one finds that in the elastic material (region 2) $u_\rho^{(2)}$, $u_\psi^{(2)}$, $T_{\rho\rho}^{(2)}$, $T_{\rho\psi}^{(2)}$, $T_{\psi\psi}^{(2)}$, $T_{zz}^{(2)}$ all have a $\sin[k_{zp}(z + L/2)]$ z-dependence while $u_z^{(2)}$, $T_{\rho z}^{(2)}$, $T_{\psi z}^{(2)}$ have a $\cos[k_{zp}(z + L/2)]$ z-dependence. Therefore since $k_{zp} = p\pi/L$ the displacements $u_\rho^{(2)}$ and $u_\psi^{(2)}$ and the stresses $T_{\rho\rho}^{(2)}$, $T_{\rho\psi}^{(2)}$, $T_{\psi\psi}^{(2)}$ and $T_{zz}^{(2)}$ vanish at all points on the "ends" of the shell (i.e. for $b \le \rho \le a$) at $z = \pm L/2$. The displacement $u_z^{(2)}$ and the stresses $T_{\rho z}^{(2)}$, $T_{\psi z}^{(2)}$ need not vanish at the "ends". Note also that in the fluid interior $T_{zz}^{(3)}$ has a $\sin[k_{zp}(z + L/2)]$ z-dependence and also vanishes at the "ends". This has the consequence that in the interior fluid the "ends" are in effect pressure release boundaries and no energy is transmitted through the "open" end of the "finite" cylinder. Most often in the present work it is assumed that the interior is a vacuum and therefore this boundary condition on the interior fluid is unimportant; however, in Chapter 7 experiments are performed for water-filled shells (without endcaps) and the results compared with the approximate PWS solution developed here. In this case it must be understood that the present solution may include significant reflections of sound from the "ends" which would not be present in the experiments.

Upon substitution of the reduced general solutions, Eqs. (5.19), into Eqs. (5.14) and Eqs. (5.28), and then in the boundary conditions, Eqs. (5.22) - Eqs. (5.24), one obtains the set of linear equations $\boldsymbol{M} \cdot \boldsymbol{A} = \boldsymbol{C}$ where $\boldsymbol{M}$ is an 8 x 8 matrix and $\boldsymbol{A}$ and $\boldsymbol{C}$ are 8 element column vectors. The matrix elements are listed in Section 5.A. For numerical implementation an alternate form is also given which does not explicitly include derivatives of Bessel functions. The second expression for each matrix element (where present) is a simplified version of the first which has been rewritten using the appropriate recursion relation for each Bessel function to remove derivatives with respect to the argument. These recursion relations are

$$\begin{aligned} xZ_n' &= nZ_n - xZ_{n+1} \qquad Z_n \to J_n, N_n, K_n \\ xI_n' &= nI_n + xI_{n+1} \\ xZ_n' &= -nZ_n + xZ_{n-1} \qquad Z_n \to J_n, N_n, I_n \\ xK_n' &= -nK_n - xK_{n-1}. \end{aligned} \tag{5.29}$$

The following convention is used:

	$k_{zp}^2 < \frac{\omega^2}{c_L^2}$	$\frac{\omega^2}{c_L^2} < k_{zp}^2 < \frac{\omega^2}{c_S^2}$	$\frac{\omega^2}{c_S^2} < k_{zp}^2$
$h_p =$	$\sqrt{\omega^2/c_L^2 - k_{zp}^2}$	$\sqrt{k_{zp}^2 - \omega^2/c_L^2}$	$\sqrt{k_{zp}^2 - \omega^2/c_L^2}$
$K_p =$	$\sqrt{\omega^2/c_S^2 - k_{zp}^2}$	$\sqrt{\omega^2/c_S^2 - k_{zp}^2}$	$\sqrt{k_{zp}^2 - \omega^2/c_S^2}$
$U_n(h_p a, h_p b) =$	$J_n(h_p a, h_p b)$	$I_n(h_p a, h_p b)$	$I_n(h_p a, h_p b)$
$V_n(h_p a, h_p b) =$	$N_n(h_p a, h_p b)$	$K_n(h_p a, h_p b)$	$K_n(h_p a, h_p b)$
$U_n(K_p a, K_p b) =$	$J_n(K_p a, K_p b)$	$J_n(K_p a, K_p b)$	$I_n(K_p a, K_p b)$
$V_n(K_p a, K_p b) =$	$N_n(K_p a, K_p b)$	$N_n(K_p a, K_p b)$	$K_n(K_p a, K_p b)$
$\delta =$	1	−1	−1
$\kappa =$	1	1	−1

(5.30)

The matrices are

$$\boldsymbol{M} = \begin{bmatrix} M_{11} & 0 & M_{13} & M_{14} & M_{15} & M_{16} & M_{17} & M_{18} \\ 0 & M_{22} & M_{23} & M_{24} & M_{25} & M_{26} & M_{27} & M_{28} \\ M_{31} & 0 & M_{33} & M_{34} & M_{35} & M_{36} & M_{37} & M_{38} \\ 0 & M_{42} & M_{43} & M_{44} & M_{45} & M_{46} & M_{47} & M_{48} \\ 0 & 0 & M_{53} & M_{54} & M_{55} & M_{56} & M_{57} & M_{58} \\ 0 & 0 & M_{63} & M_{64} & M_{65} & M_{66} & M_{67} & M_{68} \\ 0 & 0 & M_{73} & M_{74} & M_{75} & M_{76} & M_{77} & M_{78} \\ 0 & 0 & M_{83} & M_{84} & M_{85} & M_{86} & M_{87} & M_{88} \end{bmatrix} \qquad \boldsymbol{A} = \begin{bmatrix} g_{n,\,p} \\ q_{n,\,p} \\ a_{n,\,p} \\ b_{n,\,p} \\ c_{n,\,p} \\ d_{n,\,p} \\ e_{n,\,p} \\ f_{n,\,p} \end{bmatrix} \tag{5.31}$$

$$\boldsymbol{C} = \frac{\rho_2}{\rho_1}\beta_p \begin{bmatrix} -(k_{\perp i}a)J_n'(k_{\perp i}a) = -[nJ_n(k_{\perp i}a) - (k_{\perp i}a)J_{n+1}(k_{\perp i}a)] \\ 0 \\ \lambda_1[(k_{\perp i}a)^2 + (k_{zp}a)^2]J_n(k_{\perp i}a) \\ 0 \\ 0 \\ 0 \\ 0 \\ 0 \end{bmatrix} \tag{5.32}$$

The elements of the matrix $\boldsymbol{M}$ can be found in Section 5.A. A solution for the expansion coefficient $g_{n,p}$, which corresponds to the scattered portion of the solution in region 1, is provided by Cramer's rule. Let $\boldsymbol{D} = \det[\boldsymbol{M}]$ and $\boldsymbol{N}_1 = \det[\boldsymbol{M}_1]$ where $\boldsymbol{M}_1$ is the matrix defined by replacing the 1st column of $\boldsymbol{M}$ with the column vector $\boldsymbol{C}$. For $\boldsymbol{D} \neq 0$ the coefficient has the unique solution $g_{n,p} = \boldsymbol{N}_1/\boldsymbol{D}$. The condition $\boldsymbol{D} = 0$ defines the normal modes of the shell, e. g. as discussed in Chapter 4, for particular values of γ, ka, n, and k_{zp}. No attempt has been made to localize these roots.

The displacement potential in the external region is now given by

$$\Phi^{(1)} = \frac{-1}{\rho_1\omega^2}\sum_{n=0}^{\infty}\sum_{p=1}^{\infty}\varepsilon_n i^n\left[\beta_p J_n(k_{\perp i}\rho) + \left(\frac{\mathbf{N}_1}{\mathbf{D}}\right)_{n,\,p}\begin{Bmatrix} H_n^{(1)}(h_{1p}\rho) \\ K_n(h_{1p}\rho) \end{Bmatrix}\right]\cos(n\psi) \times \sin[k_{zp}(z + L/2)]. \tag{5.33}$$

It now remains to show how this displacement potential is used in the Kirchhoff integral to

obtain an approximate solution for the finite cylinder.

5.4 Approximate Far Field Scattered Pressure Due to a Finite Section of the Infinite Cylinder

The scattered displacement potential derived in the previous section is now used as the source in the Kirchhoff integral; the result is an approximation of the far field scattered pressure from a finite quasi "simply supported" cylinder. Once Eq. (5.33) is inserted into the expression for the scattered pressure, Eq. (5.7), the integrals $\mathrm{I_I}$ and $\mathrm{I_{II}}$ can be evaluated in a straightforward manner. The following definition and properties of the Bessel function are necessary, however

$$\begin{aligned} J_n(z) &= \frac{1}{2\pi}\int_{\alpha}^{2\pi+\alpha} e^{i(n\theta - z\sin\theta)}d\theta \\ J_{-n}(z) &= (-1)^n J_n(z) \\ 2J_n'(z) &= J_{n-1}(z) - J_{n+1}(z). \end{aligned} \tag{5.34}$$

Here α is an arbitrary constant, n is any integer and z is an arbitrary complex number. These may be found, for example, in Ref. [80]. Upon evaluation one finds,

$$\begin{aligned} \mathrm{I_I} = \sum_{n=0}^{\infty}\sum_{p=1}^{\infty} \varepsilon_n i^n \left[\beta_p (k_{\perp i}a) J_n'(k_{\perp i}a) + \left(\frac{\mathbf{N}_1}{\mathbf{D}}\right)_{n,p} (h_{1p}a) H_n^{(1)\prime}(h_{1p}a)\right] \\ \times 2\pi(-1)^n (i)^n \cos(n\phi) J_n((ka)\sin\theta)\Gamma_p \end{aligned} \tag{5.35}$$

and

$$\begin{aligned} \mathrm{I_{II}} = i(ka)\sin\theta \sum_{n=0}^{\infty}\sum_{p=1}^{\infty} \varepsilon_n i^n \left[\beta_p J_n(k_{\perp i}a) + \left(\frac{\mathbf{N}_1}{\mathbf{D}}\right)_{n,p} H_n^{(1)}(h_{1p}a)\right] \\ \times 2\pi(-1)^{n-1} (i)^{n-1} \cos(n\phi) J_n'((ka)\sin\theta)\Gamma_p \end{aligned} \tag{5.36}$$

where

$$\Gamma_p = i^{p-1}\left\{\frac{\sin\left[(k_{zp}-k\cos\theta)\frac{L}{2}\right]}{(k_{zp}-k\cos\theta)}-(-1)^p\frac{\sin\left[(k_{zp}+k\cos\theta)\frac{L}{2}\right]}{(k_{zp}+k\cos\theta)}\right\}. \tag{5.37}$$

Combining these together and writing in terms of the complex dimensionless form function in spherical coordinates

$$P(r,\theta,\phi) = P_o\left(\frac{a}{2r}\right)f(\theta,\phi)e^{ikr} \tag{5.38}$$

gives

$$f(\theta,\phi)\cong\frac{-1}{2\pi a}[\mathrm{I_I}+\mathrm{I_{II}}] \tag{5.39}$$

or explicitly

$$\begin{aligned} f(\theta,\phi)\cong&\sum_{n=0}^{\infty}\sum_{p=1}^{\infty}\varepsilon_n\cos(n\phi)\left(\frac{\Gamma_p}{a}\right) \\ &\times\left\{-\left[\beta_p(k_{\perp i}a)J_n'(k_{\perp i}a)+\left(\frac{\mathbf{N}_1}{\mathbf{D}}\right)_{n,p}(h_{1p}a)H_n^{(1)\prime}(h_{1p}a)\right]J_n((ka)\sin\theta)\right. \\ &\left.+\left[\beta_pJ_n(k_{\perp i}a)+\left(\frac{\mathbf{N}_1}{\mathbf{D}}\right)_{n,p}H_n^{(1)}(h_{1p}a)\right](ka)\sin\theta J_n'((ka)\sin\theta)\right\}. \end{aligned} \tag{5.40}$$

In the special case of backscattering in the direction opposite the incident wavevector, $\theta = \pi/2+\gamma$ and $\phi = \pi$ giving $\Gamma_p = (L/2)\beta_p$. In this case Eq. (5.40) reduces somewhat to

$$f(\pi/2+\gamma,\pi) \cong \frac{1}{2}\sum_{n=0}^{\infty}\sum_{p=1}^{\infty}\varepsilon_n(-1)^n\left(\frac{L}{a}\right)\beta_p \tag{5.41}$$
$$\times \left\{-\left[\beta_p(k_{\perp i}a)J_n{}'(k_{\perp i}a)+\left(\frac{\mathbf{N}_1}{\mathbf{D}}\right)_{n,p}(h_{1p}a)H_n^{(1)\prime}(h_{1p}a)\right]J_n((ka)\cos\gamma)\right.$$
$$\left.+\left[\beta_p J_n(k_{\perp i}a)+\left(\frac{\mathbf{N}_1}{\mathbf{D}}\right)_{n,p}H_n^{(1)}(h_{1p}a)\right](ka)\cos\gamma J_n{}'((ka)\cos\gamma)\right\}.$$

In the numerical evaluation of Eq. (5.41) for the far field scattering shown in Figs. 2.4(a) and 2.5(a), the terms $\beta_p(k_{\perp i}a)J_n{}'(k_{\perp i}a)$, and $\beta_p J_n(k_{\perp i}a)$ in the square brackets above are not included. These represent the incident plane wave field, which was assumed to have infinite extent in both the spatial and temporal dimensions, at the observer. This "steady state" field is not present in the experiments and is therefore left out of the calculations. The final expression for the far field backscattering (monostatic) form function is:

$$f(\pi/2+\gamma,\pi) \cong \frac{1}{2}\sum_{n=0}^{\infty}\sum_{p=1}^{\infty}\varepsilon_n(-1)^n\left(\frac{L}{a}\right)\beta_p\left(\frac{\mathbf{N}_1}{\mathbf{D}}\right)_{n,p} \tag{5.42}$$
$$\times \{-(h_{1p}a)H_n^{(1)\prime}(h_{1p}a)J_n(k_{\perp i}a)+H_n^{(1)}(h_{1p}a)(k_{\perp i}a)J_n{}'(k_{\perp i}a)\}.$$

5.5 Numerical Results

To implement Eq. (5.42) numerically one must choose a truncation point of the infinite sums over n and p. The sum over the partial wave index n is chosen to be truncated at n_{max} in a similar fashion to previous PWS calculations[81]. The actual expression is

$$\begin{aligned} n_{max} &= 7 + nint[ka + 4.0(ka)^{1/3}] \qquad n < 8 \\ n_{max} &= 8 + nint[ka + 4.05(ka)^{1/3}] \qquad n \geq 8 \end{aligned}, \tag{5.43}$$

where *nint* represents the nearest integer. The accuracy of these truncation points was estimated by calculating values for $n_{max} = 3{*}n_{max}$ over a range of frequencies and angles.

For the frequency ranges shown in Figs. 2.4(a) and 2.5(a) the error, $\left|(\left|f_{3n_{max}}\right| - \left|f_{n_{max}}\right|)/\left|f_{3n_{max}}\right|\right|$, was typically less than 10^{-5}.

The truncation limit for the summation over p had to be chosen differently. Notice in Eq. (5.42) one must evaluate $H_n^{(1)\prime}(h_{1p}a)$ and $H_n^{(1)}(h_{1p}a)$ where

$$h_{1p} = \sqrt{\pm\left(\frac{\omega^2}{c_1^2} - k_{zp}^2\right)} = \sqrt{\pm\left(\frac{\omega^2}{c_1^2} - \left(\frac{p\pi}{L}\right)^2\right)}. \tag{5.44}$$

This poses a problem since when

$$p \approx \frac{L\omega}{\pi c_1} \approx \left(\frac{L}{a}\right)\frac{ka}{\pi} \tag{5.45}$$

the argument of the Hankel functions approach zero. Equation (5.42) diverges in this region and it does not appear possible to reduce it to a form which remains finite, even while taking into account the determinant relation. Note that it does not appear possible to reduce Eq. (5.42) with a Wronskian type relation since the form of the quantity in curly brackets is

$$H_n^{(1)}(x)yJ_n'(y) - xH_n^{(1)\prime}(x)J_n(y), \tag{5.46}$$

which does not appear to be related to expressions listed in standard tables. As a result of this divergent behavior, p_{max} was set to

$$p_{max} = nint\left[\left(\frac{L}{a}\right)\frac{(ka - 0.01)}{\pi}\right]. \tag{5.47}$$

This is equivalent to computing the scattering for supersonic axial wavenumbers only, i.e. $k_{zp} < k$. Note that Rumerman[10] limited his discussion to supersonic modes as well. Since we are primarily interested in high frequency scattering, where global motion of the shell is relatively unimportant, one would not expect subsonic axial modes to contribute significantly to the far-field scattered pressure. This can be thought of through the principle of reciprocity. Since it is not possible to *excite* subsonic axial modes of vibration

on an infinite cylindrical shell by an incident plane wave in the surrounding fluid, then one would not expect to *observe* radiation from subsonic axial modes.

It is important to recognize that this exclusion of subsonic axial modes is not the same as excluding subsonic waves such as the a_{0^-} (or the low frequency regions of the a_0), whose phase velocity is less than the sound speed in the surrounding fluid. One may observe in Figs. 4.16 and 4.20 that portions of the dispersion curves for this wave still have $k_z < k$. This is why limiting the evaluation of Eq. (5.42) to supersonic axial modes still includes the scattering enhancements due to the coincidence frequency enhancements of the a_{0^-} helical waves.

5.6 Examples

Figures 5.4 - 5.6 show examples of the evaluation of Eq. (5.42) for several *empty* shells, none of which corresponds to an actual shell examined in the experiments. The first figure (Fig. 5.4) shows the low frequency response of a very thin-walled shell (1% thick). This figure is an attempt to compare the present analysis with the thin-shell analysis of Rumerman[10]. The comparison is not completely accurate since Rumerman did not include enough information about the shell he used to reproduce his results. Values of cylinder length and water sound speed are estimated. Nevertheless the comparison is good and all pertinent features are reproduced. The shape of these enhancement curves (due to the s_0 and T_0 waves) is often referred to as a "chalice" presumably because of its resemblance to a chalice cup.

Figure 5.5 shows the scattering response at high frequencies for a thin-walled shell (2% thick). Since most theoretical investigations of thin-walled structures are performed at frequencies well below the coincidence frequency, where thin shell mechanics is appropriate, it is not often one sees evidence of the coincidence frequency enhancement for these cases. Figure 5.5 shows that the present method of analysis recovers the coincidence frequency effects for thin shells at high frequency. The wide area of individual enhancements stretching from broadside to about 70° is almost certainly due to the

coincidence frequency enhancement of the helical a_{0^-} waves. One may also just make out the beginning of the meridional ray enhancement of the a_0 to the right of these features. As it is presently implemented this figure represents the rough limit of reasonable calculations for our scattering code. At these frequencies floating point exceptions are common and the Bessel function routines used produce errors. It is reasonable to assume that modifications to the code could enable better accuracy at high frequencies; however, the computations are still slow on presently available computers.

Figure 5.6(a) and (b) represent two cylinders that are between those of Shell A and Shell B in thickness-to-radius ratio (b/a). Figures 2.4(a), 5.6(a), 5.6(b) and 2.5(a) show results for a progression of shell thickness of 7.6%, 10%, 12%, and 16.25%, respectively. By comparing these it is possible to observe how the shell thickness influences such things as: the location and number of the coincidence frequency a_{0^-} helical wave enhancements, the position of the a_0 meridional ray enhancement curve, and the relative amplitude of the a_0 helical wave contributions. Generally speaking as the relative thickness of the shell increases all effects shift towards lower values of ka. In addition, the amplitude of the a_0 helical waves increases and apparently the number of helical a_{0^-} waves contributing to that enhancement increases.

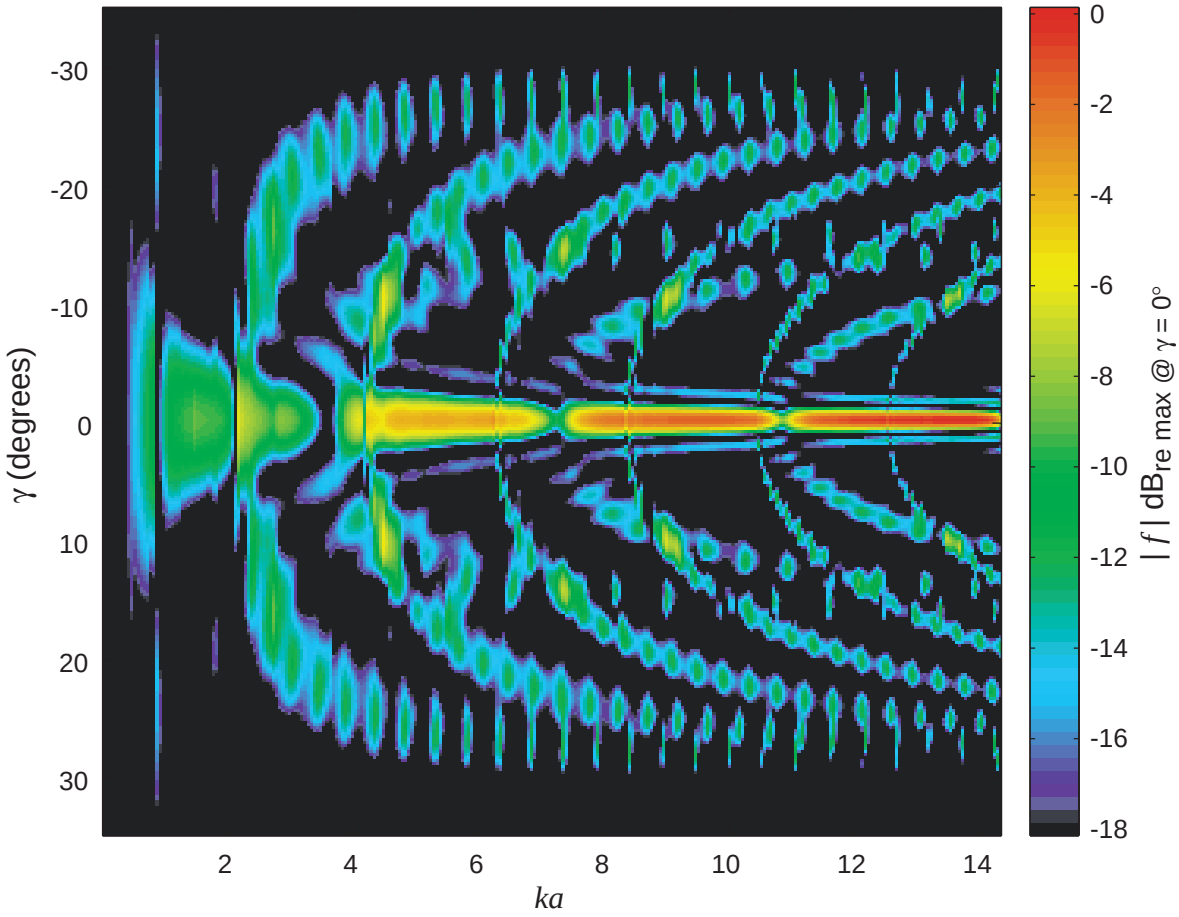

FIG. 5.4 Calculated backscattering form function for a 1% thick steel shell showing membrane wave coupling regions. This cylinder is close to that found in the paper by Rumerman, Ref. [10]. The results here compare well with the thin shell mechanics approach used in that paper. Shell and water parameters are: $c_w = 1.483$, $c_L = 5.74$, $c_s = 3.07$ (in mm/μs), $\rho = 1.0$, $\rho_e = 7.8$ (in g/cm^3), $L/a = 12$ and $b/a = 0.99$. This color raster image represents the sampling intervals: (a) $\Delta ka = 0.05$, $\Delta\gamma = 0.25°$.

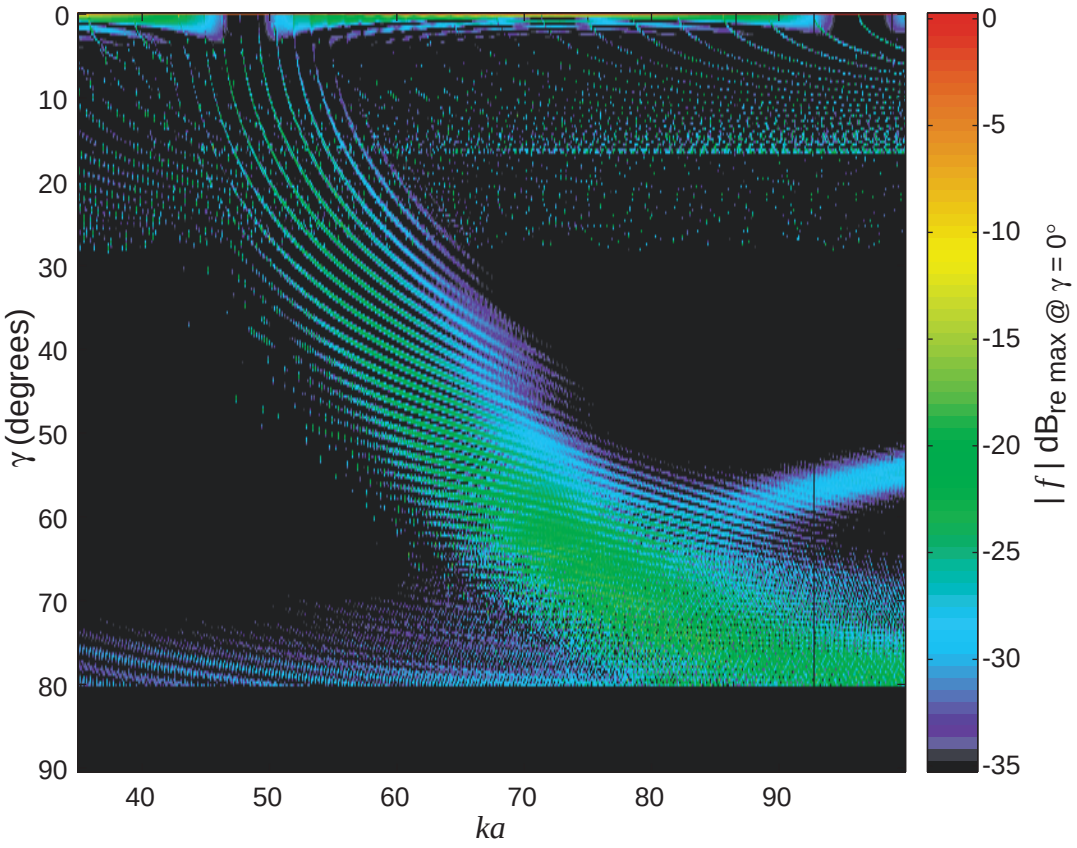

FIG. 5.5 Calculated backscattering form function for a 2% thick SS304 shell. Shell (see Table 2) and water parameters are: $c_w = 1.483$, $c_L = 5.675$, $c_s = 3.141$ (in mm/μs), $\rho = 1.0$, $\rho_e = 7.57$ (in g/cm^3), $L/a = 12$ and $b/a = 0.98$. Calculations at these high ka values are presently very slow (3 days computing time on a 300MHz Digital AlphaStation for this figure) and are prone to floating point exceptions (i.e. the vertical line at $ka = 92.6$) and errors in Bessel function routines. This color raster image represents the sampling intervals: (a) $\Delta ka = 0.1$, $\Delta\gamma = 0.3125°$.

FIG. 5.6 Calculated backscattering form function for a 10% (a) and 12% (b) thick SS304 shell. These shells are between Shell A and Shell B in thickness [i.e. compare these results with Figs. 2.4(a) and 2.5(a)]. Shell (see Table 2) and water parameters are: $c_w = 1.483$, $c_L = 5.675$, $c_s = 3.141$ (in mm/μs), $\rho = 1.0$, $\rho_e = 7.57$ (in g/cm^3), $L/a = 12$ and $b/a = 0.90$ & 0.88. These color raster images represent the sampling intervals: $\Delta ka = 0.05$, $\Delta\gamma = 0.3125°$.

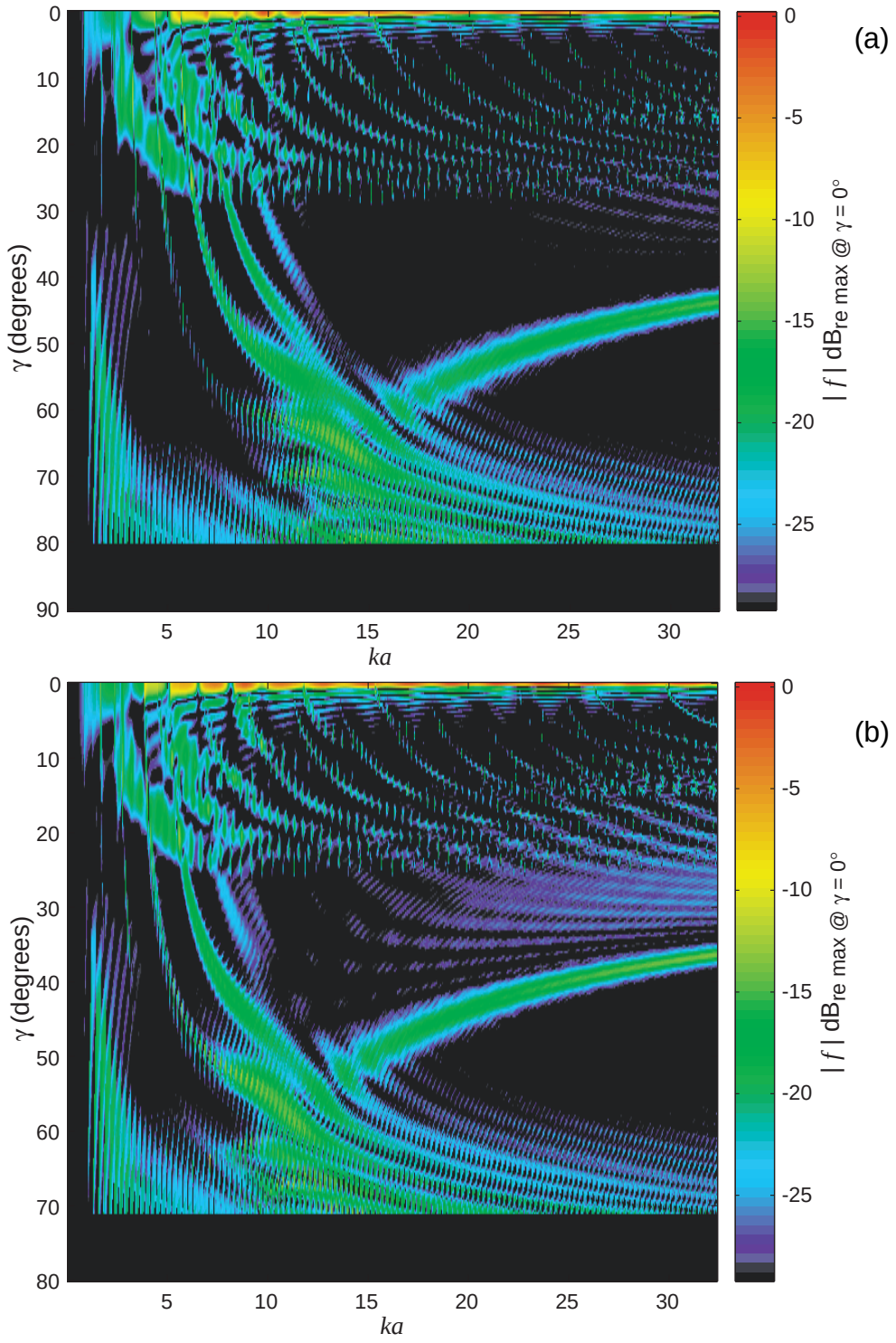
(a)
γ (degrees)
ka
| f | dBre max @ γ = 0°
0
10
20
30
40
50
60
70
80
90
5
10
15
20
25
30
-5
-10
-15
-20
-25
(b)
γ (degrees)
ka
| f | dBre max @ γ = 0°

5.A Matrix Elements

$$[u_\rho^{(1)} - u_\rho^{(2)}]\Big|_{\rho = a} = 0 : \tag{5.48}$$

$$\begin{aligned}
M_{11} &= \frac{\rho_2}{\rho_1}(h_{1p}a)\begin{Bmatrix} H_n^{(1)\prime}(h_{1p}a) \\ K_n'(h_{1p}a) \end{Bmatrix} = \frac{\rho_2}{\rho_1}\left[n\begin{Bmatrix} H_n^{(1)}(h_{1p}a) \\ K_n(h_{1p}a) \end{Bmatrix} - (h_{1p}a)\begin{Bmatrix} H_{n+1}^{(1)}(h_{1p}a) \\ K_{n+1}(h_{1p}a) \end{Bmatrix}\right] \\
M_{12} &= 0 \\
M_{13} &= (h_p a)U_n'(h_p a) = [nU_n(h_p a) - \delta(h_p a)U_{n+1}(h_p a)] \\
M_{14} &= (h_p a)V_n'(h_p a) = [nV_n(h_p a) - (h_p a)V_{n+1}(h_p a)] \\
M_{15} &= (-k_{zp}a)U_{n+1}(K_p a) \\
M_{16} &= (-k_{zp}a)V_{n+1}(K_p a) \\
M_{17} &= nU_n(K_p a) \\
M_{18} &= nV_n(K_p a)
\end{aligned} \tag{5.49}$$

$$[u_\rho^{(2)} - u_\rho^{(3)}]\Big|_{\rho = b} = 0 : \tag{5.50}$$

$$\begin{aligned}
M_{21} &= 0 \\
M_{22} &= \frac{\rho_2}{\rho_3}(h_{3p}b)\begin{Bmatrix} J_n'(h_{3p}b) \\ I_n'(h_{3p}b) \end{Bmatrix} = \frac{\rho_2}{\rho_3}\left[n\begin{Bmatrix} J_n(h_{3p}b) \\ I_n(h_{3p}b) \end{Bmatrix} - (h_{3p}b)\begin{Bmatrix} J_{n+1}(h_{3p}b) \\ -I_{n+1}(h_{3p}b) \end{Bmatrix}\right] \\
M_{23} &= (h_p b)U_n'(h_p b) = [nU_n(h_p b) - \delta(h_p b)U_{n+1}(h_p b)] \\
M_{24} &= (h_p b)V_n'(h_p b) = [nV_n(h_p b) - (h_p b)V_{n+1}(h_p b)] \\
M_{25} &= (-k_{zp}b)U_{n+1}(K_p b) \\
M_{26} &= (-k_{zp}b)V_{n+1}(K_p b) \\
M_{27} &= nU_n(K_p b) \\
M_{28} &= nV_n(K_p b)
\end{aligned} \tag{5.51}$$

$$[T_{\rho\rho}^{(1)} - T_{\rho\rho}^{(2)}]\Big|_{\rho = a} = 0 : \tag{5.52}$$

$$\begin{aligned}
M_{31} &= -\lambda_1 \frac{\rho_2}{\rho_1}\left(\frac{\omega a}{c_1}\right)^2 \begin{Bmatrix} H_n^{(1)}(h_{1p}a) \\ K_n(h_{1p}a) \end{Bmatrix} \\
M_{32} &= 0 \\
M_{33} &= 2\mu(h_p a)^2 U_n''(h_p a) - \lambda\left(\frac{\omega a}{c_L}\right)^2 U_n(h_p a) \\
&= -\lambda\left(\frac{\omega a}{c_L}\right)^2 U_n(h_p a) + 2\mu[(n^2 - \delta(h_p a)^2 - n)U_n(h_p a) + \delta(h_p a)U_{n+1}(h_p a)] \\
M_{34} &= 2\mu(h_p a)^2 V_n''(h_p a) - \lambda\left(\frac{\omega a}{c_L}\right)^2 V_n(h_p a) \\
&= -\lambda\left(\frac{\omega a}{c_L}\right)^2 V_n(h_p a) + 2\mu[(n^2 - \delta(h_p a)^2 - n)V_n(h_p a) + (h_p a)V_{n+1}(h_p a)] \\
M_{35} &= 2\mu(-k_{zp}a)(K_p a)U_{n+1}'(K_p a) \\
&= 2\mu(-k_{zp}a)[-(n+1)U_{n+1}(K_p a) + (K_p a)U_n(K_p a)] \\
M_{36} &= 2\mu(-k_{zp}a)(K_p a)V_{n+1}'(K_p a) \\
&= 2\mu(-k_{zp}a)[-(n+1)V_{n+1}(K_p a) + \kappa(K_p a)V_n(K_p a)] \\
M_{37} &= 2\mu n[(K_p a)U_n'(K_p a) - U_n(K_p a)] = 2\mu n[(n-1)U_n(K_p a) - \kappa(K_p a)U_{n+1}(K_p a)] \\
M_{38} &= 2\mu n[(K_p a)V_n'(K_p a) - V_n(K_p a)] = 2\mu n[(n-1)V_n(K_p a) - (K_p a)V_{n+1}(K_p a)]
\end{aligned} \tag{5.53}$$

$$[T_{\rho\rho}^{(2)} - T_{\rho\rho}^{(3)}]\Big|_{\rho = b} = 0 : \tag{5.54}$$

$$\begin{aligned}
M_{41} &= 0 \\
M_{42} &= -\lambda_3 \frac{\rho_2}{\rho_3}\left(\frac{\omega b}{c_3}\right)^2 \begin{Bmatrix} J_n(h_{3p}b) \\ I_n(h_{3p}b) \end{Bmatrix} \\
M_{43} &= 2\mu(h_p b)^2 U_n''(h_p b) - \lambda\left(\frac{\omega b}{c_L}\right)^2 U_n(h_p b) \\
&= -\lambda\left(\frac{\omega b}{c_L}\right)^2 U_n(h_p b) + 2\mu[(n^2 - \delta(h_p b)^2 - n)U_n(h_p b) + \delta(h_p b)U_{n+1}(h_p b)] \\
M_{44} &= 2\mu(h_p b)^2 V_n''(h_p b) - \lambda\left(\frac{\omega b}{c_L}\right)^2 V_n(h_p b) \\
&= -\lambda\left(\frac{\omega b}{c_L}\right)^2 V_n(h_p b) + 2\mu[(n^2 - \delta(h_p b)^2 - n)V_n(h_p b) + (h_p b)V_{n+1}(h_p b)] \\
M_{45} &= 2\mu(-k_{zp}b)(K_p b)U_{n+1}'(K_p b) \\
&= 2\mu(-k_{zp}b)[-(n+1)U_{n+1}(K_p b) + (K_p b)U_n(K_p b)] \\
M_{46} &= 2\mu(-k_{zp}b)(K_p b)V_{n+1}'(K_p b) \\
&= 2\mu(-k_{zp}b)[-(n+1)V_{n+1}(K_p b) + \kappa(K_p b)V_n(K_p b)] \\
M_{47} &= 2\mu n[(K_p b)U_n'(K_p b) - U_n(K_p b)] = 2\mu n[(n-1)U_n(K_p b) - \kappa(K_p b)U_{n+1}(K_p b)] \\
M_{48} &= 2\mu n[(K_p b)V_n'(K_p b) - V_n(K_p b)] = 2\mu n[(n-1)V_n(K_p a) - (K_p a)V_{n+1}(K_p a)]
\end{aligned} \tag{5.55}$$

$$T^{(2)}_{\rho\psi}\Big|_{\rho=a} = 0 : \tag{5.56}$$

$$\begin{aligned}
M_{51} &= 0 \\
M_{52} &= 0 \\
M_{53} &= 2n[-(h_p a)U_n'(h_p a) + U_n(h_p a)] = 2n[(1-n)U_n(h_p a) + \delta(h_p a)U_{n+1}(h_p a)] \\
M_{54} &= 2n[-(h_p a)V_n'(h_p a) + V_n(h_p a)] = 2n[(1-n)V_n(h_p a) + (h_p a)V_{n+1}(h_p a)] \\
M_{55} &= (-k_{zp}a)[(K_p a)U_{n+1}'(K_p a) - (n+1)U_{n+1}(K_p a)] \\
&= (-k_{zp}a)[-2(n+1)U_{n+1}(K_p a) + (K_p a)U_n(K_p a)] \\
M_{56} &= (-k_{zp}a)[(K_p a)V_{n+1}'(K_p a) - (n+1)V_{n+1}(K_p a)] \\
&= (-k_{zp}a)[-2(n+1)V_{n+1}(K_p a) + \kappa(K_p a)V_n(K_p a)] \\
M_{57} &= 2(K_p a)U_n'(K_p a) + [(K_p a)^2 - 2n^2]U_n(K_p a) \\
&= [-2n^2 + \kappa(K_p a)^2 + 2n]U_n(K_p a) - 2\kappa(K_p a)U_{n+1}(K_p a) \\
M_{58} &= 2(K_p a)V_n'(K_p a) + [(K_p a)^2 - 2n^2]V_n(K_p a) \\
&= [-2n^2 + \kappa(K_p a)^2 + 2n]V_n(K_p a) - 2(K_p a)V_{n+1}(K_p a)
\end{aligned} \tag{5.57}$$

$$T^{(2)}_{\rho\psi}\Big|_{\rho=b} = 0 : \tag{5.58}$$

$$\begin{aligned}
M_{61} &= 0 \\
M_{62} &= 0 \\
M_{63} &= -2n[(h_p b)U_n'(h_p b) - U_n(h_p b)] = 2n[(1-n)U_n(h_p b) + \delta(h_p b)U_{n+1}(h_p b)] \\
M_{64} &= -2n[(h_p b)V_n'(h_p b) - V_n(h_p b)] = 2n[(1-n)V_n(h_p b) + (h_p b)V_{n+1}(h_p b)] \\
M_{65} &= (-k_{zp}b)[(K_p b)U_{n+1}'(K_p b) - (n+1)U_{n+1}(K_p b)] \\
&= (-k_{zp}b)[-2(n+1)U_{n+1}(K_p b) + (K_p b)U_n(K_p b)] \\
M_{66} &= (-k_{zp}b)[(K_p b)V_{n+1}'(K_p b) - (n+1)V_{n+1}(K_p b)] \\
&= (-k_{zp}b)[-2(n+1)V_{n+1}(K_p b) + \kappa(K_p b)V_n(K_p b)] \\
M_{67} &= 2(K_p b)U_n'(K_p b) + [(K_p b)^2 - 2n^2]U_n(K_p b) \\
&= [-2n^2 + \kappa(K_p b)^2 + 2n]U_n(K_p b) - 2\kappa(K_p b)U_{n+1}(K_p b) \\
M_{68} &= 2(K_p b)V_n'(K_p b) + [(K_p b)^2 - 2n^2]V_n(K_p b) \\
&= [-2n^2 + \kappa(K_p b)^2 + 2n]V_n(K_p b) - 2(K_p b)V_{n+1}(K_p b)
\end{aligned} \tag{5.59}$$

$$T_{\rho z}^{(2)}\Big|_{\rho = a} = 0 : \tag{5.60}$$

$$\begin{aligned}
M_{71} &= 0 \\
M_{72} &= 0 \\
M_{73} &= 2(k_{zp}a)(h_p a)U_n{}'(h_p a) = 2(k_{zp}a)[nU_n(h_p a) - \delta(h_p a)U_{n+1}(h_p a)] \\
M_{74} &= 2(k_{zp}a)(h_p a)V_n{}'(h_p a) = 2(k_{zp}a)[nV_n(h_p a) - (h_p a)V_{n+1}(h_p a)] \\
M_{75} &= -n(K_p a)U_{n+1}{}'(K_p a) + [(K_p a)^2 - n(n+1) - (k_{zp}a)^2]U_{n+1}(K_p a) \\
&= [\kappa(K_p a)^2 - (k_{zp}a)^2]U_{n+1}(K_p a) - n(K_p a)U_n(K_p a) \\
M_{76} &= -n(K_p a)V_{n+1}{}'(K_p a) + [(K_p a)^2 - n(n+1) - (k_{zp}a)^2]V_{n+1}(K_p a) \\
&= [\kappa(K_p a)^2 - (k_{zp}a)^2]V_{n+1}(K_p a) - \kappa n(K_p a)V_n(K_p a) \\
M_{77} &= n(k_{zp}a)U_n(K_p a) \\
M_{78} &= n(k_{zp}a)V_n(K_p a)
\end{aligned} \tag{5.61}$$

$$T_{\rho z}^{(2)}\Big|_{\rho = b} = 0 : \tag{5.62}$$

$$\begin{aligned}
M_{81} &= 0 \\
M_{82} &= 0 \\
M_{83} &= 2(k_{zp}b)(h_p b)U_n{}'(h_p b) = 2(k_{zp}b)[nU_n(h_p b) - \delta(h_p b)U_{n+1}(h_p b)] \\
M_{84} &= 2(k_{zp}b)(h_p b)V_n{}'(h_p b) = 2(k_{zp}b)[nV_n(h_p b) - (h_p b)V_{n+1}(h_p b)] \\
M_{85} &= -n(K_p b)U_{n+1}{}'(K_p b) + [(K_p b)^2 - n(n+1) - (k_{zp}b)^2]U_{n+1}(K_p b) \\
&= [\kappa(K_p b)^2 - (k_{zp}b)^2]U_{n+1}(K_p b) - n(K_p b)U_n(K_p b) \\
M_{86} &= -n(K_p b)V_{n+1}{}'(K_p b) + [(K_p b)^2 - n(n+1) - (k_{zp}b)^2]V_{n+1}(K_p b) \\
&= [\kappa(K_p b)^2 - (k_{zp}b)^2]V_{n+1}(K_p b) - \kappa n(K_p b)V_n(K_p b) \\
M_{87} &= n(k_{zp}b)U_n(K_p b) \\
M_{88} &= n(k_{zp}b)V_n(K_p b)
\end{aligned} \tag{5.63}$$

[This page is intentionally left blank.]

6

Scattering from an Infinite Cylindrical Shell in the Meridional Plane: Meridional Ray Amplitudes

6.1 Introduction

The results of Chapter 2 (Ref. [8]), as well as the investigations by Kaduchak[1] and Dodd[2], have shown that significant enhancements to the backscattering by tilted finite cylindrical shells (both empty and fluid-filled) and solid cylinders[47] are due to the launching of a meridional leaky wave which reflects off the cylinder truncation and reradiates into the backscattering direction. A meridional wave propagates strictly in the axial direction and for the high frequencies studied in the references above, it is well suited for interpretation by ray approaches. The meridional ray path on the cylinder, shown in

Fig. 2.1, lies in the plane defined by the incident wavevector and the cylinder axis. This axial path can be thought of as one of the limiting paths taken by helical waves on the cylinder, the other being a purely circumferential path. A meridional ray enhancement can be significantly greater in amplitude than the edge diffracted returns from the ends of the cylinder. The meridional leaky ray is launched when the angle of incidence of an impinging acoustic plane wave nears a leaky wave coupling angle. This angle is determined by the phase velocity of the (necessarily supersonic) leaky wave on the cylinder through the trace velocity matching condition as

$$\gamma \approx \theta_l = \sin^{-1}\left(\frac{c}{c_l}\right), \qquad c_l > c, \tag{6.1}$$

where c_l is the phase velocity of the l^{th} class of leaky wave and c is the speed of sound in the surrounding fluid. One can see from Eq. (6.1) that the angle at which an enhancement may be found for a particular frequency is dependent on the dispersion characteristics of the leaky wave. For a relatively dispersionless leaky wave, e.g. a meridional leaky Rayleigh wave on a solid cylinder, which has similar propagation characteristics to a Rayleigh wave on an elastic half space, the enhancement angle is relatively constant[5,47]. For the enhancements first observed on cylindrical shells[1,2] the contributing leaky waves were the generalizations of the a_0 and s_0 leaky Lamb waves, which are not particularly dispersive over the frequency range studied by those authors. To investigate more thoroughly the conditions for these effects, Morse (Ref. [8], Chapter 2) carried out broadband impulse response measurements on empty thick cylindrical shells which showed continuous enhancement curves in frequency-angle space, some of which extended to end-on incidence near the coincidence frequency. The leaky waves responsible for the enhancements at large cylinder tilt angles were identified as the generalizations of the a_0 and a_{0-} meridional and helical waves, respectively. These waves are highly dispersive in the frequency range studied, which explains the large range of angles over which the enhancements were observed. Lesser contributions were observed from a_0, s_0 and T_0 (shear) helical waves. That investigation also showed that the general locations of the measured backscattering enhancements were consistent with an approximate partial wave

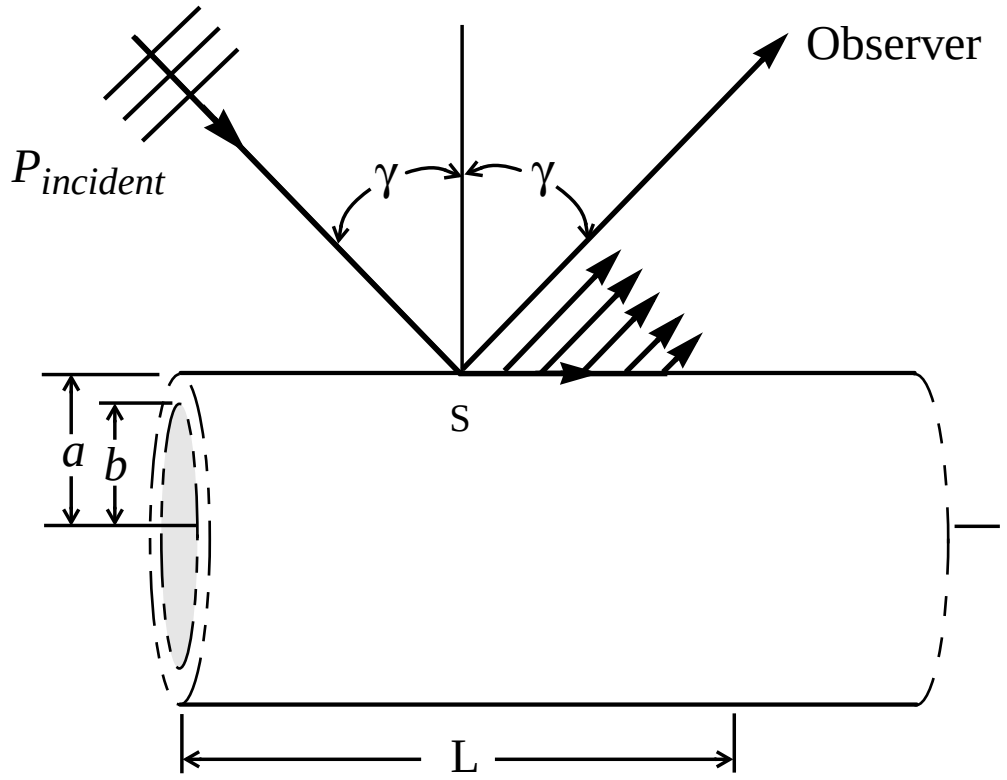

FIG. 6.1 Schematic of scattering (bistatic) from an infinite cylindrical shell. A plane wave is incident on the cylinder at an angle γ with respect to the normal. The observer is situated in the far-field in the meridional plane (defined by the incident wavevector and the cylinder axis) at an angle γ in the specular direction. Scattering in this direction includes the strong specular contribution as well as contributions from leaky waves launched on the shell. In particular a strong enhancement occurs when $\gamma \approx \theta_l$ as a leaky ray is launched along the cylinder meridian. This meridional ray then reradiates sound at an angle θ_l.

series solution (which reproduced most of the observed enhancement features).

For the purpose of estimating the amplitudes of these enhancements on more complicated objects it is desirable to develop and verify a quantitative ray theory for these enhancement processes. A successful ray treatment of the problem would be useful, for example, in interpreting images from high-frequency imaging or scanning sonar systems

or in predicting the response of materials and structures with cracks or truncations examined with acoustic non-destructive evaluation techniques. Marston[3-6] has previously developed a ray theory for this process which utilizes an approximation of spatial amplitudes of leaky waves on weakly curved elastic structures. It has already proven successful in modeling the meridional plane backscattering enhancement by leaky Rayleigh waves on an infinite solid cylinder[5], and on a finite solid cylinder[47]. The present work extends these comparisons to leaky waves on hollow infinite cylindrical shells and hollow and fluid-filled finite cylindrical shells (Chapter 7).

6.2 Global Scattering Response in the Meridional Plane from the Exact PWS Solution

Figure 6.1 shows a diagram of a scattering geometry which provides for a comparison of the ray theory with an exact partial wave series solution (PWS) of the scattered field. A time-harmonic plane wave is incident at an angle γ on an infinite hollow cylindrical shell in an ideal fluid of infinite extent. The exact solution to this problem under the framework of linearized 3-D elasticity is given in Ref. [14] and in Chapter 4. Figures 6.2 and 6.3 show the results of this PWS calculation of the far-field scattering form function for Shells A and B, respectively, examined in earlier chapters. They show the global scattering response as a function of frequency and angle. Since only the scattering response associated with the elastic behavior is desired a "background", corresponding to the exact scattering by a rigid cylinder, has been subtracted from the total scattering. Explicitly, Eq. (4.9) is subtracted from Eq. (4.8) before taking the absolute magnitude. If one were to plot the full scattering response it would include the interference between the specular reflection and the reradiation of any elastic waves launched on the shell; as a result it would be much more difficult to interpret. The subtraction method works well except at low frequencies and large tilt angles.

Figures 6.2 and 6.3 are strikingly similar to Figs. 2.4 and 2.5, respectively. All the elastic features previously identified are present in Figs. 6.2 and 6.3. The a_0 meridional ray enhancement peak dominates the response at these frequencies and is fairly isolated from the other features, making it a good candidate for comparison with the ray theory.

FIG. 6.2 Calculated form function modulus for scattering in the specular direction (i.e. bistatic) in the meridional plane for Shell A. The exact form function expression for a rigid cylinder has been subtracted. The highest ka displayed ($f \approx 990$ kHz) is below the mode thresholds for the generalizations of the s_1 and a_1 waves. The primary contributions to the scattering are from the generalizations of the a_0, a_{0-}, s_0 and T_0 waves. This color raster image represents the sampling intervals: $\Delta ka = 0.05$ ($\Delta f = 619$ Hz), $\Delta\gamma = 0.2°$. The amplitude scale is in dB with respect to the maximum response at $\gamma = 0°$.

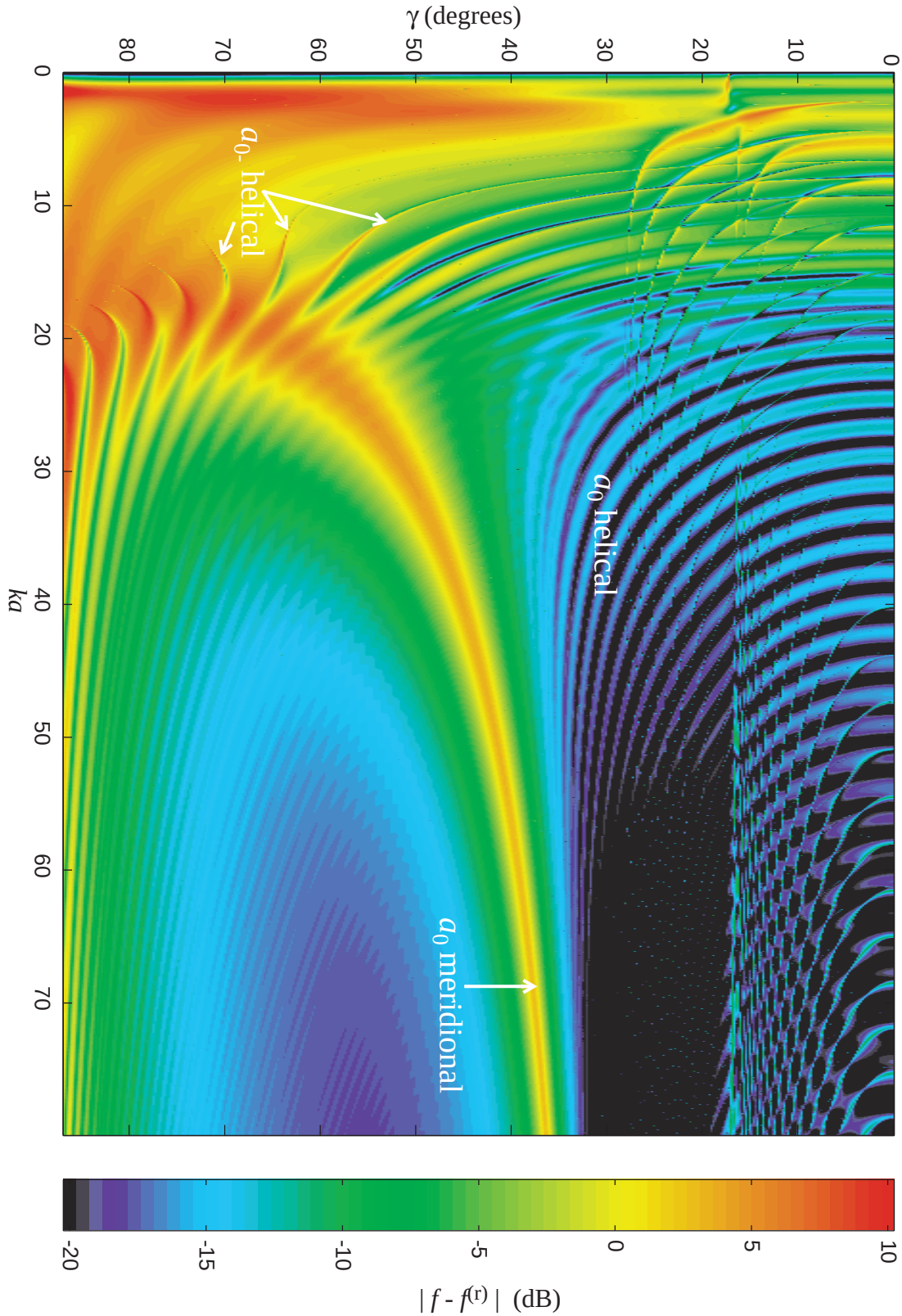

$\frac{b_1}{a} = 0.924$

FIG. 6.3 Calculated form function modulus for scattering in the specular direction (i.e. bistatic) in the meridional plane for Shell B. The exact form function expression for a rigid cylinder has been subtracted. The range of ka displayed (up to $f \approx 1.0$ MHz) includes portions of the s_1, s_2, s_{2b}, and a_1 waves, in addition to the a_0, $a_{0\text{-}}$, s_0 and T_0. This color raster image represents the sampling intervals: $\Delta ka = 0.05$ ($\Delta f = 561$ Hz), $\Delta\gamma = 0.2°$. The amplitude scale is in dB with respect to the maximum response at $\gamma = 0°$.

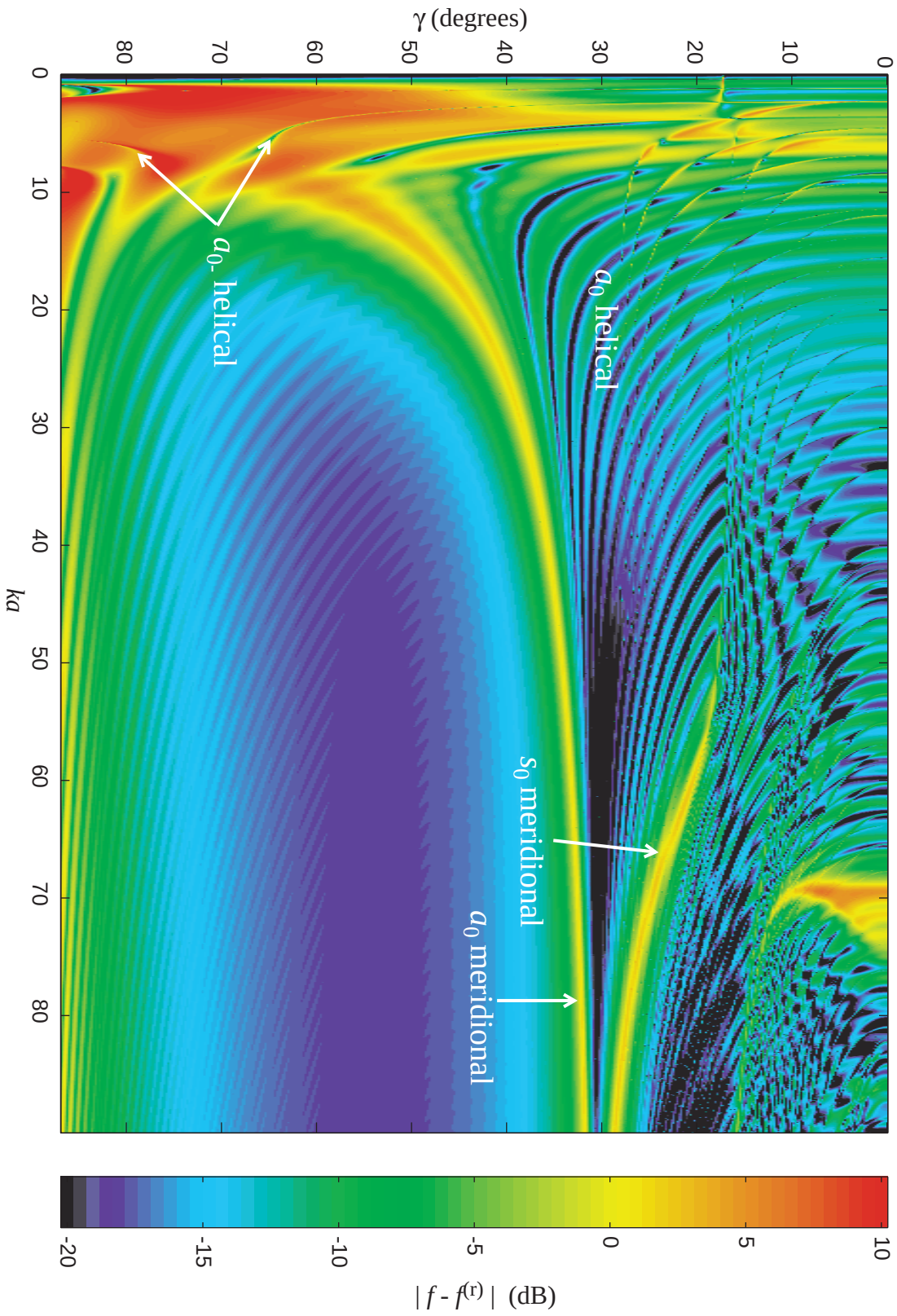
γ (degrees)
0
10
20
30
40
50
60
70
80
ka
0
10
20
30
40
50
60
70
80
a_0 helical
a_{0-} helical
s_0 meridional
a_0 meridional
-20
-15
-10
-5
0
5
10
| f - f(r) | (dB)
b/a = 0.8375

6.3 Meridional Plane Scattering Amplitude from Approximate Ray Analysis

The approximate ray analysis of Ref. [5] provides an expression for the far-field scattering form function for backscattering in the meridional plane from an infinite solid cylinder near a leaky wave coupling angle. No modification is required to extend this result to the case of an infinite hollow cylindrical shell. The modulus of the far-field form function for the l^{th} meridional ray is given as a function of incidence angle by

$$\left| f_l(\gamma) \right| \approx 2^{3/2} \frac{\left| \left(\frac{\alpha}{\nu} \right) F(\mu'') \right|}{\sqrt{1 + 2\mu \left[\frac{1}{F(\mu)} - 1 \right]}}, \tag{6.2}$$

where the wavenumber associated with the meridional leaky ray is

$$k_p = k_l + i\alpha, \tag{6.3}$$

and

$$\begin{aligned} \nu &= \alpha + i(k \sin\gamma - k_l) \\ \mu &= (\alpha a) \tan\theta_l \\ \mu'' &= \mu \left(\frac{\cos\theta_l}{\cos\gamma} \right) \left(\frac{\nu}{\alpha} \right) \end{aligned}, \tag{6.4(a)-(c)}$$

$$F(\xi) = e^{\xi} \sqrt{\pi \xi} \operatorname{erfc}(\sqrt{\xi}). \tag{6.5}$$

The leaky wave coupling angle is

$$\theta_l = \sin^{-1}(c/c_l) = \sin^{-1}(k_l/k), \tag{6.6}$$

where $k = \omega/c$; also, a is the cylinder radius and erfc is the complementary error function. Equation (6.5) must be evaluated numerically. Equation (6.2) is valid for a small

range of angles near the leaky wave coupling angle. A noteworthy approximation used in the derivation of Eq. (6.2) is that the curvature of the radiated wavefront is approximated by using values derived for $\gamma = \theta_l$ even when $\gamma \neq \theta_l$. This is because the reduction in amplitude when $\gamma \neq \theta_l$ should be dominated by dephasing. To evaluate Eq. (6.2) for the form function one must possess knowledge of the meridional leaky wavenumber, k_p. For a hollow cylindrical shell (or a solid cylinder) the meridional wavenumber may be approximated by the wavenumber of the axisymmetric mode of the cylinder, which may be found, as in Chapter 4 for $n = 0$, by locating the appropriate root of the characteristic equation for that problem[5,61]. Alternately the meridional wavenumber may be approximated with the wavenumber of the corresponding Lamb wave on a fluid loaded plate (single-sided).

If the shell is sufficiently thin and contains fluid on the interior, rather than being hollow, the expressions above must be modified to account for the leaky wave radiation into the fluid interior. Specifically Eq. (6.2) should be multiplied by $(1/2)$ and the appropriate wavenumber [Eq. (6.3)] chosen accordingly (see Section I of Ref. [4] where in the notation used there j becomes 1). For a fluid-filled cylindrical shell the wavenumber cannot be found directly as was done in Chapter 4 for a hollow cylinder. The modes of vibration of the shell, in this case, cannot be separated from the modes of the fluid interior—eliminating the possibility of finding a single leaky wave pole corresponding to the doubly fluid-loaded problem. It is often sufficient to simply approximate this leaky wavenumber with that for a hollow shell with the modification of doubling the damping rate. This modification accounts for the leakage of energy into the fluid on both sides of the elastic material rather than on only one side and can be implemented by multiplying the imaginary part of the wavenumber by 2.

6.4 Comparison of the Ray Theory with the Exact PWS Solution

The approximate ray theory reviewed above will now be compared with the exact PWS solution discussed in Chapter 4 and Ref. [14]. Figures 6.4 and 6.5 show this comparison for six successive frequencies (ka) as a function of cylinder tilt angle for Shell A. These show the full range of angles while Figs. 6.6 and 6.7 display only a close-up of the meridional ray peak for each frequency. Figures 6.8 - 6.11 show similar calculations for Shell B. For the PWS calculations each of these figures corresponds to a horizontal slice through Fig. 6.2 or 6.3.

For Shell A the prominent enhancement feature is due to the a_0 meridional ray. The solid points in Figs. 6.4 - 6.7 are calculated with the ray theory, Eq. (6.2), using wavenumbers calculated for the axisymmetric mode of a hollow infinite cylindrical shell corresponding to the generalization of the a_0 leaky Lamb wave (see Section 4.3). The results for Shell B are similar; however, in this case a significant enhancement from the s_0 meridional ray is also present above $ka \approx 60$ at a lesser tilt angle. Table 6.1 lists the wavenumbers used in the ray calculations and also shows the comparable wavenumbers for a flat plate of the same material and thickness as the cylindrical shell with fluid-loading on one side.

The agreement between the ray theory and exact PWS result is very good. For example the average percent error ($||f_{pws}|-|f_{ray}||/|f_{pws}|$) between the peak values predicted by the ray theory and the PWS solution is 0.36% for Shell A and 1.96% for Shell B, for the figures shown (a_0 peak only). The average percent error in the angular location of the peak enhancement is 0.06% and 0.09%, respectively . If the wavenumbers for the flat plate were used instead of the exact cylinder wavenumbers the average percent errors for the magnitude of the form function are 0.29% and 0.63%, respectively, for an average percent error in the angular location of the peak enhancement of 0.13% and 0.27%. Similar comparisons for the s_0 meridional ray peak, such as is found in Figs. 6.9 and 6.11, are not nearly as good. This is because the s_0 meridional ray enhancement peak is found over a

region where other helical wave responses are present. These additional, mostly smaller, responses interfere with the meridional ray response and tend to confuse the comparison with the single meridional ray contribution. The panel of Fig. 6.11 for $ka = 60$ shows this clearly. This illustrates why the a_0 meridional ray was chosen for comparison with the ray theory.

Table 6.1: Meridional ray wavenumbers

	Shell A: a_0		Shell B: a_0, (s_0)	
ka	$k_p a_{\text{cylinder},n=0}$	$k_p a_{\text{plate}}$	$k_p a_{\text{cylinder},n=0}$	$k_p a_{\text{plate}}$
20			13.7506+i 0.2302	13.8658+i 0.2184
30	23.2856+i 0.5908	23.3423+i 0.5780	18.5529+i 0.2033	18.6222+i 0.1930
40	28.2585+i 0.4927	28.3065+i 0.4821	23.2728+i 0.1997	23.3219+i 0.1890
50	33.0842+i 0.4492	33.1208+i 0.4394	27.9945+i 0.2058	28.0324+i 0.1935
60	37.8336+i 0.4275	37.8629+i 0.4180	32.7439+i 0.2176 20.7627+i 0.3681(s_0)	32.7749+i 0.2031 20.8253+i 0.3735(s_0)
70	42.5476+i 0.4172	42.5720+i 0.4077	37.5283+i 0.2341 29.2365+i 0.4777(s_0)	37.5546+i 0.2162 29.3016+i 0.4833(s_0)
80	47.2490+i 0.4139	47.2698+i 0.4040		

c=1.483, c_L=5.675, c_S=3.141 (mm/μs); Shell A: a=19.05 mm, h/a=0.076; Shell B: a=21.02 mm, h/a=0.1625

The ray theory also correctly models the shape of the enhancement peak, for a limited range of angles. Generally, at low frequencies (ka) the peak is fairly broad and narrows as the frequency increases. The enhancement peak in the exact solution is slightly asymmetric; this characteristic is not recovered by the ray theory. Furthermore the exact solution displays a number of smaller broad enhancement peaks at tilt angles less than the meridional ray peak, which are also not present in the ray theory. These are due to various modes of the helical a_0 which necessarily circumnavigate the shell. Including these effects would require an extension of the present ray theory.

One feature which requires a comment is found in Fig. 6.9 at $ka = 70$ and $\gamma \approx 5°$ (see also the corresponding region in Fig. 6.3). This feature is associated with the onset of the s_{2b} and s_1 leaky waves on the cylinder (see Fig. 4.5 on page 103 and Figs. 8.1 and 8.2

starting on page 259). Because of its angular location it is most likely due to the s_{2b} meridional ray, which is a backward wave[81] (i.e. its group and phase velocity have opposite signs).

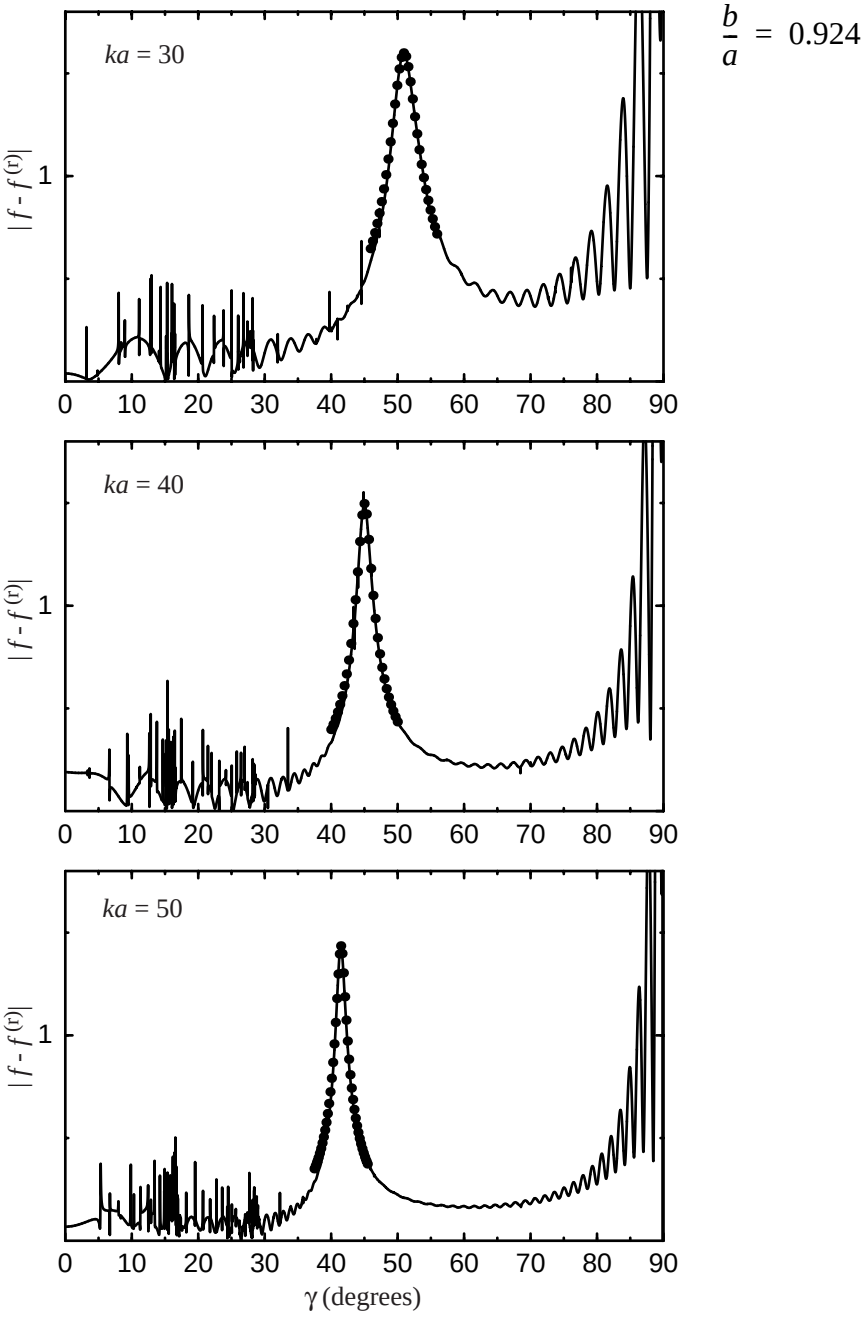

FIG. 6.4 Meridional plane scattering form function for an infinite hollow cylindrical shell in water corresponding to Shell A for several values of *ka*. The solid curve is the exact PWS result with a rigid cylinder background subtracted while the solid points are the results of the ray formulation discussed in Section 6.3. *The principle enhancement feature is due to the* a_0 *meridional ray.*

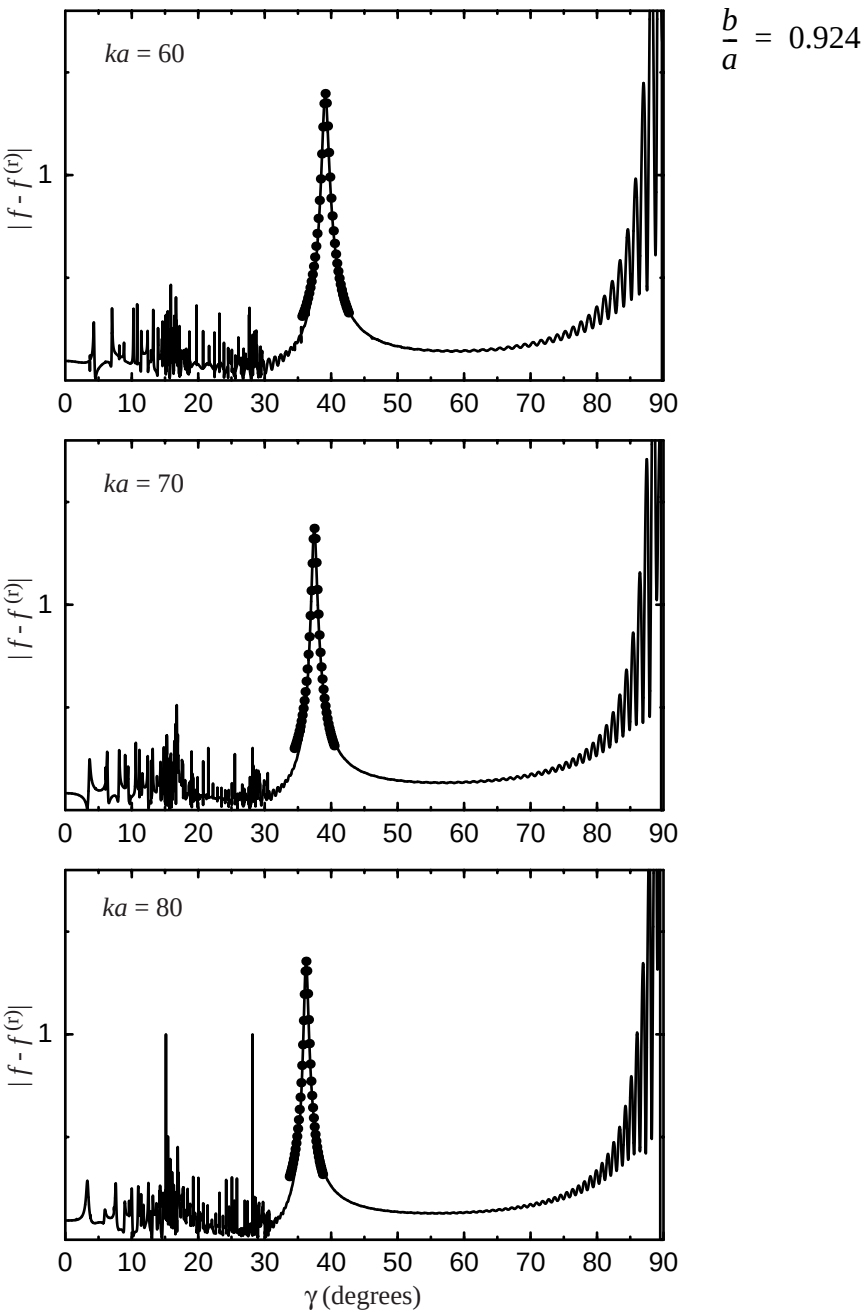

FIG. 6.5 Meridional plane scattering form function for an infinite hollow cylindrical shell in water corresponding to Shell A for several values of *ka*. The solid curve is the exact PWS result with a rigid cylinder background subtracted while the solid points are the results of the ray formulation discussed in Section 6.3. *The principle enhancement feature is due to the* a_0 *meridional ray.*

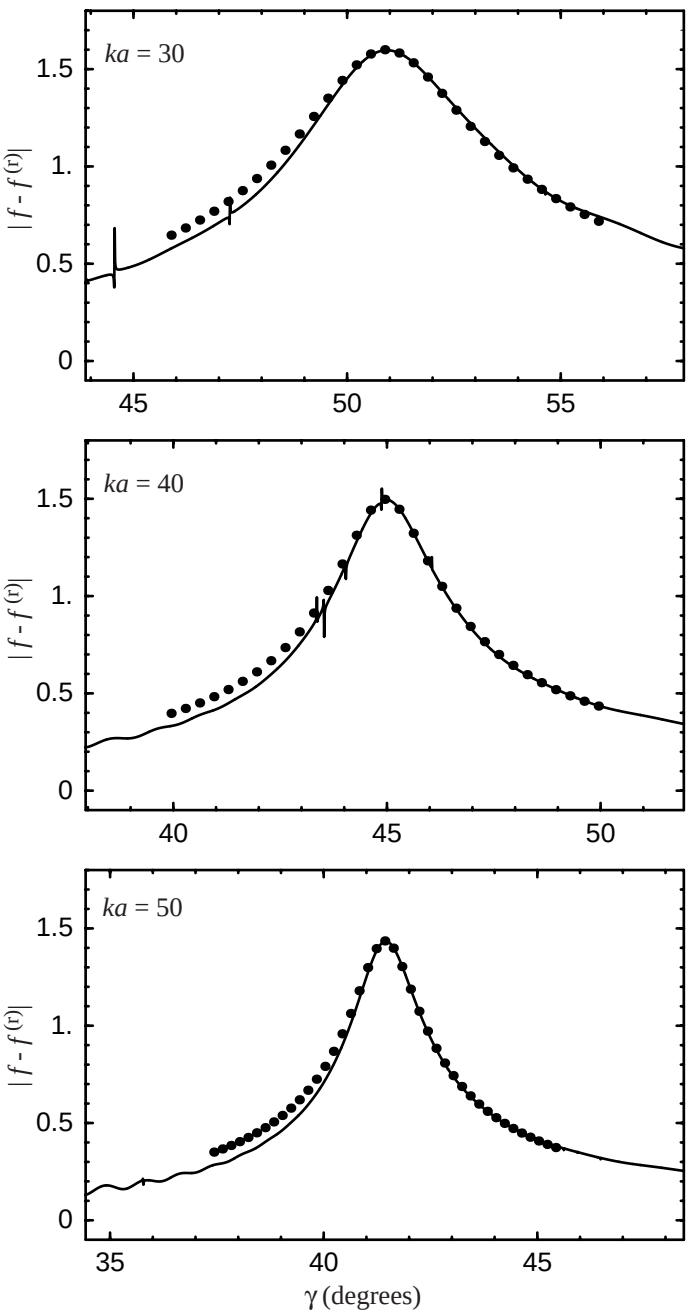

FIG. 6.6 Close-up of the a_0 meridional ray peaks in Fig. 6.4 for Shell A.

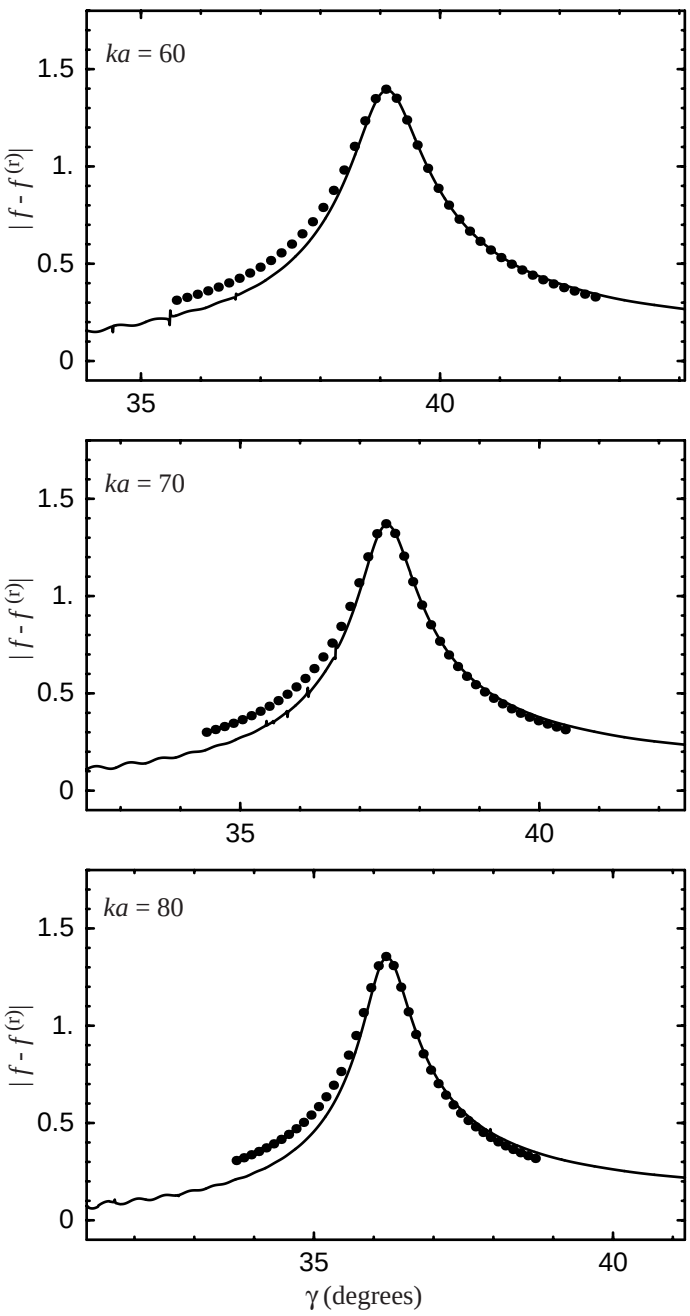

FIG. 6.7 Close-up of the a_0 meridional ray peaks in Fig. 6.5 for Shell A.

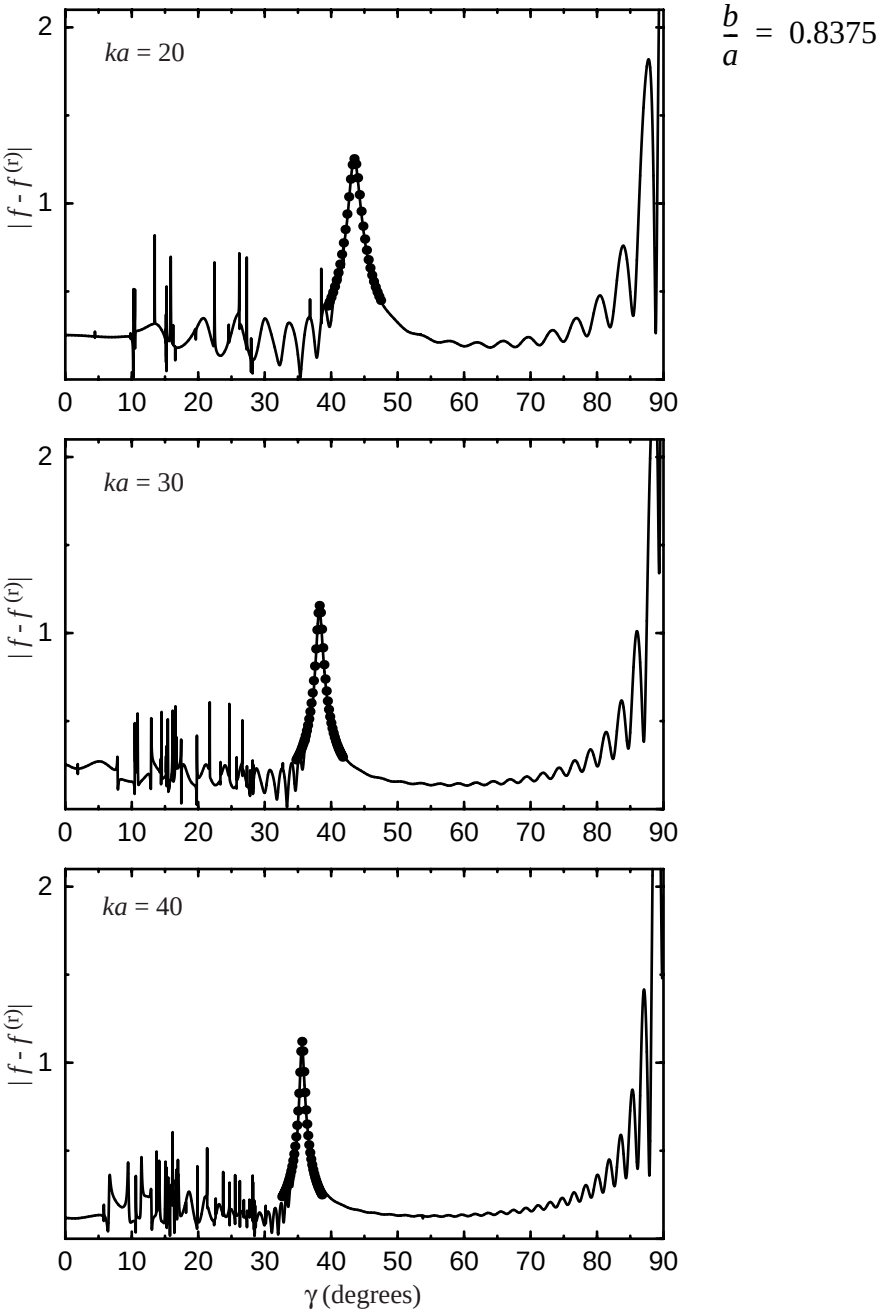

FIG. 6.8 Meridional plane scattering form function for an infinite hollow cylindrical shell in water corresponding to Shell B for several values of *ka*. The solid curve is the exact PWS result with a rigid cylinder background subtracted while the solid points are the results of the ray formulation discussed in Section 6.3. *The principle enhancement feature is due to the* a_0 *meridional ray.*

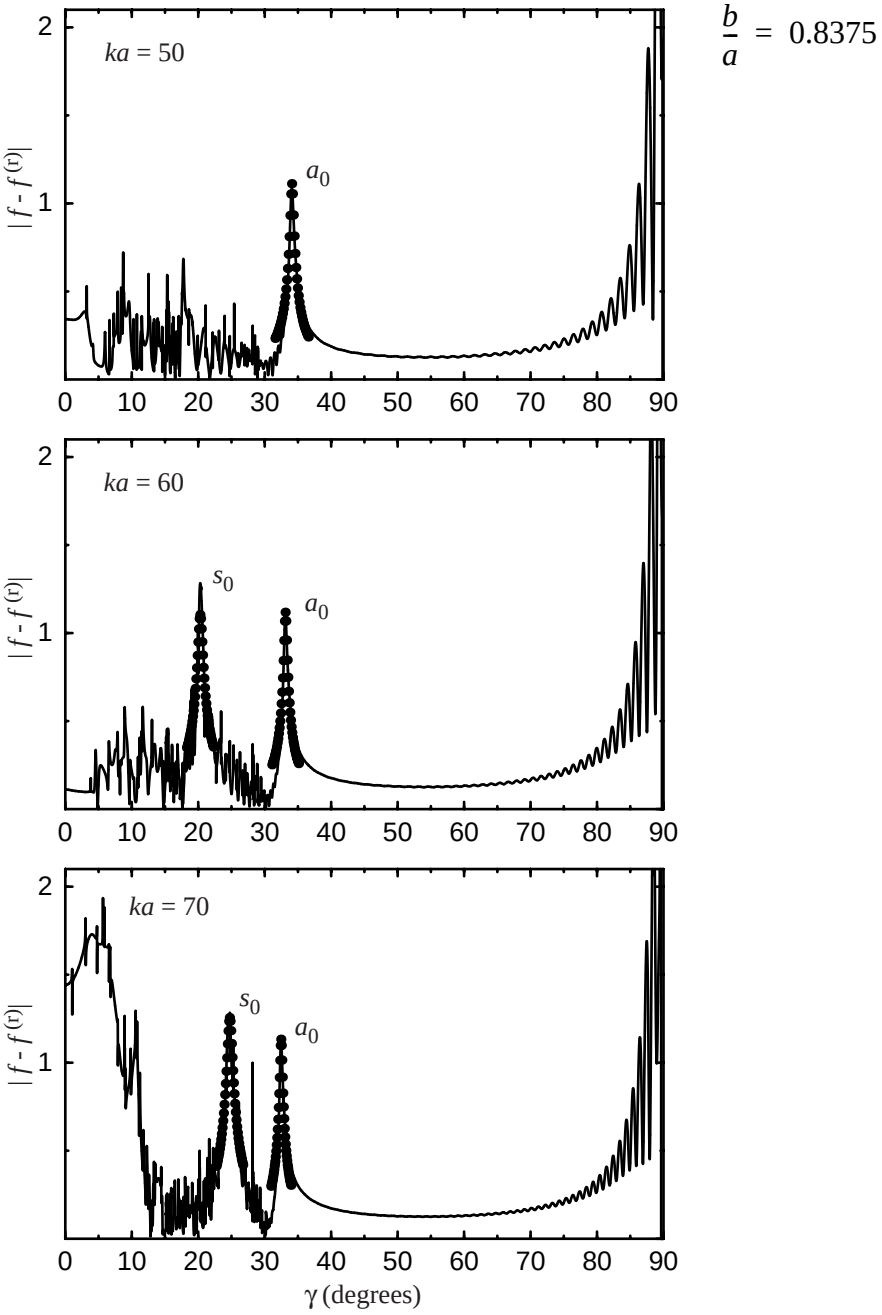

FIG. 6.9 Meridional plane scattering form function for an infinite hollow cylindrical shell in water corresponding to Shell B for several values of *ka*. The solid curve is the exact PWS result with a rigid cylinder background subtracted while the solid points are the results of the ray formulation discussed in Section 6.3. For *ka* = 60 and *ka* = 70, besides the a_0 meridional ray an enhancement due to the s_0 meridional ray is present. The large peak near $\gamma = 5°$ is associated with the mode thresholds of the s_1 and s_{2b} leaky waves (see Fig. 6.3).

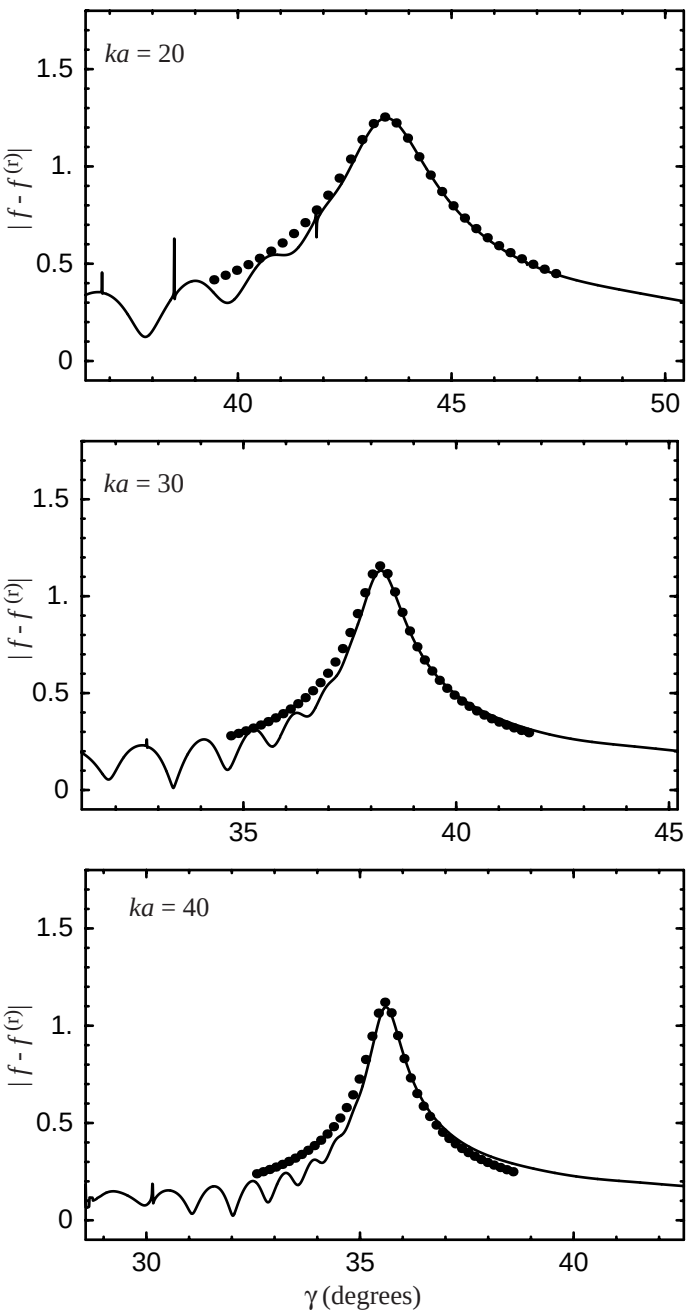

FIG. 6.10 Close-up of the a_0 meridional ray peaks in Fig. 6.8 for Shell B.

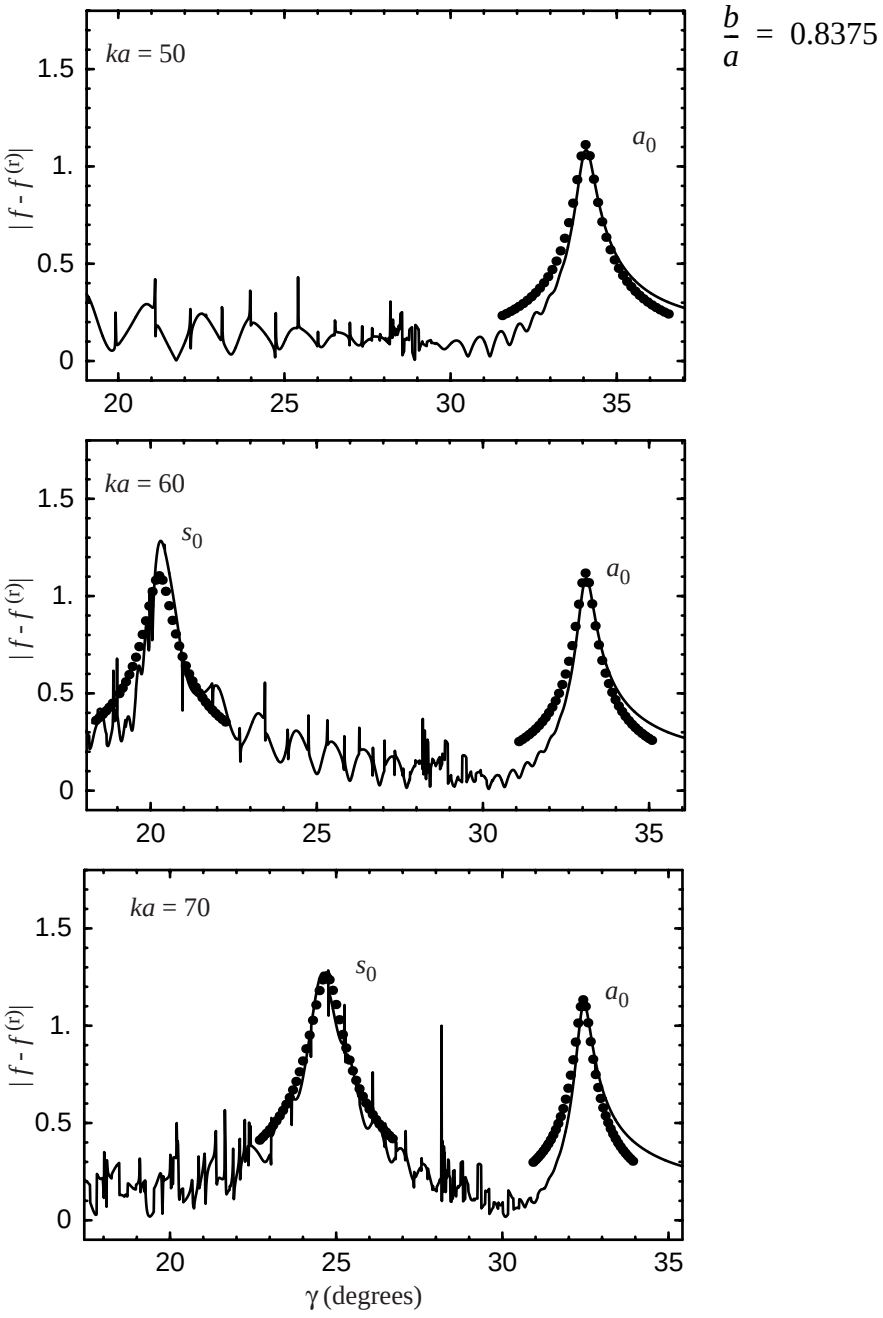

FIG. 6.11 Close-up of the a_0 and s_0 meridional ray peaks in Fig. 6.9 for Shell B.

6.5 Discussion

The results presented here show the ray theory developed by Marston is applicable to meridional Lamb-type waves on hollow cylindrical shells in regions where the meridional ray feature is isolated from other Lamb wave responses. The agreement between the ray theory and the exact PWS solution is good, though it is noteworthy that the tails of the angular maxima differ slightly from the PWS solutions. It is not clear whether this small discrepancy arrives from interference with helical waves not included in the model or from the approximation of the wavefront curvature for $\gamma \neq \theta_l$ previously noted. These results are significant since the ray theory may be modified to apply to similar high-frequency scattering by *finite* cylindrical shells (e.g. Chapter 7).

[This page is intentionally left blank.]

7

Backscattering from a Finite Cylindrical Shell in the Meridional Plane: Meridional Ray Amplitudes

7.1 Introduction

The far-field backscattering by submerged finite cylindrical shells is known to be enhanced when the incident acoustic radiation excites a leaky wave on the shell. For a tilted cylindrical shell these leaky waves typically follow a helical path on the shell and radiate into the backscattering direction after reflection from the shell truncation[10,12,13,16,17]. Recently, experiments have revealed a new class of enhancements which may dominate the monostatic backscattering response at high frequencies for tilted shells[1,2,8]. The enhancements reported are due to a meridional leaky Lamb wave[5] which is

launched along the cylinder's meridian when the aspect angle, γ, of the cylinder nears a leaky wave coupling angle,

$$\gamma \approx \theta_l = \sin^{-1}(c/c_l)\,, \qquad (7.1)\text{(a)-(c)}$$

where c is the speed of sound in the fluid and c_l is the phase velocity of the leaky wave. This condition is the familiar trace velocity matching condition for launching a supersonic surface guided wave. The process is not limited to a particular leaky wave but may include compressional and flexural waves on shells or Rayleigh waves on solids. Some types of waves are excluded, however, because of their propagation characteristics. An example of this is the meridional and circumferential transversely polarized (with respect to the incident wavevector) shear wave, labelled T_0, which is not coupled to the external fluid.

Figure 2.1 shows a ray diagram of the meridional ray enhancement process. The meridional ray lies on the shell in the plane defined by the incident wavevector and the cylinder axis. The enhancement arises when this meridional ray reflects off the cylinder truncation and radiates into the backwards direction, along the angle θ_l. (It is expected that a strong circumferential discontinuity in shell material or curvature, such as a rib stiffener, weld or endcap, would also produce a reflected leaky wave in much the same manner.) This process gives rise to large backscattering amplitudes for primarily two reasons. The first is that it can be shown the Gaussian curvature of the backwards directed wavefront vanishes (Ref. [5]), which leads to a far-field caustic or focusing[82]. The second reason is that the meridional leaky ray need not propagate very far on the shell, as opposed to a helical wave which necessarily traverses the back side of the shell. The result is that less energy is lost through radiation damping in the forward scattering direction before reflection. Of course a limiting factor is the actual elasto-dynamic reflection process at the truncation, which can be very complicated. (For simplicity only a flat perpendicular truncation is considered here.) An elementary analysis of the reflection mechanics will be discussed in Chapter 8. For the cylinders investigated in Refs. [1], [2], [5], and [8] mentioned above, the radiation damping of the meridional leaky wave is large enough that only a small fraction of the length of the cylinder, at it's far end, contributes significantly to

the backscattering enhancement process (see Fig. 3.20 and Section 3.6 starting on page 79). Any waves launched earlier on the shell are too reduced in amplitude to contribute significantly because of the large radiation damping levels. This enhancement process highlights the truncation of the cylinder and has been shown to greatly enhance the visibility of the cylinder end in high-resolution sonar images[1]. Applications of this backscattering enhancement process may include remote non-destructive evaluation (NDE) of cracks or junctions in elastic structures, where Lamb waves are often of interest, or detection of cylindrical objects on the sea bottom by high frequency sonar systems. It should be pointed out that the meridional leaky wave enhancement just discussed has been observed for the case of tilted finite *solid* cylinders (Ref. [47]) in addition to empty and water-filled cylindrical shells. In the first case the leaky wave responsible is a leaky Rayleigh wave while for the latter cases it is one of often several leaky Lamb-type waves.

The previously mentioned investigations primarily focused on identifying the mechanism(s) responsible for the enhancement and then exploring the broader conditions under which it is observable. For the thick and moderately thick steel shells examined by the author in Ref. [8] (Chapter 2) the principal enhancement mechanisms, for the frequency range studied, were found to be due to the generalizations of the antisymmetric a_0 and a_{0^-} leaky Lamb waves which included helical wave contributions. The meridional ray enhancement of the supersonic a_0, however, was found to be the most prominent and was relatively easy to identify. Because the contribution to the backscattering from this mechanism is for the most part isolated from other elastic contributions, and is therefore most suitable for further study, it will be the main focus of this chapter.

The *purpose of this chapter* is to quantitatively investigate the a_0 meridional ray enhancement by comparing experimentally obtained meridional ray amplitudes with amplitudes calculated by approximate methods. This chapter is organized as follows. Section 7.2 describes the water tank scattering experiments performed to measure the time records of the enhancements. Section 7.4 describes the two theoretical calculations used to compare with the experimental results. The first theoretical approach is an extension of a ray theory developed by Marston[5]. One remarkable prediction of this ray theory is that the

amplitude of the meridional ray contribution to the far-field backscattering can be many times greater than the specular reflection from a rigid sphere having the same radius as the cylinder. The second theoretical approach is an approximate partial wave series (PWS) solution that was presented in Ref. [8]; it is discussed only briefly here but may be found in its entirety in Chapter 5. In Section 7.4 the angle dependence of the meridional ray enhancement is investigated. The experimental and theoretical meridional ray amplitudes are compared as a function of cylinder aspect angle for selected excitation frequencies. Both air-filled and water-filled shells are examined. In addition to angular comparisons the approximate PWS solution affords a comparison of the enhancements in the time domain, which is presented in Section 7.5. It is found that allowing water on the inside of the shell significantly alters the enhancements and introduces complications in the ray analysis, though the enhancements are still easily observed. Section 7.6 discusses this case further and shows the effect of internal fluid loading on the experimental backscattered spectral magnitude.

7.2 Backscattering Experiment

Narrowband backscattering experiments were carried out in a cylindrical redwood water tank (8′ ht. by 12′ dia.) for the two thick shells, labelled Shell A and B, studied in previous chapters. The experimental setup is similar to that used in Ref. [8] (Chapter 2, see Fig. 2.3 on page 14) except that the source and receiver are the same transducer, operated in a transmit-receive (TR or pulse-echo) mode. The sheet source is removed so that only the cylinder and source/receiver are in the tank. Two immersion type NDE transducers were used to cover the range of frequencies of interest, with resonances of 500 kHz and 1 MHz [Panametrics models V3386 (1.5″ dia.) and V302 (1″ dia.), respectively]. (It should be noted that the latter model had an actual resonance frequency nearer to 750 kHz.) The selected transducer was placed a distance of approximately 2.3 meters from the center of the carefully aligned cylinder and driven with a long duration tone burst (20 to 40 cycles) through a Ritec™ Clamped Diplexer (Model RCDX-2A), which performed the TR signal

switching. The aspect angle of the cylinder was set with a motorized stepper rotation stage (0.025°/step). At each selected aspect angle, multiple backscattered time records were recorded and averaged on a digital oscilloscope and subsequently downloaded to a personal computer. Reflections from the tank walls were not present in the time windows of interest.

Figure 7.1 shows an example of a portion of the raw backscattered response from Shell A (preamplifier voltage versus time) over a broad range of angles, which is intended to familiarize the reader with the typical scattering response. The excitation in this case is a 20 cycle square envelope tone burst centered at 620 kHz. Broadside incidence would be at $\gamma = 0°$ in the notation used. In this figure red corresponds to positive voltages and blue negative. In this case the shell has air on the interior and flat Plexiglas™ endcaps held in place with rubber O-rings (see Appendix A and Fig. A.3 on page 280). The meridional ray enhancement of the a_0 is found on the left side of the figure between 150 μs and 200 μs. The identification of this feature is made with knowledge of the phase velocity of the a_0 on the shell using Eq. (7.1). The phase velocity of the a_0 on an infinite cylindrical shell, for axial propagation only, at this frequency may be found with the aid of Fig. 4.3 on page 101. It is found to be $c_l/c = 1.51$, which locates the meridional ray enhancement at about $\gamma = 41.4°$ by Eq. (7.1). Note that in Chapters 2 and 4 it was shown that for the high frequencies of interest here, propagation on the shell is essentially isotropic, i.e. the propagation characteristics are nearly independent of the direction of propagation on the shell. As a result the phase velocity for propagation on a plate of the same material and thickness could have been used. Looking now at Fig. 7.1 one finds the meridional a_0 enhancement peak centered at $\gamma = 37.6°$ just after the timing of the geometric reflection from the closest rear corner of the cylinder (the latter black line labelled t_B). This feature primarily corresponds to the a_0 meridional ray enhancement although lesser features due to helical a_0 waves will be seen to be present. The discrepancy between the peak angles will be discussed in Section 7.4. At this point the reader may wish to refer to Figs. 7.11 (a) - 7.15 (a) which show individual measured waveforms at locations of peak enhancement.

Long duration tone burst excitation such as this was the method used to obtain

FIG. 7.1 Example of the measured narrow band backscattering from Shell A with air interior and endcaps, showing the meridional ray enhancement at $\gamma \approx 37.6°$. The overlaid black lines, labelled t_A and t_B, correspond to the timings of the direct ray paths through the water to the closest front and rear "corners" of the cylinder (see Section 7.A and the discussion in Section 3.B). This data was acquired with a T-R setup using the piston-style transducer driven with a 20 cycle square envelope tone burst (center frequency is 620 kHz). The amplitude scale represents 60 dB of dynamic range with respect to the maximum measured response (in this case at $\gamma = 2°$). Broadside incidence would correspond to $\gamma = 0°$.

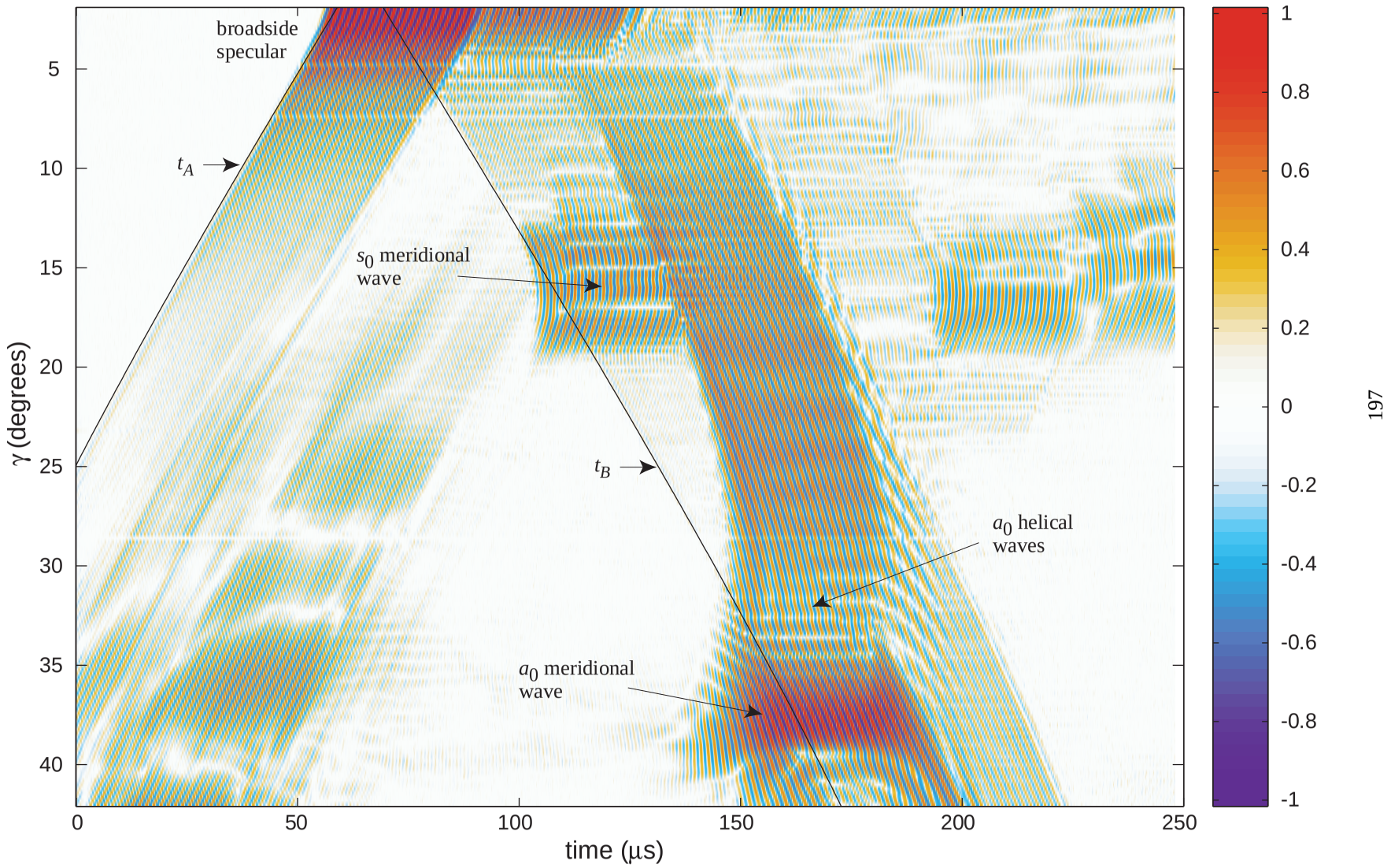
broadside
specular
t_A
s_0 meridional
wave
t_B
a_0 helical
waves
a_0 meridional
wave
γ (degrees)
time (μs)
5
10
15
20
25
30
35
40
0
50
100
150
200
250
1
0.8
0.6
0.4
0.2
0
-0.2
-0.4
-0.6
-0.8
-1
197

scattering amplitudes of the meridional ray peak under the assumption that the response of this enhancement feature would quickly approach steady state behavior during the first few cycles of the burst. The success of this method depends on their being no other significant contributions present over the time span required for the signal of interest to reach steady state behavior. Preliminary experiments demonstrated that the meridional ray enhancement is indeed isolated in the time domain and reaches steady state behavior rather quickly. In almost all the cases examined, near the angle of the peak of the meridional ray enhancement the signal response quickly approached and held a constant value for many cycles. This region of the signal was isolated, averaged and normalized to obtain a representative steady state scattering amplitude. The exact method used is the subject of Section 7.A.

7.3 Ray Theory and Approximate PWS Solution for the Meridional Ray Enhancement

The far-field pressure amplitude in the meridional plane due to the backscattered meridional ray was determined by Marston[5] for the case of a finite cylinder. The finite cylinder case was presented as an extension of the infinite cylinder case, which has been shown to produce results which compare very well with exact PWS calculations for the infinite solid cylinder[5] and infinite hollow cylindrical shell (Chapter 6). For the case of backscattering by a finite *solid* cylinder, Gipson[47] has made comparisons with experiments which also validate the ray theory results. In Ref. [5], Marston only presented the result of the meridional ray amplitude for the case of a finite cylinder tilted exactly at the leaky wave coupling angle $\gamma = \theta_l$. Recently Marston extended this result to include angles adjacent to this tilt angle. A discussion of that derivation may be found in Ref. [47] and is also summarized below.

With prior knowledge of the real and imaginary parts of the contributing meridional wavenumber on the shell, which may be approximated with the corresponding value for a

flat plate, the ray theory approach developed by Marston allows one to determine the peak amplitude of the backscattered meridional ray enhancement when the finite cylinder is tilted at the leaky wave coupling angle θ_l. The far-field backscattering form function for the meridional ray feature alone is given by

$$f_{ls} \approx -e^{-i\left(\frac{\pi}{4}\right)} e^{i\varphi_{bl}} 2B \sqrt{\frac{k_l}{\alpha}} F_e(\mu), \qquad (7.2)\text{(a)-(c)}$$

where the usual definition of the form function, Eq. (1.1), in spherical coordinates has been used,

$$\begin{aligned} F_e(\mu) &= F_\rho(\mu) e^{\mu} \int_{\mu}^{\infty} \operatorname{erfc}(\sqrt{\xi}) d\xi \\ F_\rho(\mu) &= \frac{1}{\sqrt{\frac{\mu}{F(\mu)} - \mu + \frac{1}{2}}} \\ F(\mu) &= e^{\mu} \sqrt{\pi\mu} \operatorname{erfc}(\sqrt{\mu}), \end{aligned} \qquad (7.3)\text{(a)-(c)}$$

and

$$\mu = (\alpha a) \tan\theta_l. \qquad (7.4)\text{(a)-(c)}$$

Recall that

$$\theta_l = \sin^{-1}(c/c_l) = \sin^{-1}\left(\frac{k_l a}{ka}\right). \qquad (7.5)\text{(a)-(c)}$$

In these expressions k_l and α are the real and imaginary parts of the meridional ray wavenumber, $k_p = k_l + i\alpha$, a is the cylinder outer radius, $k = \omega/c$, and B is the reflection coefficient of the leaky wave at the cylinder truncation. The phase term φ_{bl} is due to an overall background phase present in the convolution formulation used to develop the ray theory (see Appendices A and B of Ref. [6]). Equation (7.2) is applicable to a solid cylinder or a hollow cylindrical shell where the leaky wave radiates energy only into the surrounding fluid. It is possible to modify this result for a *fluid-filled cylindrical shell*

in some cases. If the shell is thin enough that the leaky wave approximately radiates energy symmetrically into each fluid, and the interior and exterior fluids are identical or nearly so, then it is a good approximation to simply replace f_{ls} by $(1/2)f_{ls}$ to account for the additional energy loss (see Sect. I of Ref. [4]). This also assumes that the wavenumbers for the doubly fluid-loaded problem have been found and used. As will be seen later, this is not always an easy task and sometimes it is necessary to make approximations using a single-sided fluid-loaded result.

The extension of the result in Eq. (7.2) to the case of angles $\gamma \neq \theta_l$ is by no means trivial. The end result for the solid cylinder or hollow cylindrical shell is

$$|f_{ls}(\gamma)| \approx 2|B|\sqrt{\frac{k_l}{\alpha}}F_\rho(\mu)\frac{e^{\mu\frac{\cos\theta_l}{\cos\gamma}}}{\left|\sqrt{\bar{\mu}\frac{\cos\theta_l}{\cos\gamma}}\right|}\left|\int_{\mu\frac{\cos\theta_l}{\cos\gamma}}^{\infty}\operatorname{erfc}(\sqrt{\xi\bar{\mu}})d\xi\right|, \qquad (7.6)\text{(a)-(c)}$$

where

$$\bar{\mu} = \left[1 + i\left(\frac{k_l}{\alpha}\right)\left(\frac{\sin\gamma}{\sin\theta_l} - 1\right)\right]. \qquad (7.7)\text{(a)-(c)}$$

One may see that by setting $\gamma = \theta_l$, then $\bar{\mu} = 1$ and Eq. (7.6) reduces to Eq. (7.2) as it should in that limit. The integral in Eq. (7.6) is easily evaluated numerically in a high-level programming language such as *Mathematica*®.

Another approach one may take in calculating the meridional ray contribution to the far-field backscattered pressure is to derive an analytical solution in terms of an approximate PWS solution. This was done first in Ref. [8] by Kaduchak and written later in more detail by the author in Chapter 5. The idea is to rewrite the PWS solution for the infinite cylindrical shell in terms of eigenfunctions which are periodic over the length of a "finite" section of the infinite cylinder. The periodic constraint chosen was for a circumferentially quasi "simply supported" cylinder. The solution for the displacement amplitude over the finite cylinder section by itself is then used as the source in the Kirchhoff diffraction integral to obtain an approximate far-field scattered pressure due to a

finite cylinder. This method has been shown in Chapters 2 and 5 to produce good results for thick and thin walled shells, except at tilt angles nearing end-on incidence. One consequence of using this method of solution, which is important for the following comparisons, is that the choice of periodic constraint assumed (i.e. quasi "simply supported") automatically demands the leaky wave reflection coefficient at the cylinder end be unimodular, i.e. for our purposes $|B| = 1$. This can be shown in the following way. The quasi "simply supported" boundary condition (BC) requires that the radial and azimuthal component of the displacement vector, as well as the axial stress resultant, vanish at the cylinder truncation. In terms of the notation of Chapter 5 one requires that

$$\begin{aligned} u_\rho\big|_{z = \pm L/2} &= 0 \\ u_\psi\big|_{z = \pm L/2} &= 0 \qquad \text{Quasi simply supported BC.} \\ T_{zz}\big|_{z = \pm L/2} &= 0 \end{aligned} \tag{7.8)(a)-(c}$$

Consider the intensity vector for simple isotropic elastic fields[83,84]

$$\boldsymbol{I} = -\left(\frac{\partial \boldsymbol{u}}{\partial t}\right) \cdot \underset{\sim}{\boldsymbol{T}} \,. \tag{7.9)(a)-(c}$$

Here $\boldsymbol{u}$ is the displacement vector and $\underset{\sim}{\boldsymbol{T}}$ is the stress dyadic. The intensity vector is often called the structural intensity. Its rigorous definition is the density of energy flow in the elastic field and has units of power per unit area. It is analogous to the Poynting vector in electromagnetics[77]. The time averaged power flow through the end of the cylindrical shell (surface S with area element dA) is then given by

$$\overline{\mathrm{P}_z\big|_{z = \pm L/2}} = \overline{\int_S \pm(\hat{z} \cdot \boldsymbol{I}) dA} = \overline{\int_S -\left(\frac{\partial u_\rho}{\partial t} T_{\rho z} + \frac{\partial u_\psi}{\partial t} T_{\psi z} + \frac{\partial u_z}{\partial t} T_{zz}\right) dA} \,. \tag{7.10)(a)-(c}$$

Because u_ρ, u_ψ, and T_{zz} must vanish on the end surfaces S, by Eqs. (7.8)(a)-(c), the total time averaged power flow through each end vanishes identically. This then forces any leaky wave reflection coefficient to be unimodular, provided conversion of energy to other modes is not allowed. This fact may be a deficiency in modeling actual finite cylinders,

where energy transmission through the end as well as mode conversion occur, but in the present case simplifies the comparison with the ray theory result, in which the reflection coefficient is an independent parameter.

7.4 Meridional Ray Amplitudes: Empty and Water-Filled Shell

The two theoretical results just discussed will now be compared with the experimental results. Two cases are examined: 1) air-filled shell with endcaps, and 2) water-filled shell with no endcaps. In both instances the shell examined is Shell A, which the reader will recall is the thinner of the two shells, having $h/a = 0.076$. For a hollow (i.e. air-filled) steel shell the sound transmitted into the interior does not play a major role in the far-field scattered pressure for the conditions of this experiment. The measured backscattering in the region near the a_0 meridional ray enhancement is fairly simple in that only one large peak is observed in both angle and time, as in Fig. 7.1, with smaller multiple peaks at lesser tilt angles. These smaller peaks, which incidentally are much larger for the thicker Shell B, are attributable to contributions from end-reflected helical waves of the a_0 (see Figs. 2.7 and 2.8 starting on page 27). When the shell is flooded with water (and the endcaps removed) the sound transmitted into the interior does play a major role in the backscattering. As was observed by Kaduchak[1] and Dodd[2] one finds several large enhancement signals delayed in time with respect to each other. This effect is manifest as multiple flashes or images delayed in time with respect to the initial meridional ray signal in the high-resolution sonar images of the finite cylinder examined in those investigations. In the present work these multiple enhancements are easily observed as individual wavepackets [see Figs. 7.16 (a) - 7.20 (a)]. This effect was attributed to multiple internal reflections through the interior fluid column in the meridional plane combined with the usual meridional ray reflection from the truncation and subsequent reradiation into the backscattering direction. This process will be discussed later.

Enhancement as a Function of Cylinder Aspect Angle

Figures 7.2 and 7.3 show experimental and theoretical results of an angle scan through the meridional ray peak for tone burst backscattering by an *air-filled* shell for six different frequencies. Once again, Section 7.A describes the method used to extract and normalize the scattering amplitudes (solid points) from the measured time series (e.g. from Fig. 7.1). Note that the amplitude scale is in terms of the form function with respect to a sphere having the same radius as the cylinder. This normalization has the significance that the form function for scattering from a rigid immovable sphere at high frequencies asymptotically approaches $|f| \approx 1$. The solid curve in each figure is the ray theory result

Table 7.1: a_0 meridional wavenumbers

Air-filled shell: n = 0 *infinite* cylindrical shell solutions; values in parentheses are for a plate with fluid loading on one side						
f (kHz)	ka	$k_l a$	αa	α/k_l	αL	μ
300	24.2542	20.2455 (20.3296)	0.7185 (0.7020)	0.0355	8.6	1.09
400	32.3390	24.4347 (24.4968)	0.5576 (0.5453)	0.0228	6.7	0.64
500	40.4237	28.4322 (28.4797)	0.4890 (0.4784)	0.0172	5.9	0.48
600	48.5085	32.3315 (32.3696)	0.4528 (0.4430)	0.0140	5.4	0.40
700	56.5932	36.1759 (36.2075)	0.4323 (0.4227)	0.0119	5.2	0.36
800	64.6780	39.9902 (40.0171)	0.4206 (0.4111)	0.0105	5.0	0.33
Shell A: c=1.4805, c_L=5.675, c_S=3.141 (mm/μs); a=19.05mm, h/a=0.076; L/a=12.0						

from Eq. (7.6). The leaky wave parameters used in the ray theory, k_l and α, are from the n = 0 solution of the dispersion relation for an infinite hollow cylindrical shell, Eq. (4.11) for $Re[k_z a]/a$ and $Im[k_z a]/a$ respectively, which correspond to the axial propagation of the a_0 leaky Lamb-type wave (see Figs. 4.3 and 4.9 and Table 7.1). Note, as in Chapter 6 wave

parameters for a flat plate of the same material and thickness are a very good approximation in this frequency range (see Table 7.1 for a comparison). The dashed curve in each figure corresponds to the approximate PWS solution of Chapter 5. One change has been made to the physical system in this case. The ray theory assumes the finite cylinder can be modeled as semi-infinite, i.e. leaky waves on the cylinder are too heavily damped for multiple lengthwise traversals to contribute to the leaky wave surface amplitude at any given point on the shell. This assumption is valid for $\alpha L \gg 1$, where the reader will recall that α is the spatial damping rate (i.e. the surface wave amplitude falls off generally as $e^{-\alpha z}$). In the present case αL ranges from about 8.6 at 300 kHz to 5.0 at 800 kHz. While large, these levels of damping may allow for some finite length effects to persist in the PWS calculation. To eliminate these possible perturbations to the scattering response and aid in the comparison with the ray theory, the length aspect ratio of the cylinder was increased to $L/a = 40$, from $L/a = 12$, in the PWS calculations. As an aside, the other assumption of the ray theory, $\alpha/k_l \ll 1$, is satisfied here where α/k_l ranges from 0.036 at 300 kHz to 0.011 at 800 kHz. See Table 7.1 for the actual wavenumbers used and the values of importance to the ray theory.

The agreement in amplitude and angular width between the ray theory and the approximate PWS calculation is excellent for each case, except at the lowest frequency where the tilt angles are large and the latter calculation begins to break down. In each case the ray theory always predicts slightly lower amplitudes than the PWS calculation. The cause of the small oscillations in the PWS calculation, which decrease in amplitude as the frequency increases, is not well understood. They are however related to $k_l L$. These oscillations do not appear to be present in the experimentally obtained amplitudes.

Table 7.2: a_0 meridional wavenumbers

Water-filled shell: n = 0 *infinite* cylindrical shell solutions*; values in parentheses are for a plate with fluid loading on both sides						
f (kHz)	ka	$k_l a$*	αa*	α/k_l	αL	μ
400	32.3718	24.4348 (24.4844)	1.1127 (1.0833)	0.0455	13.4	1.28
500	40.4647	28.4322 (28.4769)	0.9760 (0.9534)	0.0343	11.7	0.96
600	48.5577	32.3315	0.9040	0.0280	10.8	0.81
650	52.6042	34.2588 (34.2927)	0.8807 (0.8611)	0.0257	10.6	0.76
712	57.6218	36.6349	0.8555	0.0234	10.3	0.70
752	60.8590	38.1620 (38.1905)	0.8492 (0.8303)	0.0223	10.2	0.68
820	66.3622	40.7509	0.8367	0.0205	10.0	0.65
850	68.7900	41.8910 (41.9154)	0.8328 (0.8139)	0.0199	10.0	0.64

Shell A: c=1.479, c_L=5.675, c_S=3.141 (mm/μs); a=19.05mm, h/a=0.076; L/a=12.0

*Since the damping cannot be computed directly for the fluid-filled infinite cylindrical shell these values are for the hollow case with the damping multiplied by 2 to account for "symmetric" radiation into the interior fluid; the plate results have two sided fluid loading.

The experimental values (solid points), confirm the general amplitude and angular width of the enhancement peak over the range of frequencies shown and clearly support the theoretical approaches. It should be mentioned that because of the relatively simple automated approach used to extract these amplitudes from the sequence of time series records, which is discussed in an appendix, Section 7.A, only a small angular region, approximately 1° centered about the peak amplitude, may be considered to accurately represent steady state scattering amplitudes. For the remainder of the points, clearly the majority, the amplitudes should be regarded as close approximations of the true steady state values since it is possible that transients were included in the time-window averaging algorithm used to extract the steady state amplitude. For the small region around the peak

angle the extent of this window was checked manually to ensure that only the steady state region was included. The relative absence of scatter in the data points suggests that the transients are small compared with the steady state meridional ray amplitude. Examples of this steady state behavior during the tone burst may be seen in Section 7.5.

Comments will now be made concerning the apparent overall angular shift of the measured enhancement curve away from the theoretical curves towards lesser angles. First of all the angular shift apparent in Figs. 7.2 and 7.3 is actually quite small. It is only because a relatively narrow angular region is plotted that the shift is so apparent. When viewed on the global scale it is almost indistinguishable [e.g. see Fig. 7.7(c)]. Nonetheless a few comments are appropriate. This shift cannot be attributed to a systematic mechanical error in the angular positioning system. Nor can it be a result of the small geometric angle errors which result from the necessary finite source/receiver-to-target distance. It may be shown that this latter shift can in some cases be relatively large, on the order of $\gamma = 2°$ for the separation distances present in these experiments. However, the presence of this effect, which is discussed by Gipson in Ref. [47], was greatly reduced by shifting the source/receiver laterally with respect to the line containing the centers of the source/receiver and cylinder in order to coincide with the far cylinder end. The required shift distance may be calculated through simple geometry with knowledge of the expected peak enhancement angle, which is predicted by the ray and PWS theories. It is simply $d_{shift} = r_c \sin\delta_+$, where $r_c = \sqrt{(L/2)^2 + a^2}$ and $\delta_+ = (90° - \gamma) + \tan^{-1}(a/(L/2))$ (see Section 3.B). It is often sufficient to simply replace r_c by $L/2$ and δ_+ by 90°-γ whereby $d_{shift} \approx (L/2)\cos\gamma$. It is important to note that this shift is allowable in the present case since the backscattering mechanism of interest is confined to a small region of the cylinder near its far end (see Chapter 3). It is possible to account for a fair portion of the observable difference between the measured and calculated peaks with the uncertainty in which the material parameters of the shell are known. Standard off the shelf heat treated stainless steel tube stock (SS304, seamless) was used for the shell. Since highly accurate longitudinal and shear wave speeds could not be found for this material, non-specific published values were used. No attempt was made to measure the sound speeds by direct means due to the small wall thickness of

the specimens. A similar discrepancy between an exact theory and a measured quantity which may be attributed to insufficient knowledge of the material parameters may be seen in Fig. A.14 on page 299. It is the author's opinion that the experimental results do not provide evidence which suggests the ray theory or PWS theory need correction for the present cases.

Figures 7.5 and 7.6 show results similar to Figs. 7.2 and 7.3 but are for a *water-filled* shell (also Shell A) with no endcaps. The analysis in this case is more complex than for the air-filled shell and will be discussed in the following section. For now it is sufficient to note that the same analysis technique applies to the water-filled shell and the results are quite similar. There are no PWS results shown for this case since that approach cannot be applied directly to the water-filled shell without endcaps. In the PWS formulation there is no way to account for the loss of energy from the interior fluid through the open ends of the cylindrical shell. As a result in the PWS formulation total reflection of compressional waves within the interior fluid occurs at the ends and the backscattering response is very complicated for nearly all tilt angles.

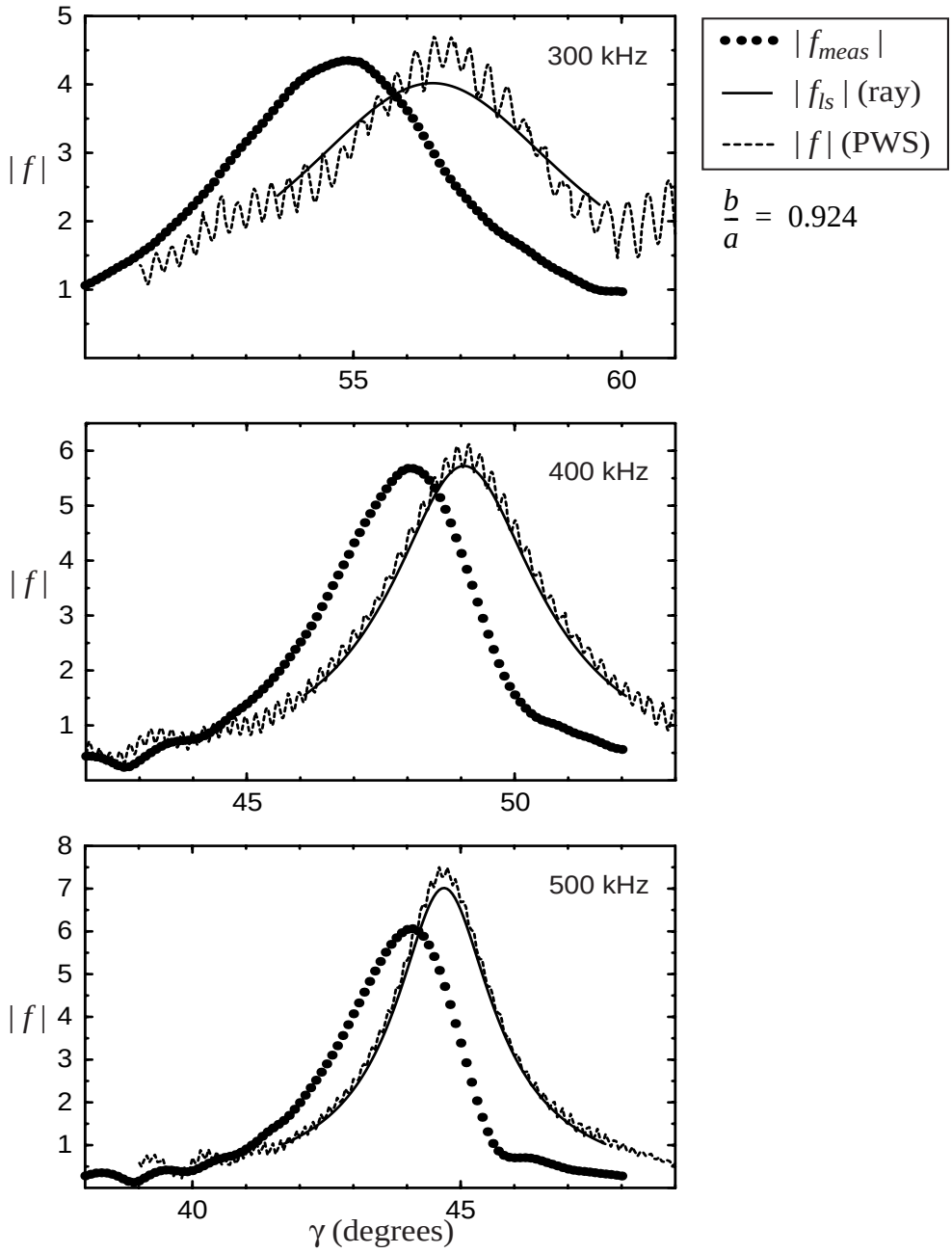

FIG. 7.2 Backscattered (monostatic) meridional ray enhancement of the a_0 for an *air-filled* finite cylindrical shell (Shell A in this case). Solid points are experimental values obtained with tone burst measurements; the continuous line is the result of the ray formulation using the infinite cylinder wavenumbers $k_l a$ and αa from Table 7.1; and, the dashed line is the result of the approximate PWS solution described in Chapter 5. Both the ray and PWS solutions use $|B| = 1$.

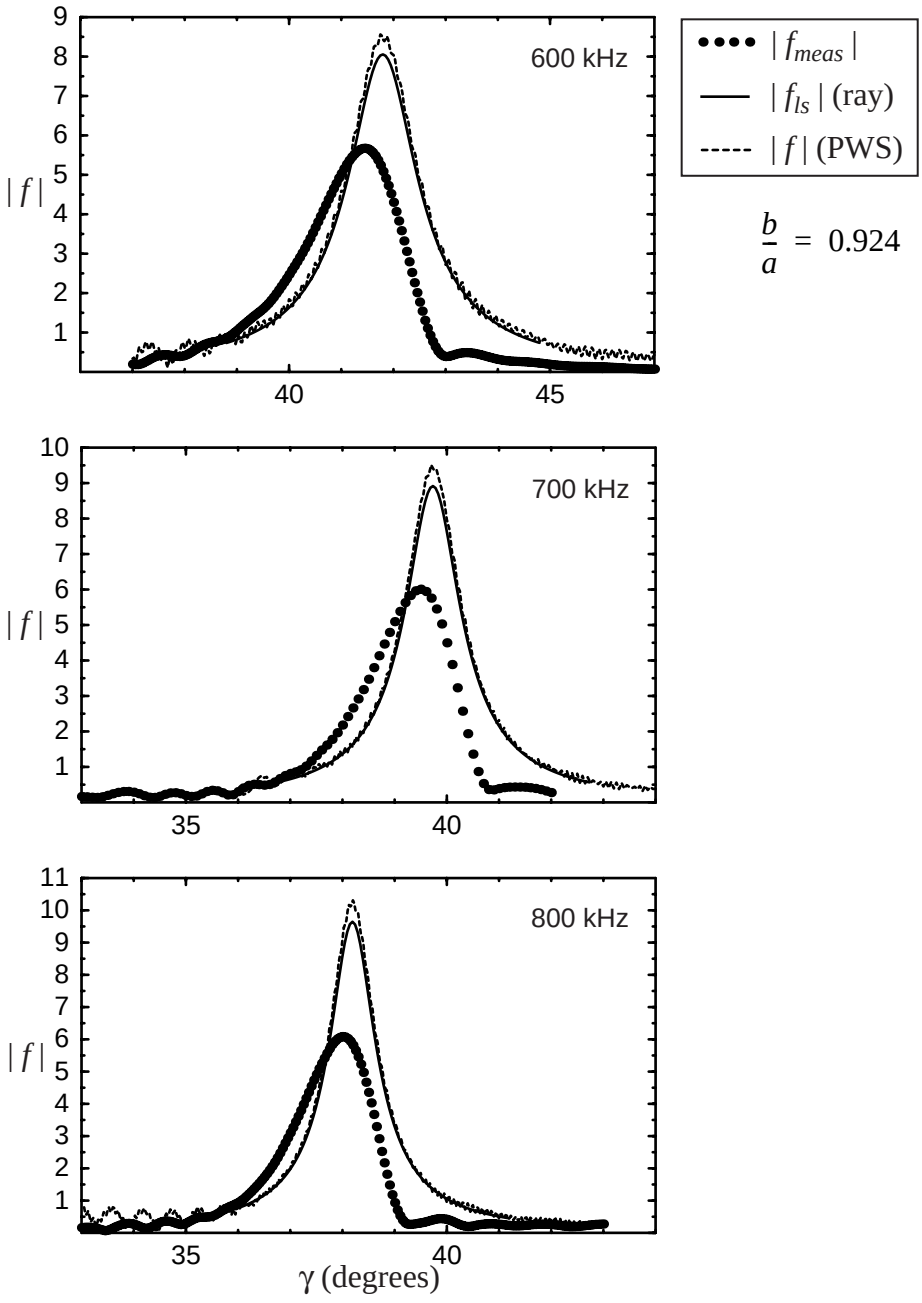

FIG. 7.3 Backscattered (monostatic) meridional ray enhancement of the a_0 for an *air-filled* finite cylindrical shell (Shell A in this case). Solid points are experimental values obtained with tone burst measurements; the continuous line is the result of the ray formulation using the infinite cylinder wavenumbers $k_l a$ and αa from Table 7.1; and, the dashed line is the result of the approximate PWS solution described in Chapter 5. Both the ray and PWS solutions use $|B| = 1$.

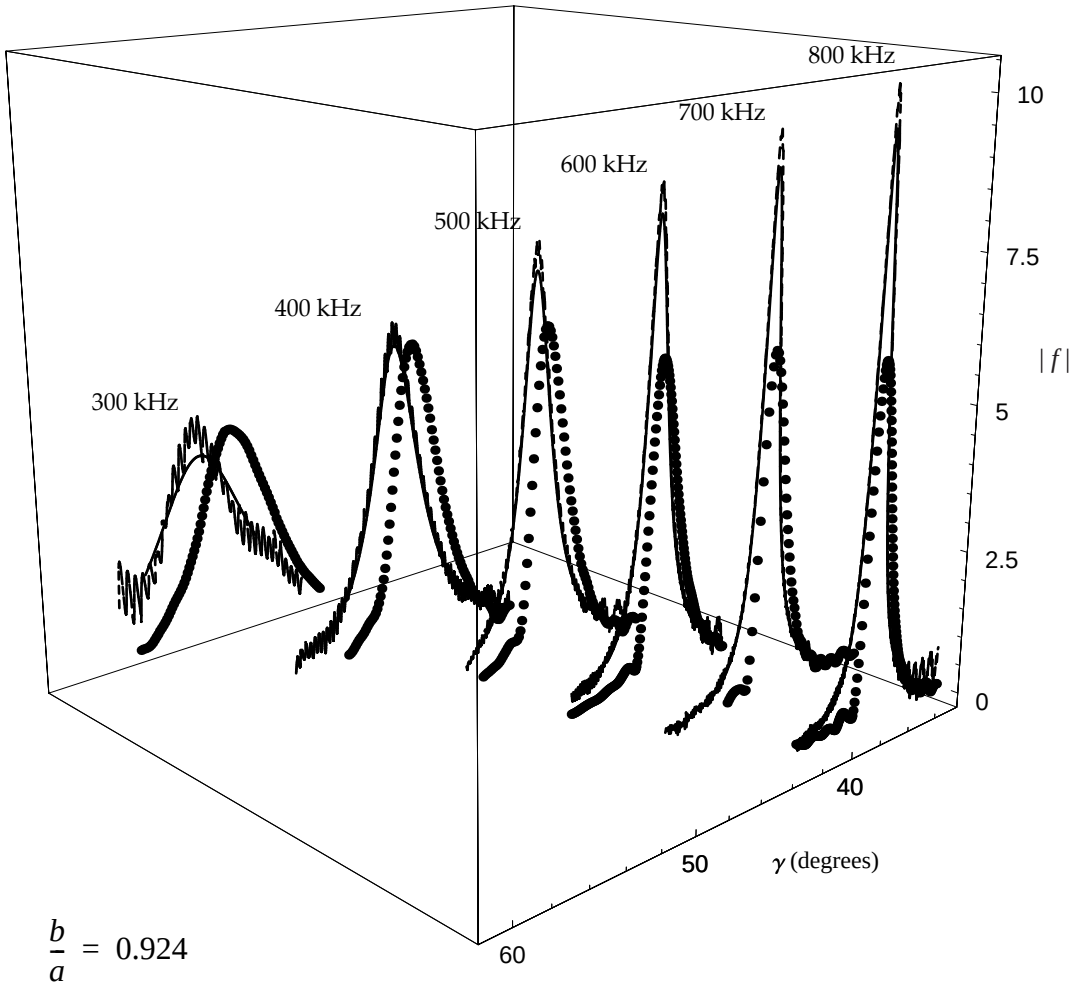

FIG. 7.4 Three dimensional representation of the backscattered meridional ray enhancements for an *air-filled* finite cylindrical shell. From Figs. 7.2 and 7.3 for Shell A.

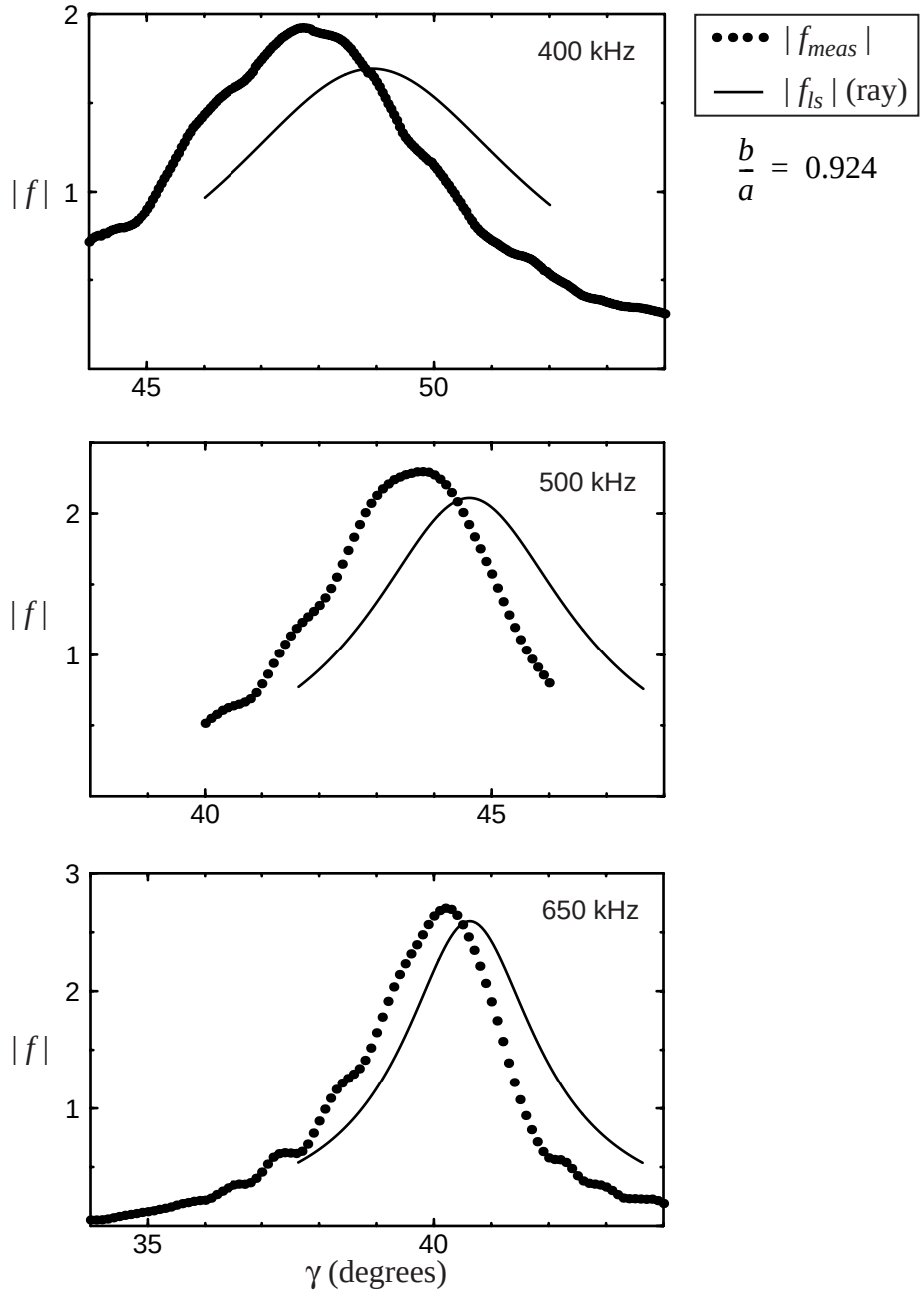

FIG. 7.5 Backscattered (monostatic) meridional ray enhancement of the a_0 for a *water-filled* finite cylindrical shell (Shell A in this case) having no endcaps. Solid points are experimental values obtained with tone burst measurements; the continuous line is the result of the ray formulation (with $|B| = 1$) using the infinite cylinder wavenumbers $k_l a$ and αa from Table 7.2.

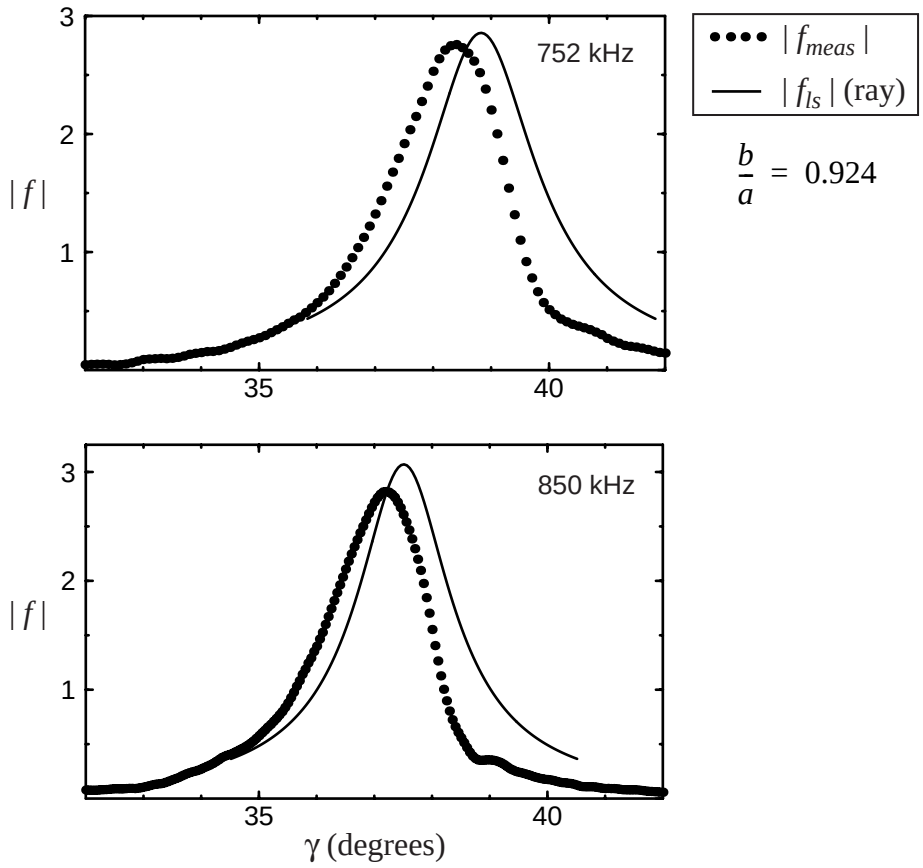

FIG. 7.6 Backscattered (monostatic) meridional ray enhancement of the a_0 for a *water-filled* finite cylindrical shell (Shell A in this case) having no endcaps. Solid points are experimental values obtained with tone burst measurements; the continuous line is the result of the ray formulation (with $|B| = 1$) using the infinite cylinder wavenumbers $k_l a$ and αa from Table 7.2.

Peak Enhancement as a Function of Frequency

The preceding figures have shown how the a_0 meridional ray enhancement behaves as a function of tilt angle for a number of fixed frequencies. These enhancement curves compare well with the theoretical approaches in both location, amplitude and angular width. One aspect of these figures not previously discussed is the dependence of peak amplitude on frequency. It is important to study this aspect of the behavior because certain phenomena are expected to limit the meridional (and helical) ray enhancement as the frequency is changed, such as mode conversion of the a_0 to other Lamb waves upon reflection from the end or losses at the ends due to the presence of the endcaps and radiation into the fluid.

For the case of a meridional Rayleigh wave on a tilted solid cylinder this comparison is rather straightforward due to the fact that the Rayleigh wave in this case is nearly dispersionless at mid to high frequencies. This has the consequence that the meridional Rayleigh wave enhancement occurs at nearly a fixed tilt angle [recall Eq. (7.1)]. The frequency dependence of the enhancement is then fairly direct. Marston[5,7] compared the exact PWS solution with his ray theory for the case of backscattering in the meridional plane, $\gamma = \theta_l$, from an infinite solid cylinder and found in both cases a smooth monotonic increase in the form function with increasing frequency (see Figs. 3 and 4 Ref. [5] and Fig. 2 of Ref. [7]). For the present case of an air-filled or water-filled cylindrical shell the particular enhancement mechanism studied is of course due to the a_0 leaky Lamb wave, which is highly dispersive in the frequency range of interest. As can be seen from Figs. 7.2 - 7.6, or simply Figs. 6.2 and 6.3, the angular location of the enhancement changes considerably with frequency, making a comparison with theory much more complex. At high frequencies it does approach a relatively constant angle, but this is beyond the range of frequencies presently studied.

An indication of the frequency behavior may first be gathered from the preceding figures, Figs. 7.2 - 7.6. One may notice a general increase in amplitude as the frequency increases. Furthermore, the amplitudes for the water-filled shell are considerably less than those for the air-filled shell. To address these frequency related issues in a more systematic

way another set of experiments was performed for both air and water-filled shells in which the peak enhancement was localized over a broader range of frequencies and compared with the predictions of the ray theory. In this way the frequency dependence of the enhancements becomes clearer and differences between the two cases are more apparent.

Using the same set-up just described the tilt angle of the cylinder was adjusted manually, together with the frequency, to localize the peak of the meridional ray enhancement in frequency-angle space. With reference to Fig. 2.4 or Fig. 3.3 the preferred method of localization may be chosen. At high frequencies, where the angle of peak enhancement is slowly varying, the tilt angle was adjusted to maximize the meridional ray signal in the time domain. At lower frequencies the condition for peak enhancement is best found by varying the tone burst frequency for a given angle. Once the peak was found a time record was averaged over many bursts to increase signal-to-noise and then downloaded to a computer and analyzed. The approximately steady state amplitude of the meridional ray enhancement was extracted from the time record as before and normalized.

Figure 7.7 shows the results of these experiments for the air-filled shell while Fig. 7.8 shows the similar results for the water-filled shell. Plotted in (a) in each figure are the measured (solid points) and calculated (open circles) form function with the same normalization as before (i.e. with respect to a rigid sphere). The calculated form function is from the ray theory, again using wave parameters from the $n = 0$ solutions of the infinite hollow cylindrical shell dispersion relation, examples of which are found in Tables 7.1 and 7.2. These use $|B| = 1$. The continuous solid curve is the same ray theory result only the wave parameters are taken from the doubly fluid-loaded flat plate problem. The a_0 leaky Lamb wave roots for the doubly fluid-loaded infinite elastic plate problem (Ref. [65]) were evaluated for a plate having the same material and thickness as the shell. The damping rate for the air-filled shell case only, Fig. 7.7, was approximated by multiplying the plate damping rate by $1/2$. For the doubly fluid-loaded plate, the leaky wave radiates energy into the fluid on both sides of the plate. When the fluid loading is light, as for the case of steel in water, it is often a good approximation to reduce the damping by a factor of 2 to account for the drop in radiation into the fluid on only one side of a one-sided fluid-loaded

FIG. 7.7 *Air-filled* shell results (Shell A, $b/a = 0.924$, *with endcaps*) for the a_0 meridional ray from tone burst measurements. (a) Form function magnitude at the peak enhancement angle as a function of frequency. The solid points are the experimental data; open circles are the results of the ray approximation using wavenumber values from the a_0, $n = 0$ dispersion curves from Chapter 4 (see Fig. 4.3) for an empty infinite cylindrical shell with exterior fluid loading (some of which are in Table 7.1). The dashed line is the same ray approximation with $|B| = 1$ using wavenumbers for a plate fluid loaded on both sides (again see Table 7.1), and the solid curve is this dashed line using the approximate reflection coefficient in (b). (b) Inferred and approximate calculated reflection coefficient for reflection of the a_0 leaky Lamb wave off the cylinder truncation. The solid line corresponds to the approximate calculation of Chapter 8 for a semi-infinite *free* plate of the same thickness as the shell. (c) Peak enhancement angle. The solid line is for a plate fluid loaded on both sides.

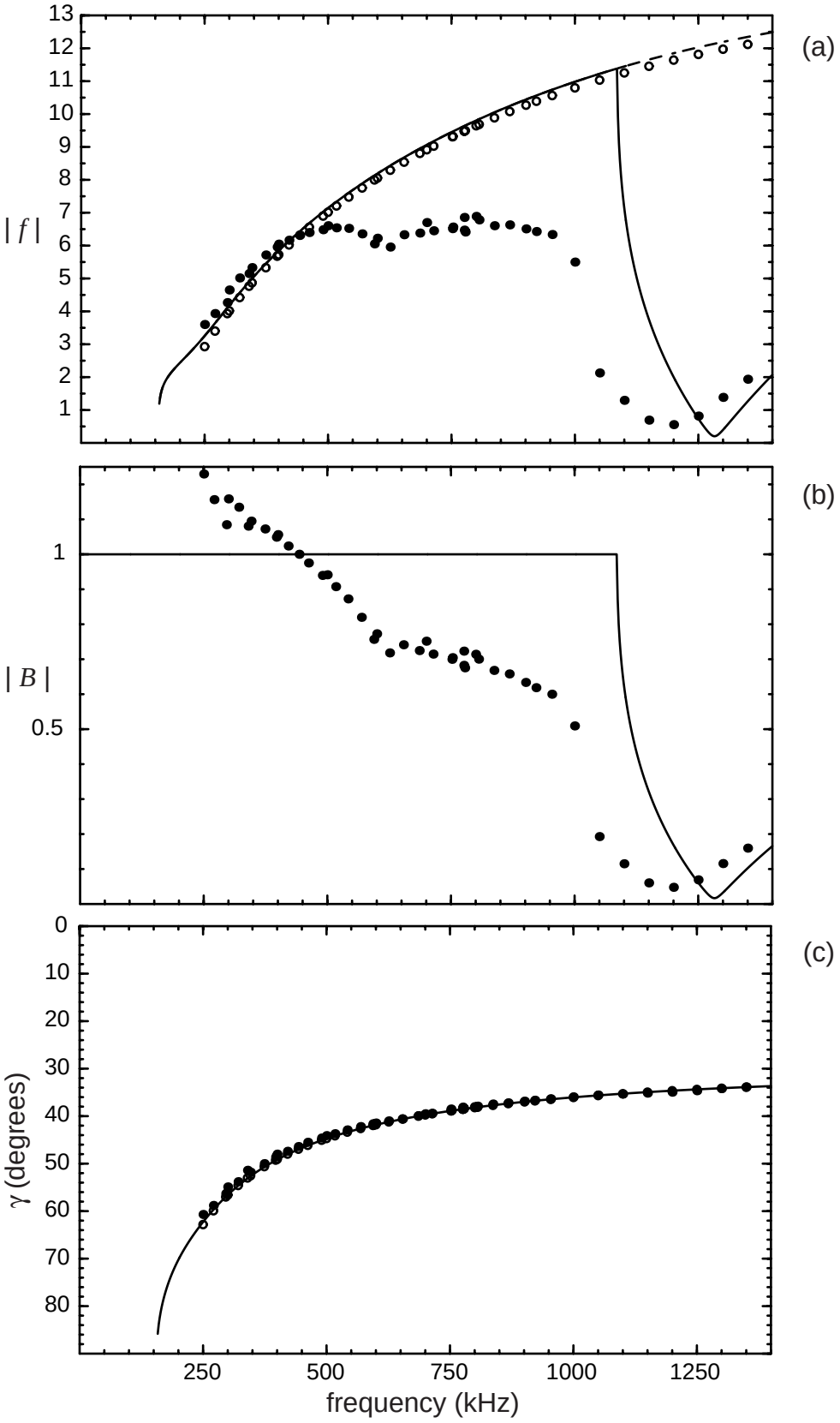
(a)
| f |
13
12
11
10
9
8
7
6
5
4
3
2
1
(b)
| B |
1
0.5
(c)
γ (degrees)
0
10
20
30
40
50
60
70
80
250
500
750
1000
1250
frequency (kHz)

FIG. 7.8 *Water-filled* shell results (Shell A, $b/a = 0.924$, *without endcaps*) for the a_0 meridional ray from tone burst measurements. (a) Form function magnitude at the peak enhancement angle as a function of frequency. The solid points are the experimental data; open circles are the results of the ray approximation using wavenumber values from the a_0, $n = 0$ dispersion curves from Chapter 4 (see Fig. 4.3) for an *empty* infinite cylindrical shell with exterior fluid loading with *twice the damping* (see the text for an explanation; some wavenumber values may be found in Table 7.2). The dashed line is the same ray approximation with $|B| = 1$ using wavenumbers for a plate fluid loaded on both sides (again see Table 7.2), and the solid curve is this dashed line using the approximate reflection coefficient in (b). (b) Inferred and approximate calculated reflection coefficient for reflection of the a_0 leaky Lamb wave off the cylinder truncation. The solid line corresponds to the approximate calculation of Chapter 8 for a semi-infinite *free* plate of the same thickness as the shell. (c) Peak enhancement angle. The solid line is for a plate fluid loaded on both sides.

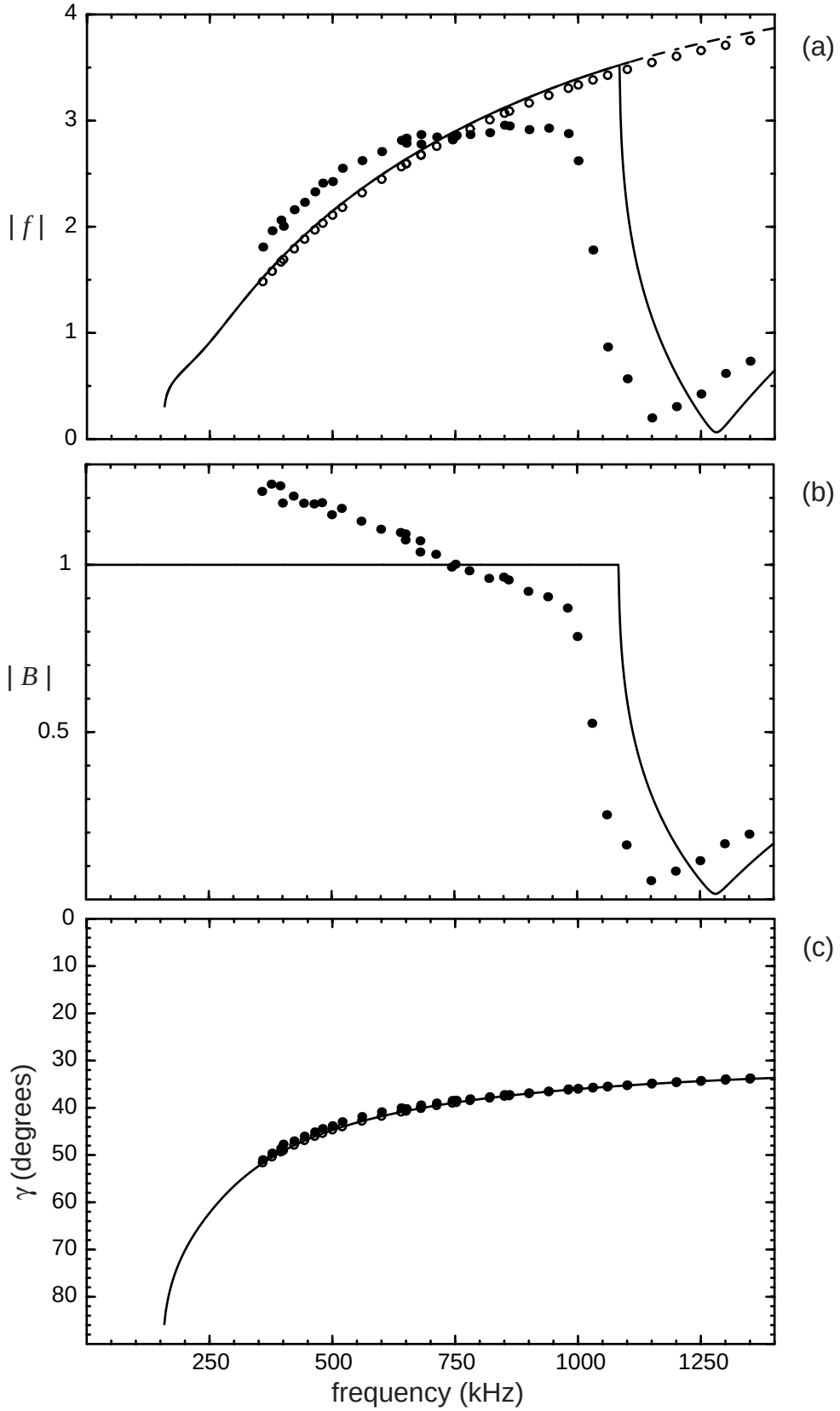
(a)
| f |
4
3
2
1
0
(b)
| B |
1
0.5
(c)
γ (degrees)
0
10
20
30
40
50
60
70
80
250
500
750
1000
1250
frequency (kHz)

plate. [An alternative would be to evaluate the roots of the asymmetrically fluid loaded plate; however, the dispersion relation for the like-fluid doubly fluid-loaded plate problem is far simpler and easier to work with. The differences between the two cases is not significant for the shell thickness and frequency ranges examined here (see Tables 7.1 and 7.2).] The dashed curve in Figs. 7.7 and 7.8 is the solid curve multiplied by an approximate leaky wave end-reflection amplitude coefficient for the a_0, which is shown as the solid curve in (b). This amplitude reflection coefficient, $|B|$, is calculated by satisfying the boundary conditions at the edge of a semi-infinite *free* plate by an approximation discussed in Chapter 8. The solid points in (b) are an inferred reflection coefficient based on the ray theory. Simply put, the measured form function, in which the actual leaky wave reflection process is unknown, is divided by the corresponding ray theory form function for which $|B| = 1$. This yields an estimate of the actual leaky wave reflection coefficient based on the ray theory. It is not intended to be a serious estimate of the reflection coefficient, which could be measured by other accurate means, at least for a plate. Rather it is intended to give the reader a better feeling for the physical behavior of the system. In the last panel of these figures is shown a comparison of the location in frequency-angle space of the peak enhancement. The solid points are again the experimental data while the open circles are locations determined by phase matching considerations [Eq. (7.1)] using the calculated dispersion curve for an infinite cylindrical shell. The latter are nearly indistinguishable on the scale plotted. The solid curve is the corresponding calculated position from phase matching to the a_0 leaky Lamb wave on the doubly fluid-loaded plate.

In general one may identify characteristics of the a_0 meridional ray enhancement from these figures. As the frequency increases the peak meridional ray amplitude increases smoothly for both the air-filled and water-filled shells just as in the case for the solid cylinder. The amplitudes for the air-filled shell are approximately 2 to 3 times those of the water-filled shell. This can be understood by examining the behavior of the ray theory for the two cases. In the present case, as has been discussed, it is a good approximation to account for the interior fluid by multiplying the damping rate by 2 and dividing the form function expression by 2. An idea of the difference in form function magnitude in the two

cases may then be made by considering the quantity

$$|f_{rel}| = \frac{|f_{hollow}|}{|f_{fluid-filled}|} \approx \frac{|f_{ls}(k_l, \alpha)|}{(1/2)|f_{ls}(k_l, 2\alpha)|} = 2\sqrt{2}\frac{F_e(\mu)}{F_e(2\mu)} \qquad (7.11)(a)\text{-}(c)$$

where α and μ are evaluated for the hollow case. Figure 7.9 shows a plot of $|f_{rel}|$ over a

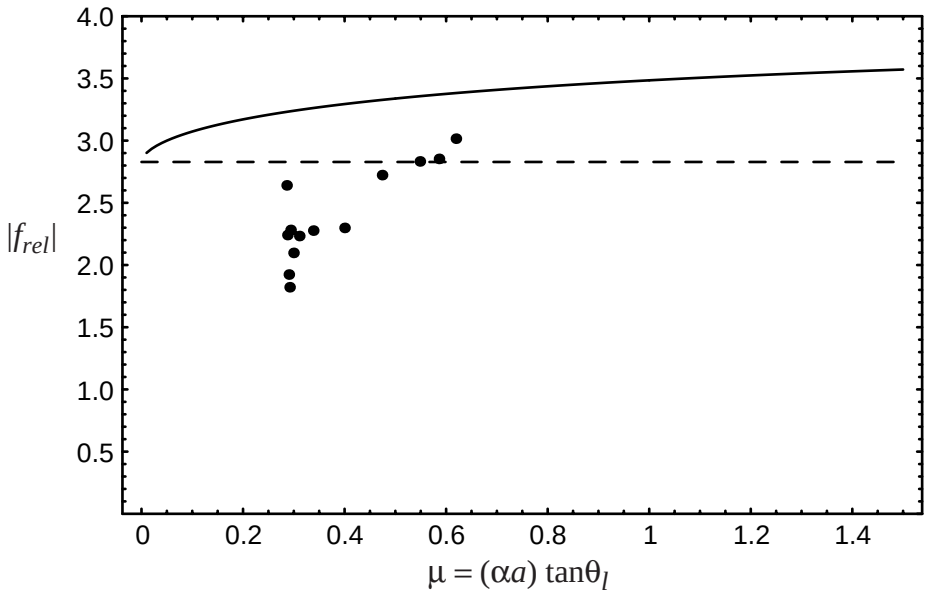

FIG. 7.9 Relative form function magnitude of the meridional ray enhancement in the meridional plane ($\gamma = \theta_l$) between a fluid-filled and hollow finite cylindrical shell. The dashed line is $|f_{rel}| = 2\sqrt{2}$. The points are experimentally obtained approximate values from Figs. 7.7 and 7.8. In general when the fluid loading is light and the dispersion curves for leaky waves on the fluid-filled shell can be obtained from the hollow shell dispersion curves, the meridional ray form function for the hollow shell is 2.8 to 3.6 times as great as for the fluid-filled shell. This reduction for the fluid-filled shell is mostly due to the additional radiation into the fluid interior, which gives rise to the $2\sqrt{2}$ factor in Eq. (7.11).

range of values of μ containing the present experiments. Higher frequencies correspond to lower values of μ in this case. The fairly large decrease in form function magnitude in the water-filled case can thus be seen to be mostly due to the additional radiation of the meridional leaky wave into the fluid interior, which leads to the factor $2\sqrt{2}$ in Eq. (7.11). The solid points are experimentally obtained approximate values for several of the data points found in Figs. 7.7 and 7.8. These are plotted with the use of Eq. (7.4) for μ, where for

each frequency the coupling angle θ_l is the experimentally determined coupling angle [Fig. 7.7 (c)] in the hollow shell case and the damping αa is taken to be the theoretical damping value for the hollow infinite cylindrical shell (some values of which are found in Table 7.1). Recall that αa is a rather slowly varying function in this frequency range [see the curve for Im[$k_z a$], which in the present notation is αa, for the $n = 0$ curve of the a_0 above $ka \approx 30$ in Fig. 4.3].

Two other interesting features of Figs. 7.7 and 7.8 are apparent. The first is the general roll-off of the measured form function at about 500 kHz for the air-filled case. There is a similar roll-off in the water-filled case at about 700 kHz but it is not nearly as pronounced. The difference in the two cases is more apparent in the inferred reflection coefficient plots. In each case the ray theory prediction of the form function is slightly less than the measured values at low frequencies, which leads to the un-physical interpretation that $|B| > 1$. Ignoring this behavior for the moment, if the ray theory approach applies equally well to the water-filled case as it does to the air-filled case, one would expect the inferred reflection coefficient to remain unchanged between the two cases. This is not the case as the air-filled shell results drop to lower values more quickly. The explanation for this behavior is most likely that the endcaps are influencing the leaky wave end-reflection mechanics. Recall that there are Plexiglas™ endcaps present for the air-filled shell and no endcaps at all for the water-filled shell. Even though the contact between the endcap and shell is mostly a "soft" boundary which uses an O-ring, it must still be degrading the end-reflection of the a_0 meridional wave. An additional set of experiments for a water-filled shell *with* endcaps could be performed to definitively resolve this issue. Since a thorough understanding of the leaky wave end-reflection process is not a principal purpose of this dissertation, no further experiments were carried out. The second interesting feature of these figures is the very sharp drop in the measured form function (and reflection coefficient) at 1 MHz. This feature is apparently not affected by the interior fluid loading. The clue to its origin comes from the dispersion curves of Figs. 4.3 and 4.4 on page 101. At about $ka = 87.5$, or $f = 1.08$ MHz, the a_1 leaky Lamb wave becomes propagating. It is known that when a Lamb wave on a *free* plate reflects from a truncation it may be partially

converted to a different mode of the same symmetry[85-90]. When all the other modes are non-propagating it is mostly the same mode which is reflected from the end. However, if another mode is propagating then a large portion of the energy can be reflected in this other mode. This will be discussed in greater detail in Chapter 8. This same sharp drop in the reflection coefficient is mirrored, albeit at a slightly higher frequency, in the approximate calculated reflection coefficient (solid curve). Simply put, this frequency marks the onset of the a_1 mode at which the magnitude of the reflection coefficient for the a_0 drops due to mode conversion from the a_0 into the a_1. The reflected a_1 mode does not radiate into the direction of the receiver, due to it's higher phase velocity [see Fig. 4.3 (a)], and is not picked up in the measured backscattering. At the present time a direct measurement of the mode converted reflected a_1 in a bistatic scattering experiment has not been attempted.

Before leaving the discussion of the frequency dependence of the meridional ray amplitudes, the author would like to point out the overall large amplitude of the measured and predicted responses. Even with the presence of limiting factors, such as the effect of the endcap and mode conversion, the measured responses are up to 6 times (3 times) the magnitude of a rigid sphere having the same radius as the air-filled (water-filled) cylindrical shell. Other high frequency enhancement mechanisms such as the coincidence frequency[31,27,28] and backwards wave[34,91] enhancements for spherical shells can yield amplitudes of 3 to 6 times the reflection from a rigid sphere. But the present meridional ray enhancement is for reflection from a tilted cylindrical shell where by far the majority of the reflected energy propagates away in the specular direction away from a receiver in the backscattering direction. Even if the cylindrical shell is capped with hemispherical end pieces the present results suggest the meridional ray enhancement may be as large or larger than the specular reflection from the leading endcap.

It is possible the apparent shift in frequency between the measured and calculated locations of the a_1 mode threshold effect (i.e. the sharp drop in Figs. 7.7 and 7.8) may be due to insufficient knowledge of the actual thickness of the shell. The frequency for the a_1 mode threshold is sensitive to the shell wall thickness.

7.5 Meridional Ray Enhancements in the Time Domain

Besides investigating the meridional ray enhancement in the angle and frequency domains it is useful to go back and look at the time domain responses directly. This should give the reader a better feel for how the response directly manifests itself in scattering records and how it might be observed in other real systems.

The approximate PWS solution has already proven itself to be quite useful in modeling the scattering in the frequency-angle domain. It would also be useful to examine its predictions in the time-angle domain and make comparisons with the measured time records. The synthesis of the theoretical time signal from the complex valued form function is a fairly straightforward procedure[27,20]. To obtain the impulse response one need only evaluate an inverse FFT of the complex form function. For a specific incident pulse or burst one must first multiply the complex form function by the spectrum of the incident signal and then perform the inverse FFT. Section 7.B briefly discusses some important matters to consider in implementing the synthesis algorithm. Figure 7.10 shows a sample of the synthesized backscattering for a 20 cycle tone burst by Shell A (air-filled). The center frequency of the tone burst is 400 kHz (ka = 32.28) which places it just at the upper limit of the form function response seen in Fig. 2.4 on page 17. At this frequency the principal response is the a_0 meridional ray enhancement at about $\gamma \approx 49°$. Other smaller contributions will be present from the helical s_0 and T_0 waves as well. As can be seen by comparing this figure with the experimental results of Fig. 7.1 the synthesized response displays the majority of the important scattering features. The comparison cannot be made directly in this case as the excitation frequency for the experimental figure is 620 kHz as opposed to 400 kHz for the synthesis. The synthesis was performed at a lesser frequency because of time considerations involved in evaluating the partial wave series at high frequencies. Even in Fig. 7.10 the form function is undersampled (i.e. the sampling rate in ka is too coarse). This undersampling results in the "wrap-around" signals which are clearly evident in the figure at the non-causal early times. In the following computations

FIG. 7.10 Synthesized tone burst backscattering time series for Shell A (20 cycle square envelope burst having a center frequency of 400 kHz or $ka = 32.28$). Dynamic range shown is 55 dB with respect to the maximum response at broadside incidence. The corresponding form function is sampled at $\Delta ka = 0.05$ and has a maximum frequency of $ka = 45$. A raised cosine window was applied over the region of $38 < ka < 45$ to smooth the transition to $f = 0$ at $ka = 45$. The unphysical early time arrivals (before the nearest corner reflection t_B) which carry on in to the scattering regions are due to wrap-around effects in the inverse Fourier transform used to calculate this figure. Sampling the form function at smaller intervals ($\Delta ka < 0.05$) would improve the synthesis in this regard; doing so, however, makes for very lengthy computation times.

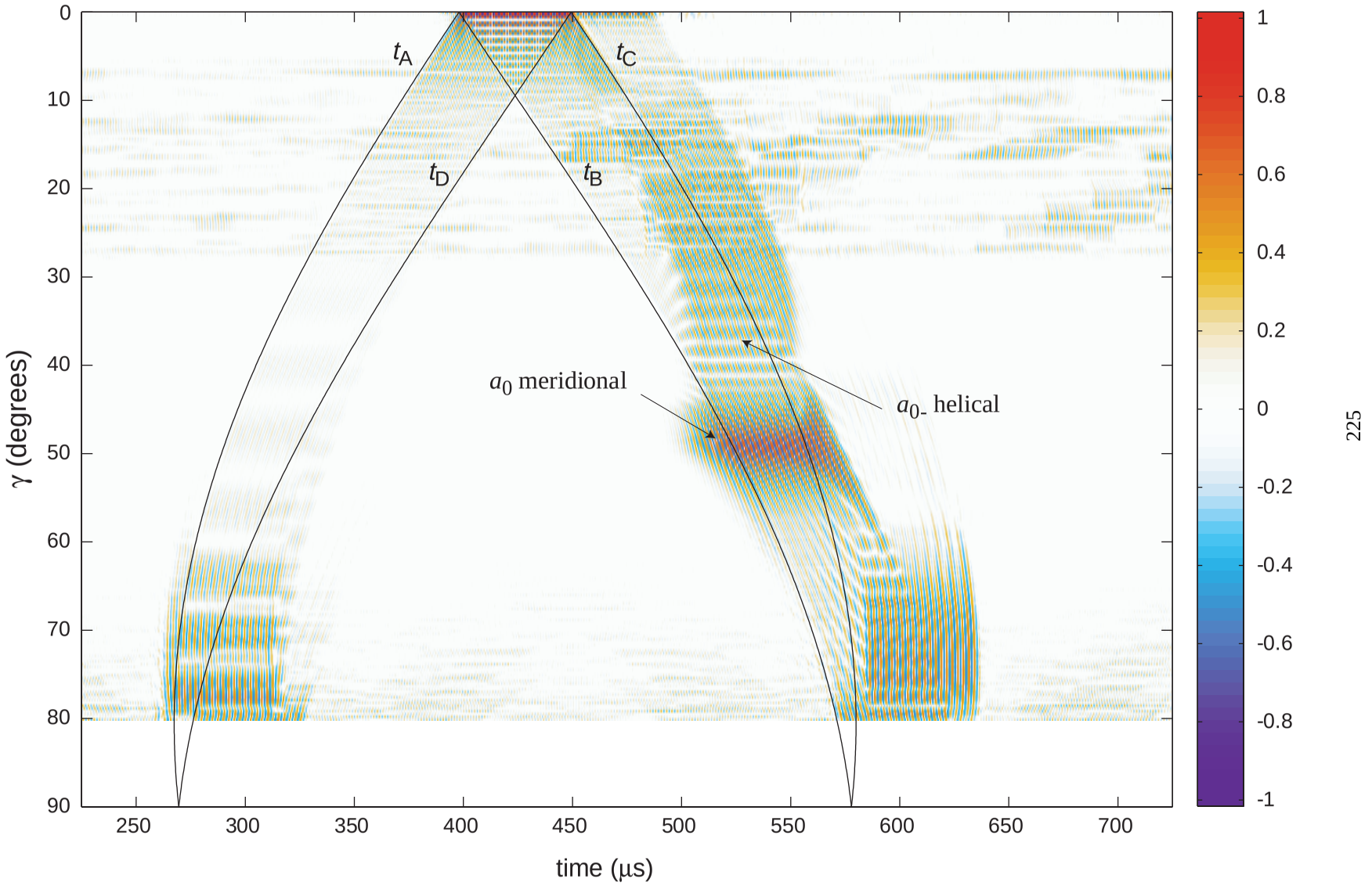
t_A
t_C
t_D
t_B
a_0 meridional
a_{0-} helical
γ (degrees)
time (μs)
0
10
20
30
40
50
60
70
80
90
250
300
350
400
450
500
550
600
650
700
1
0.8
0.6
0.4
0.2
0
-0.2
-0.4
-0.6
-0.8
-1
225

performed at a single tilt angle the sampling was increased and sufficient to avoid this effect for the most part.

Now that the global aspect of the scattering response has been confirmed in the theoretical synthesis it will be investigated how the theory and experiment compare at specific tilt angles. The feature studied here is the same a_0 meridional ray enhancement examined in the preceding sections and in most cases the frequencies and tilt angles are the same as in the angle scan figures, Figs. 7.2 - 7.6.

Air-Filled Cylindrical Shell

The first case to be considered is the air-filled shell with endcaps. The scattering in this case is relatively simple: the meridional ray enhancement is manifest as a single large feature well isolated in time from other effects. Figures 7.11 through 7.15 show the experimental and theoretical time records for five successive frequencies. The top figure is the experimental trace while the bottom figure is the synthesized trace. The respective frequencies and tilt angles are given. The time reference in these figures is the timing of the specular reflection at broadside incidence. In the experimental figures this time reference was obtained with a backscattering measurement at broadside incidence. For the synthesized time records it is relevant to note that the approximate PWS form function from Chapter 5 [Eq. (5.42)], from which these time records are synthesized, is time referenced to the center of the cylinder. Multiplying the form function by a phase factor ($e^{-i2(ka)}$) shifts the time reference to the outer radius a in the backscattering direction and thus references the backscattering time records to the broadside specular reflection. Typically the phase factor actually used was increased to ($e^{-i33(ka)}$) so that all reflections off the tilted cylinder would be present in the synthesized scattering records (i.e. the reflections off the front corners of the tilted cylinder near times t_A and t_D). This explains why the specular reflection at broadside in Fig. 7.10 is located at $t = (33-2)(a/c) = 399\,\mu s$. In Figs. 7.11 - 7.20 this additional time advance was taken into account. Panels (a) and (b) in Figs. 7.11 - 7.15 (and Figs. 7.16 - 7.20) each display 200 μs

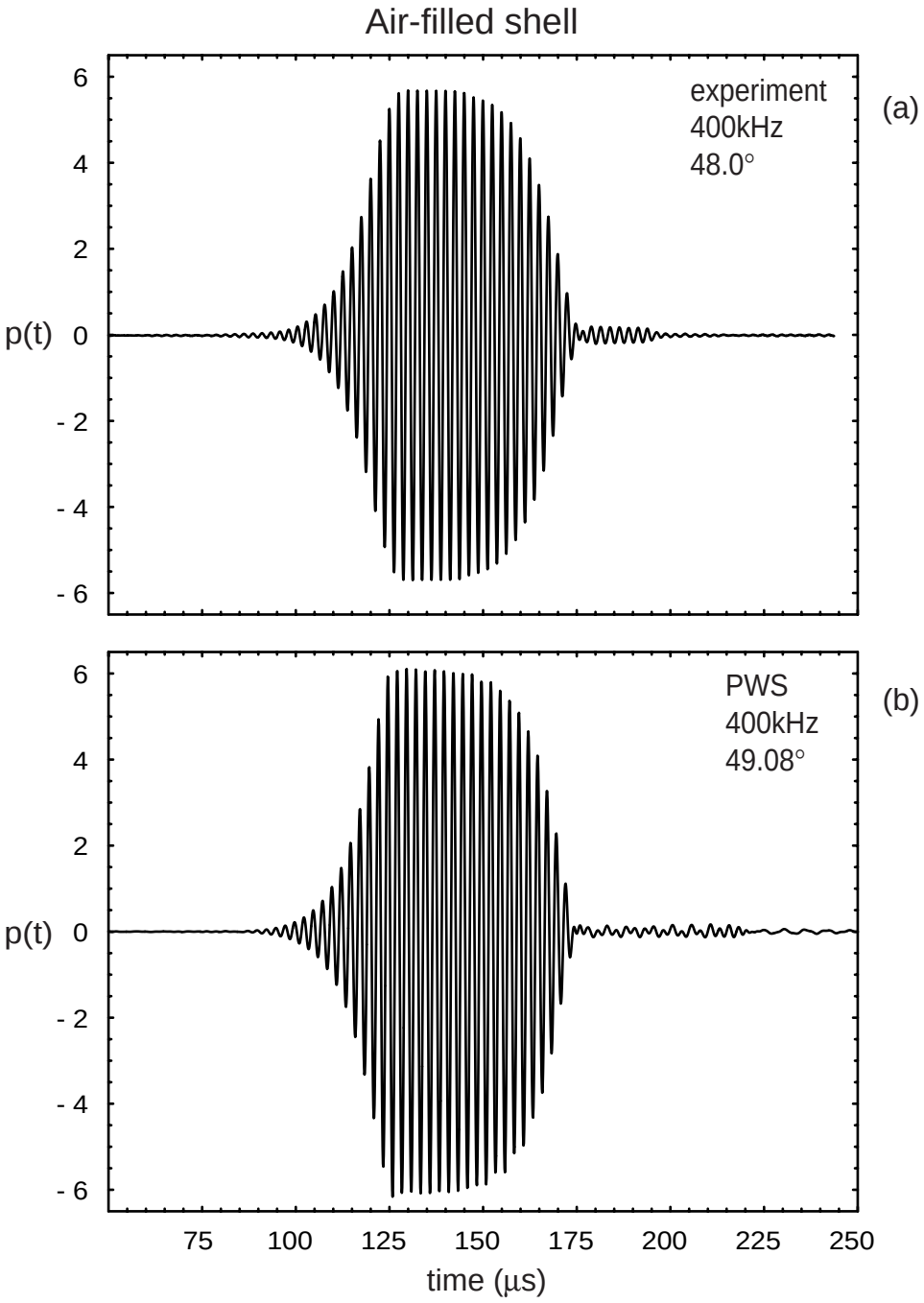

FIG. 7.11 (a) Measured backscattering time series at the peak meridional ray amplitude for Shell A (*air-filled with endcaps*) at $\gamma = 48.0°$ (see Fig. 7.2) for a 20 cycle tone burst having a center frequency of 400 kHz, and (b) approximate PWS synthesized time series for the same shell and incident burst at $\gamma = \theta_l = \sin^{-1}[(k_l a)/(ka)] = 49.08°$, where $k_l a$ is the infinite cylindrical shell wavenumber taken from Table 7.1 for this frequency. The time scale is referenced to the specular reflection from the cylinder at broadside incidence.

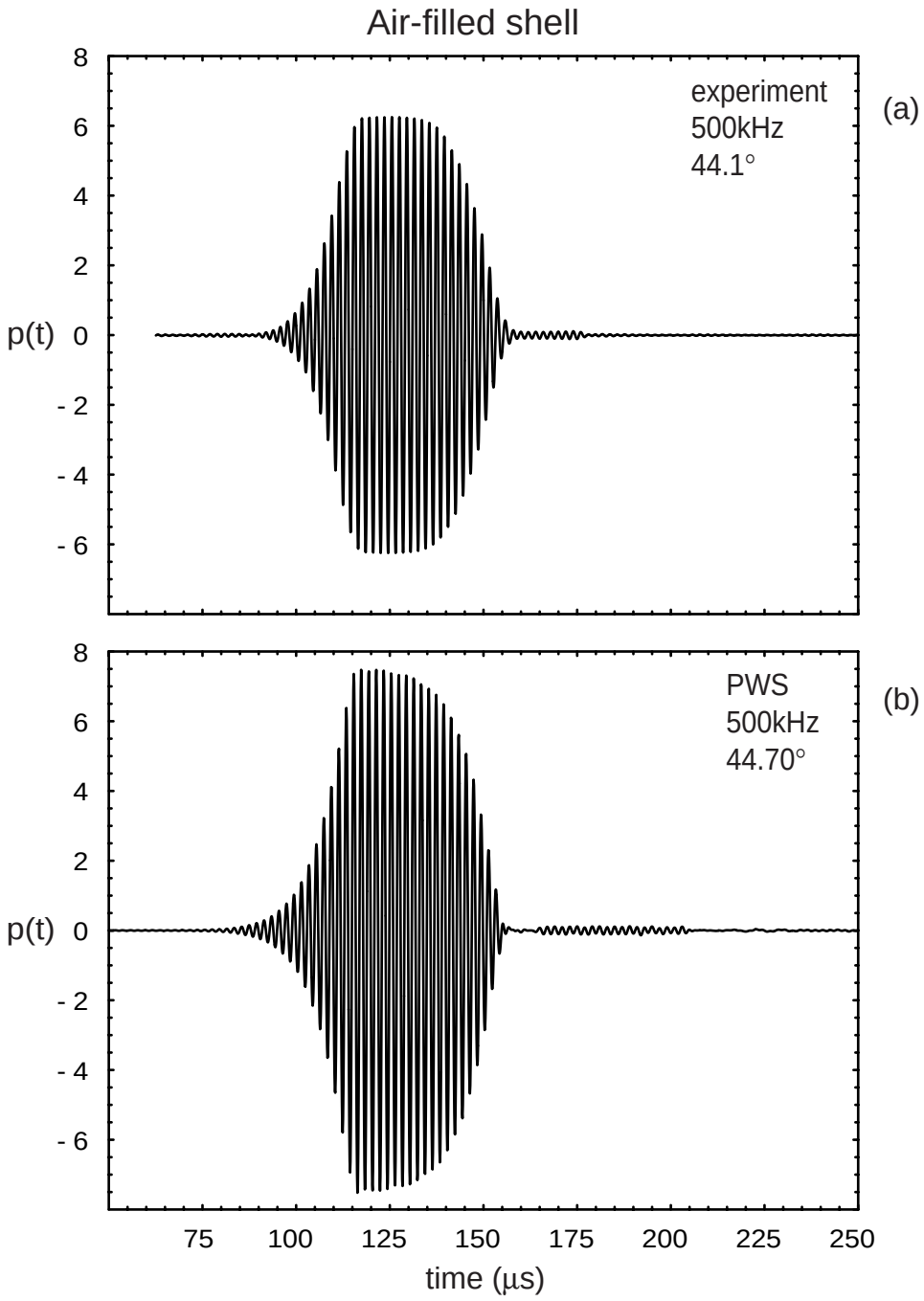

FIG. 7.12 (a) Measured backscattering time series at the peak meridional ray amplitude for Shell A (*air-filled with endcaps*) at $\gamma = 44.1°$ (see Fig. 7.2) for a 20 cycle tone burst having a center frequency of 500 kHz, and (b) approximate PWS synthesized time series for the same shell and incident burst at $\gamma = \theta_l = \sin^{-1}[(k_l a)/(ka)] = 44.70°$, where $k_l a$ is the infinite cylindrical shell wavenumber taken from Table 7.1 for this frequency. The time scale is referenced to the specular reflection from the cylinder at broadside incidence.

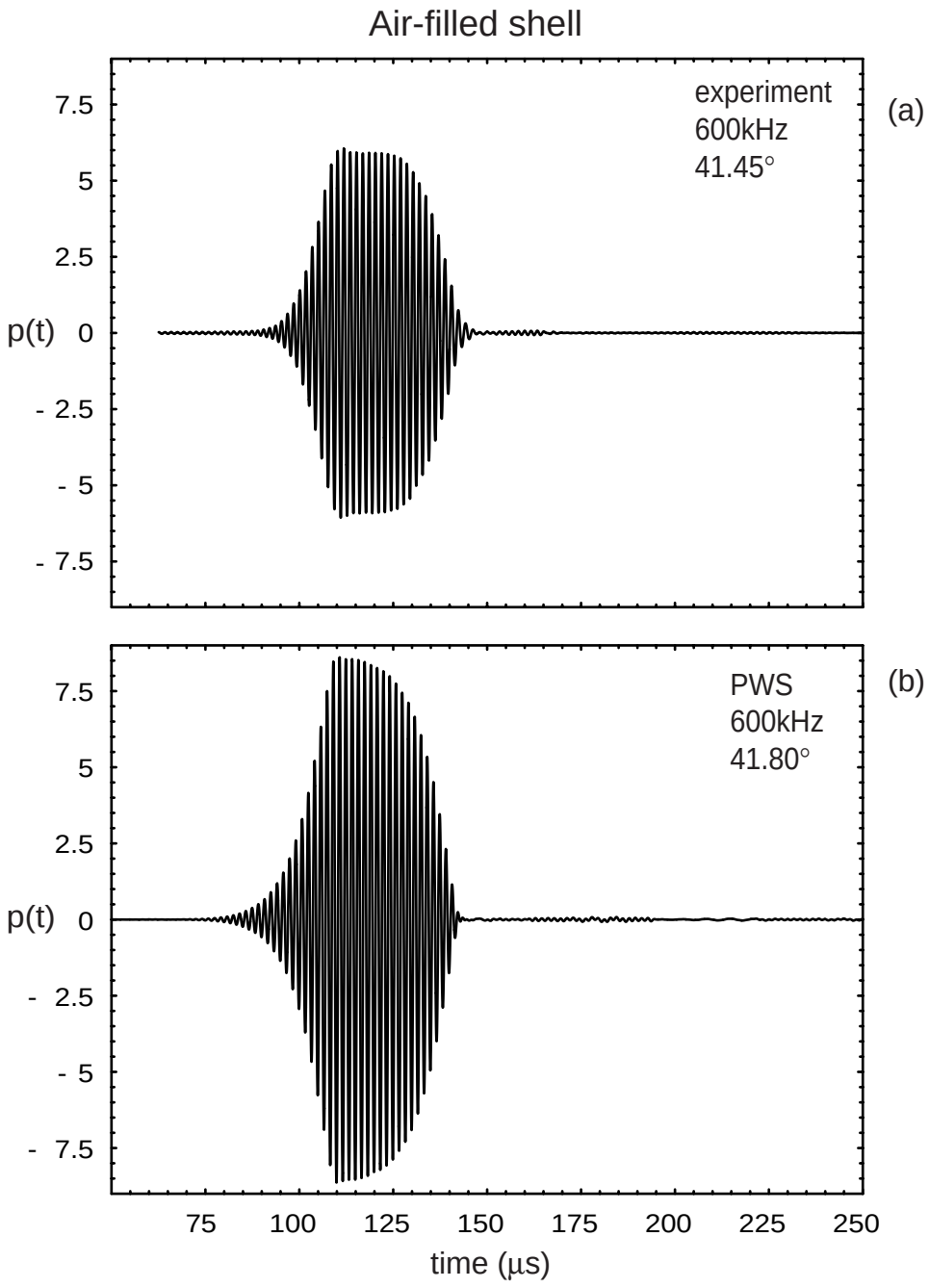

FIG. 7.13 (a) Measured backscattering time series at the peak meridional ray amplitude for Shell A (*air-filled with endcaps*) at $\gamma = 41.45°$ (see Fig. 7.3) for a 20 cycle tone burst having a center frequency of 600 kHz, and (b) approximate PWS synthesized time series for the same shell and incident burst at $\gamma = \theta_l = \sin^{-1}[(k_l a)/(ka)] = 41.80°$, where $k_l a$ is the infinite cylindrical shell wavenumber taken from Table 7.1 for this frequency. The time scale is referenced to the specular reflection from the cylinder at broadside incidence.

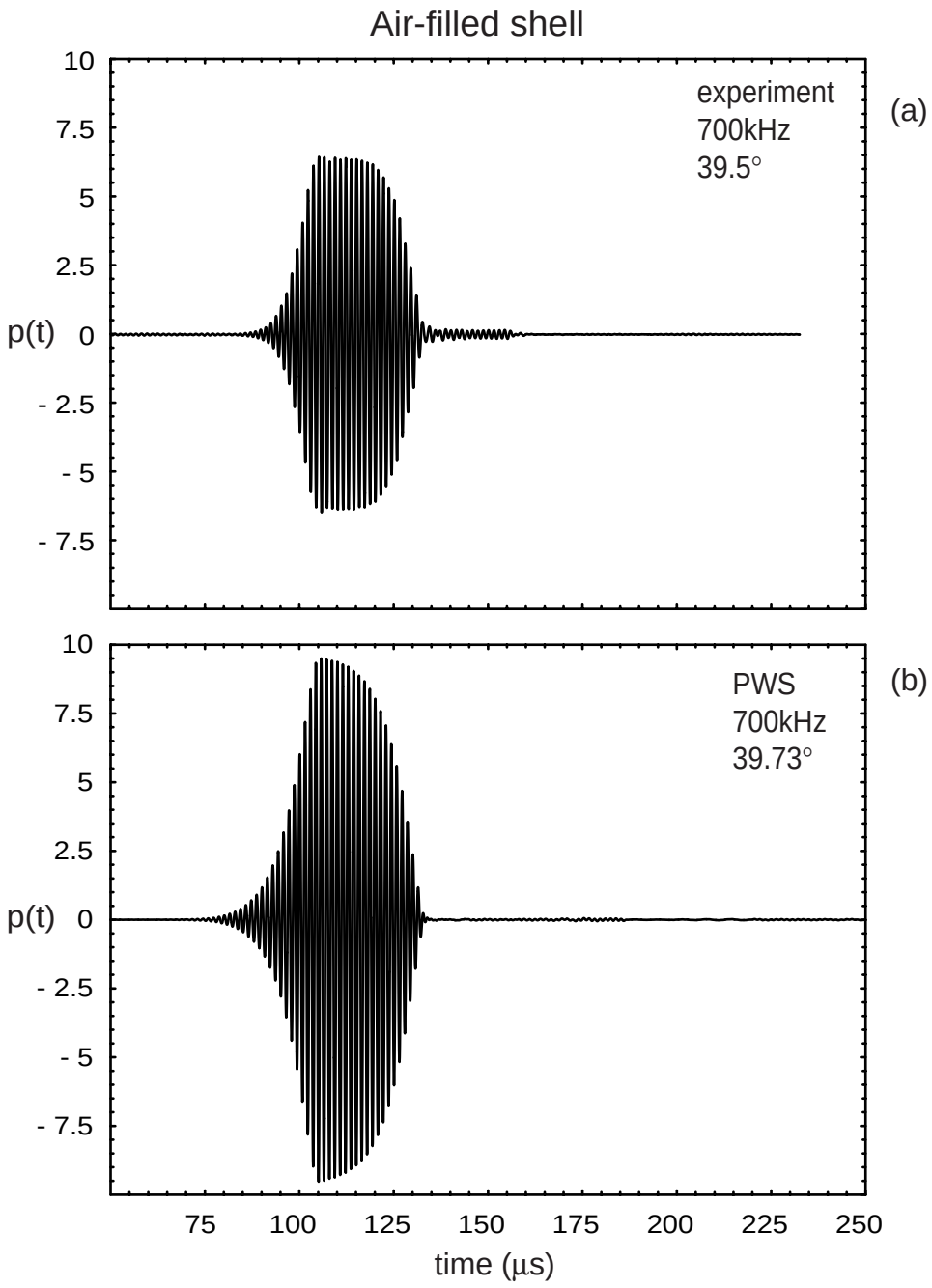

FIG. 7.14 (a) Measured backscattering time series at the peak meridional ray amplitude for Shell A (*air-filled with endcaps*) at $\gamma = 39.5°$ (see Fig. 7.3) for a 20 cycle tone burst having a center frequency of 700 kHz, and (b) approximate PWS synthesized time series for the same shell and incident burst at $\gamma = \theta_l = \sin^{-1}[(k_l a)/(ka)] = 39.73°$, where $k_l a$ is the infinite cylindrical shell wavenumber taken from Table 7.1 for this frequency. The time scale is referenced to the specular reflection from the cylinder at broadside incidence.

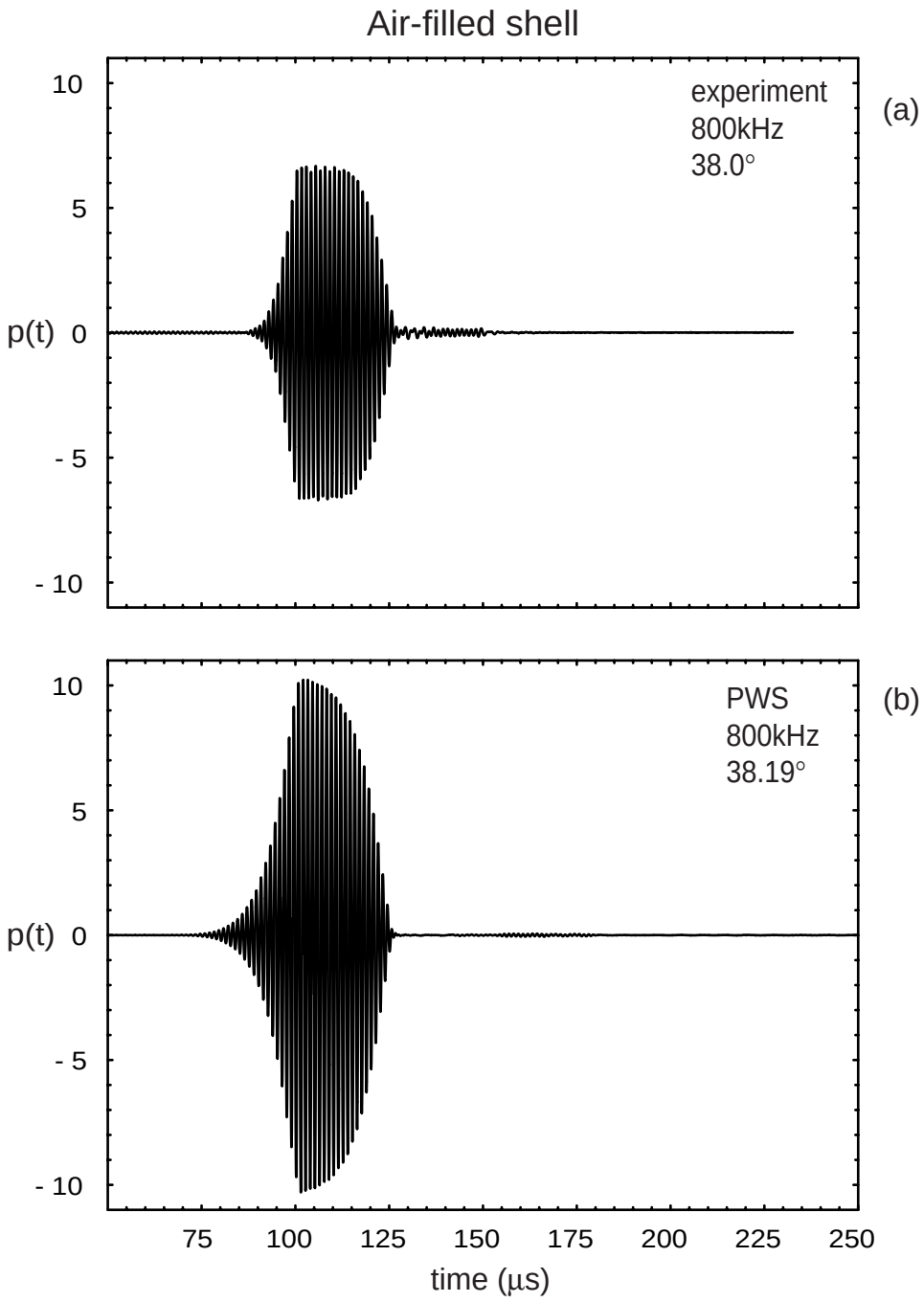

FIG. 7.15 (a) Measured backscattering time series at the peak meridional ray amplitude for Shell A (*air-filled with endcaps*) at $\gamma = 38.0°$ (see Fig. 7.3) for a 20 cycle tone burst having a center frequency of 800 kHz, and (b) approximate PWS synthesized time series for the same shell and incident burst at $\gamma = \theta_l = \sin^{-1}[(k_l a)/(ka)] = 38.19°$, where $k_l a$ is the infinite cylindrical shell wavenumber taken from Table 7.1 for this frequency. The time scale is referenced to the specular reflection from the cylinder at broadside incidence.

of the backscattered response. Recall that the peak enhancement angles do not exactly coincide. As a result it was necessary to evaluate the theoretical response at a slightly larger angle. This angle corresponds to the leaky wave coupling angle associated with the calculated axial wavenumber in Table 7.1 (or Table 7.2 for the water-filled shell). The amplitude scale has been normalized to the specular reflection amplitude for a rigid sphere as before. The comparison in each case is quite good. The initial ramp-up time is comparable as is the apparent lack of ringing after the pulse ends. At the lowest frequency, 400 kHz, the amplitudes and pulse shapes are very similar. At higher frequencies the experimental records drop in amplitude with respect to the theory, just as was seen earlier. The theory traces also do not appear to reach a steady state amplitude for the higher frequencies, for 20 cycle bursts, as the experimental traces do.

Water-filled Cylindrical Shell

Now consider the case of a water-filled shell without endcaps. Figures 7.16 through 7.20 show the experimental and theoretical time records for five frequencies similar to Figs. 7.11 - 7.15. The time records in this case display multiple pulses. This behavior was observed and explained by Kaduchak[1] and Dodd[2] in high-frequency high-resolution sonar images of a freely-flooded finite cylindrical shell. Several individual pulses were observed with a similar interval separating each one. The explanation for this phenomena is as follows. The first pulse is the standard meridional ray feature which is present for air-filled shells. The delayed pulses also belong to the meridional ray class but are described by ray paths which have traversed the interior of the shell in the meridional plane an even number of times before radiating in the backscattering direction (of course after reflecting from the shell truncation). Figure 7.21 shows several possible ray paths which may describe these contributions. By simple ray tracing it is possible to determine the relative timing of each contribution. With regard to the timing of the initial meridional ray return, the subsequent pulses are predicted to arrive at intervals of

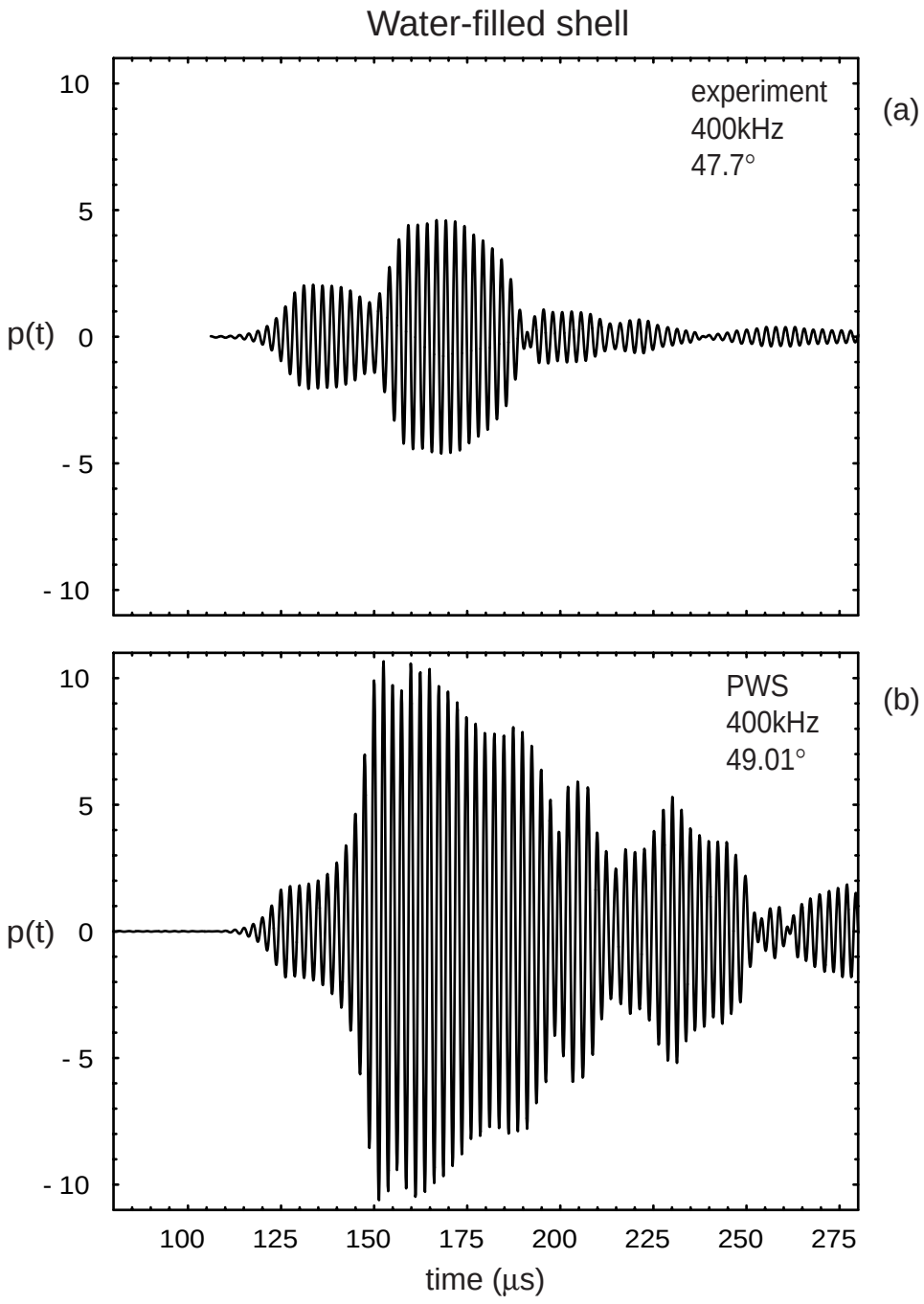

FIG. 7.16 (a) Measured backscattering time series at the peak meridional ray amplitude for Shell A (*water-filled with no endcaps*) at $\gamma = 47.7°$ (see Fig. 7.5) for a 20 cycle tone burst having a center frequency of 400 kHz, and (b) approximate PWS synthesized time series for the same shell and incident burst at $\gamma = \theta_l = \sin^{-1}[(k_l a)/(ka)] = 49.01°$, where $k_l a$ is the infinite cylindrical shell wavenumber taken from Table 7.2 for this frequency. The time scale is referenced to the specular reflection from the cylinder at broadside incidence.

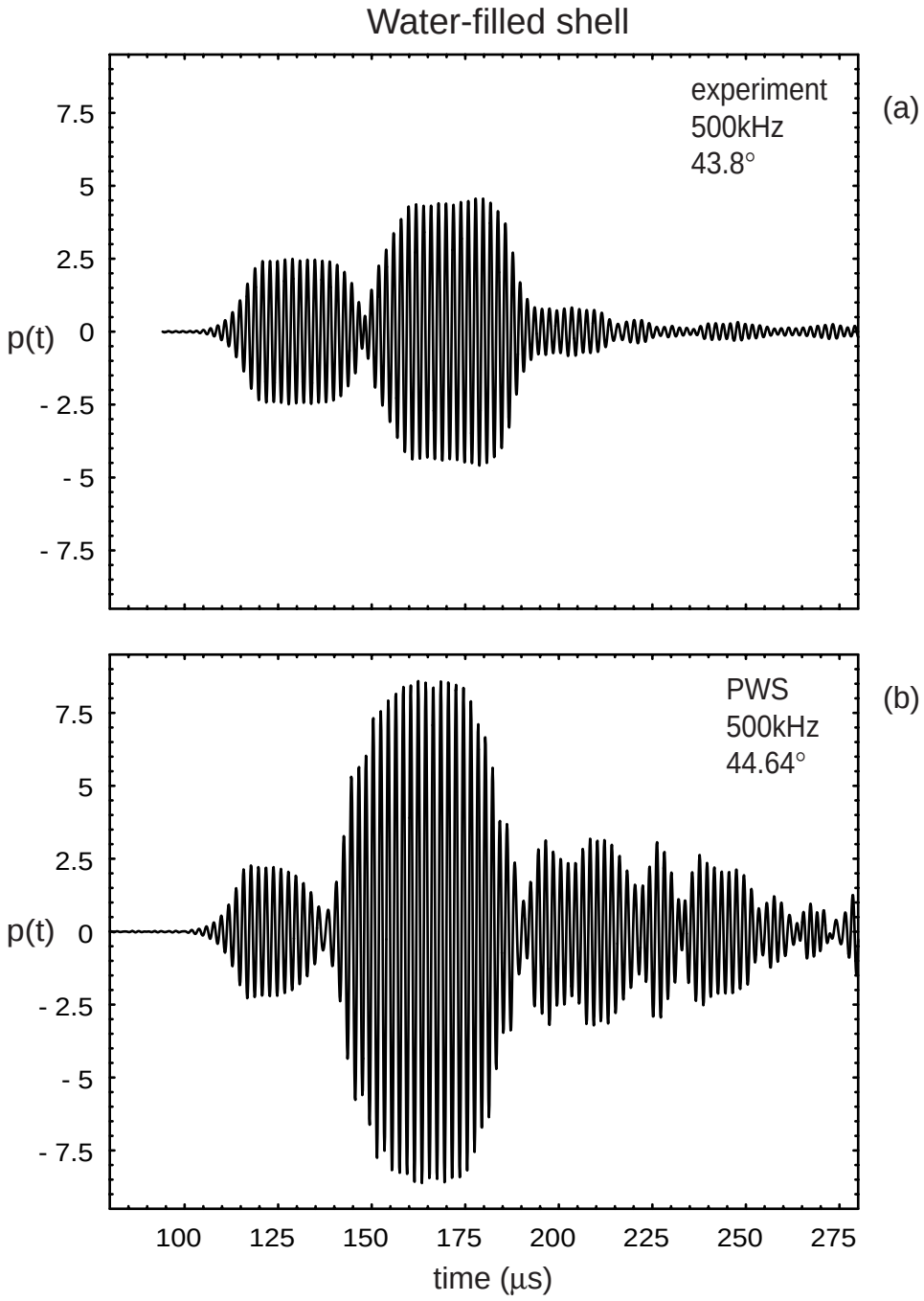

FIG. 7.17 (a) Measured backscattering time series at the peak meridional ray amplitude for Shell A (*water-filled with no endcaps*) at $\gamma = 43.8°$ (see Fig. 7.5) for a 20 cycle tone burst having a center frequency of 500 kHz, and (b) approximate PWS synthesized time series for the same shell and incident burst at $\gamma = \theta_l = \sin^{-1}[(k_l a)/(ka)] = 44.64°$, where $k_l a$ is the infinite cylindrical shell wavenumber taken from Table 7.2 for this frequency. The time scale is referenced to the specular reflection from the cylinder at broadside incidence.

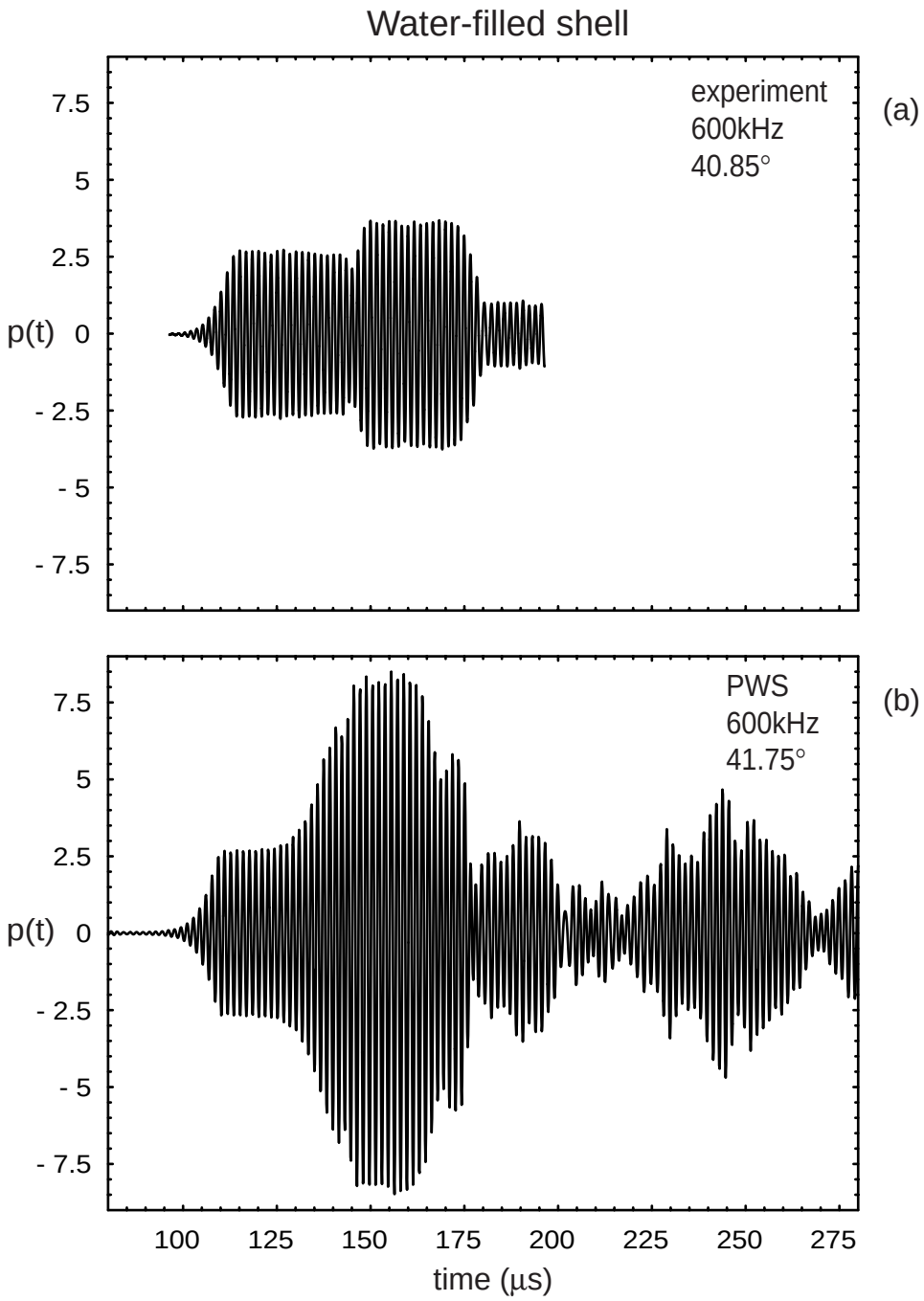

FIG. 7.18 (a) Measured backscattering time series at the peak meridional ray amplitude for Shell A (*water-filled with no endcaps*) at $\gamma = 40.85°$ for a 20 cycle tone burst having a center frequency of 600 kHz, and (b) approximate PWS synthesized time series for the same shell and incident burst at $\gamma = \theta_l = \sin^{-1}[(k_l a)/(ka)] = 41.75°$, where $k_l a$ is the infinite cylindrical shell wavenumber taken from Table 7.2 for this frequency. The time scale is referenced to the specular reflection from the cylinder at broadside incidence.

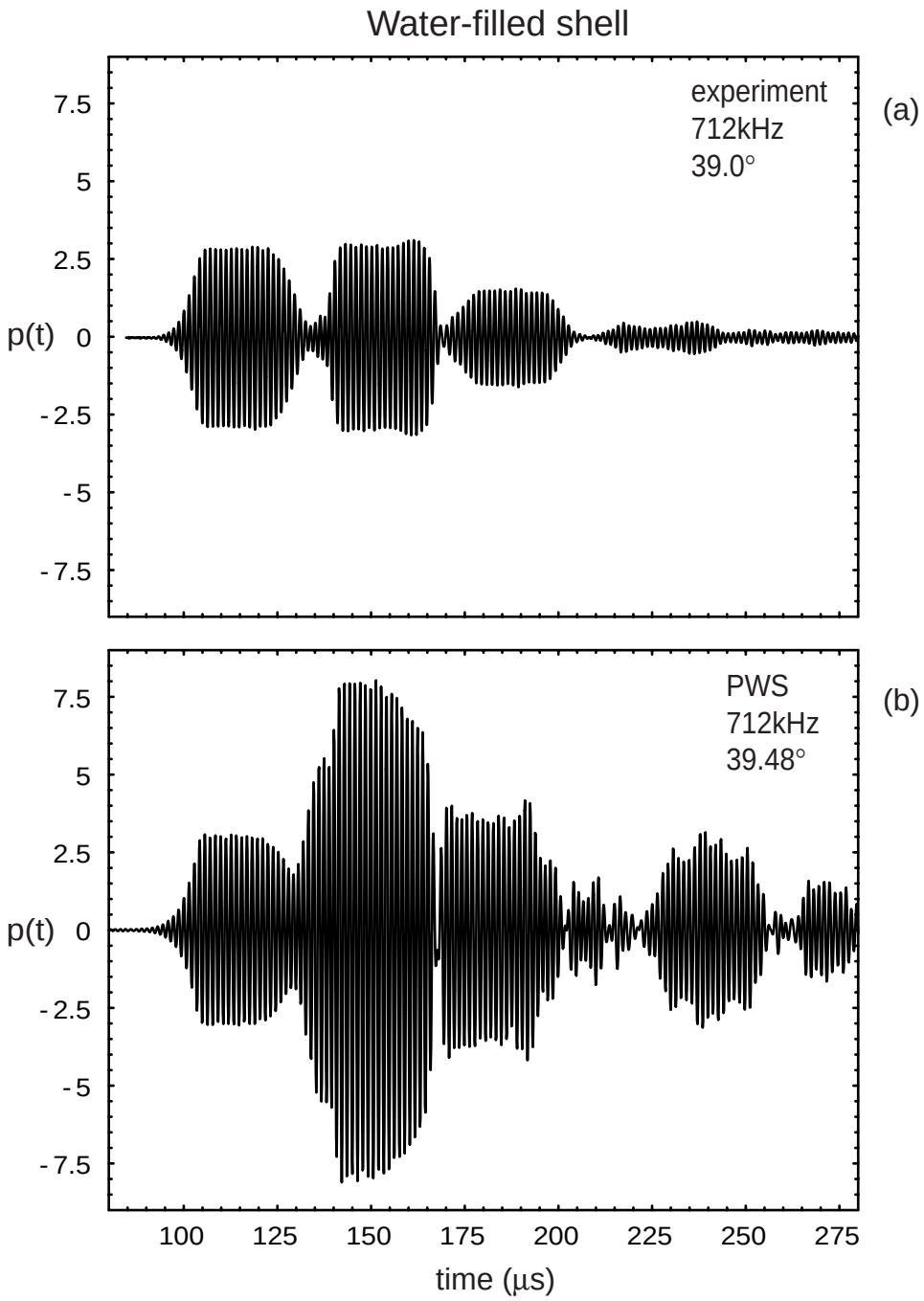

FIG. 7.19 (a) Measured backscattering time series at the peak meridional ray amplitude for Shell A (*water-filled with no endcaps*) at $\gamma = 39.0°$ for a 20 cycle tone burst having a center frequency of 712 kHz, and (b) approximate PWS synthesized time series for the same shell and incident burst at $\gamma = \theta_l = \sin^{-1}[(k_l a)/(ka)] = 39.48°$, where $k_l a$ is the infinite cylindrical shell wavenumber taken from Table 7.2 for this frequency. The time scale is referenced to the specular reflection from the cylinder at broadside incidence.

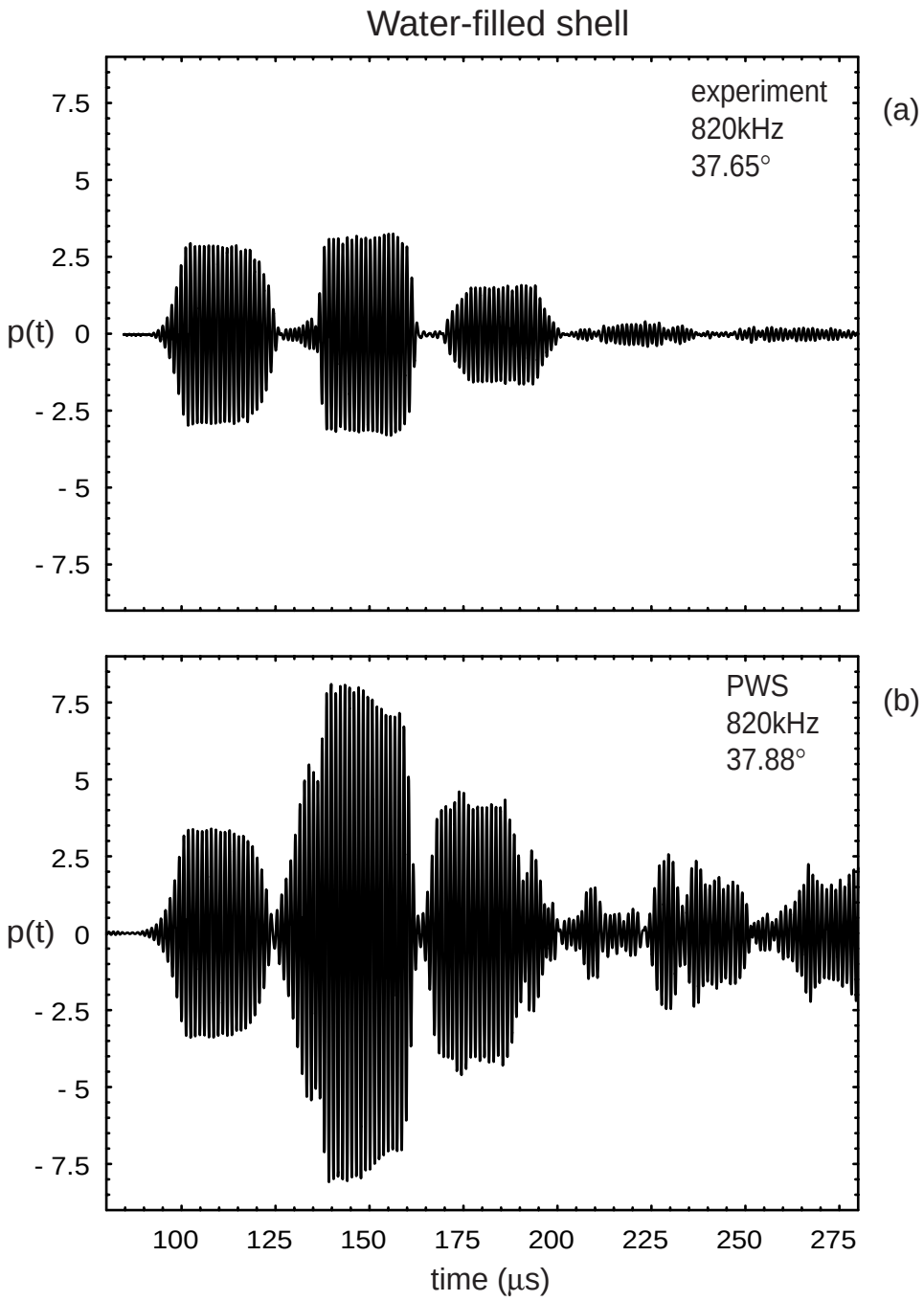

FIG. 7.20 (a) Measured backscattering time series at the peak meridional ray amplitude for Shell A (*water-filled with no endcaps*) at $\gamma = 37.65°$ for a 20 cycle tone burst having a center frequency of 820 kHz, and (b) approximate PWS synthesized time series for the same shell and incident burst at $\gamma = \theta_l = \sin^{-1}[(k_l a)/(ka)] = 37.88°$, where $k_l a$ is the infinite cylindrical shell wavenumber taken from Table 7.2 for this frequency. The time scale is referenced to the specular reflection from the cylinder at broadside incidence.

$$\Delta t = \left(\frac{1}{c}\right) 4a\cos\theta_l \,. \qquad (7.12)(a)\text{-}(c)$$

Recall that the cylinder is tilted at $\gamma \approx \theta_l$. For the present shell this reduces to $\Delta t = (51.4\cos\theta_l)\,\mu s$. Expression (7.12) neglects the small corrections associated with the transmission of a ray through the shell wall. Also it does not include any timing advances which may be due to the propagation of the leaky wave on the shell, where the group velocity often significantly exceeds the phase velocity. These corrections are expected to be small for the shells and frequencies under consideration. Recall that the leaky waves studied have rather large levels of radiation damping. This limits the lengths over which the meridional ray may propagate on the shell before reflecting from the truncation and still contribute significantly to the far-field backscattering. For the present purposes Eq. (7.12) is sufficient. It correctly predicts the timing of the additional pulses.

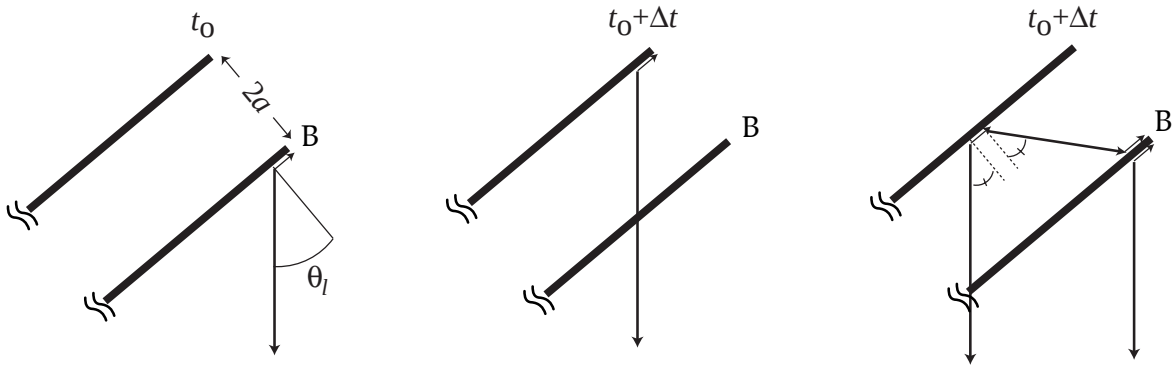

FIG. 7.21 Several meridional ray paths for the water-filled shell which explain the multiple contributions observed in the time records after the initial meridional ray return (left).

If attention is focused only on the original meridional ray return (the earliest feature evident in Figs. 7.16 - 7.20) the analysis follows just as for the air-filled shell. The amplitude and shape of the pulse match very well between the experiment and the theory.

A few observational comments are in order concerning the later returns in the measured time series. In almost all cases the second return is larger than the first meridional ray return (sometimes observed to be twice in amplitude). Also the angle at

which it is maximized was always observed to be slightly greater than the angle of the peak for the first meridional ray return. It may be possible to model these later meridional ray returns with the same ray formalism discussed in Section 7.3. That approach, however, is not directly applicable to these cases. Among other factors, the wavefront curvature for the backwards directed outgoing wave would be different for later returns (which have traversed the inside diameter of the shell) than for the first reflected meridional ray.

7.6 Scattering Spectrum for a Water-Filled Shell

It is in order at this point to ask what effect these multiple scattering returns have on the spectrum of the scattering of an impulse from the water-filled shell. For an air-filled shell the spectrum displays a smooth enhancement peak in both angle and frequency for the meridional ray enhancement. With tone burst illumination this spectral feature is manifest as a single time-domain wavepacket. Figures 7.16 through 7.20 show that for a water-filled shell there are multiple wavepackets. How are these then manifest in the spectrum? To answer this question another experiment was carried out. Instead of the previous narrowband backscattering which would allow a determination of the spectrum essentially at a single frequency, a broadband technique was applied to measure the spectrum over a broad range of frequencies in a single experiment. The impulse methods used in Chapters 2 and 3 are suitable for measurements up to about 500 kHz. However, to investigate the response over an even broader range of frequencies a chirped burst technique was used. Using the PVDF sheet source a long duration frequency modulated (FM) signal was generated. The modulation used in this case was a simple linear function. Details of this experiment are discussed in Section A.6 of Appendix A. The usable frequency range in this experiment was 300 kHz to 1 MHz.

Figure 7.22 shows the results of these measurements for the shell investigated in the preceding sections. It shows the normalized backscattering spectrum for a water-filled shell (Shell A) in the vicinity of the a_0 meridional ray enhancement (compare with Figs. 2.4(b) on page 17 and 3.3 on page 47). The a_0 meridional ray enhancement, which was

FIG. 7.22 Backscattered spectral magnitude normalized to the spectrum of the incident burst, for a *fluid-filled* Shell A. This data was acquired with the sheet source driven with a long duration linear FM chirp burst. The amplitude scale is in decibels with respect to the maximum measured value in the region shown. Vertical lines are the result of the normalization factor used in those regions.

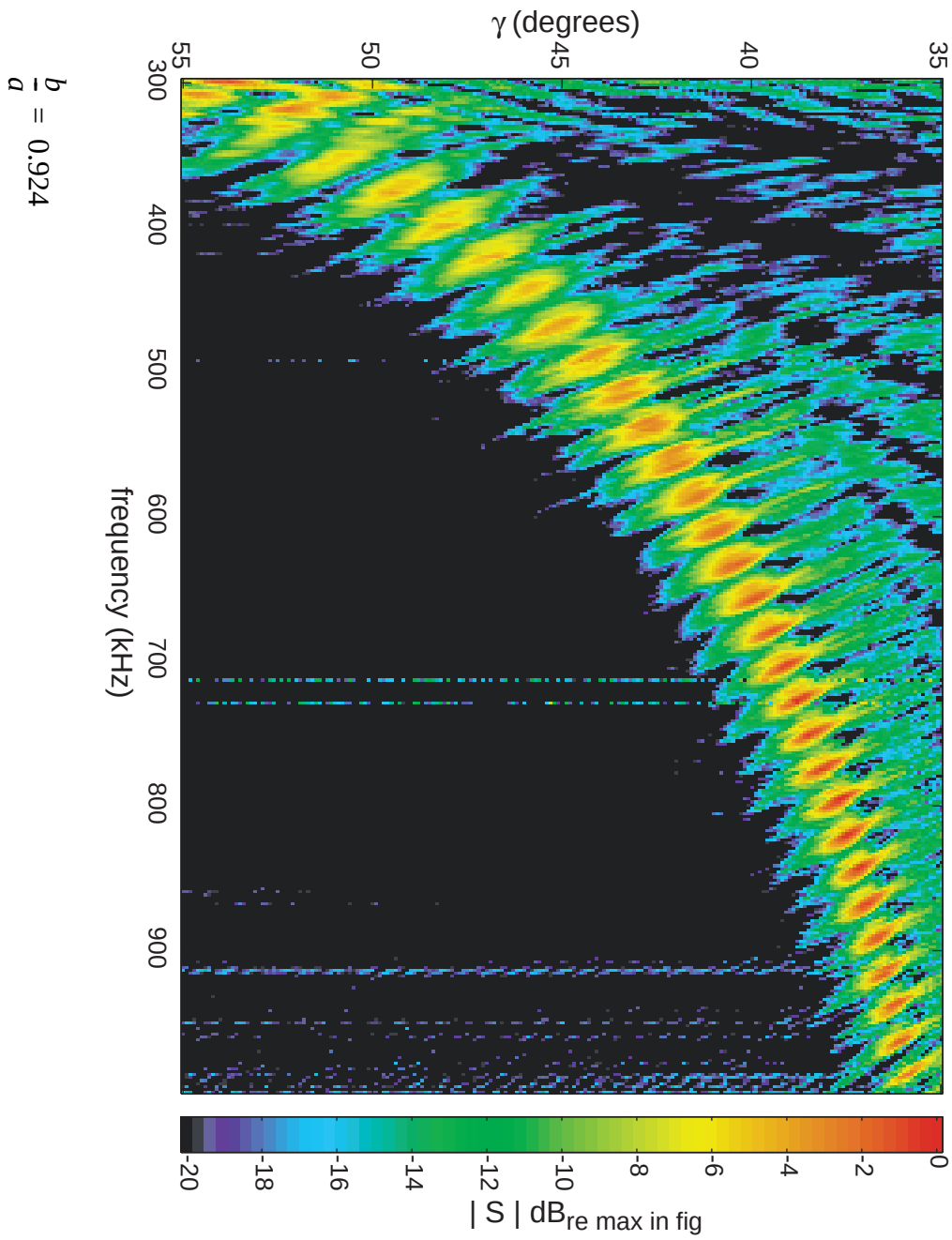
γ (degrees)
55
50
45
40
35
300
400
500
600
700
800
900
frequency (kHz)
-20
-18
-16
-14
-12
-10
-8
-6
-4
-2
0
| S | dB re max in fig
b/a = 0.924

previously smooth for an air-filled shell, is now composed of multiple regularly spaced peaks. Already possessing knowledge of the time domain scattering response these peaks may simply be interpreted as the interference pattern resulting from the interference of the internally reflected signals with the first meridional ray signal. This however does not explain the spacing of the interference pattern. A greater understanding may be gained by directly analyzing the dispersion curves for the doubly fluid-loaded cylindrical shell.

Recall that in earlier sections the wavenumber values for the water-filled shell were approximated with those for an empty shell but with twice the damping; or they were approximated with values calculated for a doubly fluid-loaded plate. The reason for this substitution will now be explained. The isolation of a *single* root of the dispersion relation for the a_0 meridional ($n = 0$) Lamb wave on an infinite cylindrical shell with fluid on the interior is simply not possible. By adding a fluid to the interior of the shell the normal modes of the elastic shell structure (discussed in Chapter 4 for an empty shell) are coupled to the modes of the enclosed fluid column. The resulting structure—fluid/shell/fluid—must be regarded as a whole and the corresponding modes of vibration found accordingly. These modes differ significantly from the modes of a hollow shell. A root finding analysis was carried out in a similar manner to that found in Chapter 4 for Shell A but with water on the interior (as well as on the exterior) in the region near the a_0 meridional ray. Figure 7.23 shows the results of those calculations for $n = 0$ which are plotted in terms of the axial phase velocity and damping. The dark solid curves in (a) are the roots which were found for the water-filled shell case while the short dashed curve is the result for the empty shell case. In both cases there is still a fluid on the exterior of the shell. The a_0 meridional ray curve splits into an infinite number of curves which cross the a_0 curve for the empty shell. At each of these crossing points the damping displays a peak. To understand this behavior consider the normal modes of the fluid column by itself. For a shell having a large impedance with respect to the fluid the boundary between the shell and the inner fluid may be considered to be a "hard" surface. What we wish to model, then, is a fluid column bounded by a rigid cylindrical boundary at a radius of the inner surface of the shell (at radius b). This is a straightforward problem (e.g. see Ref. [92] and Section 11.12 of Ref. [9])

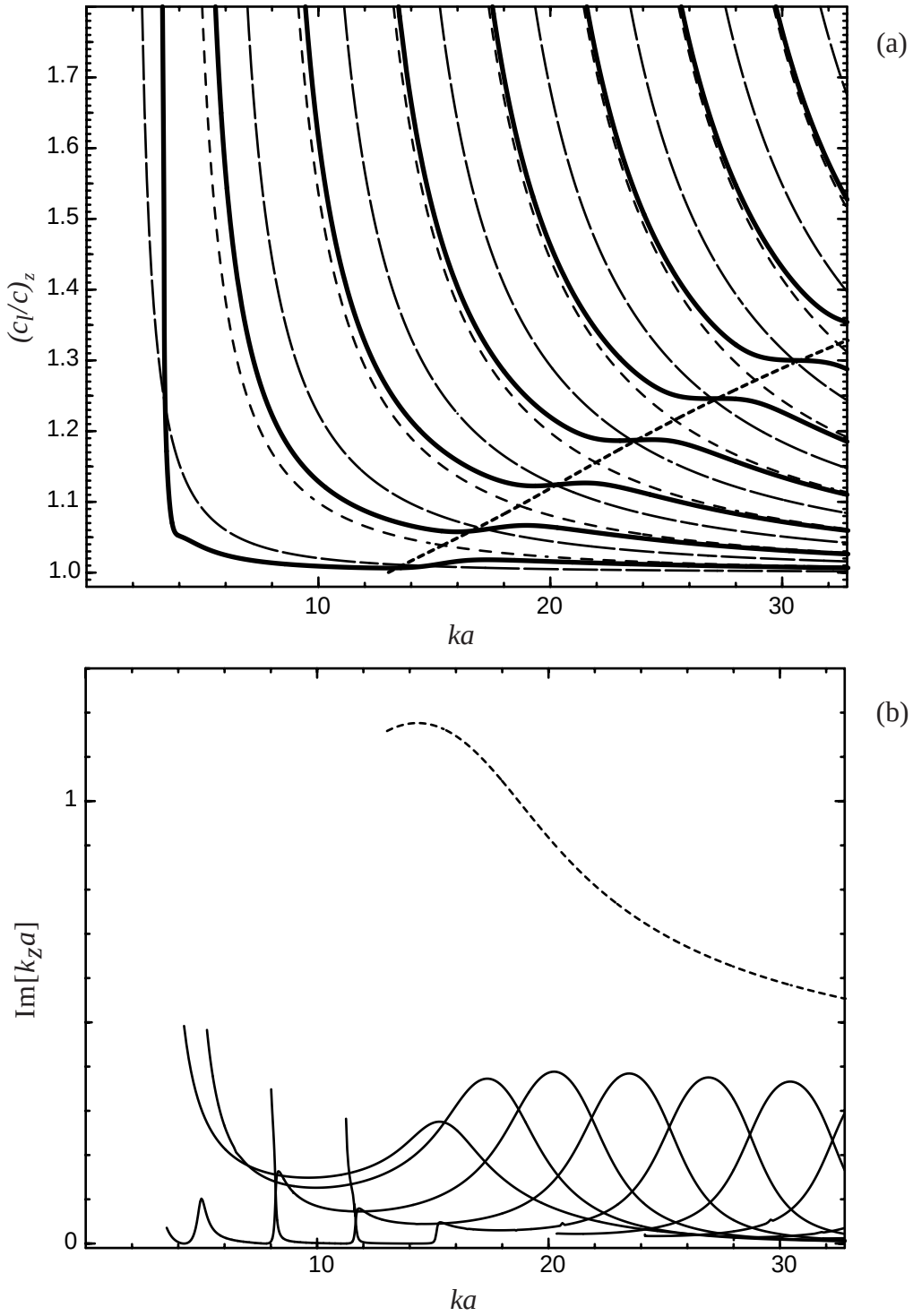

FIG. 7.23 (a) Phase velocity and (b) damping curves (solid lines) for the water-filled cylindrical shell in the vicinity of the a_0 meridional wave. The short dashed curve is for the a_0 meridional wave (n = 0) on an empty shell. The medium and long dashed curves are for a fluid column having a rigid boundary at a radius of b, for n = 0 and n = 1, respectively. They also correspond to the case of a soft boundary at b for n = 1 and n = 0, respectively.

and the dispersion relation is given by

$$\left(\frac{c_l}{c}\right)_z = \frac{ka}{k_z a} \qquad (7.13)(a)\text{-}(c)$$

where

$$k_z a = \sqrt{(ka)^2 - \left(\frac{a}{b}\right)^2 (x'_{nm})^2}\,. \qquad (7.14)(a)\text{-}(c)$$

Here the x'_{nm} is the m^{th} root of the relation

$$J_n'(\xi) = 0\,, \qquad (7.15)(a)\text{-}(c)$$

where n is the azimuthal mode number and the prime denotes the derivative with respect to the argument. Equation (7.15) results from the boundary condition at b which requires that the radial component of the velocity vanish at the rigid surface. For a soft boundary the pressure must vanish; in this case x'_{nm} is determined from the condition

$$J_n(\xi) = 0\,. \qquad (7.16)(a)\text{-}(c)$$

The first several dispersion curves for the rigid boundary $n = 0, 1$ are plotted as the medium and long dashed curves in Fig. 7.23(a).

The $n = 0$ modes of the water-filled shell can thus be seen to be a "combination" of the $n = 0$ mode of the elastic shell and the $n = 0$ modes of the interior fluid column. When not close to the empty shell modes, the curves tend toward the fluid column modes. It is highly instructive to look at these curves in frequency-angle space together with the measured spectrum. To plot this recall that coupling of the incident sound wave with a mode of the shell occurs when the axial phase matching condition is met

$$\sin\gamma = \frac{1}{(c_l/c)_z} \qquad (7.17)(a)\text{-}(c)$$

or

$$\gamma = \sin^{-1}\left[\sqrt{1-\left(\frac{x'_{nm}}{kb}\right)^2}\right]. \qquad (7.18)(a)\text{-}(c)$$

Figure 7.24 shows an overlay of these curves ($n = 0$ and $n = 1$ for the fluid column with a rigid boundary) on Fig. 7.22. The *minima* of the measured meridional ray enhancement peak occur very nearly at the intercepts of the empty shell a_0 curve with each of the $n = 0$ and $n = 1$ fluid column curves. One may recall that in previous experimental results there has been present an angular shift between the measured enhancements and theoretical predictions. It is a valid question to ask whether or not this shift could be present in Figs. 7.22 and 7.24, and as a result render the above conclusion false. Namely that this shift could have moved the measured maxima of the meridional ray enhancement off of perhaps the intercepts of the aforementioned curves to their present locations, thus completely reversing the above conclusion. In answering this question three points are noteworthy. The first is that the small angle errors (see Section 7.4) which are due to the finite separation distance of the target and receiver have been minimized in two ways. First, the receiver transducer has been shifted laterally as discussed previously and in Section 7.A. It is therefore not expected that significant small angle errors due to the receiver position are present over the relatively small angle scan (20°) represented in Figs. 7.22 and 7.24. Secondly, the sheet source has been used in this experiment to generate the incident plane wave. As a result the angle errors associated with the incident wave are expected to be very small. The second point is that the angle shifts evident in Figs. 7.2 - 7.6, 7.7 (c) and 7.8 (c) are very likely due to the fact that accurate sound speeds are not known for the elastic material making up the shell. The coupling angles for leaky waves on the shell are dependent on the leaky wave phase velocities, which in turn are sensitive to the material parameters. Finally the third point supporting the original conclusion is that the phase velocity curves for the fluid column are only dependent on the radius of the boundary, the frequency, and the material parameters of the fluid itself. Since these are all well known quantities the locations in frequency-angle space of the coupling curves for the fluid column (Fig. 7.24) should be accurate on the scale plotted. And these curves are found to intersect the a_0 meridional ray enhancement in regions of backscattering spectral minima.

FIG. 7.24 Same as Fig. 7.22 but with overlaid lines corresponding to a matching of the incident axial wavenumber to the axial wavenumber of propagating modes of a fluid cavity having a rigid boundary at $\rho = b$ (dashed white lines, $n = 0$; dot dashed white lines, $n = 1$) and the coupling curve of the a_0 meridional ray for an empty shell (in water) of the same material and parameters (solid white line).

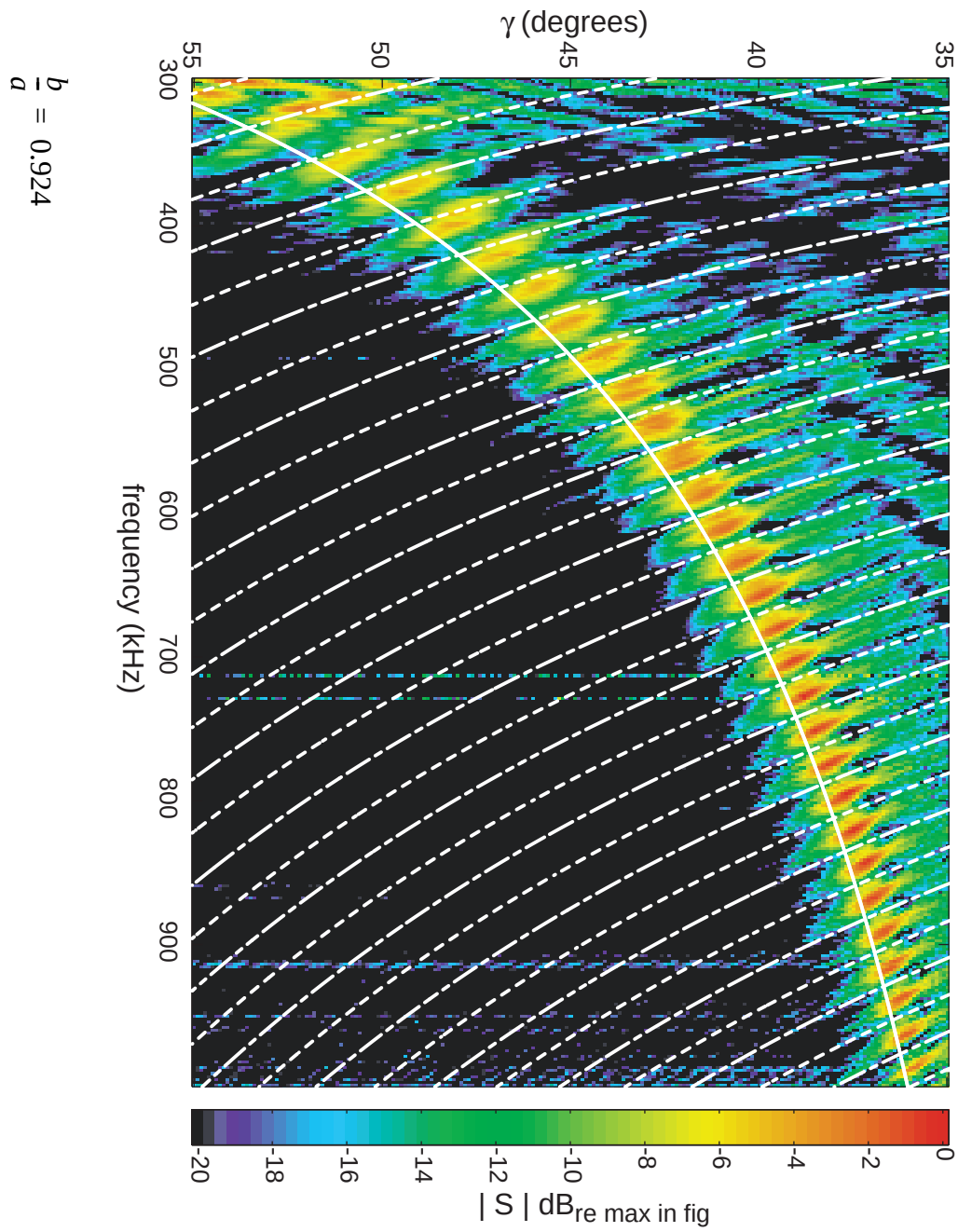
γ (degrees)
55
50
45
40
35
300
400
500
600
700
800
900
frequency (kHz)
-20
-18
-16
-14
-12
-10
-8
-6
-4
-2
0
| S | dB re max in fig
b/a = 0.924

It is interesting to note also that the modes for a fluid column with a soft boundary are nearly identical to those for the rigid boundary but with the integer n displaced by 1. The n = 0 curves for the rigid boundary are identical to the n = 1 curves for the soft boundary; while the n = 1 curves for the rigid boundary are nearly equivalent to the n = 0 curves for the soft boundary, at high frequencies. This is a consequence of the recursion relations for Bessel functions and Eqs. (7.15) and (7.16).

In summary then, it should be apparent that the coincidence of the a_0 mode of a hollow cylindrical shell with the modes of a fluid column, having either a rigid or soft boundary, describes the locations of destructive interference between the first meridional signal and the later meridional signals which have undergone internal reflections.

7.7 Discussion

The experiments described in this Chapter show that the meridional ray enhancement for a finite cylindrical shell, both air and water-filled, can be significant in amplitude. Measured backscattering levels commonly exceed the magnitude of backscattering by a rigid sphere by 3 to 6 times. An extension of a ray theory by Marston correctly predicts the meridional ray enhancement peak width and amplitude in regions where the leaky wave reflection coefficient from the cylinder end is nearly unimodular. The ray theory includes this reflection coefficient as a variable parameter so it is possible to use independent calculations of the reflection coefficient to aid in the modeling of the meridional ray enhancement behavior. The ray theory predictions also compare very well with a previously developed approximate PWS solution.

The behavior of the meridional ray enhancement has been examined as a function of frequency. It is shown that the general amplitude of the enhancement increases smoothly with frequency and is limited by the frequency dependence of the leaky wave reflection coefficient. One observed limitation is the mode conversion of the incident leaky Lamb wave into another Lamb mode. This produces a considerable and abrupt drop in the measured meridional ray amplitude.

The approximate PWS calculation permitted a comparison of the meridional ray enhancement feature in the time domain. Measured and synthesized time records compare very well at low frequencies where the leaky wave reflection coefficient appears to be nearly unimodular. Comparisons in the time domain for water-filled shells confirmed the multiple enhancement features observed by other authors. These multiple backscattering returns may be explained with simple ray tracing. A measurement of the backscattering spectrum for the water-filled shell suggests that the response may also be explained by a complicated coupling of a hollow shell with a fluid column.

7.A Method of Extracting and Normalizing the Scattering Amplitude from Measured Tone Burst Time Series

This appendix describes the method used in finding the meridional ray amplitude from the experimental time traces for the plots in Figs. 7.2 - 7.6, 7.7 and 7.8. Take Fig. 7.12 (a) as a typical example of the meridional ray enhancement feature in the time domain. We wish to establish an algorithm to isolate and evaluate the amplitude of the steady state region of the signal. To do this a relatively simple algorithm was written in Matlab®. Figure 7.25 shows a sample output of this algorithm for the same data found in Fig. 7.12(a). This figure shows the raw output from the preamplifier. The time window defined by t_1 and t_2 is set manually to contain only the steady-state portion of the signal. A Hilbert transform is applied to the time record to extract the analytic signal and envelope. (Section B.2 on page 308 of Appendix B describes the Hilbert transform and it's use.) This envelope is then averaged over the selected window to obtain the amplitude of the signal in volts.

This amplitude is for backscattering from the tilted cylindrical shell at a particular distance and for a particular driving amplitude of the source. In order to obtain a useful quantity, i.e. the form function, this result must be normalized. The approach taken here is to perform another nearly identical measurement for backscattering by a solid sphere and

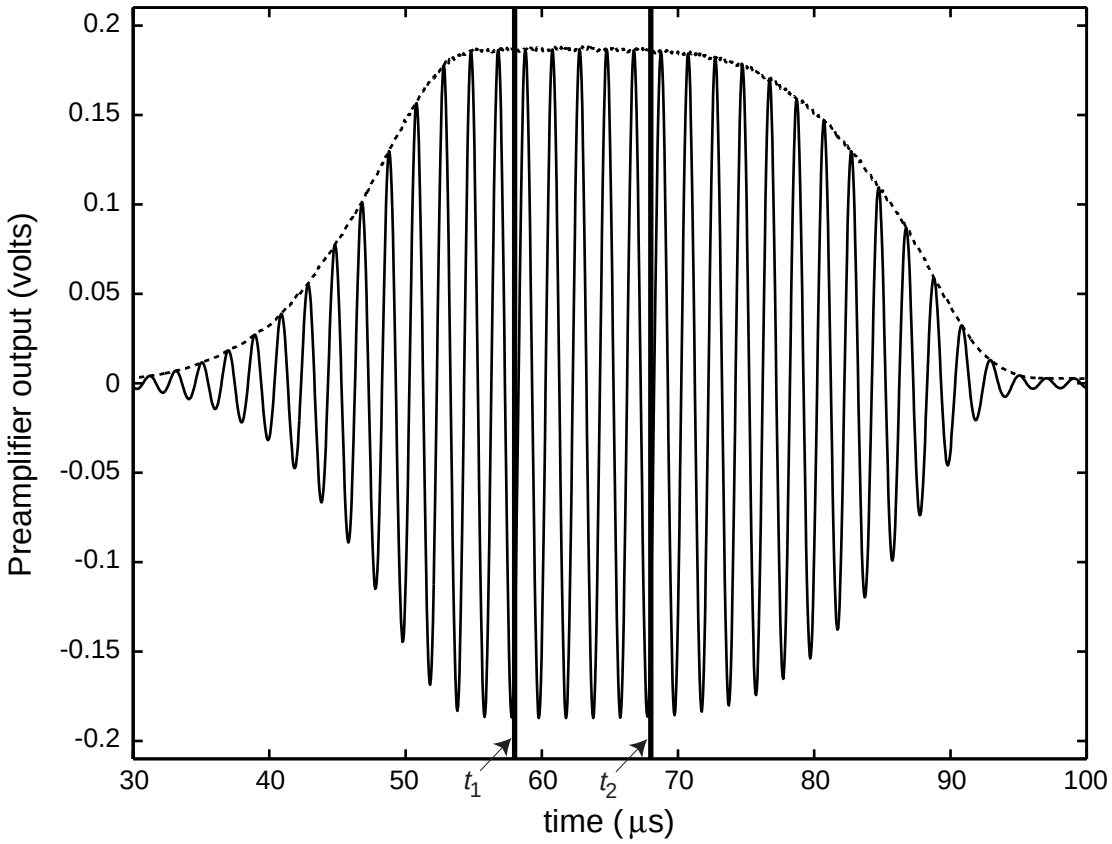

FIG. 7.25 Example of the method used to extract the steady-state backscattered meridional ray amplitude from the experimental time series. This is a close up of Fig. 7.12 which has not been normalized. The dashed line is the envelope calculated by applying the Hilbert transform to the measured time record. The vertical lines mark the beginning and end of the time window over which the envelope is averaged to obtain the amplitude. These points are set manually and in this case are $t_1 = 58$ μs, $\Delta t = 10$ μs. The time record is sampled at 0.05 μs which makes this a 300 point average. The resulting amplitude is calculated to be 0.1866 volts.

use that result to normalize the cylinder backscattering results. A solid stainless steel (SS440) sphere of nominal radius 34.925 mm was placed at approximately the same location as the cylinder and a measurement made at the same frequency, driving voltage and water temperature. The above procedure for finding the steady-state amplitude was used and an amplitude found. With knowledge of these amplitudes, as well as the distances from the source to the cylinder and the sphere, the form function may be found with the following relation[93,59,47]

$$|f_{cyl}| = \left(\frac{A_{cyl}}{A_{sph}}\right)\left(\frac{R_{cyl}}{R_{sph}}\right)^2\left(\frac{a_{sph}}{a_{cyl}}\right)|f_{sph}| \qquad (7.19)(a)\text{-}(c)$$

where A_{cyl} and A_{sph} are the measured amplitudes, R_{cyl} and R_{sph} are the separation distances of the source and target, and a_{cyl} and a_{sph} are the characteristic radii of the cylinder and sphere, respectively. The term f_{sph} is the form function of the solid sphere at this frequency. The frequencies of interest here correspond to values of ka_{sph} ranging from 44 to 180. These are sufficiently high frequencies that the amplitude of the specular reflection from the stainless steel sphere is approximately equal to the amplitude for specular reflection from an ideal rigid sphere, which is unity, the only difference being an impedance factor. The relevant specular part of the form function for the stainless steel sphere is then approximated by

$$f_{sph} \approx f_{rigid} \cdot \left(\frac{\rho_e c_L - \rho c}{\rho_e c_L + \rho c}\right) \approx 1 \cdot \left(\frac{\rho_e c_L - \rho c}{\rho_e c_L + \rho c}\right) \qquad (7.20)(a)\text{-}(c)$$

where ρ_e and c_L are the density and longitudinal sound speed of the steel sphere and ρ and c are the density and sound speed of the surrounding fluid. The material constants used for the SS440 sphere are: $\rho_e = 7.84\,\mathrm{g/cm^3}$ and $c_L = 5.854\,\mathrm{mm/\mu s}$. Using these values in addition to the material constants for water found in Table 2.2 on page 16 one finds $f_{sph} \approx 0.937$. The values used for the separation distances, R_{cyl} and R_{sph}, are taken to be the closest rear corner of the cylindrical shell and the center of the sphere, respectively. The former choice was made because it has been shown that the measured meridional ray feature is primarily due to the reradiation of the leaky wave very near to the closest rear corner of the shell (see Chapter 3 and Fig. 3.20 on page 81). That distance may be calculated by simple geometry (Fig. 7.26) to be

$$R_{cyl} = R'_{cyl} + a_{cyl}\sqrt{1 + \frac{1}{4}\left(\frac{L}{a_{cyl}}\right)^2}\,\sin\left[\gamma - \tan^{-1}\left(\frac{2}{(L/a_{cyl})}\right)\right], \qquad (7.21)(a)\text{-}(c)$$

where R'_{cyl} is the distance from the source to the center of the cylinder, L is the length of the cylinder and γ is the cylinder tilt angle. Recall that for Shell A the length aspect ratio is

(L/a_{cyl}) = 12 and a_{cyl} = 19.05 mm. Figure 7.26 shows the geometry of the experimental setup. Typical separation distances during the experiments were R'_{cyl} and R_{sph} of about 2.4 meters.

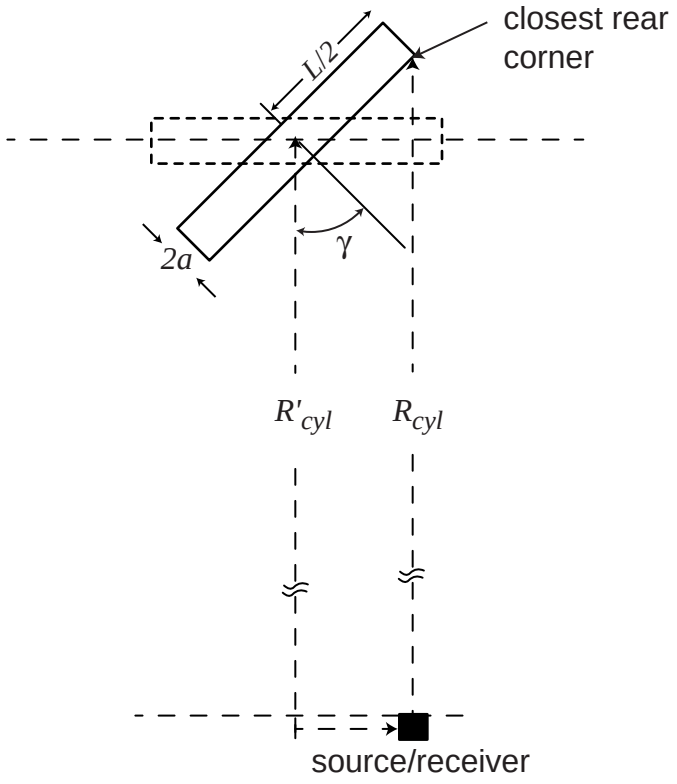

FIG. 7.26 Geometry of scattering setup (not to scale). Notice that the source has been shifted laterally to be in line with the closest rear corner of the cylinder.

The method outlined above was used in calculating the values found in Figs. 7.7 and 7.8. These were all found manually. For the angle scans of Figs. 7.2 - 7.6, however, this process would be quite tedious considering there are as many as 100 data points per plot. The process outlined above was automated to perform the amplitude analysis on multiple files all at once. The only addition to the method described above has to do with the selection of the time window over which the envelope of the signal is averaged. A single time window is chosen manually for the time record estimated to be nearest to the peak signal. This sets t_1 and t_2 - t_1. The timing to the closest rear corner, call it t_B, is calculated

using Eq. (7.21) and $t_B = 2R_{cyl}/c$.. From this window all the other windows for the other time records at different tilt angles are determined as follows. Every window has the same length. It's location is then determined by the fixed delay time t_1 - t_B. Recall that t_B is a function of the cylinder tilt angle. Any angular errors associated with the finite source-to-target distance are ignored. Since the angles over which the data were taken were small, about 10° in width, the associated distance corrections would be small. In a descriptive manner the above windowing method can be described in the following sense. The black arc (delayed one) overlaid on Fig. 7.1 corresponds to the time t_B. The fixed window used is then just delayed (either forward or backward) from this arc by the fixed amount, t_1 - t_B. The exact window length and delay were selected through trial and error to give results which best locate the steady state regions of the signal. With reference to Fig. 7.1 it can be seen that where the meridional ray feature is present it essentially follows the curve of t_B. However the helical wave responses found at lesser angles follow a different curve. As such the minor peaks visible on the left sides of Figs. 7.2 - 7.6, corresponding to the response of end reflected a_0 helical waves, should not be regarded as accurate measurements of the steady-state backscattered helical wave amplitudes. Another algorithm would need to be written to follow these contributions.

7.B Time Series Synthesis

This appendix describes minor details associated with the synthesis of the time series records from the complex form function. As was mentioned earlier the method used to perform the synthesis is found in Ref. [27]. There is one minor difference, however. In the method described in that paper the form function of length N/2 is appended with N/2 zeros to increase the file length to N+1. The resulting inverse discrete Fourier transform (DFT) results in a time series record of length N. By appending zeros to the spectrum (form function) the actual time series, which is necessarily real, must be understood as the real part of the resulting complex transform. The approach taken in this chapter is perhaps more rigorous in that the inverse transform results in a purely real time series. (In actuality

the imaginary part is zero to within machine precision.) This slightly different method of computing the inverse transform of a complex quantity which results in a real quantity is found in detail in Ref. [94]. In summary, instead of appending zeros one folds the spectrum about the midpoint (N/2) to obtain the additional points. The real part of the spectrum is folded directly while the imaginary part is folded and flipped in sign. This yields a function whose real part is even and imaginary part is odd. The inverse transform is then real.

8

Effect of the Cylinder Truncation on Lamb Wave Propagation: Reflection and Mode Conversion

8.1 Introduction

The meridional ray enhancement process for backscattering by fluid-loaded finite cylindrical objects is completely dependent on the existence of a reflection of the meridional leaky wave from some location on the meridian of the cylinder. As a consequence the magnitude of the backscattered enhancement is therefore closely related to the specific reflection mechanics of the geometry under consideration. It should be clear, then, that an understanding of the reflection process itself is crucial in interpreting experimental and theoretical results of backscattering enhancements. The purpose of this chapter is to briefly investigate the leaky wave reflection process, for the case of a meridional leaky Lamb wave reflecting from the truncation of a finite cylindrical shell, only

insofar as is necessary to understand the experimental and theoretical results of the previous chapters. Since a numerical value of the magnitude of the reflection coefficient is required for the ray theory presented in Chapter 7 an approximate calculation is carried out. A full investigation (i.e. a rigorous numerical approach), however, is beyond the scope of the present dissertation and is not attempted here.

With regard to the results of previous chapters it is desired to understand several aspects of the leaky wave reflection process. First, what is the nature of the reflection for the case of no fluid loading? Secondly, to what extent does fluid loading at the end influence the reflection? Thirdly, what role does mode conversion play?

As was discussed in Chapter 5 the finite elastic cylinder geometry does not lend itself to an exact analytical solution. This rules out the possibility of evaluating in an exact sense the scattering of a specified incident leaky wave by the cylinder end. To some extent the problem may be simplified by examining the limiting case of a flat plate. It has already been shown that in the present study, at frequencies above 100 - 200 kHz, the leaky waves of interest on the cylindrical shell are not significantly influenced by the curvature of the shell and propagate as if they were on a flat plate. This simplification is used in Section 8.3 to calculate an approximate reflection coefficient. Because it is presently only desired to obtain an estimate of the meridional leaky wave reflection coefficient at the flat perpendicular end of a finite cylinder, the only case considered will be for reflection at normal (axial) incidence. An estimate of the reflection coefficient for helical leaky waves for the same situation must necessarily include oblique incidence. The present method could be modified directly to include this case.

8.2 Summary of Observed Backscattering Features

In Chapter 7 experiments were carried out to determine the amplitude of the backscattered meridional ray enhancement for the a_0 leaky Lamb wave. In Figs. 7.2 - 7.6

the amplitude of the enhancement was measured as a function of cylinder tilt angle. For low frequencies the agreement in overall amplitude between the experimental results and the ray theory was very good. For the water-filled shell there was good agreement at higher frequencies. In these comparisons the ray theory assumed that the leaky wave reflection coefficient was unimodular. This already suggests that the reflection of the leaky wave at these frequencies is fairly efficient. Additionally the general relative drop in the experimental amplitudes with respect to the ray theory is suggestive of a greater transmission of energy through the end into the fluid as the frequency is increased. Figures 7.7 and 7.8, which use the results of the present chapter, show this effect more succinctly. Compared to a reflection coefficient of unity, the apparent reflection coefficient decreases almost linearly with increasing frequency. Overall the reflection coefficient values are quite high—well above 50% reflection at frequencies below 1 MHz for this shell (stainless steel with a wall thickness of about 1.5 mm).

An obvious feature of these figures is the abrupt drop in measured amplitude at 1 MHz. This feature was identified as resulting from the mode conversion of the a_0 into the a_1 upon reflection from the end. This frequency is very close to the frequency at which the a_1 mode transitions from a primarily evanescent mode (lower frequencies) to a mostly propagating mode at higher frequencies (see Fig. 4.3 on page 101). The frequency which marks this transition is termed the a_1 mode threshold frequency. The a_1 mode propagates at a higher phase velocity and by the trace velocity matching condition for radiation it does not radiate energy toward the receiver. The reasons why it is possible for mode conversion to occur have not yet been discussed and will be examined in the next section. This mode conversion effect was not observed before in the many investigations of the backscattering spectrum because it occurs at a higher frequency than the experimental arrangement allowed for. The frequency range where the phenomena occurs may be decreased by considering a shell having a thicker wall. To explore the broad picture of the backscattering near the mode threshold experiments were carried out for Shell B at frequencies higher than the previous investigation (e.g. Chapter 2). This involved making measurements with the PVDF sheet source driven with a chirped burst, as was the case for Figs. 7.22 and 7.24

(see also Section A.6 of Appendix A). Figure 8.1(a) shows the results of that measurement for Shell B (air-filled with endcaps). The backscattered spectral magnitude is shown over a broad range of frequencies and cylinder tilt angles. Broadside incidence corresponds to $\gamma = 0°$. The plot in (b) can be used to identify some of the important features. It shows the frequency-angle locations where trace velocity matching may occur for various meridional waves on an infinite hollow cylindrical shell. These curves are calculated as in Chapter 4 using the full three-dimensional elasticity equations. The meridional a_0 is easily identified in the spectrum as the lower limiting ridge of high backscatter. Also visible are what appear to be portions of the meridional s_0 and a_1 or s_1. The a_0 ridge displays a prominent drop in amplitude at about 440 kHz. It nearly disappears before gradually rising in amplitude from 550 kHz to 1 MHz. This drop occurs, as in the previous case for Shell A, right at the mode threshold for the a_1 meridional wave. This mode threshold may be seen in (b) where the coupling loci for the a_1 is cutoff at broadside incidence at $\approx$ 460 kHz. To further investigate this "spectral hole" an approximate PWS calculation was performed for this same spectral region using the theoretical development of Chapter 5. Figure 8.2(a) shows the calculated backscattering spectrum for this case (Shell B, air-filled). Many of the same features are evident in this figure as in the measured response. The important difference, however, is that the approximate PWS calculation shows no sign of a drop in the magnitude of the a_0 meridional ray enhancement (or in the s_0 for that matter). This suggests that the approximate PWS calculation, as it is formulated in Chapter 5, may not include the effects of mode conversion for leaky waves reflected off the shell truncation.

To better understand the nature of the reflection from the end of the cylindrical shell, the following section describes an approximate method of calculating the reflection coefficient at the end of a semi-infinite plate. The discussion should prove useful in understanding the reflection process.

FIG. 8.1 (a) Measured backscattered spectral magnitude for Shell B (*air-filled with endcaps*) at high frequencies normalized with the spectrum of the incident burst. The sheet source was driven with a 270 μs long duration linear FM chirp burst for this measurement. The amplitude scale is set such that 0 dB corresponds to the maximum measured response at $\gamma = 0°$ (broadside incidence) over the frequency range shown. (b) Calculated meridional ray coupling loci for various wave types (see Chapter 4). The "spectral hole" evident in the a_0 meridional ray enhancement near 500 kHz is due to mode conversion into the a_1 mode at frequencies near and above the mode threshold of the a_1 ($f \approx 460$ kHz or $ka \approx 41.2$). Enhancements due to the s_0, a_1 and s_1 meridional rays are also evident. There appears to be a mode threshold effect on the s_0 meridional ray also when the s_1 becomes largely propagating near $f \approx 780$ kHz, or $ka \approx 70$. This color raster image represents the sampling intervals: Δka = 0.089 (Δf = 1000 Hz), $\Delta\gamma = 0.3°$.

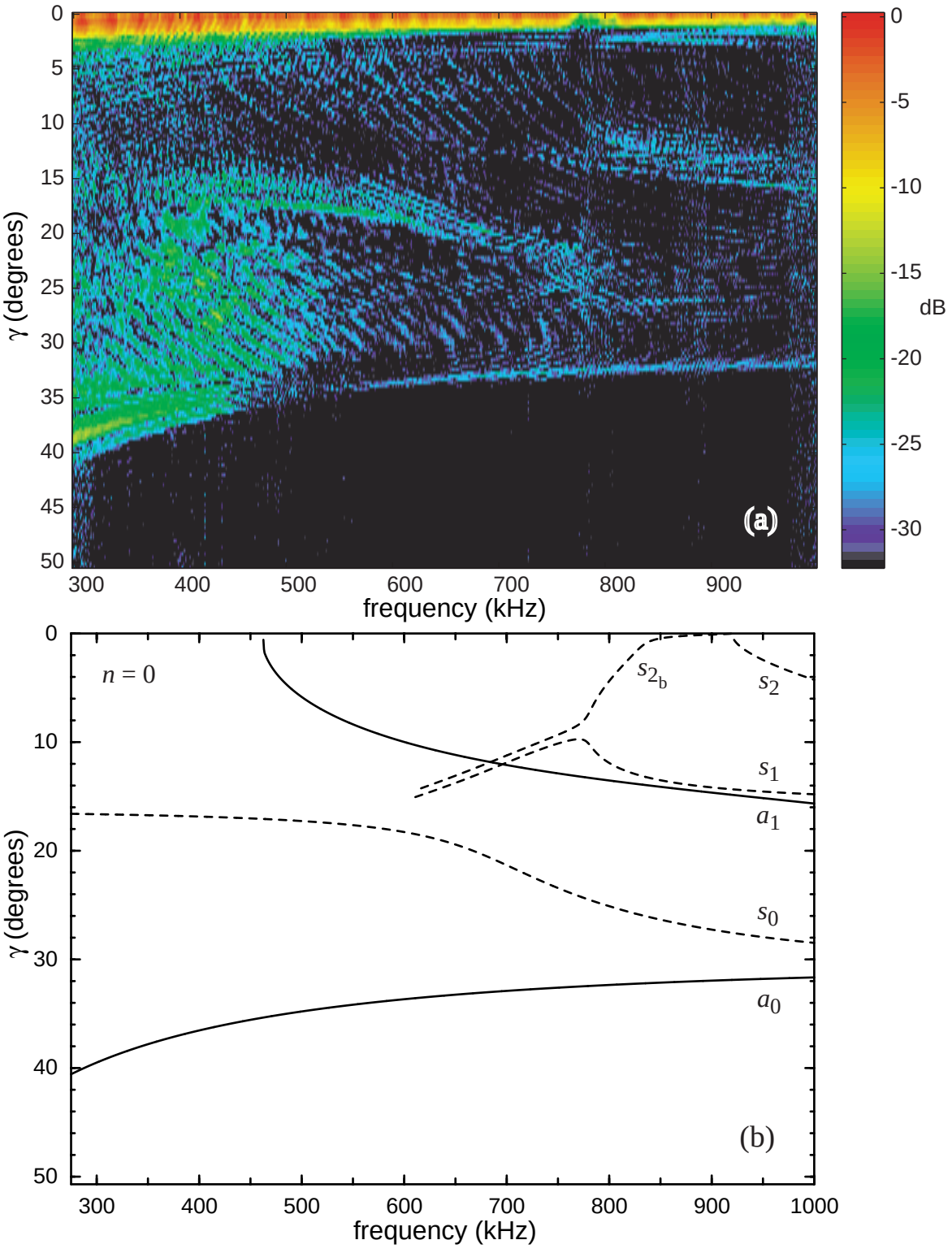
γ (degrees)
frequency (kHz)
dB
(a)
n = 0
s_{2_b}
s_2
s_1
a_1
s_0
a_0
(b)

FIG. 8.2 (a) Calculated backscattered spectral magnitude for Shell B (empty) from the approximate PWS formulation of Chapter 5. The amplitude scale is set such that 0 dB corresponds to the maximum response at $\gamma = 0°$ (broadside incidence). (b) Calculated meridional ray coupling loci for various wave types (see Chapter 4). Compare (a) with Fig. 8.1(a). No mode conversion effects appear to be present in this approximate PWS calculation. This color raster image represents the sampling intervals: $\Delta ka = 0.05$ ($\Delta f = 561$ Hz), $\Delta\gamma = 0.3125°$.

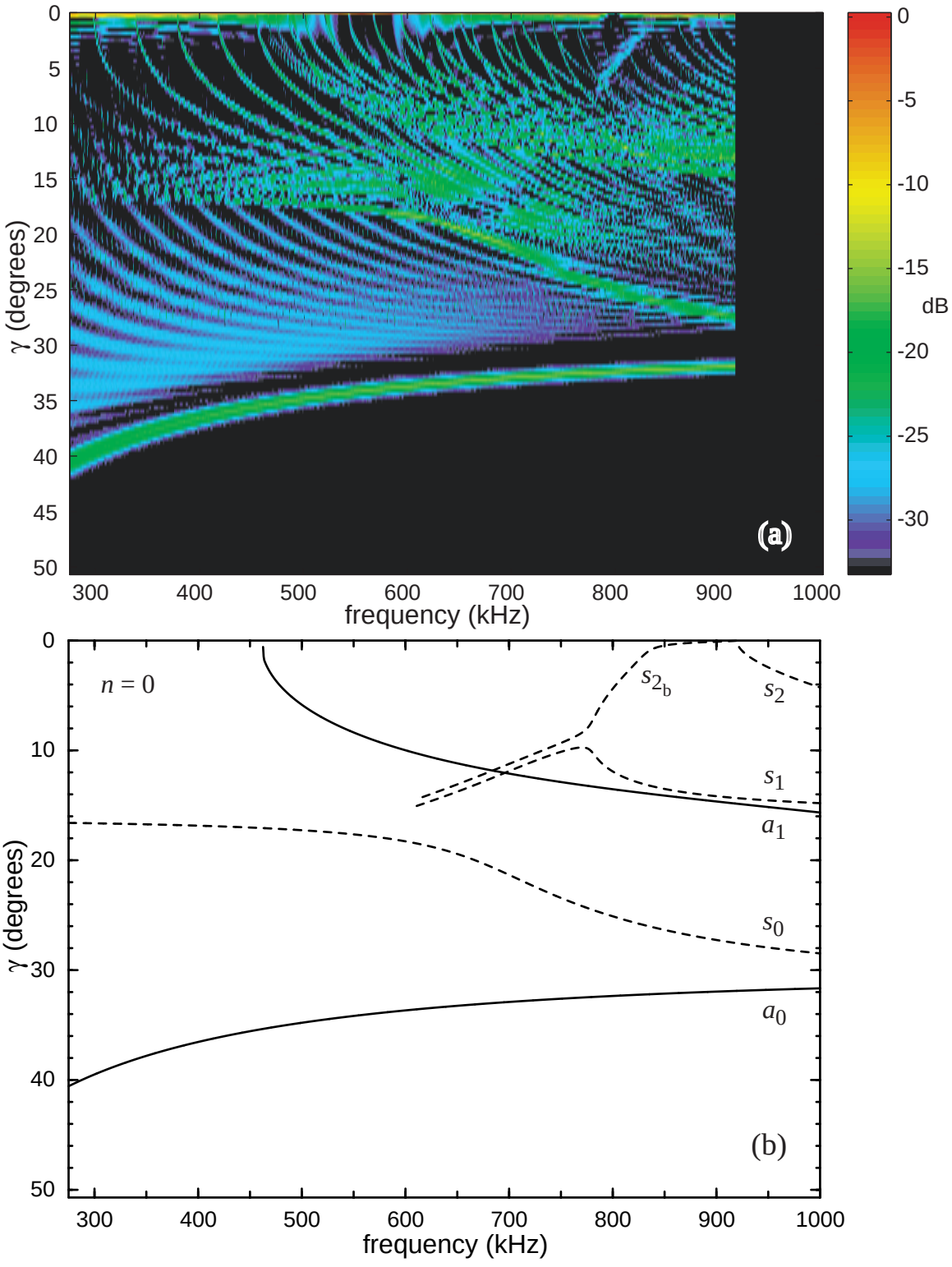
γ (degrees)
frequency (kHz)
dB
(a)
n = 0
s_{2_b}
s_2
s_1
a_1
s_0
a_0
(b)

8.3 Reflection of an Antisymmetric Lamb Wave from the End of a Semi-Infinite Plate

Ideally the problem one wishes to solve in this case is that of the reflection of a mode of a cylindrical shell from a perpendicular flat end. The shell is considered to be fluid-loaded on the exterior and on the end and perhaps as well on the interior. When the mode is selected carefully, this most closely resembles the process of the meridional ray reflection from the end of a truncated cylindrical shell. It is conceivable that a solution to this problem may be carried out using a numerical scheme such as the finite-difference time-domain method (FDTD)[100-102]. Such a solution would allow for the determination of the reflection coefficient as well as the transmission coefficient and the radiation pattern into the fluid at the end. Some results for this type of solution for the geometry of a flat plate can be found in Refs. [98] and [99]. A treatment of the problem in this fashion is beyond the scope of the present dissertation. Instead, a simpler approach is taken. First the curvature of the cylindrical shell is neglected and the problem is reduced to finding the reflection of a Lamb wave at the end of a semi-infinite plate. To simplify the problem even further only the case of a plate in vacuum is considered. This significantly reduces the complexity of the boundary condition at the end.

There have been several investigations of the reflection of a Lamb wave at the end of a semi-infinite *free* plate[85-88,95-97]. In the low frequency regime works by Kane[103] and Lu[104] are significant. In addition there have been some investigations for a semi-infinite *fluid-loaded* plate[89,90]. These investigations typically employ a variational principle or satisfy the boundary conditions at the end in a least squares sense. One approach, Ref. [90], is based on mode theory. An unsuccessful attempt was made by the author to implement the results of that paper to calculate the reflection coefficient. It appears the authors of that paper failed to define one variable; subsequently, due to the complexity of their derivation it was not attempted to re-derive their results. Incidentally there have been investigations of the reflection of waves from the end of solid cylindrical rods as well[105,106]. The approach taken here in calculating the reflection coefficient is found in Refs. [95] and [96]

and is based on a least squares solution.

Approximate Solution for a Semi-Infinite Plate in Vacuum

Consider the end region of a semi-infinite isotropic elastic plate. Figure 8.3 shows a schematic of the plate and a definition of the coordinate system used. A single propagating

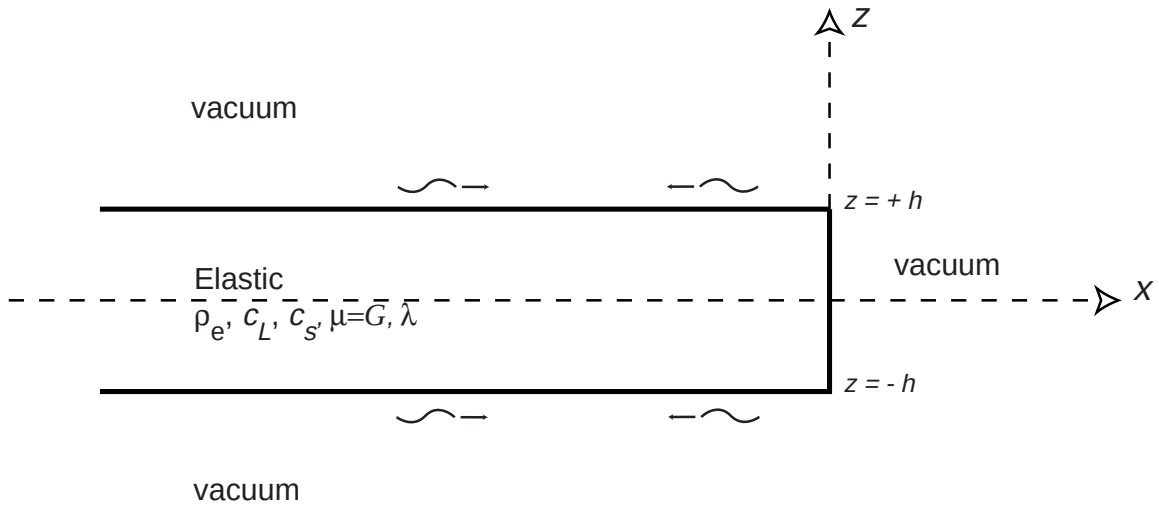

FIG. 8.3 Cross section of the end of a semi-infinite plate and the associated coordinate system. A single Lamb mode is incident from the *-x* direction which reflects off the truncation. The amplitude of the reflected wave depends on whether other modes of the same symmetry are propagating or evanescent.

Lamb mode of the plate is excited at some point at $x = -\infty$ and travels undisturbed toward the end at $x = 0$. Since the plate is not fluid loaded (and assumed to be composed of a lossless elastic material) the term propagating strictly implies that the associated wavenumber is purely real. It is easy to see then that the Lamb wave experiences no damping as it propagates towards the end. In the spirit of solutions employing Saint-Venant's Principle we assume that the incident Lamb wave disturbance may be represented by the exact solution for a Lamb wave propagating in an infinite thick plate

right up to the plate end. At distances far from the end, relative to the plate thickness, this is of course a valid assumption. Severe limitations on this assumption exist, however, even at large distances when the frequency is near or above the first mode cutoff[85]. Near the edge the stress distribution of the incident wave may vary considerably from its infinite plate counterpart. However, since no rigorous solutions for the semi-infinite or finite plate have been derived, even for stress free boundaries, we proceed with the above assumption. Considering the incident Lamb wave, with a known stress and displacement distribution, one simply wishes to satisfy the required boundary conditions at the end (zero stress) with an as yet unknown set of reflected Lamb waves. The method which will be used is a numerical scheme wherein the boundary conditions are satisfied at discrete locations on the end. The problem may be reduced to solving a severely over-determined set of linear equations. The method of least squared error will be utilized in solving these equations. Before proceeding, first examine the properties of Lamb waves in an infinite plate.

The solution for Lamb waves in thick plates is not difficult to find in the literature (see Ref. [107] or e.g. [85], [86], or [40]). The solution for the *antisymmetric case* is given here without proof. The transcendental equation describing the allowed free antisymmetric vibrations of a plate of *half thickness* h, which relates the angular frequency ω to the in-plane wavenumber ξ, is

$$(\nu^2 - \xi^2)^2 \sin(\eta h)\cos(\nu h) + 4\eta\nu\xi^2 \cos(\eta h)\sin(\nu h) = 0. \tag{8.1}$$

Here $\nu = \sqrt{(\omega/c_S)^2 - \xi^2}$ and $\eta = \sqrt{(\omega/c_L)^2 - \xi^2}$. For traveling waves with the x and t dependence noted below the stresses within the plate are

$$\begin{aligned} T_{xx} &= A\frac{G}{\sin(\nu h)}[-(\xi^2 + \nu^2 - 2\eta^2)\sin(\nu h)\sin(\eta z) - (\nu^2 - \xi^2)\sin(\nu z)\sin(\eta h)] \\ T_{zx} &= A2i\frac{G\eta\xi}{\cos(\nu h)}[\cos(\nu h)\cos(\eta z) - \cos(\nu z)\cos(\eta h)], \end{aligned} \tag{8.2(a),(b)}$$

and likewise the displacements are

$$u_x = A\frac{i}{2\xi\sin(\nu h)}[2\xi^2\sin(\nu h)\sin(\eta z) + (\nu^2 - \xi^2)\sin(\nu z)\sin(\eta h)]$$
$$u_z = A\frac{\eta}{(\nu^2 - \xi^2)\cos(\nu h)}[\cos(\nu h)\cos(\eta z) + 2\xi^2\cos(\nu z)\cos(\eta h)], \quad (8.3)(a),(b)$$

where G is the shear modulus and A is an arbitrary amplitude coefficient which is set equal to unity to simplify the notation in the discussion which follows. It should be understood that in each case an x and t dependence of $e^{i(\xi x - \omega t)}$ is assumed and is not shown. A standard convention[40] for the equations of motion and stress-displacement relations (Hooke's Law) in terms of potentials has been used to derive these equations. A discussion of the frequency spectrum of the solutions of the dispersion relation, Eq. (8.1), may be found in Ref. [108], for example. One feature of the solutions of Eq. (8.1) which is at present important is that for a given frequency there are at least two purely real roots (describing the nature of the in-plane wavenumber ξ), a finite number of purely imaginary roots and an infinite number of roots described by a complex wavenumber.

From Eqs. (8.2) it is possible to understand one very important fact about the nature of the reflection at a stress free boundary: *the reflected wave cannot be composed entirely of the same mode as the incident wave.* For the purposes of this discussion, the sign of the real part of the in-plane wavenumber, ξ, typically determines the direction of propagation of the Lamb wave. The incident wavenumber is positive whereas the reflected propagating waves have negative wavenumbers. For a given Lamb wave the in-plane component of stress, T_{xx}, is even in the wavenumber ξ whereas the tangential component, T_{zx}, is odd in ξ. This means that the tangential component of stress (T_{zx}) undergoes a change in sign upon reflection while the in-plane component (T_{xx}) does not. (Note that Torvik[85] apparently stated this just backwards[87].) Due to this fact a simple sum of an incident and reflected Lamb wave of the same mode cannot satisfy the boundary condition of zero normal and tangential stress simultaneously at the end. There must be the possibility, then, of an infinite number of reflected modes, most of which are complex and necessarily decay exponentially as $x \to -\infty$. Most of the previous investigations the author has located assume that all the reflected waves correspond to solutions of the appropriate characteristic equation for the homogeneous problem, here Eq. (8.1). Certainly for time-harmonic,

continuous wave excitation (which is assumed here) this seems appropriate. However, for any form of pulse or transient excitation a rigorous analysis must necessarily account for bulk wave reflection. Briers, *et al*[90], in their mode theory formulation of the problem for a semi-infinite fluid-loaded plate included the possibility of reflected bulk waves. It may also be shown, either by simple considerations or by using mode theory formalism[90], that an incident mode of one symmetry may not give rise to reflected modes of the opposite symmetry. This means that one only needs consider the modes of a single symmetry. This is the case only when there is no fluid-loading or symmetric fluid loading. For the case of one-sided fluid-loading the characteristic equation for Lamb waves may not be separated into symmetric and antisymmetric parts and as a result no solutions exist which have a distinct symmetry in a rigorous sense. For this case it would be necessary to consider all mode solutions.

Since there is the possibility of exciting an infinite number of reflected modes it is necessary for the subsequent calculation to carry out a search for all relevant roots (i.e. modes) of Eq. (8.1) for the specific plate considered. Such a search was carried out for the two plates (labelled A and B) corresponding in thickness and material parameters to Shells A and B, respectively (see Tables 2.1 and 2.2). An example of the lowest antisymmetric roots found for Plate B (the thicker of the two plates) is shown in Fig. 8.4 (the curves for Plate A are simply shifted as a whole in frequency and wavenumber as discussed at the bottom of Table 8.1 and are not shown). The results are plotted in the familiar form of dispersion curves, which locate the root in the complex ξ plane for a given frequency. For the case of symmetric Lamb waves a similar plot may be found in the work of Mindlin[108], for example. Only those complex modes having a negative imaginary part are shown; these are the only ones which are physical for the reflected waves. The complementary modes having a positive imaginary part grow exponentially as $x \to -\infty$ and are excluded. All the complex modes appear in what have been called "conjugate" pairs, pairs of evanescant modes, or pairs of waves having complex conjugate wavenumbers[85,87,95,105]. This refers to the fact that the complex solutions of Eq. (8.1) appear in pairs such that ξ^2 and $(\xi^2)^*$ are solutions [or ξ and $-(\xi^*)$]. (Here the asterisk denotes the complex

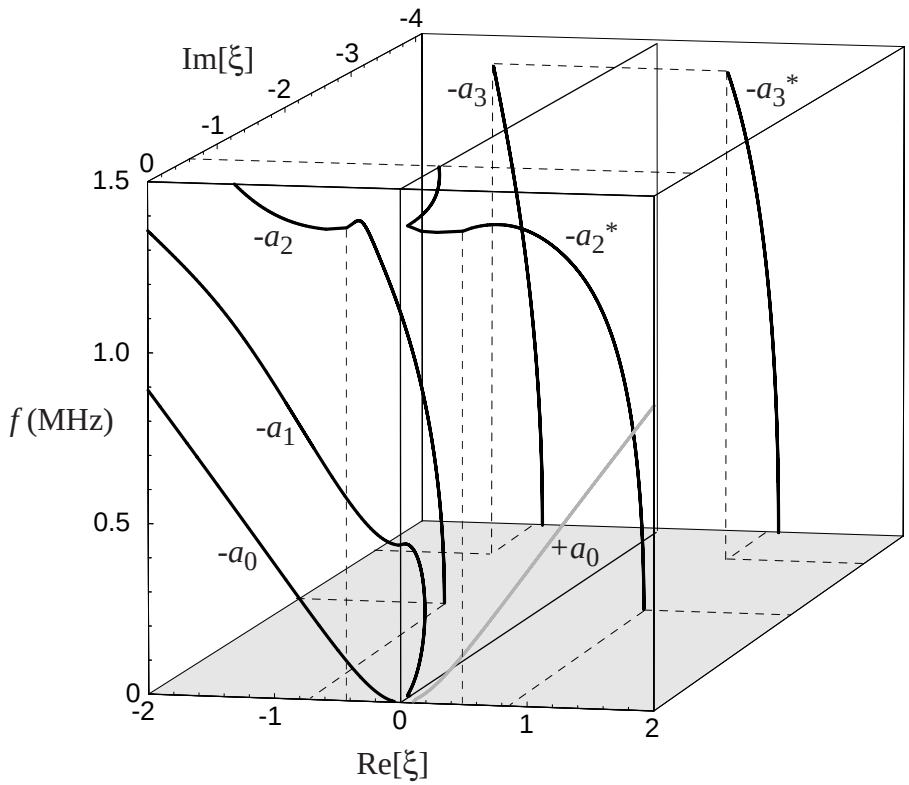

FIG. 8.4 Dispersion curves for the first several antisymmetric modes of an infinite *free* plate. The thickness of this plate (Plate B) corresponds to the wall thickness of Shell B. Modes labelled with a minus sign either propagate towards $x \to -\infty$ (where wavenumber is purely real) or decay as $x \to -\infty$ (when complex). The asterisk indicates the "conjugate" mode. The gray curve indicates the incident mode. The mode threshold of the a_1 mode is $f \approx 0.460$ MHz while that for the next higher mode, the a_2, is $f \approx 1.376$ MHz.

conjugate. In fact there are 2 pairs of complex roots: two solutions which have negative imaginary parts of the wavenumber and two which have positive imaginary parts.) A good discussion of this character of the more general Rayleigh-Lamb equation can be found in the text by Miklowitz[79]. Only 2 of the complex pairs are shown in Fig. 8.4; however, another 8 pairs were located and used in the subsequent calculation. (A sample of the actual wavenumbers for several frequencies can be found in Table 8.1.) These all have increasingly large negative imaginary parts of the wavenumber ξ and as will be seen are less important in satisfying the boundary conditions. It is these pairs of complex modes which have been used to explain the phenomena of "edge resonance" in plates, disks and rods.

Table 8.1: Antisymmetric Lamb wave roots for Plate B†

f (MHz)	ξa_0, -ξa_0	ξa_1	ξa_2, -(ξa_2)*	ξa_3, -(ξa_3)*
0.100	0.3909 + i0, - 0.3909 + i0	0 - i0.3043	-0.8112 - i2.1889, 0.8112 - i2.1889	-0.9817 - i4.0661, 0.9817 - i4.0661
0.440	1.0916 + i0, - 1.0916 + i0	0 - i0.1438	-0.8208 - i2.0730, 0.8208 - i2.0730	-0.9864 - i4.0063, 0.9864 - i4.0063
0.500	1.2112 + i0, -1.2112 + i0	-0.2175 + i0	-0.8233 - i2.0361, 0.8233 - i2.0361	-0.9877 - i3.9878, 0.9877 - i3.9878
1.000	2.2262 + i0, -2.2262 + i0	-1.1440 + i0	-0.8189 - i1.4687, 0.8189 - i1.4687	-0.9962 - i3.7309, 0.9962 - i3.7309
1.500	3.2722 + i0, -3.2722 + i0	-2.4128 + i0	-1.3119 + i0, 0 - i0.5789	-0.9620 - i3.2527, 0.9620 - i3.2527

†The wavenumbers ξ have units of 1/*mm*. To convert these roots to those for Plate A multiply f and ξ by the thickness ratio $h_B/h_A = ((h/a)_B\, a_B)/((h/a)_A\, a_A) = (0.1625*21.02\text{mm})/(0.076*19.05\text{mm}) = 2.359$
The mode thresholds for the a_1 and a_2 modes are $f \approx 0.460$ MHz and 1.376 MHz, respectively.

With knowledge of a large number of the possible Lamb waves which may propagate in the plate upon reflection from the end, in addition to the incident Lamb wave, it is possible to proceed with the calculation as follows. The boundary conditions at the end of the plate must be satisfied using the one incident mode and a large number of reflected modes. At the end the total in-plane and tangential stress must vanish:

$$\begin{aligned} \Sigma_{xx}(z) &= T^{inc}_{xx}(z) + \sum_{j=1}^{2N+2} A_j T^j_{xx}(z) = 0 \\ \Sigma_{zx}(z) &= T^{inc}_{zx}(z) + \sum_{j=1}^{2N+2} A_j T^j_{zx}(z) = 0 \end{aligned} \qquad x = 0, z \in [-h, h] \qquad (8.4)(a),(b)$$

The A_j's are the unknown amplitudes of the reflected modes. Since the stresses are derived by means of a scalar and vector potential (having only one component), which only have one amplitude constant between them, it may be easily shown that the coefficients in Eqs. (8.4)(a) and (b) are the same. It should be understood that the sums are carried out over the

lowest two modes (labelled $-a_0$ and $-a_1$ in Fig. 8.4), thus the +2, plus *N pairs* (i.e. 2*N*) of complex modes, where *N* is to be determined by the level of acceptable error in the calculation. One now evaluates these two expressions at *M*+1 evenly spaced points,

$$z_m = (2h/M)m - h, \qquad m = 0, 1, \ldots, M, \tag{8.5}$$

along the end. This results in 2(*M*+1) equations in 2*N*+2 unknowns (i.e. the A_j's). It is possible to solve this set of over-determined equations (which the reader will note are complex) approximately in a least squares sense. The mean squared error to be minimized is then

$$E = \sum_{m=0}^{M} [\,|\Sigma_{xx}(z_m)|^2 + |\Sigma_{zx}(z_m)|^2\,]. \tag{8.6}$$

A useful derivation of the least squares method, which includes a discussion on allowing the "variables" A_j to be complex, may be found in a text by Claerbout[109].

The amplitude coefficients in Eqs. (8.4) are not simply proportional to the energy in the wave. To be of use each mode must be normalized with respect to the time-averaged power flow of the incident wave. From the discussion in Section 7.3 the time averaged power flow is

$$\overline{\mathbf{P}_x|_{x=0}} = \overline{\int_{-h}^{h} (v_x T_{xx} + v_z T_{zx})\,dz}, \tag{8.7}$$

where v_x and v_z are the components of velocity and the bar indicates a time average of the underlying quantity. Since all quantities are time-harmonic, ($e^{-i\omega t}$) the real part of this expression, representing real power flow, may be written[84]

$$Re[\mathbf{P}_x]\big|_{x=0} = \int_{-h}^{h} \left\{ \frac{i\omega}{4} [(u_x^* T_{xx} + u_z^* T_{zx}) - (u_x T_{xx}^* + u_z T_{zx}^*)] \right\} dz, \tag{8.8}$$

where the asterisk denotes complex conjugation. The relative power flow for the j^{th} mode

with respect to the incident mode is then

$$\mathbf{P}_r^j = \frac{Re[\mathbf{P}_x^j]}{Re[\mathbf{P}_x^{inc}]} \ . \tag{8.9}$$

Noting that the relative reflection amplitude coefficients, A_j, are simply multiplicative in Eqs. (8.4), the reflection coefficient representative of power is found to be

$$\Re_j = (A_j^* A_j)\mathbf{P}_r^j \tag{8.10}$$

which is real. A statement of conservation of energy then follows:

$$1 = \left| \sum_{j=1}^{2N+2} \Re_j \right| . \tag{8.11}$$

Non-propagating modes may have positive or negative $\Re_j$.

An algorithm was written in Matlab® to perform the least squares minimization of Eq. (8.6) and find the coefficients A_j. (The least squares solution of a set of overdetermined linear equations is currently a built-in function in Matlab®.) It is listed in Appendix B. To compare with the results of earlier chapters the $+a_0$ mode was taken as the incident Lamb wave and the amplitude coefficients were calculated for all the other modes considered. Figure 8.5 gives the results for Plate B. It shows the reflection coefficients using Eq. (8.10) for the first several modes. It was determined that using $N = 10$ pairs of complex modes at $M+1 = 401$ discrete points was sufficient to preserve energy conservation to better than 1% over the entire range of frequencies considered. Typical error in energy conservation was on the order of 0.2%, however, near the mode threshold of the a_2 wave the error level increased. This is possibly due to small errors in calculating the dispersion curves and is not expected to significantly influence the calculated curves. Amplitude reflectivity results for Plate A are shown in Fig. 7.7(b) and 7.8(b) where $|\,B\,|$ is given by $\left|\Re_j\right|^{1/2}$ for $j = a_0$. For that case only the reflected a_0 mode is plotted. It should be noted that one may convert between Plate B and Plate A for the power reflection coefficients, $\Re_j$, by simply multiplying the frequency scale for Plate B (in Fig. 8.5) by 2.359, as noted in Table 8.1, to obtain the

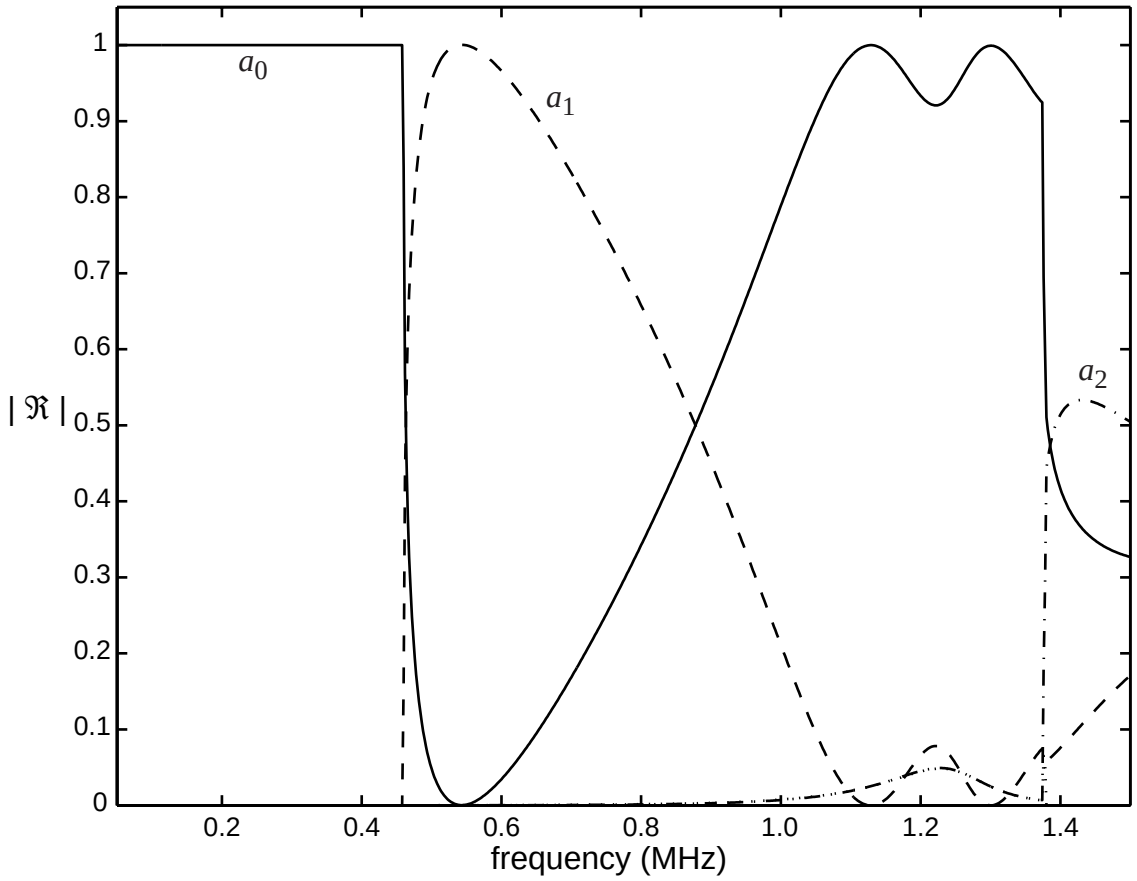

FIG. 8.5 Calculated power reflection coefficients for a free plate (Plate B) for an incident a_0 mode. The reflected waves are normalized by the energy flux of the incident wave and as such the sum of the reflection coefficients should be unity (the plate has a free end). To obtain the reflection coefficients for Plate A one need only multiply the frequency scale above by 2.359, as noted in Table 8.1. The only wave not labelled in the figure is the -a_2* mode which is given by the barely visible dotted line. Below the a_2 mode threshold at 1.376 MHz, the signs of the $\Re_j$ are such that the total power carried by the conjugate pair of a_2 modes vanishes. Therefore the small peaks shown for these sub-threshold modes just above 1.2 MHz just cancel each other in Eq. (8.11).

results for Plate A.

Before discussing the importance of the reflection coefficient results, another issue needs to be addressed. It was stated earlier that the reflected wave could not be made up entirely of the same mode as the incident mode. In this case the reflected mode cannot be entirely the a_0. This remains true despite the fact that the reflection coefficient for the a_0

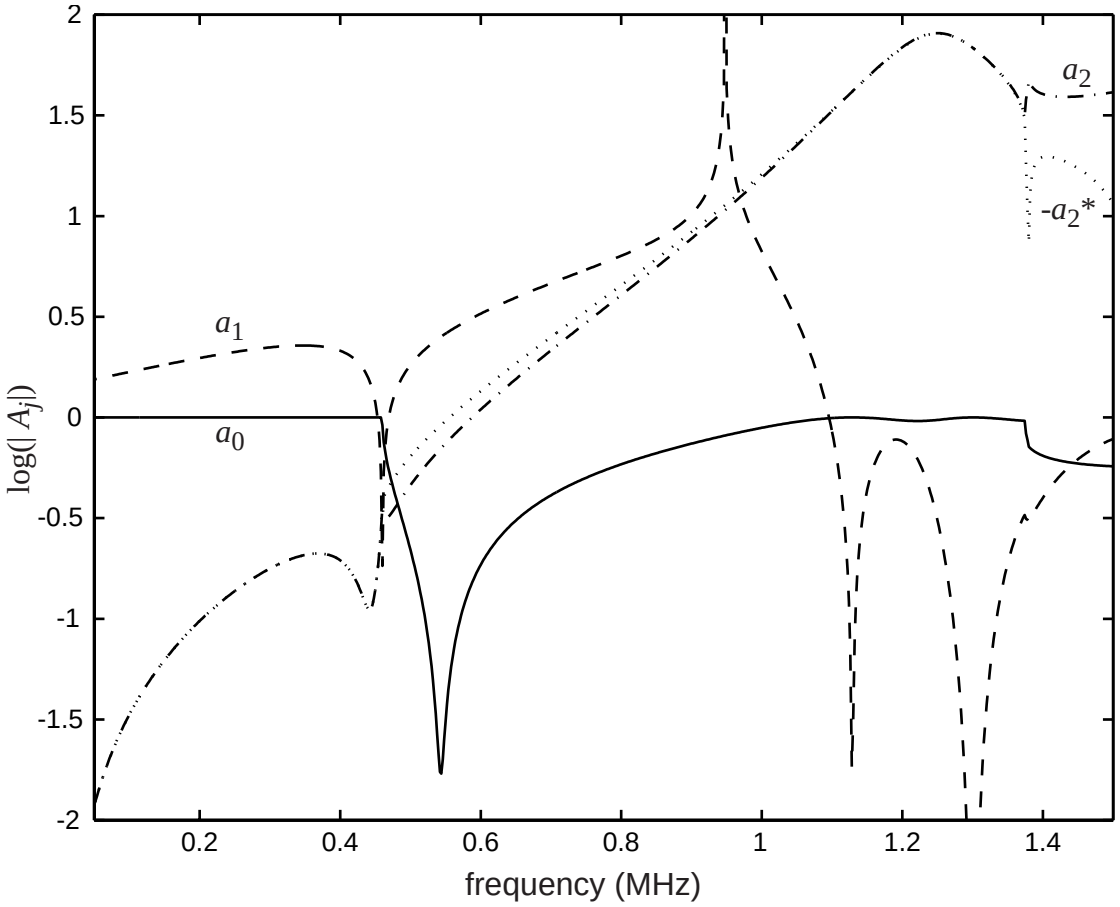

FIG. 8.6 Amplitudes of the reflected modes as a function of frequency for an incident a_0 mode. This illustrates the fact that even though the power reflection coefficient, $|\Re|$, for the a_1, for example, is zero below its mode threshold ($f \approx 0.460$ MHz) (see Fig. 8.5), representing no propagation of power towards a distant observer, an a_1 mode (as well as the higher modes) must still be excited in the reflection process to satisfy the boundary conditions at the plate end. If the plate was subject to light fluid loading such that the modal dispersion characteristics did not change significantly, the vibration of the plate near its end due to the sub-threshold a_1 mode would be expected to radiate sound into the fluid medium.

has a value of nearly unity up to the mode threshold of the a_1. The resolution comes from remembering that the reflection coefficient represents *real* power flow or *real* work done on the plate. Modes with large imaginary wavenumbers represent mostly *reactive* work done on the plate, the real work done being very small in comparison to that of the incident propagating mode. In the present case, below the mode threshold of the a_1 at $f \approx 460$ kHz

all the other modes are heavily damped and do not carry significant energy away from the end to a distant observer. The cutoff modes are still excited to the extent that the boundary condition is approximately satisfied but they are damped out at any appreciable distance from the end and therefore do not have significant power reflection coefficients. To illustrate this fact the amplitude reflection coefficient, $A_{j=a1}$, is shown in Fig. 8.6.

8.4 Discussion

The results in Fig. 8.5 are qualitatively similar to a result found in Ref. [95] for the reflection of the a_0 mode in a glass plate. Most of the other investigations mentioned above only examine the symmetric case. As can be seen from Fig. 8.5 or Fig. 7.7(b), the incident a_0 wave is almost completely reflected for frequencies below the mode threshold of the a_1. Above that frequency the reflected energy is shared by the two propagating modes. The amplitude of the a_0 drops to near zero before rising gradually to near unity. This is precisely what is observed in Fig. 8.1 for the a_0 meridional ray enhancement feature for Shell B [and Figs. 7.7(b) and 7.8(b) for Shell A].

The experiments were performed with a shell in water, where a majority of the end was also exposed to water. As can be seen from Figs. 7.7(b) and 7.8(b) for Shell A there appears to be a degradation of the reflected amplitude which increases with frequency. The degradation in the amplitude reflectivity $|\mathrm{B}|$ appears to be almost linear below the a_1 mode threshold for both the hollow and water-filled shells. This suggests that a fair amount of energy is lost into the fluid upon reflection of the leaky wave from the end. At the higher frequencies shown, the loss represents significantly more than might be expected from simple impedance considerations. Considering normal incidence of a longitudinal wave in a semi-infinite stainless steel half-space at an interface with water, one would find a power reflection coefficient of $|\Re| \approx [(\rho_e c_L - \rho c)/(\rho_e c_L + \rho c)]^2 = 0.88$. This value is meant only to emphasize the relatively large impedance difference between the two materials. The actual radiation loss into the fluid at the end is certainly expected to be quite complex (for images of radiation patterns see e.g. Refs. [98] and [99]).

One aspect of the present calculations which may have implications for the experimental results in Figs. 7.7(b) and 7.8(b) is found in Fig. 8.6. Below the mode threshold of the a_1 near $f \approx 460$ kHz (for Plate B; $f \approx 0.460*2.359 = 1.085$ MHz for Plate A) the amplitude of the reflected (evanescent) a_1 mode increases smoothly with frequency, as opposed to increasing abruptly from a small value to a large value at the mode threshold. As a consequence there are significant vibrations of the plate close to its end due to the reflected a_1 wave even when the a_1 is non-propagating (i.e. evanescent). This would not be expected to influence the reflection coefficient for the incident a_0 wave when the plate is in a vacuum; however, for a plate with fluid loading at its end one may expect to find some radiation of sound into the fluid at the end of the plate because of the displacements introduced by the reflected a_1 wave. This loss would be manifest as a reduction in magnitude of the reflected a_0 wave. In the limit of negligible fluid loading considered here, the sub-threshold a_1 motion radiates as if the a_1 wave is highly supersonic with respect to the surrounding liquid. That is because $\mathrm{Re}[\xi_{a_1}] = 0$.

8.A Reflection Coefficients for an Incident a_1 Mode

The present scheme for calculating the reflection coefficients is applied to the case of an incident a_1 mode for Plate B. For this case only the frequency range where the a_1 mode is propagating is investigated (i.e. above the a_1 mode threshold at $f \approx 460$ kHz). Figure 8.7 shows both the power and amplitude reflection coefficients. Below the mode threshold for the a_2 ($f \approx 1.376$ MHz) the power reflection coefficient calculated for the a_1 mode (when the a_1 mode is incident) displays similar features to the power reflection coefficient for the a_0 mode when the a_0 mode is incident (as in Fig. 8.5). The opposite is found as well: the power reflection coefficient calculated for the a_0 mode when the a_1 mode is incident displays similar features to the power reflection coefficient for the a_1 mode when the a_0 mode is incident. Results appearing in Ref. [88] display this "reciprocal" behavior as well.

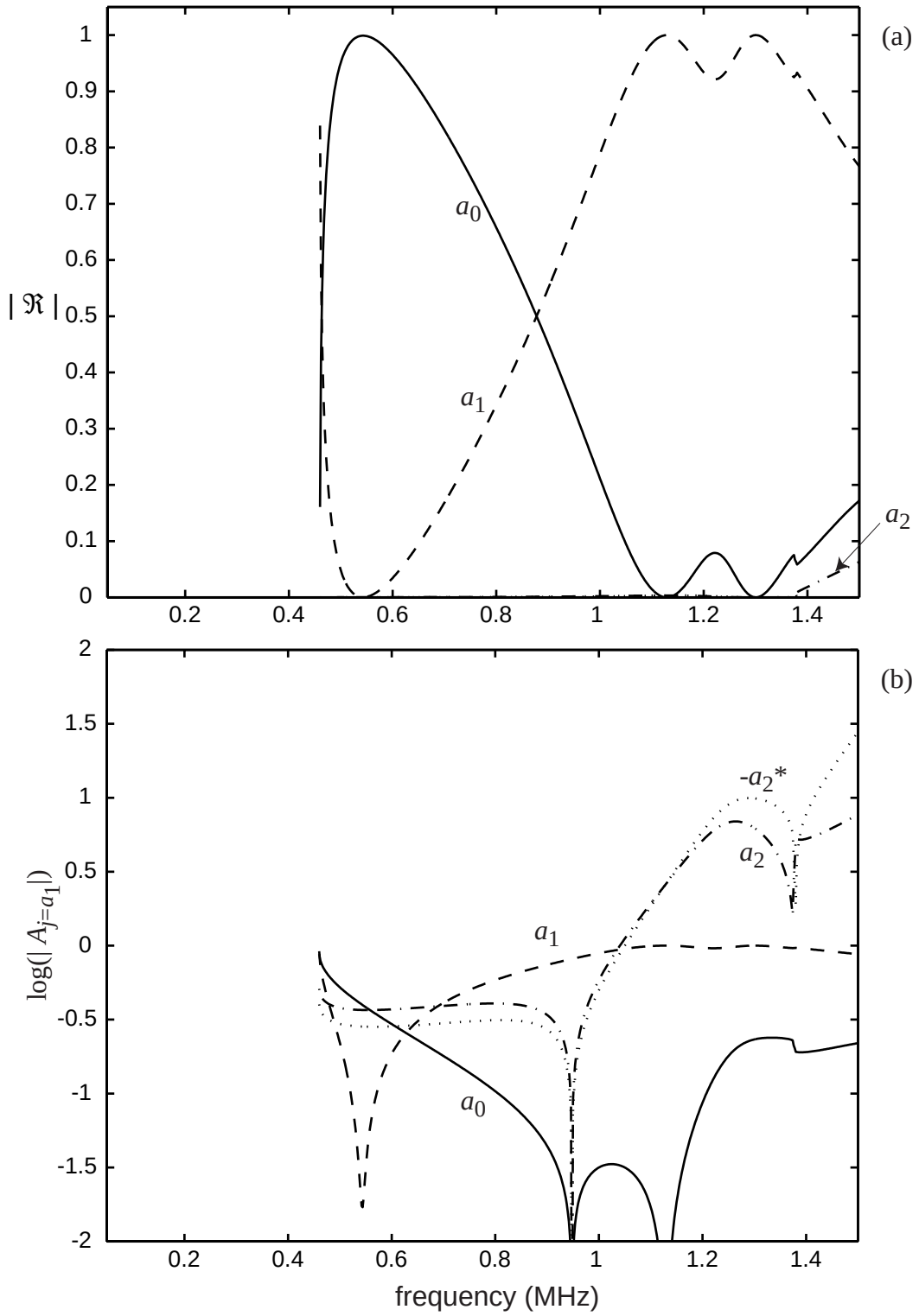

FIG. 8.7 Calculated (a) power reflection coefficients and (b) amplitudes (|*Aj*|) for Plate B for an incident a_1 mode. Recall that the a_1 mode threshold is at $f \approx 0.460$ MHz.

Appendix A Experimental Details

A.1 Introduction

This appendix discusses many of the details associated with the experiments that have not appeared in the main text. It has already been stated that all the experiments were performed in a 12 foot diameter by 8 foot tall redwood tank. This tank is located on the campus of Washington State University in Pullman, Washington. It is filled with fresh water which is nearly always at ambient room temperature. Seasonal variations in this temperature were on the order of 1.5°C and ranged from 19.0° to 20.2°C. The actual temperature was measured during the experiments and the value used for the speed of sound in water was adjusted using published values[110].

The geometries of the finite cylindrical shells examined have been given (see Table 2.1 on page 16) but not much has been said about the endcaps used in some of the experiments. Since it has been shown (in the latter part of Section 7.4) that the endcaps do in fact influence the meridional ray enhancement amplitude it is important to document the actual endcaps used. Section A.2 shows pictures of one of the cylinders with its

endcaps.

Since all the experiments were performed with relatively small distances separating the source and the target it is important to discuss the extent to which "far-field" conditions were achieved. All the theoretical treatments in this dissertation assumed that the receiver was in the far-field. Section A.3 discusses these concerns.

Section A.4 discusses the construction of the PVDF sheet source and the spectral normalization used in many of the figures of this dissertation which accounts for the specific source and receiver characteristics. Section A.5 shows circuit diagrams for the experimental setups. Section A.6 provides information about the *extra* high-bandwidth experiments which were performed with the PVDF sheet source. This refers to the "chirp" experiments in relation to the already high-bandwidth impulse experiments.

A.2 Cylindrical Shells Used in Experiments

Figure A.1 shows a picture of one of the shells used in the experiments. It shows Shell A with the endcaps in place being suspended by thin diameter fishing line. The shell was precisely cut from a length of stainless steel 304 tube stock (1.5"o.d. x 0.065"). It has no visible seams and is smooth. Shell B is nearly identical but has a greater wall thickness. The endcaps, which are made of Plexiglas™, are shown in Figs. A.2 and A.3. A rubber O-ring ensured a water-tight seal and the endcaps were held in place by a light rubber band which was stretched between the two endcaps inside the shell. These endcaps were used for all experiments *except* those of Figs. 2.4(b) and 2.5(b). (That is these were used for Shell A; nearly identical ones were used for Shell B, which has larger radial dimensions.) The experiments leading to Figs. 2.4(b) and 2.5(b) used an earlier generation of endcaps in which the contact with the cylinder was made through O-rings placed on the *end* of the shell (instead of against the inside surface as can be seen in Figs. A.1, A.2 and A.3). These endcaps were slightly larger and had more Plexiglas™ material extending from the cylinder's ends.

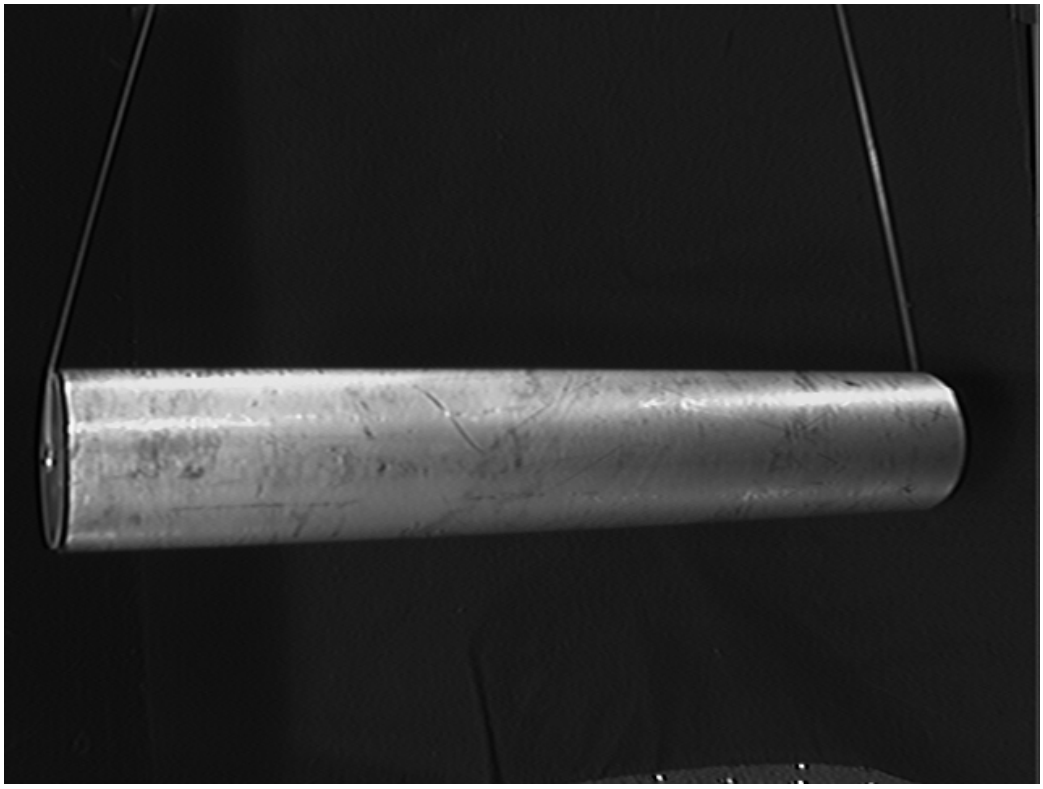

FIG. A.1 Picture of Shell A with endcaps and fishing line supports.

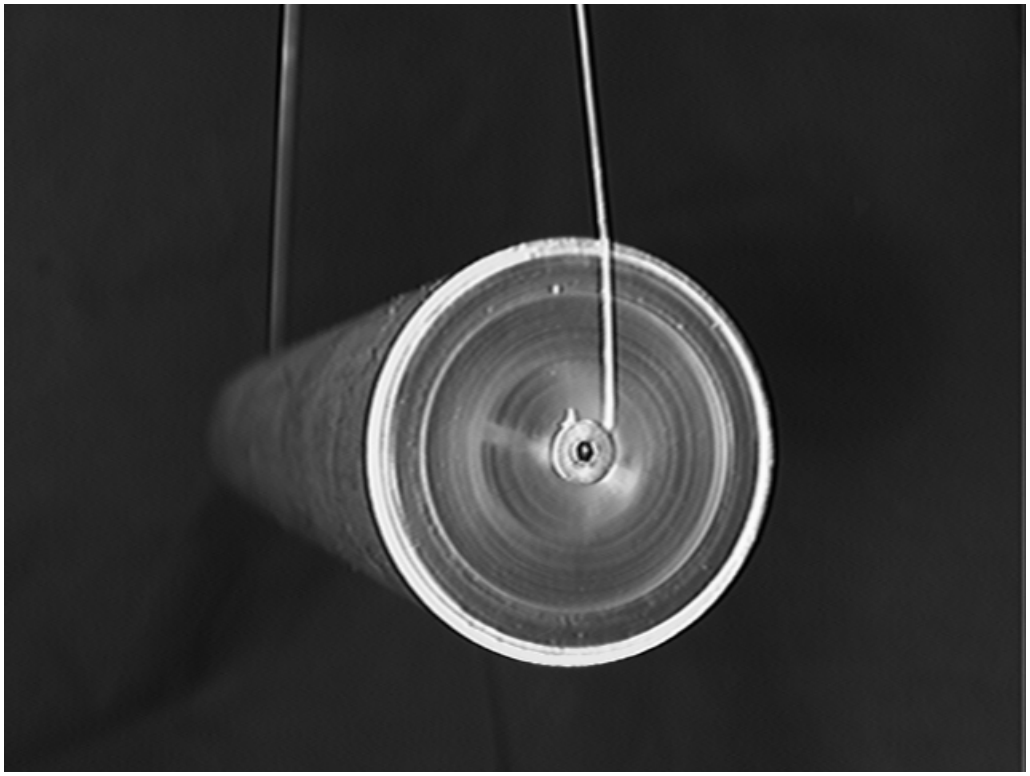

FIG. A.2 Close-up of the end of Shell A.

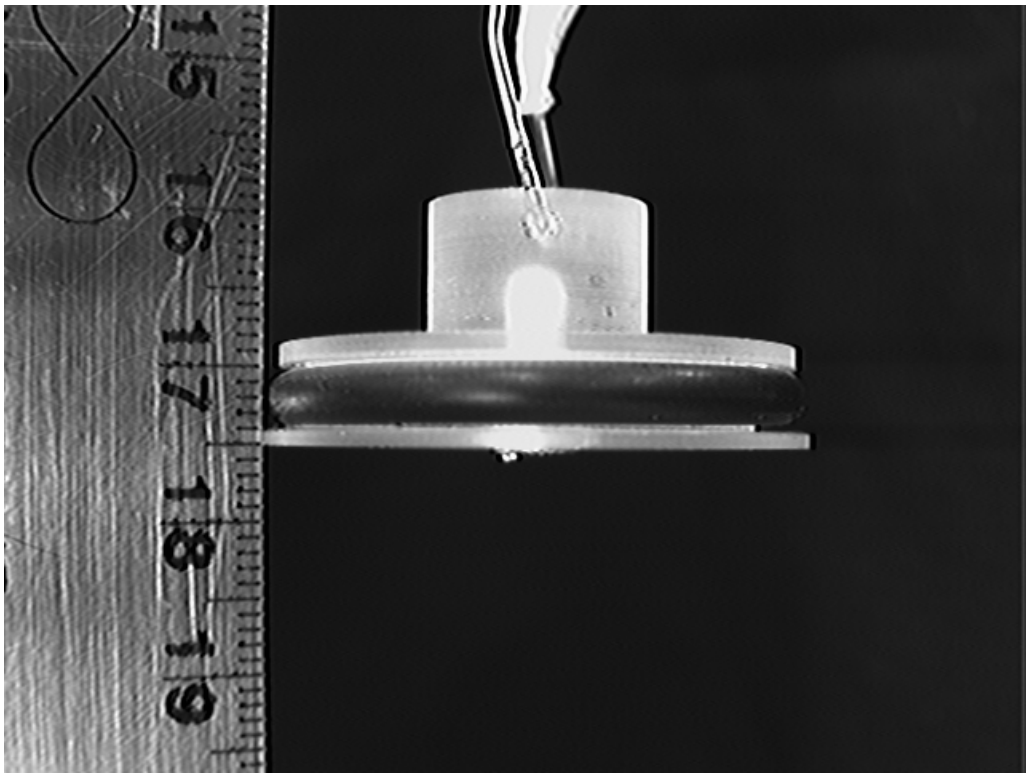

FIG. A.3 Close-up of the endcap used with Shell A.

A.3 Experimental Setup and the Far-Field Assumption

Two questions arise when considering far-field conditions. First, and perhaps simpler, is whether or not the target is in the far-field of the source transducer. Secondly, is the receiver transducer in the far-field of the target?

Consider the first question. In all the experiments performed it is desired to have a plane wave incident on the target. When the large PVDF sheet source is used an approximate plane wave is generated directly. The quality of this plane wave depends first on the ability to excite the thickness mode of the PVDF film in a uniform manner over the dimensions of the sheet. Two steps were taken to ensure the best possible performance in this area. First, electrical contacts were made at locations on each of the four sides and

corners of the sheet. Secondly the PVDF film with the best available surface conductivity was used. The first sheet source constructed had a Ni-Cu coating (not used). The improved sheet source used in the present experiments has an Ag-ink coating. This decreased the surface resistivity from 2.0 to 0.1 Ω/square. Modelling the electrode and sheet source as a distributed resistance and capacitance network would give a phase shift between the applied voltage and the voltage across the center of the sheet. It is assumed that this phase delay to excite the center of the film is small compared to the period of the driving signal. A spatial mapping of the pressure field of this transducer has not been performed. The extent to which the plane wave is uniform over the entire target depends on the size and proximity of the target with respect to the sheet source. The sheet source used was square, having a side length of 28 inches. The longest cylinder examined was 9 inches in length. In all cases the target was placed as close to the center of the sheet as timing considerations allowed. Since the targets were small compared with the dimensions of the sheet and located very close to the PVDF film it is assumed that the incident acoustic wave is approximately planar.

For the *tone burst measurements* of Chapter 7 a simple piston-style immersion transducer was used to generate the incident acoustic wave. In this case the intent is to place the transducer sufficiently far away from the target that the incident wave is approximately planar over the dimensions of the target. Furthermore the amplitude of the incident plane wave should be approximately uniform over the lateral dimension of the target. Consider the transducer for a moment to be an ideal point source which emanates a perfect spreading spherical wave of wavelength λ. A target is placed a distance R away, which has a principle length parameter r_o (i.e. radius or half length) and a radius of a (for nondimensionalization purposes). Through geometrical consideration of the phase error it may be said that the spherical wave at the target is approximately planar for $R \gg (1/2)kr_o^2$ which gives $ka \ll 2aR/r_o^2$. For one of the cylinders used in the present experiments (where $R \approx 2.3$ m, $r_o = L/2 = 114.3$ mm and $a = 19.05$ mm) this requires $ka \ll 7$. This is clearly *not* satisfied for most frequencies considered. One consequence of this is that there will be small variations in the angle of incidence of the impinging wave at different locations along

the cylindrical shell. This effect has been observed in the course of the experiments, e.g. see Section 7.4 of Chapter 7. Next, consider the radiation field of the transducer. In modeling the response of piston style transducers it is often convenient to first approximate their behavior with the response of an ideal circular piston. If the source transducer is considered to be an ideal circular cylindrical piston of radius a_o then one finds a second requirement for the target to be in the far field. In order to assume that the target is in the Fraunhofer regime of the source one must have $ka \ll 2aR/a_o^2$ (e.g. see Sect. 5.2 of Ref. [9]). For one of the transducers (1″ dia.) this requires that $ka \ll 540$. This is satisfied in the present experiments and so it is possible to assume that the target is in the far field of the source transducer. The far-field radiation pattern of a circular piston can be easily calculated[9]. Its angular pressure amplitude dependence is proportional to $J_1(ka_o \sin\theta)/(ka_o \sin\theta)$, where J_1 is the 1st order Bessel function. For a typical experimental setup the -3 dB intensity beamwidth at the target location is expected to be on the order of 560 mm for ka = 20, 280 mm for ka = 40 and 140 mm for ka = 80. The incident pressure amplitude is therefore fairly uniform over the length of the cylinder (L = 228.6 mm) for $ka < 40$ or $f \approx 500$ kHz. As will be discussed below, when examining the meridional ray enhancement it is often only a small part of the cylinder, near the far end, which is responsible for the enhancement. As a result the uniformity of the incident pressure amplitude is certainly adequate at frequencies as high as 1 MHz.

Now consider the scattered response. The worst case scenario is for the cylindrical shell at broadside incidence. The backscattering response at the shell is obviously very complex, both spatially and temporally. However the backscattered field at the receiver transducer may be considered to be the result of the radiation from a particular rectangular aperture of approximate dimensions L by $2a$. As was mentioned above it is desired that the receiver be in the Fraunhofer regime for the aperture (e.g. see Sect. 8.3.3 of Ref. [45]). For the rectangular aperture it is required that $R \gg (1/2)k(L/2)^2$, which translates into $ka \ll 2aR/(L/2)^2$. This means that in the present experiments at broadside incidence $ka \ll 7$, which as stated above is not satisfied. Evidence of near-field scattering (as opposed to the far-field Fraunhofer scattering) has been observed in the backscattering results of

angular scans about broadside incidence. The results presented in this dissertation for broadside incidence should be regarded with this in mind. The focus of this dissertation, however, is the backscattering response at oblique incidence. As the cylinder is tilted the length of the effective aperture decreases. This relaxes the above far-field condition in a simple manner: $ka \ll 2aR/(\cos\gamma L/2)^2$. Since the meridional ray feature studied is typically found at angles ranging from $\gamma = 35°$ to 65° one finds that $ka \ll 10$ or $ka \ll 38$. It is also known that the enhancement resulting from this meridional ray feature is primarily due to radiation from a localized region near the end of the cylinder. The other regions on the cylinder being far less important to the backscattered field. This region is approximately determined by the attenuation length, L_e, of the meridional leaky wave under consideration. In general the aperture of overall length L may be replaced by $L_e = a/Im[k_z a]$, which is on the order of 25 mm (see Section 3.6 on page 79, Eq. [3.4] and Fig. 3.20). With this in mind the far-field condition is relaxed even further to requiring that $ka \ll 840$. There is obviously no difficulty in meeting this requirement.

A.4 PVDF Sheet Source: Construction, Spectrum and Normalization

This appendix discusses the construction of the PVDF sheet source and the normalization used in the experimental spectral data. A diagram of the sheet source is shown in Fig. A.4. It is constructed of a 110 μm thick Kynar® polyvinylidene fluoride (PVDF) film, metallized on both sides and sandwiched in a copper frame. This film was purchased from AMP Inc. of Valley Forge, PA. Figure A.5 shows more of the particulars of the sheet construction. This particular company could only manufacture the PVDF film to a maximum of 14 inches wide. As a consequence, to construct a large sheet (here 28″ x 28″) it was necessary to combine two sheets together. This was done by taping the two together as shown, being careful to match the polarities of the individual sheets. To decrease the electrical coupling through the water and protect the surface metallization a thin sheet of

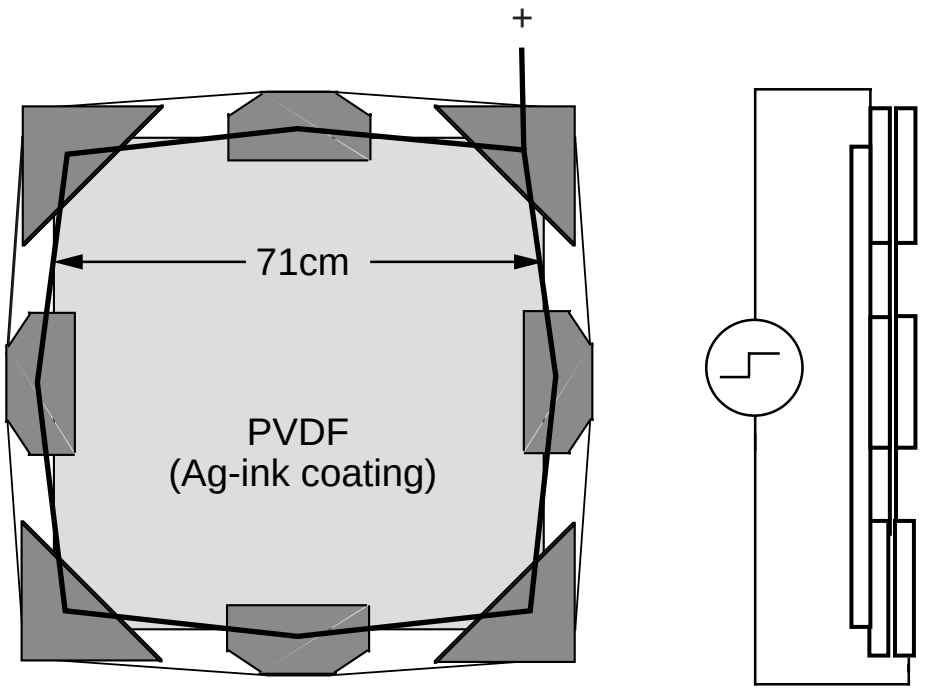

FIG. A.4 Schematic of the PVDF sheet source. The front view (left) shows the sheet held by a rectangular copper frame. Electrical contacts (+ side) are shown "daisy-chained" around the perimeter of the frame. The side view (right) shows the sandwiched construction.

adhesive backed Mylar was laid down over the film as shown. To further insulate the transducer, all conducting surfaces connected to the positive side of the sheet were coated with either Kapton® adhesive tape or a low viscosity epoxy. Some properties of the sheet which are of importance are: surface resistivity, 0.1 Ω/square; electrical capacitance, ≈ 102 pF/cm^2; sound speed in the thickness direction 2200 m/s; sound speed in stretch direction, 1500 m/s; Young's Modulus, 2-4 x 10^9 N/m^2; mass density, 1780 kg/m^3; water absorption, < 0.02%; maximum operating voltage, 750 volts/mil (obtained from Amp Inc.). The sheet source represents a relatively large capacitive load (measured static capacitance $C \approx 0.44$ μF) and must be driven with a pulse generator or amplifier capable of driving such loads. The pulse generator used, made by Avtech Electrosystems LTD. (model AVO-8C-C) and designed to drive low impedance laser diodes, was capable of driving such a load with a rise time on the order of 200 ns. The pulse width of this unit was selectable from 2 μs - 200 ms. When tone bursts were desired the sheet was driven with a Hi-Fi audio amplifier

Thick (Ag ink) Metallization Thin Piezo Film Sheets. (2 sheets consisting of Parts A and B shown below)

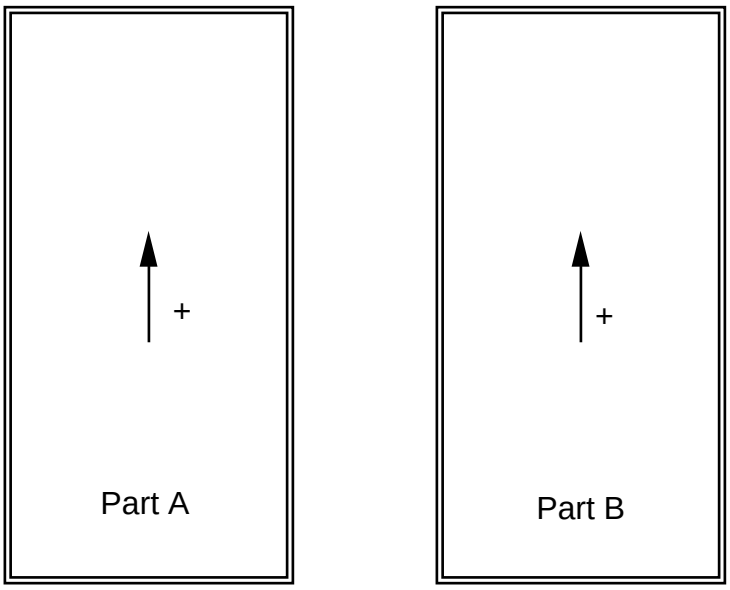

Parts A and B each have 1 layer of 0.001" mylar on both sides.
NOTE shape and positioning of mylar relative to Piezo Sheets shown below.

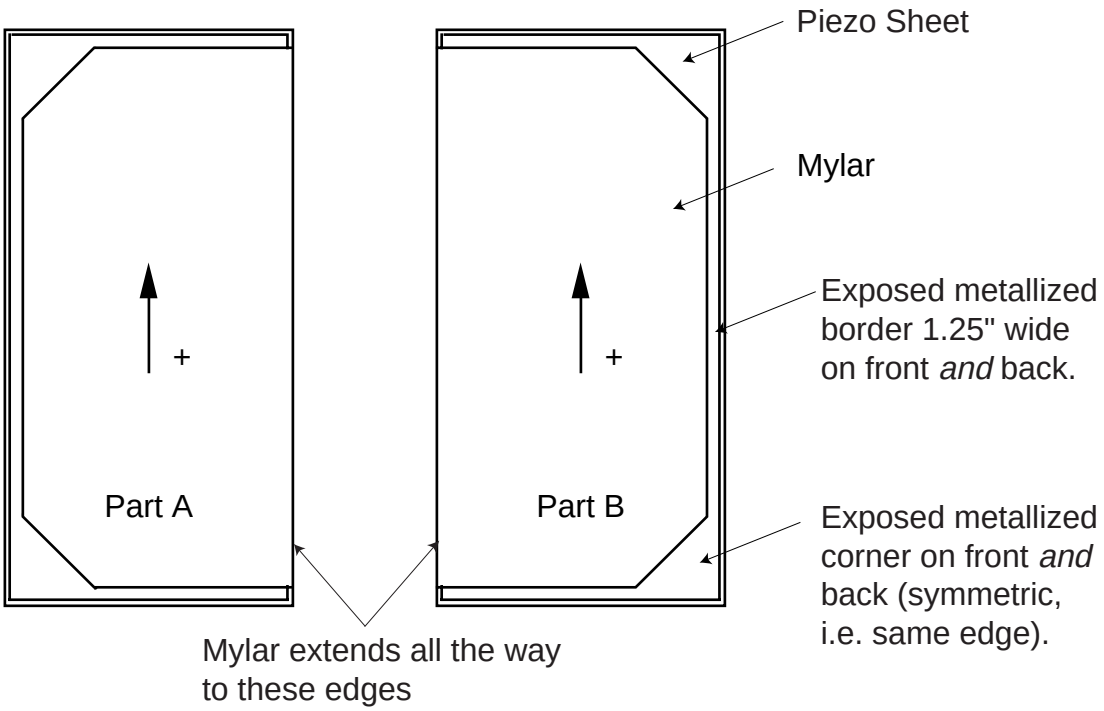

FIG. A.5 Details of the PVDF sheet construction. The sheet transducer is composed of two individual sheets of PVDF film joined together by Kapton® tape.

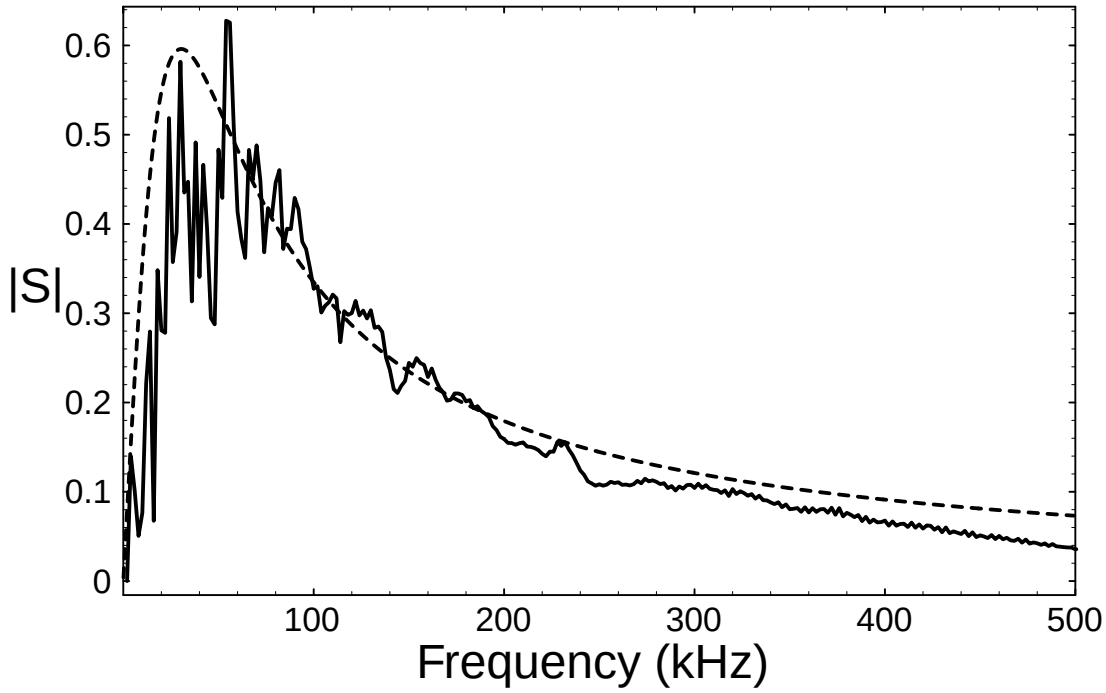

FIG. A.6 Measured spectrum of the pressure impulse generated by the sheet source (solid line). A simple lumped parameter model of the source and receiver system yields a good approximation (dashed line) of the measured spectrum.

made by Hafler®. This particular amplifier, Model 9505 (375 wpc @ 4Ω, 150V/μs slew rate), although rated to 300kHz could produce usable waveforms to 1MHz (see Section A.6).

To characterize the performance of the sheet source a system impulse response was measured with the hydrophone placed approximately at the target location. The solid line in Fig. A.6 shows the Fast Fourier Transform (FFT) of the measured pulse. The smooth dashed curve is the expected spectrum from an idealized source-receiver model to be described subsequently. The spectrum of the source-receiver impulse response is taken to be the best fit of this model to the measured spectrum. The FFT of each time record in the scattering experiment was divided by this smooth estimate of the system impulse response to obtain the measured scattering spectrum.

To approximate the spectrum of the source a simple lumped electrical parameter circuit model was introduced. Figure A.7 shows this circuit model where the source is taken to be an idealized capacitor in series with a small resistor. The acoustic pressure generated by the PVDF is approximately proportional to the current (e.g. see Ref. [20]), which for a step

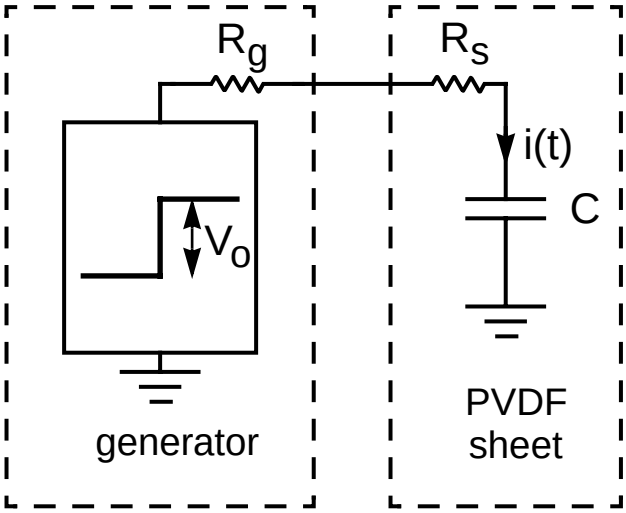

FIG. A.7 Lumped electrical parameter circuit model which is used to model the frequency response of the PVDF sheet source.

voltage input gives the *unipolar* pressure pulse

$$p(t) = Ki(t) = K\Theta(t)i_o e^{-t/RC} \tag{A.1}$$

$$i_o = V_o/R, \qquad R = R_g + R_s$$

where K is a constant determined by the piezoelectric properties, $\Theta(t)$ is the unit step function, C denotes the capacitance of the sheet, and R is the sum of the generator and effective sheet resistances. The magnitude of the spectrum associated with this pressure is

$$|S(\omega)| = [1 + (RC\omega)^2]^{-1/2} \tag{A.2}$$

where $\omega = 2\pi f$. The spectral amplitude given in Eq. (A.2) has a value of unity at zero frequency. In the experiment the low frequency response is limited by the roll-off of the hydrophone, which is governed largely by the load resistance R_h and hydrophone capacitance C_h. The normalized low frequency behavior of the receiver can be approximated as a high-pass filter with frequency response

$$|S_h(\omega)| = [1 + (R_h C_h \omega)^{-2}]^{-1/2} \quad . \tag{A.3}$$

At frequencies well below the fundamental hydrophone resonance ($f \approx 750$ kHz) the approximate spectrum of the source-receiver system is the product of $|S(\omega)|$ and $|S_h(\omega)|$. Figure A.6 shows that this simple model overestimates the high frequency response of the source above about 230 kHz; as a result, it is necessary to multiply Eq. (A.2) by a slowly decaying function of ω for use in the actual normalization of the experimental spectra. This function is $[1 + (RC\omega)^2]^{-0.25}$ and is thought to be a consequence of the specific receiver used, which was originally designed as an NDT immersion transducer. The resulting fit to the experimental source spectrum is a four parameter fit: RC, R_hC_h, the exponent (0.25) and the overall amplitude factor. For the fit shown in Fig. A.6 $RC = 6.07 \times 10^{-6}$ and $R_hC_h = 4.5 \times 10^{-6}$. Comparing the fitted parameter RC with the approximate measured source capacitance ($C \approx 2.4$ μF) yields $R \approx 2.5\ \Omega = R_s + R_g = R_s + 0.2\ \Omega$. This value is compatible with the expected sheet resistance. The value reported above for the measured source capacitance was obtained with the sheet source wet, i.e. submerged in the water tank. When dry the measured sheet source capacitance (C ≈ 0.44 μF) is much closer to the expected capacitance (C ≈ 0.52 μF) based on the capacitance per area of 102 pF/cm^2 reported by the manufacturer for the sheet [with each side of the sheet measuring 14″ x 28″ = 2529 cm^2 and the two sides of the sheet together(see Fig. A.5) treated as two capacitors in parallel]. It is noteworthy to point out that different values were measured for the capacitance of the submerged sheet over intervals of months during which the sheet source was used considerably. These values ranged from 2.4 μF to 6.0 μF. The cause of this change is not well understood. No appreciable change was observed in the measured capacitance of the sheet when dry over a 34 month interval (measurements ranged from 0.457 μF to 0.438 μF). All capacitance measurements were performed with a Hewlett Packard Universal Bridge (Model 4260A) at 1 kHz. The normalization function shown above was used in the normalization of Figs. 2.4(b) and 2.5(b). The normalization used in Chapter 3 is different since the sheet source was driven in a different mode, as discussed below.

It is also possible to drive the sheet source with a voltage *pulse* instead of a voltage step. This produces a *bipolar* pressure pulse, which can have several advantages over the unipolar pulse. Figure A.8 shows a comparison of the two modes of driving the sheet

source. For each mode the driving voltage, either a step or pulse, is 5.7 volts. (During the experiments typically this voltage is 18 V for the step mode and 32 V for the pulse mode. The relatively low voltages used in Fig. A.8 was used for illustration purposes since higher voltages overdrive the preamplifier during the acoustic pulse travelling directly from the sheet to the hydrophone.) For the step mode the pulse width, Δt_{pulse}, was on the order of 2 ms while for the pulse mode it was $\Delta t_{\text{pulse}} \approx 1.6$ μs. The experimental setup is identical between the two cases and the receiver transducer is placed very close to the sheet (15.7cm away). The step mode displays better low frequency response but the pulse mode has better high frequency performance. While neither mode displays considerable ringing after the initial pulse, the pulse mode is substantially quieter in this region. This often enables better background subtraction during the experiments and increases the signal-to-noise ratio. Since the spectrum of the pulse in this mode is different than for the step mode one must use a different normalization function in normalizing the experimental backscattering spectrum. All the figures shown in Chapter 3 which involve the backscattering spectrum (i.e. Figs. 3.3 - 3.9) have been normalized with the following function, which has been determined with a fit to the measured spectrum of the incident pulse as shown for example in Fig. A.8,

$$|S(f)| = A_s \frac{|\sin(\pi t_p f)|}{[1 + (2\pi RCf)^2]^{3/2}[1 + (2\pi R_h C_h f)^{-2}]^{0.45}} + A_g \exp[-g(f - f_o)^2]. \qquad \text{(A.4)}$$

The constants used in this expression were explicitly: $A_s = 250$; $t_p = 1.40\times10^{-6}$ s; $RC = 1.25369\times10^{-6}$; $R_hC_h = 0.250\times10^{-6}$; $A_g = 6.6$; $g = 5.91716\times10^{-10}$; and $f_o = 1.71\times10^5$ Hz.

In both cases, either for the step or pulse voltage excitation, spectral normalization is difficult below about 25 kHz. Often the normalization functions approach zero amplitude quicker than the experimental spectrum as the frequency approaches zero. This results in large amplitude normalized spectra which are not due to the backscattered signal. To minimize this effect the amplitude of the normalization function was held at its value at 25 kHz for all frequency components below 25 kHz. In Fig. 3.3 the entire region below 35 kHz was simply zeroed out to eliminate these low frequency errors.

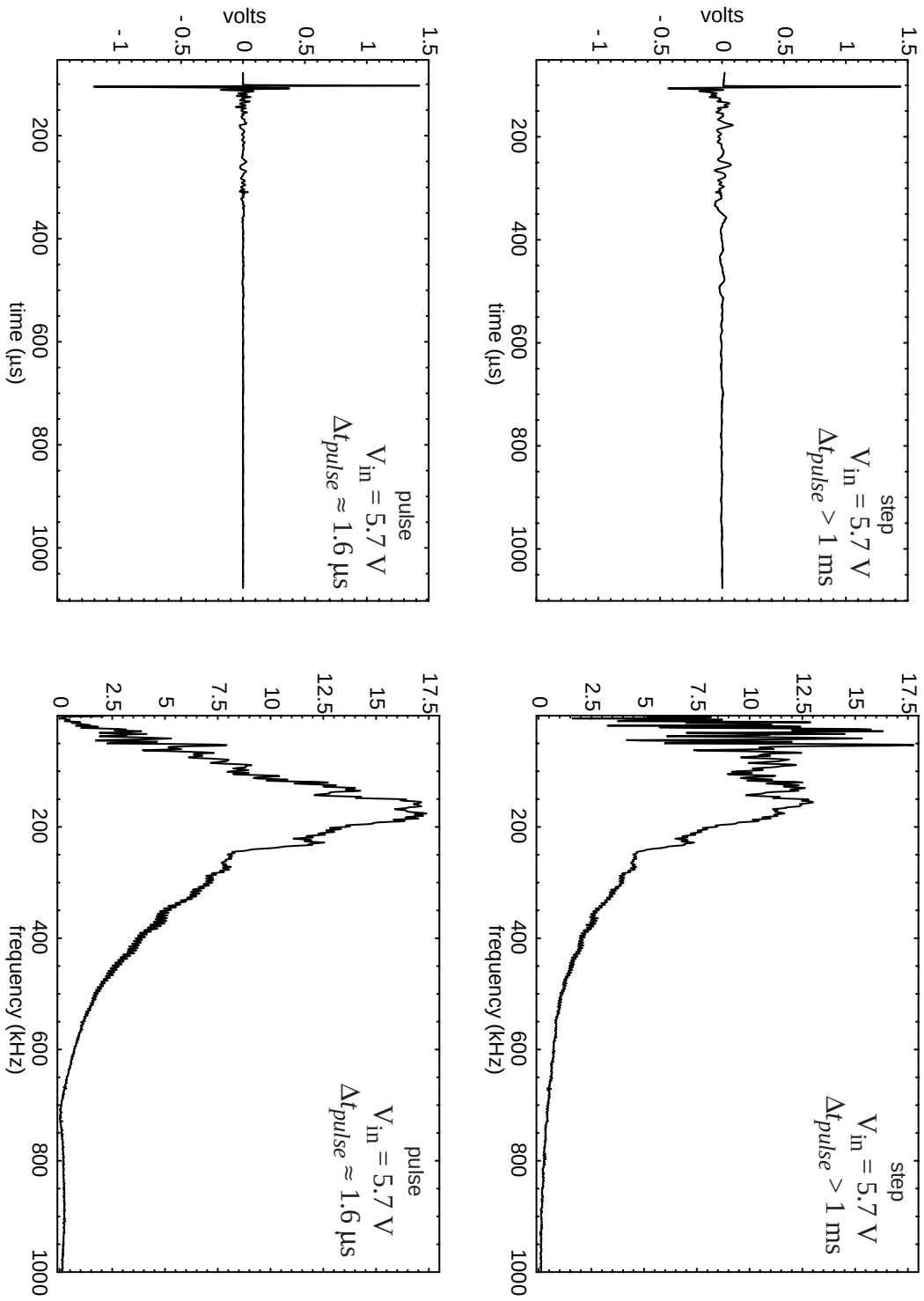

FIG. A.8 A comparison of the two types of pressure pulses generated by the sheet source. Measured pressure pulse (top) and its corresponding spectrum (bottom) for a step (right) or a pulse (left) voltage input. The step mode has a better low frequency response while the pulse mode displays better high frequency response. For both cases the receiver transducer is placed 15.7 cm away from the sheet.

Two final comments are made about the spectra shown. The null evident at about 700 kHz for the pulse mode is not an artifact. It can be shown that this frequency is related to the width of the initial pressure pulse. Decreasing the pulse width would have the effect of shifting the null to higher frequencies. The cause of the large oscillations below 100kHz in the spectrum of the step mode is not understood. These may be a result of the finite width ($L_s = 71$ cm) of the source. Notice , however, that in the near-field (adjacent to the center of the source) for the step mode the low frequency response should remain flat down to a frequency of $c_{water}/L_s \approx 2$ kHz and the low frequency roll-off is a consequence of pulses from the source edge.

A.5 Circuit Diagrams and Setup

For the experiments which used a transmit-receive setup the circuit diagram used is shown in Fig. A.9. These experiments did not use the sheet source but rather the piston style transducers. For the experiments using the sheet source (unipolar or bipolar impulse response or chirp experiments) Fig. A.10 shows relevant circuit diagrams for driving the sheet as well as the setup used for the receiving hydrophone. Since the sheet source is highly capacitive it was found to be beneficial to include a resistance in parallel with the sheet. To insure that these load resistors did not introduce any unnecessary inductive load only carbon or special low inductance wire-wound resistors were used.

In the receiving setup the resistor to ground is used to set the low frequency roll-off behavior of the system. Together with the capacitance of the hydrophone this acts as a high-pass filter with a 3 dB point of $f_{3\text{dB}} \approx 1/(2\pi RC)$. The series resistance is necessary to prevent the preamplifier from feedback oscillations which result from the highly capacitive load of the hydrophone.

Transmit-Receive (TR) setup:

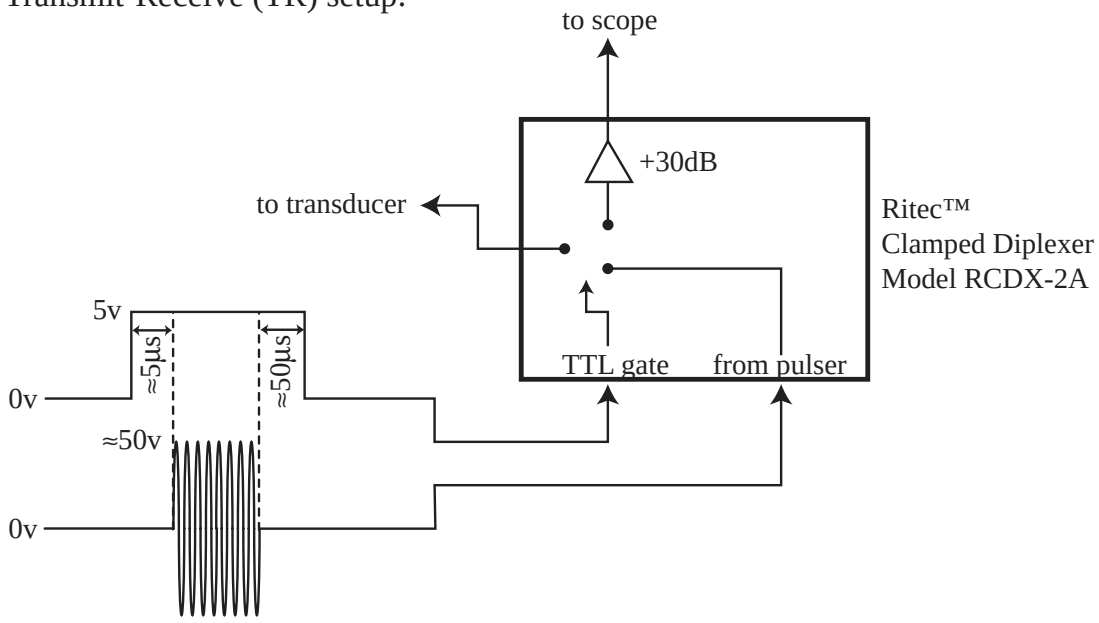

More precisely:

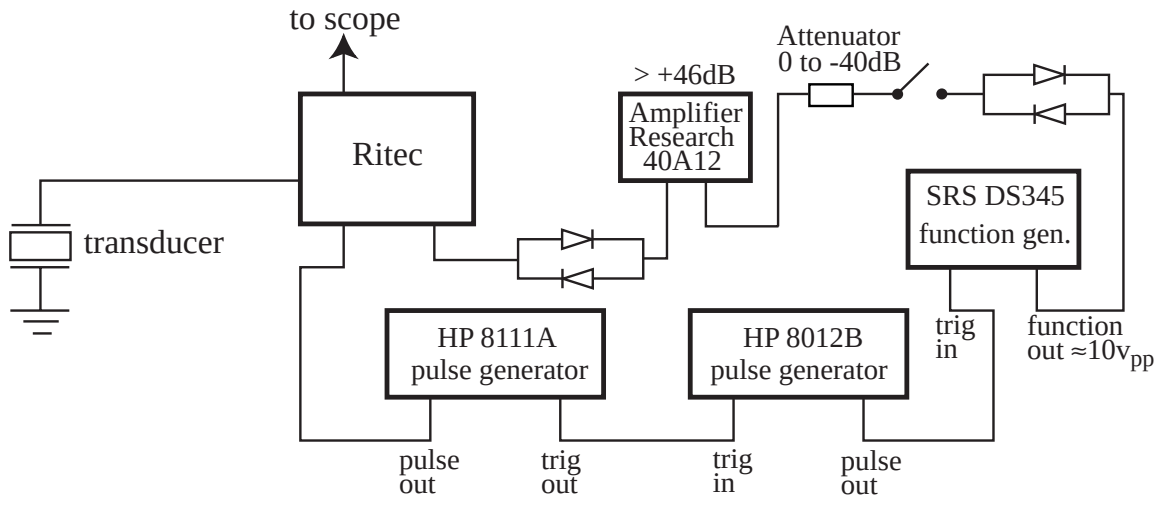

FIG. A.9 Circuit diagram for the transmit-receive (TR) experiments. The transducers used for these experiments were the piston style transducers.

Sheet source setups:

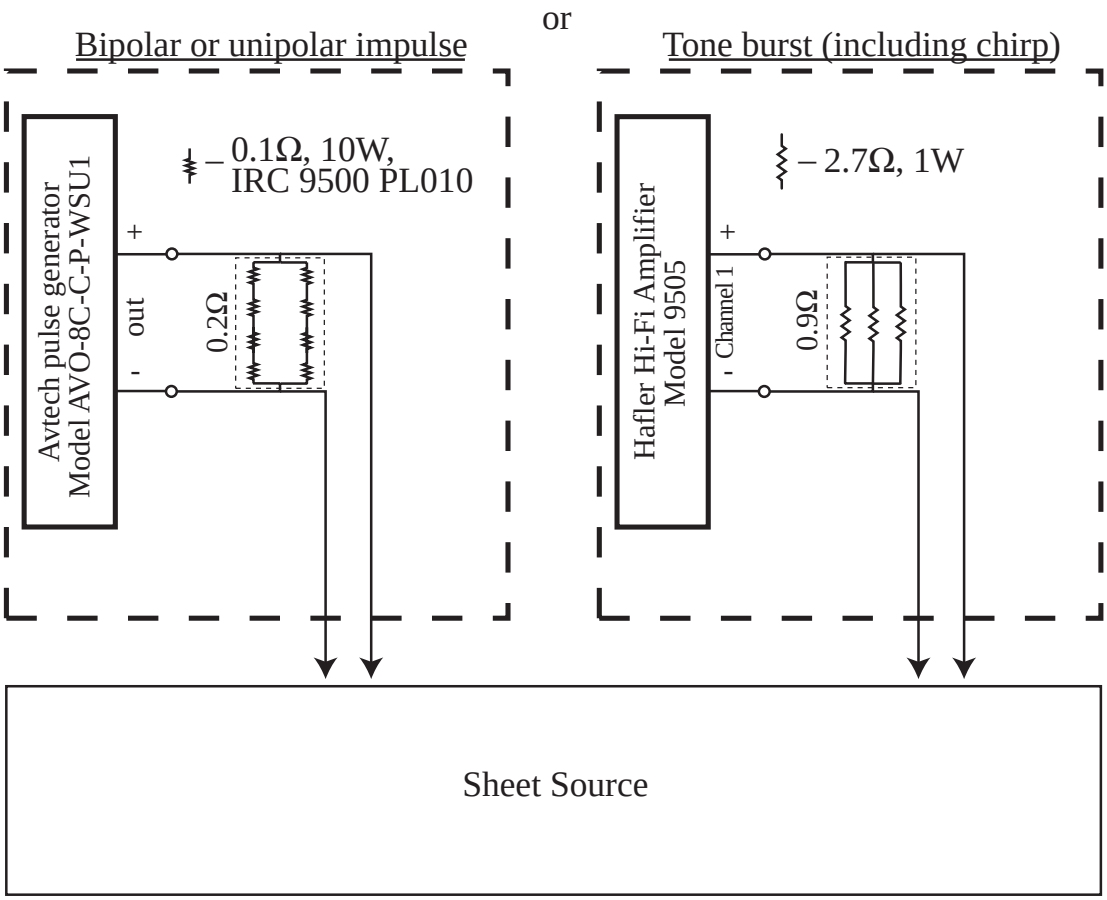

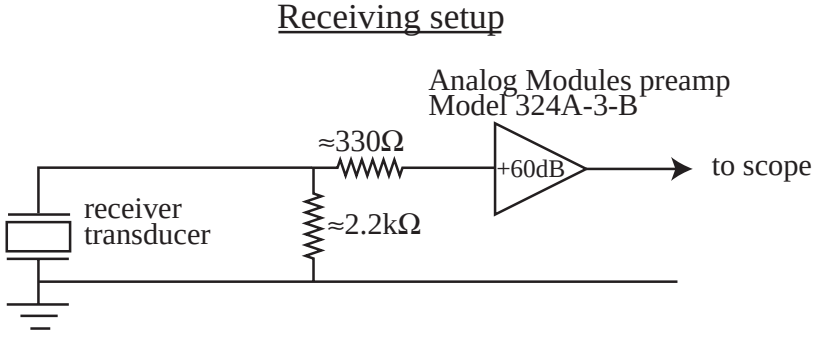

FIG. A.10 Circuit diagram for the driving and receiver systems for the impulse or chirp experiments using the sheet source and a separate hydrophone. Note the load resistors on the output of the driving systems.

A.6 Sheet Source Driven with a Linear Frequency Modulated (FM) Input

Yet another way to drive the sheet source is with a tone burst. Experiments have shown that it is capable of producing crisp high quality tone bursts as low as 1 kHz and as high as 1 MHz. It has been used to excite modes of oscillation of a submerged large hollow spherical shell below 20 kHz using tone bursts[111]. Due to its extremely high bandwidth capabilities an enticing experiment to perform is that of a chirped burst experiment. The idea behind this can be easily seen by considering the following example. Figure A.11 shows the Fourier transforms of two simple time series. The first is a simple sine wave tone burst. Its transform has the form of the familiar $\sin(f)/f$, or "sinc" function. If the frequency is allowed to increase during the burst, e.g as

$$P(t) = \sin\left[2\pi\frac{1}{2}(f_o + \beta t)t\right] \tag{A.5}$$

then it is possible to increase the width of the spectral peak. Equation (A.5) is an example of a linear FM pulse, or "chirp" signal (for $\beta > 0$). One can see that this increase in bandwidth is at a cost of spectral amplitude. Regardless, in this way it is possible to perform extra-high bandwidth experiments. Figure A.12 shows the measured pressure and spectral response for just such a signal driving the sheet source. A hydrophone placed 45 cm away from the sheet recorded this signal. The driving parameters were set to: $f_o = 0.3$ MHz, $\beta = 2.59 \times 10^{-3}$ MHz/μs, and $t_m = 270$ μs (pulse length). The Fourier transform in (b) confirms that the spectral response is similar to the chirped burst of Fig. A.11.

The generation of this signal was by no means trivial. Finding an amplifier and receiver transducer which have flat signal responses over these frequencies would be difficult to say the least. This keeping in mind that the sheet source represents a largely capacitive load to the amplifier. The sheet source was driven with a Hafler® Hi-Fi amplifier (see the preceding section). The frequency response of this amplifier is relatively uniform up to about 300 kHz but then begins to roll off. The transducer used for this measurement

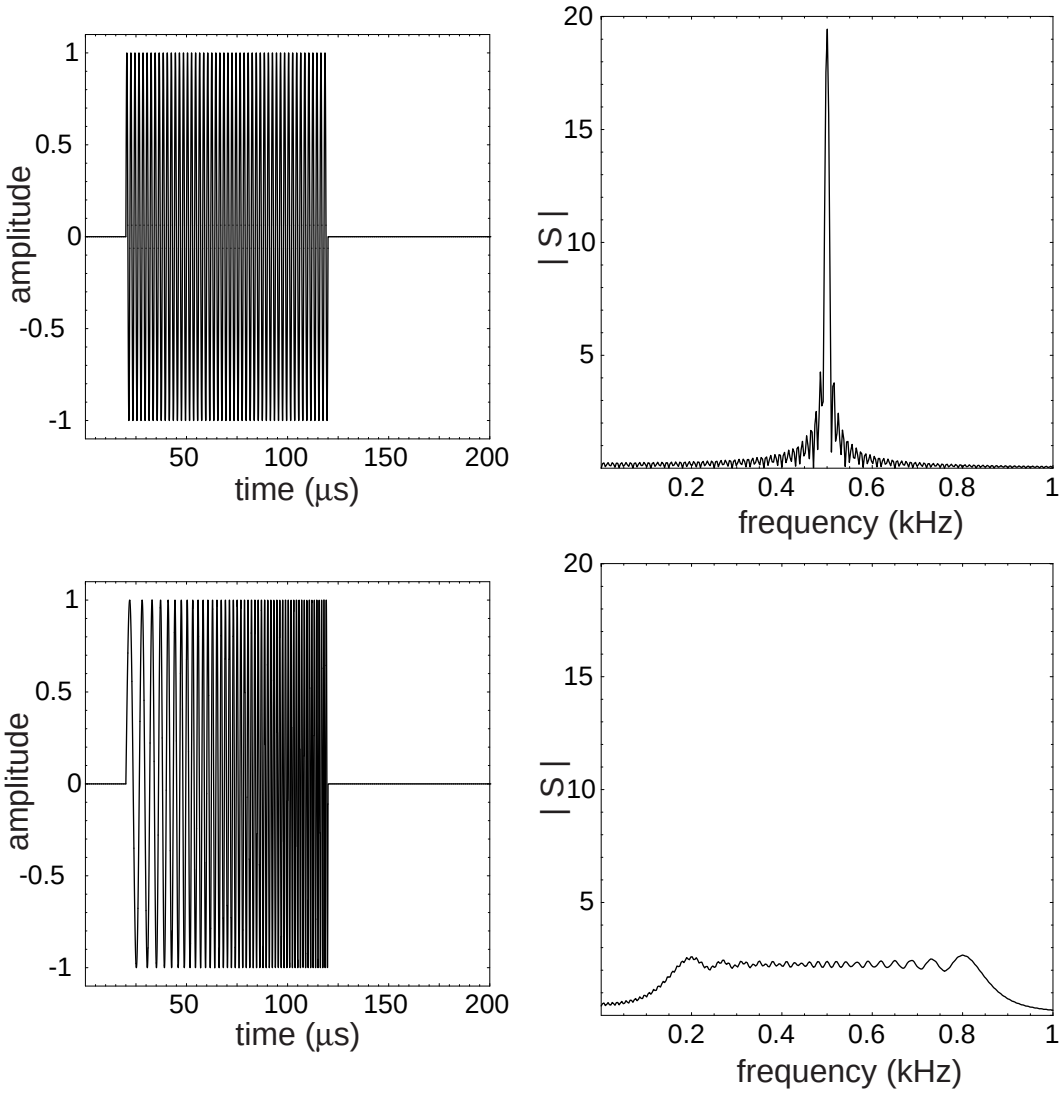

FIG. A.11 Comparison of the spectra of a simple tone burst and a chirped burst. Top row: sine wave tone burst having f_c = 0.5 MHz, Δt = 100 μs and its Fourier transform. Bottom row: sine wave chirped burst having f_o = 0.25 MHz, β = 0.5 MHz/μs, Δt = 100 μs and its Fourier transform. The chirped burst has much greater frequency content at the cost of spectral amplitude.

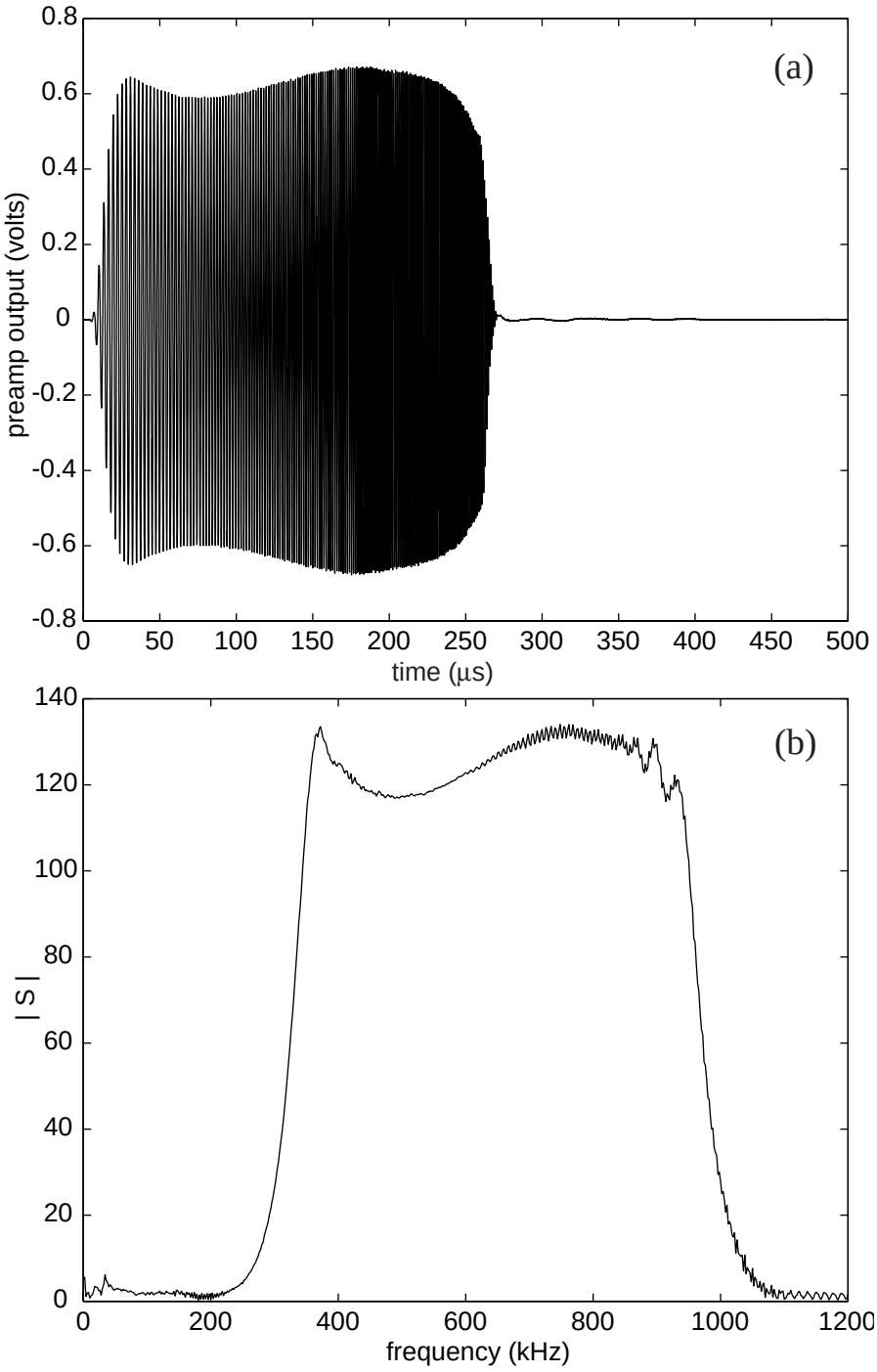

FIG. A.12 An example of the sheet source driven with a linear FM chirp input. (a) Time record of direct signal from the sheet with the hydrophone (Panametrics, model V3261) positioned 45cm away. (b) Spectrum of (a). See the text for special considerations needed to obtain this spectrum.

had a resonance frequency of 1 MHz. Due to these factors simply driving the sheet with a square envelope chirped burst as in Fig. A.11 resulted in a waveform which dropped to near zero signal at high frequency. To account for this the input voltage waveform was amplitude modulated and had the following form:

$$v(t) = A\frac{[1+(1-e^{0.4(t-t_m)})]}{[1+e^{0.4(t-t_m)}]}\frac{[-1+e^{0.2(t-5)}]}{[1+e^{0.2(t-5)}]}(3+4.804\times10^{-3}t)^{12} \times \sin\left[2\pi\left(f_o t+\frac{1}{2}\beta t^2\right)\right] \quad \text{(A.6)}$$

where A is an overall amplitude factor, t_m is the pulse length, f_o is the starting frequency, and β is the chirp parameter (increasing linear FM signal). This envelope was determined by trial and error and was only used for t_m = 270 μs, f_o = 0.3 MHz, β = 2.59 x 10^{-3} MHz/μs, where A = -3.90 x 10^{-7}. For other pulse lengths or frequency parameters the amplitude parameter A and various exponents must be changed to yield a suitable waveform. Because the shape of the spectrum of the measured acoustic chirp signal changed with the overall input voltage (i.e. the frequency response depends on input voltage in a nonlinear way) the author found it difficult to apply simple linear mathematical methods to obtain a measured waveform with a constant amplitude (i.e. a square waveform). Much trial and error was required to obtain the output shown. Figure A.13 shows the actual input signal used, from Eq. [A.6], and its corresponding spectrum.

Figure A.14 shows the backscattering spectrum for Shell B (air-filled with endcaps) at broadside incidence. The impulse experiments of Chapter 2 enabled the spectrum in this case to be measured up to 400 kHz [see Fig. 2.6(b)]. The present technique extends that range up to 1 MHz. The normalization procedure is the same as before. The measured backscattered time record is Fourier transformed. Its magnitude is then divided by the magnitude of the system spectrum [Fig. A.12(b)]. Finally a frequency independent amplitude factor is applied to enable a comparison with the calculated form function. In this case the measured spectrum is compared with the infinite PWS result and the approximate finite cylinder PWS result from Chapter 5. The dip near 800 kHz is the result of what has been called the thickness quasi-resonance[24]. It is also associated with the onset

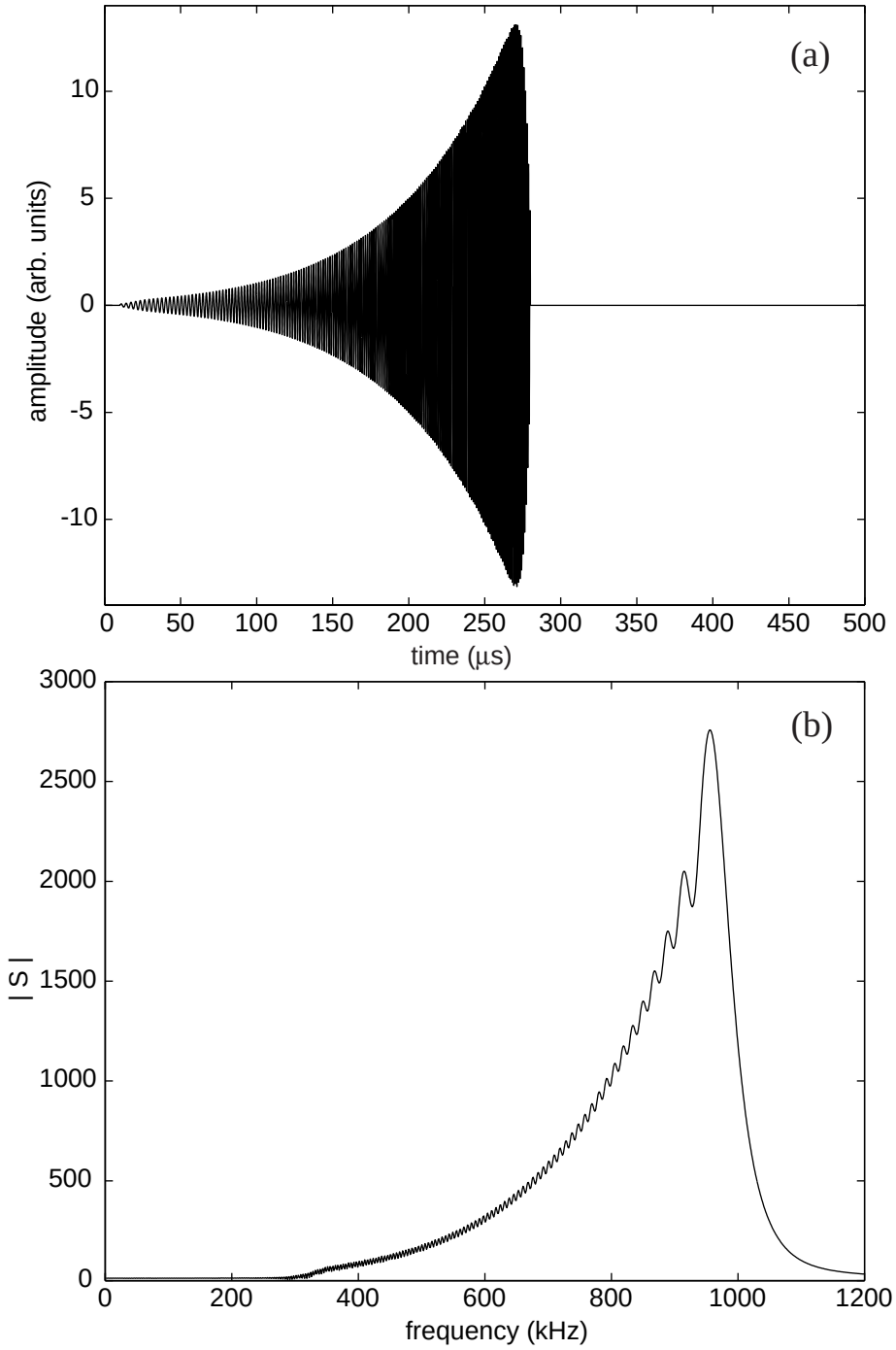

FIG. A.13 An example of the input signal for the sheet source driven with a linear FM chirp burst. (a) Time record of input voltage signal (Eq. [A.6]). (b) Spectrum of (a). With this input signal the acoustic signal (output) measured by a hydrophone is shown in Fig. A.12.

of the s_{2b} "backwards wave"[81]. Figures 7.22 and 8.1 were also obtained using the present technique.

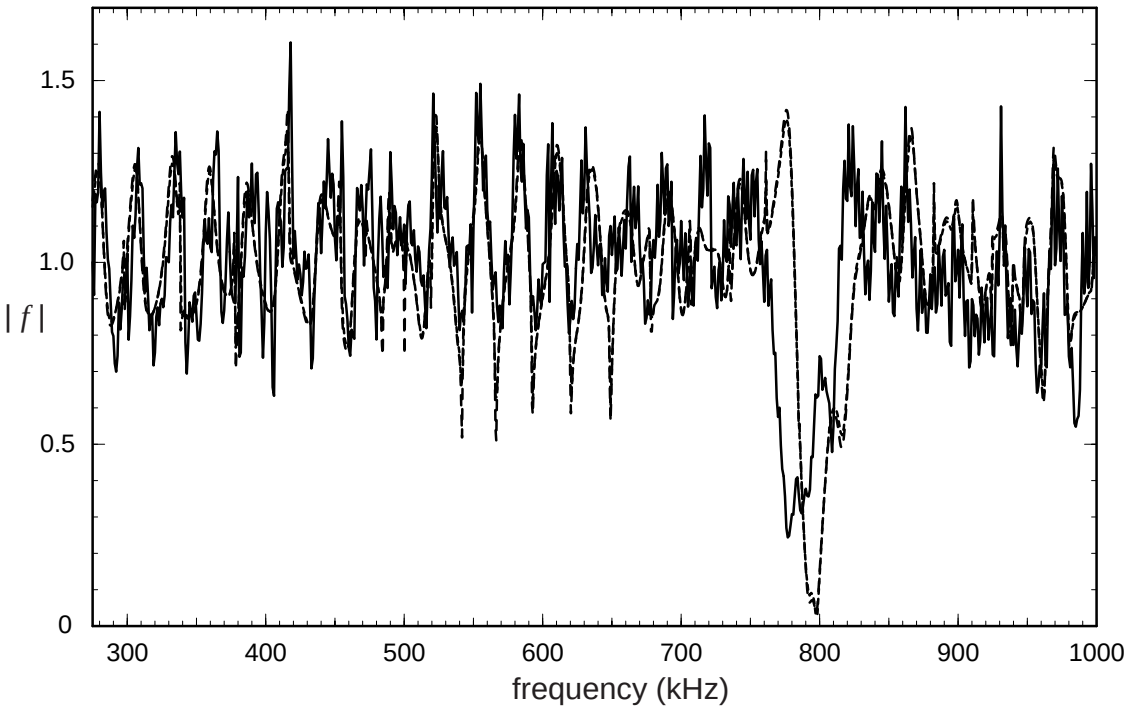

FIG. A.14 Normalized spectral magnitude for backscattering from Shell B (air interior with endcaps) using a 270 μs long chirp input. The lines correspond to: solid line, measured response; short dashed line, adjusted finite cylinder solution from Chapter 5 (see main text and Section 2.3); long dashed line, infinite PWS cylinder solution. The experimental response was normalized with the spectrum of the incident pulse measured with the system at the closest source-receiver separation distance possible and then multiplied by an overall constant (frequency independent) to qualitatively fit the two theoretical curves shown above.

[This page is intentionally left blank.]

Appendix B Computer Algorithms and Data Analysis

B.1 Short Time Fourier Transform (STFT)

The following code was used to calculate the time-frequency figures of Chapter 3.

sigcore_12.m

```
%  This Matlab m-file performs a STFT on a single time series data file.
%  This datafile consists of two columns, (t,v (voltage output from
%  preamp)).  This version is intended for use with experimental data.
%  Written by Scot Morse (4/10/97)
%  Version 1.1 makes a movie.
%  Version 1.2 is updated to include normalization for the new sheet.
%  Now writes to tiff files for better quality movies (i.e. download
%  directly to a vcr).
%  Last updated 11/4/97.

%
%.......Load time series data into variable full_data using built in GUI.
%

[file_name,path_name]=uigetfile('*.dat','Load initial time series data
                      file');
```

```
full_name=strcat(path_name,file_name);
fid=fopen(full_name,'r');
full_data=fscanf(fid,'%e',[2,Inf]);
full_data=full_data';
fclose(fid);

taxisdata=full_data(:,1)-full_data(1,1);  %Shift zero to start of file
valuedata=full_data(:,2);
valuedata=-1*(valuedata-mean(valuedata)); %Flip DC meaned voltage data

tlen=length(full_data);
dt=(taxisdata(2)-taxisdata(1))/1.0E-6;    %Time step in microseconds
tmax=dt*tlen;                             %Maximum time in raw data

df=1000/(dt*tlen);                        %Frequency step size in kHz.
flen=tlen/2-1;
faxisdata=(0:flen)*df;
fmax=faxisdata(flen);

max_time=input('Enter maximum time to display in microseconds: ');
max_time_int=round(max_time/dt);
max_freq=input('Enter maximum frequency to display in kHz: ');
max_freq_int=round(max_freq/df);
tnum=input('Enter the number of points in time to compute in the STFT: ');
Tp=input('Enter the length of the Blackman window in microseconds: ');
highest_value=input('Enter the amplitude reference with which to normalize
              the dB scale: ');
min_db=input('Enter the minimum value of signal to plot in -dB: ');
other_info=input('Enter primary descriptive string: ','s');
tilt_angle=input('Enter tilt angle of the cylinder: ');

%
%.....Create time series plot
%

ent_fig=figure(1);
  set(gcf,'Position',[180 180 610 457]);
axh11=subplot('Position',[0.1,0.7,0.50,0.3]);
  f1=plot(dt*[1:max_time_int],valuedata(1:max_time_int),'k-' ,'EraseMode'
     ,'background');
  ha=gca;
  set(ha,'Linewidth',1,'FontSize',9,'PlotBoxAspectRatio',[1.0,0.30,1.0]);
% xlabel('t (microseconds)')
% ylabel('P')
  title('Raw time data')
  time_ymin=min(valuedata)-0.05;
  time_ymax=max(valuedata)+0.05;
  axis([0.0 max_time time_ymin time_ymax])

%
%  Compute full forward FFT to see this data in the frequency domain
%

fzdata=fft(valuedata);
```

```
frdata=abs(fzdata(1:flen+1));

%
%  Divide by spectrum of the impulse response of the system
%

lowfreqcut=25.0;                          % Transition frequency (kHz)
lowfreqlim=round(lowfreqcut/df)-1;
%scalef=250.0;                            % Amplitude factor
rc1=1.253690E-6;                          % Low freq. RC time const.
rc2=0.250E-6;                             % High freq. RC time const.

%frnorm_old=zeros(flen+1,1);
frnorm=([0:df:flen]')*1000;               % Fill in freq vector (in Hz)

frnorm(1:lowfreqlim)=ones(lowfreqlim,1)*frnorm(lowfreqlim);
scalef=230.0;
frnorm=abs(scalef*sin(pi*1.40E-6*frnorm)./
       ((sqrt((1.0+(2.0*pi*rc1*frnorm).^2)).^3).*(1+(2*pi*rc2*frnorm).^-
       2).^0.4)+6.6*exp(-((frnorm-1.71E+5).^2)*5.91716E-10));

frnorm(1)=1000.0;
frnorm(2)=1000.0;
frnorm(3)=1000.0;
frdata=frdata./frnorm;
frnorm_mat=(ones(tnum,1)*(frnorm'))';

%
%.....Create full transform plot of the time series data
%

axh22=subplot('Position',[0.71,0.1,0.315,0.6]);
 f2=plot(frdata(1:max_freq_int),faxisdata(1:max_freq_int),'k-',
    'EraseMode','background');
  ha=gca;
  set(ha,'Linewidth',1,'FontSize',9,'PlotBoxAspectRatio',[0.5,1.0,1.0]);
% xlabel('f (kHz)')
% ylabel('|f|')
  title('Full spectrum')
  freq_ymax=max(frdata(1:500))+0.05;
  axis([0 freq_ymax 0.0 max_freq])

%
%.....Put in legend data and cylinder cartoon
%

axh12=axes('Position',[0.65,0.85,0.1,0.1],'Visible','off','NextPlot',
      'replace');
fig_info=char('STFT',strcat('Tp = ',num2str(Tp),' \mus'),other_info,
         file_name,strcat('\gamma',' = ',num2str(tilt_angle),'\circ'));
fig_text=text('String',fig_info,'Position',[0.0,0.05],'FontSize',14);

axh12p=axes('Position',[0.81,0.80,0.18,0.18],'Visible','off','NextPlot',
       'replace');
```

```
set(gca,'DataAspectRatio',[1,1,1]);
line([0 1],[-.6 -.6]);
line([0 1],[-.7 -.7]);
line([0 1],[-.8 -.8]);
line([.5 .5],[-0.9 -0.45]);
line([.44 .5],[-.51 -.45]);
line([.56 .5],[-.51 -.45]);
cyl_pic=patch([.1 .9 .9 .1],[-.0665 -.0665 .0665 .0665],'k');
rotate(cyl_pic,[0 0 1],tilt_angle,[.5 0 0]);

%
%.....Compute a 2-D Short Time Fourier Transform (STFT)
%

work_mat=(ones(tnum,1)*(valuedata'))';    % Fill time matrix with
identical columns

window_mat=zeros(tlen,tnum);              % Start constructing complete
window matrix

num=tlen;
num2=round(num/2);
twindfn=zeros(tlen,1);
taumin=0.0;
dtau=max_time/tnum;
for j=1:tnum
   tau=taumin+(j-1)*dtau;
   tauaxisdata(j)=tau;
   for i=1:tlen
     time=(i-1)*dt;
      t=time-tau+Tp/2;
     if (t > 0)&(t < Tp)
        twindfn(i)=(7938+9240*cos(2*pi*(t/Tp-0.5))+1430*
                   cos(4*pi*(t/Tp-0.5)))/18608;
     else
        twindfn(i)=0.0;
     end
   end
  window_mat(:,j)=twindfn;
end

allspec_mat=abs(fft(work_mat.*window_mat));

% Normalize with system impulse response

stftmat=allspec_mat(1:num2,:)./frnorm_mat;
%
%.......Normalize amplitude with user selected value
%.......(normally from peak at broadside)
%

stftmat=20*log10(stftmat/highest_value+eps);
shortmat=stftmat(1:max_freq_int,:);
min_reas_freq=round((1000/Tp)/df);
```

```
shortmat(1:min_reas_freq,:)=zeros(min_reas_freq,tnum)-90.0;

%
%.......Set a single coordinate to zero so imagesc can be used later
%.......instead of having to map values directly to the colormap using
%.......image.
%

shortmat(1,1)=0.0;

%
%.....Draw spectrogram
%

axh21=subplot('Position',[0.1,0.1,0.58,0.6]);
img=imagesc(shortmat,'XData',[0 max_time],'YData',[0 max_freq],
    'EraseMode','background');
axis xy;
caxis([min_db,0]);
  colormap(jet);
  ha=gca;
  set(ha,'FontSize',12);
  xlabel('t (microseconds)');
  ylabel('f (kHz)');
  barobj=colorbar('vert');

%
%.....Add in arrow pointing to position of back corner
%

  la=input('Enter L/a: ');
  cyl_radius=input('Enter cylinder radius: ');
  sound_speed=1.483;
  cent_dist=input('Enter Rs (distance in mm from source to center of
           cylinder): ');
  broad_offset=input('Enter relative time of front of specular in
              microseconds: ');
  delta12=pi/2-tilt_angle*pi/180+atan(2/la);
  sqrla=cyl_radius*sqrt(0.25*la*la+1);
%  c12_point=broad_offset+2*(sqrt((sqrla*sin(delta12)).^2+
            (cent_dist+sqrla*cos(delta12)).^2)-
            (cent_dist-cyl_radius))/sound_speed;
  c12_point=broad_offset+(cyl_radius+sqrla*cos(delta12)+
           sqrt((sqrla*sin(delta12)).^2+
           (cent_dist+sqrla*cos(delta12)).^2)-
           (cent_dist-cyl_radius))/sound_speed;

%
%.....Add line to density plot
%

  hold on
  plot([c12_point c12_point],[0 1000],'w-');
  hold off
```

```
%_____________________________Movie_____________________________________
%
%.....Start iteration on subsequent data files taking advantage of
%.....previously calculated window_mat and frnorm_mat.  These later files
%.....need to be identical in form to the first file.
%
%_______________________________________________________________________

file_basename=input('Enter file base name: ','s');
fileint_start=input('Enter starting integer of first file to load: ');
fileint_end=input('Enter starting integer of last file to load: ');
fileint_inc=input('Enter integer number to in(de)crement: ');
angle_start=input('Enter starting angle: ');
angle_inc=input('Enter the angle in(de)crement per selected file: ');
%
%.....Initialize movie matrix at start (much faster than dynamically
%.....adjusting matrix).
%
no_of_frames=(fileint_end-fileint_start)/fileint_inc;
%M=moviein(no_of_frames,ent_fig);
frame_no=1;
tilt_angle=angle_start-angle_inc;
fileint=fileint_start-fileint_inc;
for kk=fileint_start:fileint_inc:fileint_end
  tilt_angle=tilt_angle+angle_inc;
  fileint=fileint+fileint_inc;
  full_name=strcat(path_name,file_basename,num2str(fileint),'c.dat');
  fid=fopen(full_name,'r');
  full_data=fscanf(fid,'%e',[2,Inf]);
  full_data=full_data';
  fclose(fid);
  taxisdata=full_data(:,1)-full_data(1,1);
  valuedata=full_data(:,2);
  valuedata=-1*(valuedata-mean(valuedata));
  ent_fig=figure(1);
  set(gcf,'Position',[180 180 610 457]);
  subplot('Position',[0.1,0.7,0.50,0.3]);
    f1=plot(dt*[1:max_time_int],valuedata(1:max_time_int),'k-');
    ha=gca;
  set(ha,'Linewidth',1,'FontSize',9,'PlotBoxAspectRatio',[1.0,0.30,1.0]);
    title('Raw time data');
    time_ymin=min(valuedata)-0.05;
    time_ymax=max(valuedata)+0.05;
    axis([0.0 max_time time_ymin time_ymax]);
  fzdata=fft(valuedata);
  frdata=abs(fzdata(1:flen+1));
  frdata=frdata./frnorm;
  subplot('Position',[0.71,0.1,0.315,0.6]);
   f2=plot(frdata(1:max_freq_int),faxisdata(1:max_freq_int),'k-');
    ha=gca;
  set(ha,'Linewidth',1,'FontSize',9,'PlotBoxAspectRatio',[0.5,1.0,1.0]);
    title('Full spectrum');
    axis([0 freq_ymax 0.0 max_freq]);
  delete(fig_text);
```

```
axh12=axes('Position',[0.65,0.85,0.1,0.1],'Visible','off','NextPlot',
      'replace');
  fig_info=char('STFT',strcat('Tp = ',num2str(Tp),' \mus'),
           other_info,file_name,strcat('\gamma',' = ',num2str(tilt_angle),
            '\circ'));
  fig_text=text('String',fig_info,'Position',[0.0,0.05],'FontSize',14);
  delete(axh12p);
axh12p=axes('Position',[0.81,0.80,0.18,0.18],'Visible','off','NextPlot',
       'replace');
  set(gca,'DataAspectRatio',[1,1,1]);
  line([0 1],[-.6 -.6]);
  line([0 1],[-.7 -.7]);
  line([0 1],[-.8 -.8]);
  line([.5 .5],[-0.9 -0.45]);
  line([.44 .5],[-.51 -.45]);
  line([.56 .5],[-.51 -.45]);
  cyl_pic=patch([.1 .9 .9 .1],[-.0665 -.0665 .0665 .0665],'k');
  rotate(cyl_pic,[0 0 1],tilt_angle,[.5 0 0]);
  work_mat=(ones(tnum,1)*(valuedata'))';
  allspec_mat=abs(fft(work_mat.*window_mat));
  stftmat=allspec_mat(1:num2,:)./frnorm_mat;
  stftmat=20*log10(stftmat/highest_value+eps);
  shortmat=stftmat(1:max_freq_int,:);
  shortmat(1:min_reas_freq,:)=zeros(min_reas_freq,tnum)-90.0;
  shortmat(1,1)=0.0;
 subplot('Position',[0.1,0.1,0.58,0.6]);
  img=imagesc(shortmat,'XData',[0 max_time],'YData',[0
max_freq],'EraseMode','background');
  axis xy;
  caxis([min_db,0]);
    ha=gca;
    set(ha,'FontSize',12);
    xlabel('t (microseconds)');
    ylabel('f (kHz)');
    barobj=colorbar('vert');
    delta12=pi/2-tilt_angle*pi/180+atan(2/la);
  sqrla=cyl_radius*sqrt(0.25*la*la+1);
c12_point=broad_offset+2*(sqrt((sqrla*sin(delta12)).^2+
          (cent_dist+sqrla*cos(delta12)).^2)-(cent_dist-cyl_radius))/
          sound_speed;
  hold on
  plot([c12_point c12_point],[0 1000],'w-');
  hold off
%  M(:,frame_no)=getframe(ent_fig);
  frame_no=frame_no+1;
  if (kk<10)
    inst_filename=strcat('00',num2str(kk))
  else
    if (kk<100)
      inst_filename=strcat('0',num2str(kk))
    else
      inst_filename=num2str(kk);
    end
  end
```

```
  [x,map]=getframe(ent_fig);
  imwrite(x,map,inst_filename,'tiff');
end

%figure(2);
%set(gcf,'Position',[180 180 610 457]);
%axes('Position',[0.0,0.0,1.0,1.0],'Visible','off');
%kwait=waitforbuttonpress;
%movie(M,3,5);
```

B.2 Quadrature and Envelope of the Time Series: Analytic Signal

This section is intended to demonstrate the concept of the analytic signal as it is applied in the analysis of experimental data in this dissertation. In-depth discussions of the analytic signal and it's applicability may be found elsewhere (see e.g. Ref. [112]). In Chapter 3 it was desired to obtain quadrature (phase) information for multiple backscattered time records so that a synthetic aperture algorithm could be implemented. In Chapter 7 the envelope of a time record was needed. Both the quadrature and magnitude (envelope) may be obtained with what is often called the analytic signal. For the present purposes a graphical description of the analytic signal is sufficient. Figure B.1 shows the analytic signal for an experimental time record (an example of the a_0 meridional ray enhancement from Chapter 7). The original voltage signal is the black curve while the dashed helical curve is the analytic signal. In this case it is obtained by the built in function "hilbert" in Matlab®. Typically the Hilbert transform is defined as a real quantity (see below) which represents the quadrature or out of phase component of the original real-valued signal. When combined in complex form with the original signal one obtains the complex analytic signal. It is this complex analytic signal which was used in the synthetic aperture algorithm of Chapter 3. To obtain the envelope one may simply take the magnitude of the complex analytic signal. The quality of this envelope may be gauged by examining the example in Fig. 7.25 on page 250. For signals with an appreciable DC offset or unwanted low frequency components the envelope obtained in this way is not accurate.

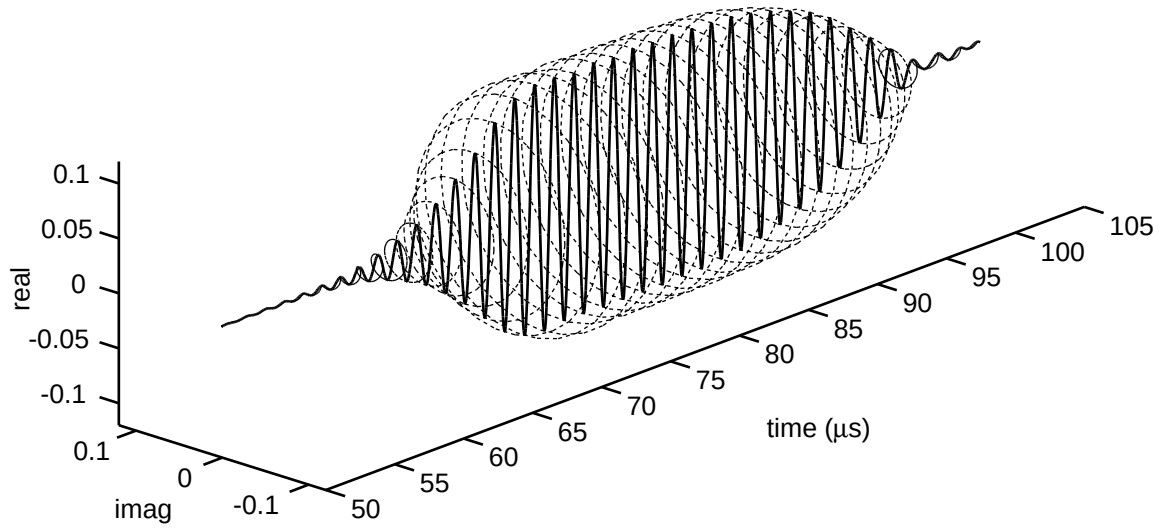

FIG. B.1 Solid line: experimental time record of a meridional ray backscattered return from a finite cylindrical shell; dashed line: analytic signal of the experimental record used to calculate the envelope of the time series.

A simple solution is to apply a high-pass digital filter to the time record before computing the envelope.

The definition of the Hilbert transform may be found, for example, in Ref. [112] and is given by,

$$F_{Hi}(t) = \frac{1}{\pi}\int_{-\infty}^{\infty} \frac{f(t')}{t'-t}dt' \tag{B.1}$$

where $f(t')$ is a real valued function. One can see that the Hilbert transform is a real quantity as well. The analytic signal is then defined to be the complex function,

$$f_{AS}(t) = f(t) - iF_{Hi}(t). \tag{B.2}$$

It is apparent that both the Hilbert transform and the analytic signal at a given time t depend on all past and future values of the function $f(t)$. The actual evaluation of the Hilbert transform is not as difficult as it may appear from Eq. (B.1). The Hilbert transform

may be thought of as a 90° phase shift filter—all sine components of a waveform transform into cosines and all cosine components transform into negative sines. This may be implemented with the Fourier transform[113]. One takes the Fourier transform of $f(t)$, replaces all the negative frequency components of the transform with zero, multiplies all the positive frequency components by two and performs an inverse Fourier transform. The imaginary part of the result is the Hilbert transform and the real part is the original time series.

B.3 Lamb Wave Reflection From the End of a Semi-Infinite Plate in Vacuum

The following code was used to calculate the reflection coefficients shown in Figs. 7.7(b), 7.8(b), and 8.5. This code requires input of the roots of all Lamb modes of importance.

Reflallvac.m

```
%.....Matlab program to calculate the reflection
%     coefficient for a single ANTISYMMETRIC Lamb
%     wave incident on a plate FREE edge using
%     eigenfunctions for an infinite plate in vacuum.
%     Input of the appropriate roots as a function
%.....of frequency is required.

%.....Written by Scot Morse, 3/5/98.
%.....Updated 5/29/98 for Plate B case.

%__________________BEGIN_____________________________
%.....SS304 Material parameters
  ct=3.141;
  cl=5.6750;
  rhoe=7.57;
  mu2=rhoe*ct*ct;
  lambda2=rhoe*(cl*cl-2*ct*ct);
%.....Plate B (Shell B) half thickness in mm
  h=0.50*0.1625*21.02;

%.....Load previously calculated roots:

file1='a0.dat';                          % Incident wave -->
file2='a0r.dat';                         % Reflected waves <--
```

```
file3='a1r.dat';                              %       ""
file4='num0r.dat';
file5='num0rc.dat';
file6='num1r.dat';
file7='num1rc.dat';
file8='num2r.dat';
file9='num2rc.dat';
file10='num3r.dat';
file11='num3rc.dat';
file12='num4r.dat';
file13='num4rc.dat';
file14='num5r.dat';
file15='num5rc.dat';
file16='num6r.dat';
file17='num6rc.dat';
file18='num7r.dat';
file19='num7rc.dat';
file20='num8r.dat';
file21='num8rc.dat';
file22='num9r.dat';
file23='num9rc.dat';

numfiles=23;

%.....Initilize full data matrix.  The column format
%.....assumed for the above files is
%  "frequency    real(kx)   imag(kx)   anything else"
%     1.5 MHz      xxxx      xxxx
%     1.498 MHz    xxxx      xxxx
%     . . .        . . .     . . .
%     0.002 MHz    xxxx      xxxx
% --> 750 rows

fulldata=zeros(750,3,numfiles);

for ii=1:numfiles
  filename=eval(strcat('file',num2str(ii)));
  fid=fopen(filename,'r');
  data=fscanf(fid,'%e',[5,Inf]);
  fclose(fid);
  fulldata(:,:,ii)=(data(1:3,:)).';
  clear('data');
end

%_____________________Begin main loop_____________________

%.....Initialize matrix that will hold all the reflection
%.....coefficients as well as frequency and error.

rcoeff=zeros(750,2*(numfiles-1)+2);

%.....Initialize matrix that will hold the power flow values
%.....for each mode.
```

```
powermat=zeros(750,numfiles);

jj=0;

for j=1:1:750

  jj=jj+1;
  clear('Rvec','Amat','Cvec');

  freqpos=750-(j-1);
  f=fulldata(freqpos,1,4);
  rkx=reshape(fulldata(freqpos,2,1:numfiles),numfiles,1);
  ikx=reshape(fulldata(freqpos,3,1:numfiles),numfiles,1);

%     Incident wave --> +a0 (the first component in kx)

  kx=rkx+i*ikx;
  w=2*pi*f;
  ks=w/ct;
  kl=w/cl;
  eta2=sqrt(kl*kl-kx.*kx);
  nu=sqrt(ks*ks-kx.*kx);

  lenkx=length(kx);

  zpos=[-1:.005:1]*h;                    % Discretization of end face
  znum=length(zpos);
  mat1=ones(1,znum);

%.....Stress equations (x=0) First column is incident
%     wave at each z position (-h,  0,  h).'.  Remaining
%.....columns are reflected waves at each z position.

  T31A=(2*i*mu2*(eta2.*kx)*mat1.*(cos(eta2*zpos)-((cos(eta2*h)./
       cos(nu*h))*mat1).*cos(nu*zpos))).';
  T11A=(mu2*(((2*eta2.*eta2-ks.*ks)*mat1).*sin(eta2*zpos)-(((nu.*nu-
       kx.*kx).*sin(eta2*h)./sin(nu*h))*mat1).*sin(nu*zpos))).';

%.....Displacement equations (x=0).  Used for normalization.

  uxA=(i*(kx*mat1).*sin(eta2*zpos)+((i*(nu.*nu-kx.*kx).*sin(eta2*h)./
      (2*kx.*sin(nu*h)))*mat1).*sin(nu*zpos)).';
  uzA=((eta2*mat1).*cos(eta2*zpos)+((2*eta2.*kx.*kx.*cos(eta2*h)./
      ((nu.*nu-kx.*kx).*cos(nu*h)))*mat1).*cos(nu*zpos)).';

%.....Normalize with the appropriate component of the energy flux vector
%.....of the incident mode: (vector velocity) dot (vector stress).
%.....Presently only calculates real part of P.

  power_rvec2=0.25*i*w*(2*h/znum)*sum(conj(uxA).*T11A+conj(uzA).*T31A-
              uxA.*conj(T11A)-uzA.*conj(T31A));


%.....Calculate the power flow ratio for each mode.  Use for checking
```

```
%.....the direction of energy flow of each mode.
  powermat(jj,:)=real(power_rvec2(1,:))/abs(power_rvec2(1));

  power_rvec=power_rvec2;

%.....Now assemble overdetermined set of equations A.r=C
%     where the r's are the unknown reflection coefficients
%     A is the matrix of stress values of the reflected
%     waves and C is the vector of stress values of the
%.....incident wave.

  Amat=ones(2*znum,lenkx-1);
  Amat(1:znum,:)=T31A(:,2:lenkx);
  Amat(znum+1:2*znum,:)=T11A(:,2:lenkx);
  Cvec=ones(2*znum,1);
  Cvec(1:znum,1)=-T31A(:,1);
  Cvec(znum+1:2*znum,:)=-T11A(:,1);

%.....Compute reflection coefficients using built in Matlab
%.....least square capability.

  Dvec=Amat\Cvec;
  power_ratio=(real(power_rvec(2:numfiles))/(real(power_rvec(1)))).';
  power_ratioimag=(imag(power_rvec(2:numfiles))/(real(power_rvec(1)))).';
  Rvec=(conj(Dvec).*Dvec).*power_ratio;
  Rvecimag=(conj(Dvec).*Dvec).*power_ratioimag;

%.....Mean square error

  Error_vec=(Amat*Dvec-Cvec);
%  err=Cvec'*Cvec-Cvec'*Amat*Rvec;
  mserror=(Error_vec'*Error_vec)*2*h/znum;

  rcoeff(jj,1)=f;
  rcoeff(jj,2*numfiles)=mserror;
  rcoeff(jj,2:2:2*(numfiles-1)+1)=real(Rvec.');
  rcoeff(jj,3:2:2*(numfiles-1)+1)=real(Rvecimag.');

end

%.....Plot the reflection coefficients

  figure(1)
%  plot(rcoeff(1:jj,1),rcoeff(1:jj,2),'b-');
  plot(rcoeff(1:jj,1),abs(rcoeff(1:jj,2)),'k-');    % a0
  hold on
  plot(rcoeff(1:jj,1),abs(rcoeff(1:jj,4)),'k--');   % a1
  plot(rcoeff(1:jj,1),abs(rcoeff(1:jj,6)),'k-.');   % a2
  plot(rcoeff(1:jj,1),abs(rcoeff(1:jj,8)),'k:');    % a2*
  hold off
  xlabel('frequency (MHz)');
  ylabel('|d|^2 Pr');

%.....Plot the mean squared error
```

```
  figure(2)
  plot(rcoeff(1:jj,1),rcoeff(1:jj,2*numfiles),'k-');
  xlabel('frequency (MHz)');
  ylabel('error');

%.....Calculate and plot the total energy

  propdir=sign(powermat(1:jj,2:numfiles)+eps);

  tot_energy=sum((abs(rcoeff(1:jj,2:2:2*(numfiles-1)+1)).*propdir).');
  figure(3)
  plot(rcoeff(1:jj,1),tot_energy.','k-');
  max(tot_energy)
  min(tot_energy)
  axis([0 1.5 0.99 1.01]);
```

References

[1] G. Kaduchak, C. M. Wassmuth, and C. M. Loeffler, "Elastic wave contributions in high resolution acoustic images of fluid-filled, finite cylindrical shells in water," J. Acoust. Soc. Am. **100**, 64-71 (1996).

[2] S. S. Dodd, "Sonar Imaging of Elastic Fluid-Filled Cylindrical Shells," Ph.D. dissertation, University of Texas, Austin, Applied Research Laboratories (1995).

[3] P. L. Marston, "Leaky waves on curved scatterers. I. Fresnel width of coupling regions and elliptical Fresnel patches," J. Acoust. Soc. Am. **96**, 1893-1898 (1994).

[4] P. L. Marston, "Leaky waves on weakly curved scatterers. II. Convolution formulation for two-dimensional high-frequency scattering," J. Acoust. Soc. Am. **97**, 34-41 (1995).

[5] P. L. Marston, "Approximate meridional leaky ray amplitudes for tilted cylinders: End-backscattering enhancements and comparisons with exact theory for infinite solid cylinders," J. Acoust. Soc. Am. **102**, 358-369 (1997).

[6] P. L. Marston, "Spatial approximation of leaky wave surface amplitudes for three-dimensional high-frequency scattering: Fresnel patches and application to edge-excited and regular helical waves on cylinders," J. Acoust. Soc. Am. **102**, 1628-1638 (1997).

[7] P. L. Marston, "Approximations for Leaky Wave Amplitudes in Acoustic Imaging: Applications to High Frequency Sonar," in *Acoustical Imaging*, edited by S. Lees and L. A. Ferrari (Plenum Press, New York, 1997), Vol. **23**, pp. 369-374.

[8] S. F. Morse, P. L. Marston, and G. Kaduchak, "High-frequency backscattering

enhancements by thick finite cylindrical shells in water at oblique incidence: Experiments, interpretation and calculations," J. Acoust. Soc. Am. **103**, 785-794 (1998).

[9] M. C. Junger and D. Feit, *Sound, Structures, and Their Interaction*, (AIP published by the Acoustical Society of America), 1993.

[10] M. L. Rumerman, "Contribution of membrane wave reradiation to scattering from finite cylindrical steel shells in water," J. Acoust. Soc. Am. **93**, 55-65 (1993).

[11] A. N. Norris and D. A. Rebinsky, "Acoustic coupling to membrane waves on elastic shells," J. Acoust. Soc. Am. **95**, 1809-1829 (1994).

[12] C. N. Corrado, "Mid-frequency acoustic backscattering from finite cylindrical shells and the influence of helical membrane waves," Ph.D. dissertation, Massachusetts Institute of Technology, Department of Ocean Engineering (1993).

[13] M. Conti, "Mid-frequency Acoustic Scattering from Finite Internally-loaded Cylindrical Shells Near Axial Incidence," Ph.D. dissertation, Massachusetts Institute of Technology, Department of Ocean Engineering (1995).

[14] F. Léon, F. Lecroq, D. Décultot, and G. Maze, "Scattering of an obliquely incident acoustic wave by an infinite hollow cylindrical shell," J. Acoust. Soc. Am. **91**, 1388-1397 (1992).

[15] M. Tran-Van-Nhieu, "Scattering from a finite cylindrical shell," J. Acoust. Soc. Am. **91**, 670-679 (1991).

[16] X-L. Bao, "Echoes and helical surface waves on a finite elastic cylinder excited by sound pulses in water," J. Acoust. Soc. Am. **94**, 1461-1466 (1993).

[17] V. V. Muzychenko and S. A. Rybak, "Low-frequency resonance scattering of sound by finite cylindrical shells (review)," Sov. Phys. Acoust. **34**, 325-333 (1988).

[18] The plate speed is defined to be $c_p \equiv [E/\rho(1-\nu^2)]^{1/2}$ where E is Young's modulus,

ρ is the density and ν is Poisson's ratio. Alternately
$c_p = 2c_s[2-(c_l^2-2c_s^2)/(c_l^2-c_s^2)]^{-1/2}$. Using the parameters listed in Table I, the plate speed for SS304 is $c_p = 5.232$ km/s.

[19] V. V. Muzychenko, A. P. Paniklenko, and S. A. Rybak, "Dispersion curves for normal modes in cylindrical shell and conditions for spatial coincidence in the vicinity of the critical frequencies," Sov. Phys. Acoust. **30**, 47-51 (1984).

[20] G. Kaduchak, C. S. Kwiatkowski, and P. L. Marston, "Measurement and interpretation of the impulse response for backscattering by a thin spherical shell using a broad-bandwidth source that is nearly acoustically transparent," J. Acoust. Soc. Am. **97**, 2699-2708 (1995).

[21] The properties of this PVDF sheet differing from those found in Ref. 20 are its surface resistivity (0.1 Ω/square) and electrical capacitance (≈102 pF/cm^2). The PVDF film was purchased from AMP Inc., Valley Forge, PA.

[22] I.B. Andreeva and V.G. Samovol'kin, "Sound scattering by elastic cylinders of finite length," Sov. Phys. Acoust. **22**, 361-364 (1977).

[23] N.H. Sun and P.L. Marston, "Ray synthesis of leaky Lamb wave contributions to backscattering from thick cylindrical shells," J. Acoust. Soc. Am. **91**, 1398-1402 (1992)

[24] S. G. Kargl and P. L. Marston, "Ray synthesis of the form function for backscattering from an elastic spherical shell: Leaky Lamb waves and longitudinal resonances," J. Acoust. Soc. Am. **89**, 2545-2558 (1991).

[25] N. D. Veksler, V. M. Korsunskii, and S. A. Rybak, "Scattering of an obliquely incident plane wave by a circular cylindrical shell," Sov. Phys. Acoust. **36**, 5-7 (1990)

[26] J. M. Conoir, P. Rembert, O. Lenoir, and J. L. Izbicki, "Relation between surface helical waves and elastic cylinder resonances," J. Acoust. Soc. Am. **93**, 1300-1307 (1993).

[27] L. G. Zhang, N. H. Sun, and P. L. Marston, "Midfrequency enhancement of the backscattering of tone bursts by thin spherical shells," J. Acoust. Soc. Am. **91**, 1862-1874 (1992).

[28] G. Kaduchak and P. L. Marston, "Observation of the midfrequency enhancement of tone bursts backscattered by a thin spherical shell in water near the coincidence frequency," J. Acoust. Soc. Am. **93**, 224-230 (1993).

[29] P. L. Marston and N. H. Sun, "Backscattering near the coincidence frequency of a thin cylindrical shell: Surface wave properties from elasticity theory and an approximate ray synthesis," J. Acoust. Soc. Am. **97**, 777-783 (1995).

[30] M. Talmant, G. Quentin, J. L. Rousselot, J. V. Subrahmanyam and H. Überall, "Acoustic resonances of thin cylindrical shells and the resonance scattering theory," J. Acoust. Soc. Am. **84**, 681-688 (1988).

[31] G. S. Sammelmann, D. H. Trivett, and R. H. Hackman, "The acoustic scattering by a submerged, spherical shell. I: The bifurcation of the dispersion curve for the spherical antisymmetric Lamb wave," J. Acoust. Soc. Am. **85**, 114-124 (1989).

[32] L. B. Felsen, J. M. Ho, and I. T. Lu, "Three-dimensional Green's function for fluid-loaded thin elastic cylindrical shell: Alternative representations and ray acoustic forms," J. Acoust. Soc. Am. **87**, 554-569 (1990); erratum *ibid*. **89**, 1463-1464 (1991).

[33] N. Yen, L. R. Dragonette, and S. K. Numerich, "Time-frequency analysis of acoustic scattering from elastic objects," J. Acoust. Soc. Am. **87**, 2359-2370 (1990).

[34] D. H. Hughes, "Backscattering of sound by spherical shells in water," Ph. D. dissertation, Washington State University, 1992.

[35] L. R. Dragonette, D. M. Drumheller, C. F. Gaumond, D. H. Hughes, B. T. O'Connor, N-C. Yen, and T. J. Yoder, "The application of two-dimensional signal transformations to the analysis and synthesis of structural excitations observed in

acoustical scattering," Proc. IEEE **84**, 1249-1262 (1996).

[36] P. L. Marston, "Phase velocity of Lamb waves on a spherical shell: Approximate dependence on curvature from kinematics," J. Acoust. Soc. Am. **85**, 2663-2665 (1989).

[37] L. Cohen, "Time-Frequency Distributions — A Review," Proc. IEEE **77**, 941-981 (1989).

[38] S. Gade and K. Gram-Hansen, "The Analysis of Nonstationary Signals," Sound and Vibration **31**, 40-46 (1997).

[39] L. Cohen, *Time-Frequency Analysis*, (Prentice Hall, New Jersey, 1995).

[40] W. M. Ewing, W. S. Jardetzky, and F. Press, *Elastic Waves in Layered Media*, (McGraw-Hill, New York, 1957).

[41] K. F. Graff, *Wave Motion in Elastic Solids*, (Dover, New York, 1991).

[42] W. G. Carrara, R. S. Goodman, and R. M. Majewski, *Spotlight Synthetic Aperture Radar Signal Processing Algorithms*, (Artech House, Inc., Norwood, 1995).

[43] M. P. Hayes and P. T. Gough, "Broad-band Synthetic Aperture Sonar," IEEE J. Oceanic Eng. **17**, 80-94 (1992).

[44] D. L. Mensa, *High Resolution Radar Imaging*, (Artech House, Inc., Dedham, 1981).

[45] M. Born and E. Wolf, *Principles of Optics*, 6th ed. (Permagon, Oxford, 1980).

[46] G. Kaduchak and P. L. Marston, "Backscattering of chirped bursts by a thin spherical shell near the coincidence frequency," J. Acoust. Soc. Am. **93**, 2700-2706 (1993).

[47] K. Gipson, "Leaky Rayleigh Wave Ultrasonic Backscattering Enhancements: Experimental Tests of Theory for Tilted Solid Cylinders and Cubes," Ph.D. dissertation, Washington State University, Department of Physics (1998). For those persons interested in this work or in examining the sections referred to from within the present dissertation, it is expected that Gipson will shortly publish some of the dissertation results in the J. Acoust. Soc. Am.

[48] K. L. Williams, "Acoustical Scattering from an Elastic Sphere in Water: Surface Wave Glory, Resonances, and the Sommerfeld-Watson Transformation for Amplitudes," Ph.D. dissertation, Washington State University, Department of Physics (1985).

[49] G. V. Frisk, J. W. Dickey, and H. Überall, "Surface wave modes on elastic cylinders," J. Acoust. Soc. Am. **58**, 996-1008 (1975).

[50] N. D. Veksler, "Dispersion curves for the phase velocities of Lamb-type circumferential waves excited in a circular cylindrical shell in the scattering of a plane acoustic wave by the shell," Sov. Phys. Acoust. **35**, 600-602 (1990).

[51] P. L. Marston, "GTD for backscattering from elastic spheres and cylinders in water and the coupling of surface elastic waves with the acoustic field," J. Acoust. Soc. Am. **83**, 25-37 (1988).

[52] L. Flax, V. K. Varadan and V. V. Varadan, "Scattering of an obliquely incident acoustic wave by an infinite cylinder," J. Acoust. Soc. Am. **68**, 1832-1835 (1980).

[53] R. M. White, "Elastic Wave Scattering at a Cylindrical Discontinuity in a Solid," J. Acoust. Soc. Am. **30**, 771-785 (1958).

[54] L. M. Lyamshev, Sov. Phys. Acoust. **4**, 161 (1958).

[55] J. E. Greenspon, Doctoral dissertation, The Johns Hopkins University, June, 1956.

[56] J. E. Greenspon, "Flexural vibrations of a thick walled circular cylinder," Proceedings of the Third U. S. National Congress of Applied Mechanics, 163-173 (1958).

[57] D. C. Gazis, "Three-Dimensional Investigation of the Propagation of Waves in Hollow Circular Cylinders. I. Analytical Foundation," J. Acoust. Soc. Am. **31**, 568-573 (1959); and D. C. Gazis, "Three-Dimensional Investigation of the Propagation of Waves in Hollow Circular Cylinders. II. Numerical Results," *ibid*. **31**, 573-578 (1959).

[58] A. E. Armenakas, D. C. Gazis and G. Herrmann, *Free Vibrations of Circular Cylindrical Shells* (Pergamon Press, Oxford,1969).

[59] S. G. Kargl and P. L. Marston, "Observations and modeling of the backscattering of short tone bursts from a spherical shell: Lamb wave echoes, glory, and axial reverberations," J. Acoust. Soc. Am. **85**, 1014-1028 (1989); Errata, **89**, 2462 (1991).

[60] S. K. Numrich and H. Überall, "Scattering of Sound Pulses and the Ringing of Target Resonances," in *Physical Acoustics, High Frequency and Pulse Scattering*, edited by A. D. Pierce and R. N. Thurston (Academic, San Diego, 1992), Vol. 21, pp. 235-318.

[61] B. K. Sinha, T. J. Plona, S. Kostek, and S-K. Chang, "Axisymmetric wave propagation in fluid-loaded cylindrical shells. I: Theory," J. Acoust. Soc. Am. **92**, 1132-1143 (1992). B. K. Sinha, T. J. Plona, S. Kostek, and S-K. Chang, "Axisymmetric wave propagation in fluid-loaded cylindrical shells. II: Theory versus experiment," *ibid*, **92**, 1144-1155 (1992).

[62] F. Fahy, *Sound and Structural Vibration: Radiation, Transmission and Response*, (Academic, Orlando, 1985); see also, F. Fahy, "Acoustic Interaction Between Structures and Fluids," in *Handbook of Acoustics*, edited by M. J. Crocker, (John Wiley & Sons, Inc., New York, 1998), Chapter 10, pp. 127-144.

[63] R. H. Hackman, "Acoustic Scattering from Elastic Solids," in *Physical Acoustics, Underwater Scattering and Radiation*, edited by A. D. Pierce and R. N. Thurston (Academic, San Diego, 1992), Vol. 22, pp. 1-194.

[64] P. W. Smith, Jr., "Phase Velocities and Displacement Characteristics of Free Waves in a Thin Cylindrical Shell," J. Acoust. Soc. Am. **27**, 1065-1072 (1955).

[65] M. F. M. Osborne and S. D. Hart, "Transmission, Reflection, and Guiding of an Exponential Pulse by a Steel Plate in Water. I. Theory," J. Acoust. Soc. Am. **17**, 1-18 (1945).

[66] W. H. Press, S. A. Teukolsky, W. T. Vetterling, and B. P. Flannery, *Numerical Recipes in Fortran 77: The Art of Scientific Computing*, Volume 1 of *Fortran Numerical Recipes*,

(Cambridge, New York, 1996).

[67] J. F. M. Scott, "The free modes of propagation of an infinite fluid-loaded thin cylindrical shell," Journal of Sound and Vibration **125**, 241-280 (1988).

[68] M. A. Heckl, "Vibrations of One- and Two-Dimensional Continuous Systems," in *Handbook of Acoustics*, edited by M. J. Crocker, (John Wiley & Sons, Inc., New York, 1998), Chapter 49, pp. 579-596.

[69] J. Dickey and G. Maidanik, "The splitting of dispersion curves for the fluid-loaded plate," J. Acoust. Soc. Am. **98**, 2365-2367 (1995).

[70] H. Dabirikhah and C. W. Turner, "The coupling of the A_0 and interface Scholte modes in fluid-loaded plates," J. Acoust. Soc. Am. **100**, 3442-3445 (1996).

[71] F. Honarvar and A. N. Sinclair, "Acoustic wave scattering from transversely isotropic cylinders," J. Acoust. Soc. Am. **100**, 57-63 (1996).

[72] J. J. Faran, Jr., "Sound Scattering by Solid Cylinders and Spheres," J. Acoust. Soc. Am. **23**, 405-418 (1951).

[73] R. R. Goodman and R. Stern, "Reflection and Transmission of Sound by Elastic Spherical Shells," J. Acoust. Soc. Am. **34**, 338-344 (1962).

[74] R. D. Doolittle and H. Überall, "Sound Scattering by Elastic Cylindrical Shells," J. Acoust. Soc. Am. **39**, 272-275 (1965).

[75] A. I. Lur'e, Three-Dimensional Problems of the Theory of Elasticity, (Interscience Publishers, New York, 1964), Chapter 7, p. 381.

[76] Z. Ye, "A novel approach to sound scattering by cylinders of finite length," J. Acoust. Soc. Am. **102**, 877-884 (1997).

[77] J. D. Jackson, *Classical Electrodynamics*, 2nd ed. (Wiley, New York, 1975) Sec. 9.

[78] A. Leissa, *Vibrations of Shells*, (AIP, published by the Acoustical Society of America, 1993).

[79] J. Miklowitz, *The Theory of Elastic Waves and Waveguides*, (North-Holland, New York, 1978), pp. 62-63, 152-154.

[80] G. N. Watson, *A Treatise on the Theory of Bessel Functions*, 2nd ed. (Cambridge University Press, Cambridge, 1995) Secs. 2.1 - 2.2.

[81] G. Kaduchak and P. L. Marston, "Traveling-wave decomposition of surface displacements associated with scattering by a cylindrical shell: Numerical evaluation displaying guided forward and backward wave properties," J. Acoust. Soc. Am. **98**, 3501-3507 (1995).

[82] P. L. Marston, "Geometrical and Catastrophe Optics Methods in Scattering," in *Physical Acoustics, High Frequency and Pulse Scattering*, edited by A. D. Pierce and R. N. Thurston (Academic, San Diego, 1992), Vol. 21, pp. 1-234.

[83] P. M. Morse and H. Feshbach, *Methods of Theoretical Physics* (McGraw-Hill, New York, 1953), Part I, p. 151.

[84] S. L. Means and R. R. Goodman, "Structural intensity of acoustically excited waves in a fluid-loaded elastic plate," J. Acoust. Soc. Am. **102**, 335-341 (1997).

[85] P. J. Torvik, "Reflection of Wave Trains in Semi-Infinite Plates," J. Acoust. Soc. Am. **41**, 346-353 (1967).

[86] I. A. Viktorov, *Rayleigh and Lamb Waves*, (Plenum Press, New York, 1967).

[87] B. A. Auld, and E. M. Tsao, "A Variational Analysis of Edge Resonance in a Semi-Infinite Plate," IEEE Trans. Sonics and Ultras., **SU-24**, 317-326 (1977).

[88] S. Y. Zhang, J. Z. Shen, and C. F. Ying, "The Reflection of the Lamb Wave by a Free Plate Edge: Visualization and Theory," Materials Evaluation **46**, 638-641 (1988).

[89] M. Ech-Cherif El-Kettani, P. Pareige, F. Luppé, J. Ripoche, "Experimental Study of the Conversion of Lamb Waves at the End of an Immersed Plate," Acustica **82**, 251-259 (1996).

[90] R. Briers, O. Leroy, and G. N. Shkerdin, "Conversion of a Stoneley wave at the extremity of a fluid loaded plate," J. Acoust. Soc. Am. **101**, 1347-1357 (1997).

[91] G. Kaduchak, D. H. Hughes, and P. L. Marston, "Enhancement of the backscattering of high-frequency tone bursts by thin spherical shells associated with a backwards wave: Observations and ray approximation," J. Acoust. Soc. Am. **96**, 3704-3714 (1994).

[92] P. M. Morse, *Vibration and Sound* (Acoustical Society of America, AIP, 1995), 5^{th} printing, pp. 305-307.

[93] L. R. Dragonette, S. K. Numrich, and L. J. Frank, "Calibration technique for acoustic scattering measurements," J. Acoust. Soc. Am. **69**, 1186-1189 (1981).

[94] E. O. Brigham, *The Fast Fourier Transform and its Applications*, (Prentice Hall, New Jersey, 1988), sec. 9.4.

[95] J. Shen, S. Zhang, and C. Ying, "The reflection of the Lamb wave in a semi-infinite plate," Chinese J. Acoustics **9**, 27-35 (1990).

[96] K. Portz, G. I. Stegeman, and A. A. Maradudin, "Rayleigh wave reflection at plate edges," Appl. Phys. Lett. **38**, 856-858 (1981).

[97] R. D. Gregory and I. Gladwell, "The reflection of a symmetric Rayleigh-Lamb wave at the fixed or free edge of a plate," J. of Elasticity **13**, 185-206 (1983).

[98] Q. -G. Zhu, H. J. Ruf, and W. G. Mayer, "Lamb wave radiation from plate termination in a liquid," Ultrasonics **29**, 459-463 (1991).

[99] J. -F. Piet, G. Quentin, M. de Billy, Q. -G. Zhu, and W. G. Mayer, "Phase of Lamb wave radiation from a plate immersed in a liquid," Ultrasonics **30**, 297-300 (1992).

[100] J. Virieux, "P-SV wave propagation in heterogeneous media: Velocity-stress finite difference method," Geophysics **51**, 889-901 (1986).

[101] J. G. Maloney and K. E. Cummings, "Adaptation of FDTD techniques to acoustic

modeling," in 11th Annual Review of Progress in Applied Computational Electromagnetics, Monterey, CA, 1995, Vol. 2, pp. 724-731.

[102] F. D. Hastings, J. B. Schneider, and S. L. Broschat, "Application of the perfectly matched layer (PML) absorbing boundary condition to elastic wave propagation," J. Acoust. Soc. Am. **100**, 3061-3069 (1996).

[103] T. R. Kane, "Reflection of Flexural Waves at the Edge of a Plate," J. Appl. Mech. **21**, 213-220 (1954); T. R. Kane, "Reflection of Dilatational Waves at the Edge of a Plate," *ibid*. 219-227, June (1957).

[104] I-Tai Lu, H. L. Bertoni, and H-Y. Chen, "Coupling of plate waves at joints," J. Acoust. Soc. Am. **92**, 510-526 (1992).

[105] H. D. McNiven, "Extensional Waves in a Semi-Infinite Elastic Rod," J. Acoust. Soc. Am. **33**, 23-27 (1961).

[106] J. Zemanek, Jr., "Experimental and Theoretical Investigation of Elastic Wave Propagation in a Cylinder," Ph.D. thesis, Univ. of Calif., Los Angeles (1962).

[107] H. Lamb, "On Waves in an Elastic Plate," Proc. Roy. Soc. (London), **93**, 114-128 (1917).

[108] R. D. Mindlin, "Waves and Vibrations in Isotropic, Elastic Plates," in *Structural Mechanics*, Proceedings of the First Symposium on Naval Structural Mechanics (Pergamon, Oxford, 1960), pp. 199-232.

[109] J. F. Claerbout, *Fundamentals of Geophysical Data Processing with Applications to Petroleum Prospecting*, (McGraw-Hill, New York, 1976), pp. 105-110.

[110] V. A. Del Grosso and C. W. Mader, "Speed of Sound in Pure Water," J. Acoust. Soc. Am. **52**, 1442-1446 (1972).

[111] S.F. Morse, B. T. Hefner, P. L. Marston, and K. L. Williams, "Wide bandwidth and low-frequency target response measurements with a large PVDF sheet source outside the laboratory," J. Acoust. Soc. Am. **101**, 3198 (1997).

[112] R. Bracewell, *The Fourier Transform and its Applications*, (McGraw-Hill, New York, 1965).

[113] *Signal Processing Toolbox User's Guide*, Matlab (The Math Works, Inc., December, 1996).